SMALL INTESTINAL TUFT CELL SPECIFICATION AND BEHAVIOR IN HOMEOSTASIS AND INTESTINAL INFLAMMATORY DISEASE

By

Amrita Banerjee

Dissertation

Submitted to the Faculty of the

Graduate School of Vanderbilt University

In partial fulfillment of the requirements

For the degree of

DOCTOR OF PHILOSOPHY

in

Cell and Developmental Biology

May 10, 2019

Nashville, TN

Approved:

Guoqiang Gu, Ph.D.

Christopher Wright, D.Phil.

Robert J. Coffey, M.D.

Christopher Williams, M.D., Ph.D.

Ken S. Lau, Ph.D.

For my family, without whose support

this work would not have been possible.

ACKNOWLEDGEMENTS

I am deeply indebted to my mentor Dr. Ken Lau for his support and guidance during my five years in his lab. He has afforded me every opportunity to develop my research, writing, and computational skills. He encourages me to think deeply about my experiments without forgetting about the big picture. My progress in all aspects of my training are due to his patience and tutelage. Thank you for giving me the freedom to explore my intellectual curiosity as well as the support to ensure that I did not go astray. I would like to thank my committee members: my chair Dr. Guoqiang Gu, my co-chair Dr. Chris Wright, Dr. Robert Coffey, and Dr. Christopher Williams for their many years of guidance and encouragement. From my first class with Dr. Gu, he has always expressed a willingness to offer his mentorship and assistance in making me a better scientist. I am grateful to Dr. Wright for acting as the co-chair of my committee and providing his support to ensure that everything remained on track. I am thankful to Dr. Coffey, who in classes, one-on-one meetings, and presentations, has always asked the most perspicacious questions to broaden my thinking. And finally, I am thankful toward Dr. Williams, whose insight into my work I have always valued. I am deeply grateful for all the constructive criticism, insight, and encouragement each has offered towards my science and my career.

Science does not happen in a vacuum and my work is no exception. I am incredibly thankful for the supportive and collaborative atmosphere that Dr. Lau has fostered in his lab, which made all the difference during my training. Chuck, thank you for your scientific contributions to my work but also for offering your wit and humor from as near as the next bay over to as far as Western Australia. Joey, I cannot overstate how valuable your help and advice has been to my graduate training. Cherie', thanks for always thinking the same and keeping your Slack window open at all times. Hyeyon, my undergraduate extraordinaire, I appreciate your persistence with any project that I handed you as your efforts were invaluable in the completion of this dissertation. Thank you all for your friendship and support these past four and a half years. I also want to thank

all the members of the Lau, Coffey, and Goldenring labs, past and present, for their advice, encouragement, and guidance throughout my graduate training. I am incredibly fortunate to have been a part of the Cell and Developmental Biology Department and the Epithelial Biology Center these past years. I also want to acknowledge the funding sources that have supported my graduate training, including NIH Grant RO1 DK103831 as well as support from the Crohn's and Colitis Foundation of America and the Vanderbilt Microbiome Institute. Finally, the shared resources from the Vanderbilt DDRC, Flow Cytometry Core, TPSR, and DAC were essential to this work.

Outside of the lab, I have been blessed with the most wonderful friends and family. Joan, thank you for your friendship from our first days in Alspaugh on East Campus to graduate school in Nashville for me and medical school in Cleveland for you. I am so excited to see and share in all the amazing things you are sure to accomplish. I want to thank my family, both present and absent, for shaping me into the person I am. To the memory of Lt. Col. Bimal Chandra Banerjee and Smt. Amita Roy, who left behind a wonderful legacy as well as the finest parents a person could ask for. To the late Dr. Minakshi Midya, whose presence and wisdom is still felt after more than a decade. To my grandmother, Smt. Anjali Banerjee, who always keeps me in her thoughts and lets me recite Keats to her. To my grandfather, Dr. Indra Shekhar Roy, whose devotion to the health and welfare of his community has been an inspiration. I am also grateful to my entire family in Kolkata and elsewhere who, despite the distance, have shown me nothing but support and encouragement.

Finally, to Ma, Baba, and Dada – I cannot say enough times or with sufficient accuracy what our foursome means to me. Thank you for all the "one last thing(s)" you have to say to me and for celebrating all the highs and cheering me on through the lows. I cherish the adventures we have experienced thus far and am so excited for the numerous that lie ahead.

TABLE OF CONTENTS

Section Page

Dedication ii
Acknowledgements iii
List of Figures ix
List of Tables xi
Preface xii

Chapter

I. Background – The small intestinal epithelium in health and disease 1
Inflammatory bowel disease 1
The intestinal stem cell niche 3
Paneth cell differentiation and function 5
The commensal microbiome and microbial-derived metabolites 7
Population-level microbiome analysis 9
Host metabolites 10
Organoid culture 12
Systems biology and single-cell analysis 14
Background on DISSECT-CyTOF 15
Background on droplet-based single-cell RNA-sequencing (scRNA-seq) 15
Background on p-Creode 16
Mouse models 17
TNF$^{\Delta ARE/+}$ model of Crohn's-like ileitis 17

II. Background – Specification and function of small intestinal tuft cells 19
Small intestinal tuft cells are a rare chemosensory cell type 19
Tuft cell morphology 20
Intracellular tuft cell structure 22

Small intestinal tuft cell specification 25
Tuft cell gene signature 28
Colonic tuft cells 29
Tuft cells in intestinal epithelial damage response 30
Tuft cells in gastrointestinal helminth infection 34

III. Single-cell analysis of differential response to inflammatory stimuli 40
Introduction 40
Results 43
A novel disaggregation procedure for investigating epithelial signaling heterogeneity 43
DISSECT application of CyTOF identifies a differentially signaling enterocyte subpopulation that is sensitized to TNF-α-induced cell death 44
Divergently responding enterocytes are neighbors within the intestinal epithelium 48
Discussion 50
Methods 54
Animal experiments and tissue collection 54
Declaration of approval for animal experiments 55
Cytometry analyses 55
Quantitative immunoblotting 55
Quantitative immunofluorescence imaging 55
Data analysis 56
Antibody reagents 56

IV. Trajectory mapping of single-cell data reveals an alternate origin for small intestinal tuft cells 59
Introduction 59
Results 61
p-Creode analysis of MxIF data generates robust topologies depicting intestinal cell specification 61
Tuft cells are specified outside the *Atoh1*-dependent secretory lineage in the small intestine in contrast to the colon 66
p-Creode application on scRNA-seq data generated from mouse colon reveals additional 6cell transition relationships 72

Discussion 74
Methods 78
Mouse experiments 78
Mass cytometry analysis 79
MxIF analysis 79
Single-cell RNA-sequencing 79
scRNA-seq data analysis 80
p-Creode overview 81

V. Small intestinal tuft cell specification and function in ileal inflammatory disease 82
Introduction 82
Results 84
Reduced tuft cell numbers are correlated to areas of ileal inflammation in human and mouse 84
Tuft cells are specified outside of the secretory lineage in the small intestine 91
Alterations in TCA metabolic pathways along the tuft cell trajectory are associated with induced tuft cell specification 98
Non-parasite-derived sources of succinate drive tuft cell specification 104
Microbiome sequencing identified expansion of Firmicutes in the AtohKO ileum 109
Succinate treatment ameliorates inflammation in the *TNF*$^{\Delta ARE/+}$ model 112
Discussion 114
Methods 118
Human tissue 118
Mouse experiments 119
Immunofluorescence staining and imaging 119
Image quantification 122
Immunohistochemistry staining 122
Enteroid experiments 124
Enteroid immunofluorescence staining 124
inDrops single-cell RNA sequencing 126
Pre-processing and batch correction of scRNA-seq data 127
p-Creode mapping and trajectory analysis 127

Trend analysis overview 127
Visualization and significance testing of trend analysis 129
Gene set enrichment analysis (GSEA) of differential expression 129
DNA extraction and 16s rRNA sequencing 130
Light chromatography-mass spectrometry (LC-MS) analysis of cecal luminal contents and whole tissue 130

VI. Discussion and future directions 132
Summary 132
Future Directions 136
Elucidating the mechanism of tuft cell hyperplasia in the AtohKO model 136
Succinate-induced suppression of inflammation in the *TNF*$^{\Delta ARE/+}$ model 137
Leveraging tuft cells therapeutically in the treatment of Crohn's disease 141

References 144

LIST OF FIGURES

Figure Page

1. The stem cell niche of the small intestine 4
2. Distinct metabolic pathways drive epithelial cell function in the small and large intestine 8
3. Recapitulation of the stem cell niche in organoid culture 13
4. Structural characteristics of intestinal tuft or caveolated cells 23
5. Small intestinal tuft cells induce a type 2 immune response following eukaryotic colonization of the gut 38
6. TNF-α induces heterogeneous villus epithelial cell death 42
7. DISSECT disaggregation applied to CyTOF to investigate TNF-α signaling heterogeneity at single-cell resolution 45
8. Analysis and modeling of 21-dimensional data over multiple biological replicates 47
9. p-ERK activated in cells neighboring the dying cell promotes survival 49
10. p-Creode analysis of single-cell multiplex immunofluorescence (MxIF) data reveals an alternate origin for tuft cells in small intestine versus colon 63
11. Robust sampling of p-Creode results from the gut epithelium 65
12. Overlay of different epithelial cell-specific protein markers on p-Creode topologies 67
13. p-Creode analysis of small intestinal cell trajectories without proliferative markers 68
14. Tuft cells respond to exogenous stimulus in a different way compared to other secretory epithelial cells 69
15. Tuft cells have alternative specification requirements in small intestine versus the colon 71
16. Tuft cells specification as a function of *Atoh1* 73
17. inDrops scRNA-seq reveals the developmental trajectory of Reg4+ secretory cells in the murine colon 75
18. scRNA-seq data generated from the colonic epithelium by inDrops 77
19. Human tuft cells are decreased in patients with ileal Crohn's disease 85
20. Decreased tuft cell number is correlated to high inflammation in a the $TNF^{\Delta ARE/+}$ model 88
21. Image processing of immunofluorescence staining was used to quantify DCLK1+ tuft cell number versus severity of inflammation 90
22. p-Creode trajectory analysis of ileal epithelial scRNA-seq data supports an alternate origin for small intestinal tuft cells 92
23. t-SNE analysis of scRNA-seq of cell identity genes 94

24. Classification of p-Creode topology maps based upon tuft cell placement within absorptive or secretory lineage....97
25. Cell identity gene overlay on p-Creode graphs....99
26. Gene expression overlay of tuft cell-specific genes on p-Creode graphs....101
27. p-Creode analysis of small intestinal epithelium with enteroendocrine cells....103
28. p-Creode analysis of GSE92332 scRNA-seq dataset....105
29. Analysis of AtohKO tuft cell gene expression identified upregulation in metabolic pathways....107
30. Trend dynamic analysis for p-Creode cell lineages....110
31. TCA cycle genes in the wildtype and AtohKO tuft cell lineages....113
32. Gene expression analysis of wildtype and AtohKO tuft cells....115
33. Tuft cell hyperplasia is microbiome-dependent....117
34. Luminal succinate is increased in the AtohKO model....120
35. Ileal microbiome distribution is altered in the AtohKO ileum....123
36. Succinate treatment mitigates inflammation in the *TNF*$^{\Delta ARE/+}$ model....125
37. AtohKO tuft cells express a similar transcriptional signature as wildtype tuft cells....134
38. Colonic tuft cells do not express the succinate-sensing receptor, *Sucnr1*....140

LIST OF TABLES

Table Page

1. Dimensions of enterocyte and tuft cell microvilli in mouse and human small intestine 21
2. Intestinal tuft cell markers and their proposed role in tuft cell function 27
3. Antibodies utilized for immunofluorescence imaging and flow cytometry.....58
4. Total number of villi counted for tuft cell quantification.....90

PREFACE

This dissertation is structured into six different chapters as outlined in the table of contents. Chapters I-IV are recreated from published literature, denoted by the citations at the beginning of each corresponding chapter. Chapter V is adapted from a manuscript in preparation at the time this dissertation was submitted. In addition, the introduction is divided into two separate chapters. Chapter I reviews the function of the small intestinal epithelium in homeostasis and disease while chapter II summarizes current literature on intestinal tuft cell specification. Figures, tables, and their corresponding legends from chapters I-IV are recreated from the relevant publications.

Chapter I

BACKGROUND

THE SMALL INTESTINAL EPITHELIUM IN HEALTH AND DISEASE

Recreated from: Sun Wook Kim, **Amrita Banerjee**, et al. “Defining the Intestinal Stem Cell Niche for Tissue Engineering and Disease Modeling.” *Encyclopedia of Tissue Engineering and Regenerative Medicine.* Jan 2018.

and

Jesse Lyons, Charles A. Herring, **Amrita Banerjee**, et al. "Multiscale Analysis of the Murine Intestine for Modeling Human Diseases." *Integrative Biology.* 2015. Print.

Inflammatory bowel disease

Inflammatory bowel diseases (IBD), such as Crohn’s disease (CD) and ulcerative colitis (UC), are a complex group of intestinal disorders believed to result from inappropriate interactions between commensal flora and the host immune system (Barthel *et al*, 2014; Manichanh *et al*, 2006; Laukoetter *et al*, 2008). Crohn’s ileitis, a CD subtype, is characterized by immune cell infiltration, goblet cell hyperplasia, and Paneth cell abnormalities in the ileum (Manichanh *et al*, 2006; Laukoetter *et al*, 2008). The global landscape of Crohn’s disease has changed profoundly in the last half century. Increasing industrialization in developing nations has altered environmental exposures and lifestyle behaviors, leading to dramatic increases in Crohn’s disease incidence (Molodecky *et al*, 2012; Murthy & van Lookeren Campagne, 2014). Yet, developed economies, such as those in Europe and North America, are still outpacing the rest of the global community in the incidence of this debilitating condition (Molodecky *et al*, 2012). Relapsing-remitting Crohn’s disease is diagnosed in young adulthood and, due to its lack of mortality, persists as a lifelong

condition (Halme *et al*, 2006). Precipitous outbreaks of abdominal constriction, diarrhea, fever, and other symptoms have a considerable impact on productivity and quality of life (Halme *et al*, 2006). In the absence of a curative therapy and increasing incidence, Crohn's disease will continue to be a significant global health concern. While Crohn's disease can affect the entire gastrointestinal tract, the American Gastroenterology Association approximates that 20% of patients have strictly ileal disease (Naser *et al*, 2012). Genome-wide association studies (GWAS) have identified 163 risk loci linked to Crohn's disease incidence (Naser *et al*, 2012; Spalinger *et al*, 2014; Burton, 2009). Three of the most frequently reported genes, *ATG16L1, NOD2*, and *XBP1*, are intestinal epithelial cell-specific hits that affect secretory Paneth cells (Barrett *et al*, 2009; Kaser & Blumberg, 2011; Patel & Stappenbeck, 2014). These genes control pathways crucial to Paneth cell function and their variants may, under the right circumstances, facilitate induction of ileal-specific Crohn's disease (Murthy *et al*, 2014; Lassen *et al*, 2014). GWAS identified a T300A polymorphism in autophagy-related gene 16L (*ATG16L*), a key component of the autophagy pathway (Murthy *et al*, 2014). Mice with a homologous variant, T316A, exhibited reduced cellular autophagy, a conserved degradation process, as well as abnormal lysozyme distribution in ileal Paneth cells (Lassen *et al*, 2014; Saitoh *et al*, 2008; Glick *et al*, 2010; Feng *et al*, 2015). Nucleotide-binding oligomerization domain-containing protein 2 (*NOD2*) is a pattern recognition receptor, that escorts Atg16L to the plasma membrane, contributing to autophagy induction (VanDussen *et al*, 2014). Approximately a third of Crohn's disease patients carry *NOD2* risk variants, while ileal biopsies from these patients show diminished or diffuse lysozyme content within Paneth cells (VanDussen *et al*, 2014; Yano & Kurata, 2009; Grootjans *et al*, 2011; Adolph *et al*, 2014). Yet, despite, these lines of evidence, neither *Nod2*$^{-/-}$ nor *Atg16L*$^{-/-}$ mice acquire spontaneous ileitis, indicating that the absence of these genes alone is not necessarily causative for development of ileal Crohn's disease (Deuring *et al*, 2014; Kaser *et al*, 2009). However, deletion of the X-box-binding protein 1 (Xbp1) in intestinal epithelial cells results in increased spontaneous enteritis, suggesting a critical role for the unfolded protein response and

endoplasmic reticulum stress in IBD pathogenesis (Kaser *et al*, 2009; Stappenbeck, 2010). Moreover, reduced autophagy and Paneth cell function was observed in Xbp1-null mice (Kaser *et al*, 2009; Stappenbeck, 2010). By these lines of evidence, autophagy and secretory function in Paneth cells are linked and have important implications for ileal Crohn's disease (Stappenbeck, 2010; Cadwell *et al*, 2009).

The intestinal stem cell niche

Small intestinal and large intestinal (colonic) tissues completely turnover in three to five days in the mouse, and five to seven days in the human (Darwich *et al*, 2014; Creamer *et al*, 1961). The unilaminar epithelium serves major functions in the small intestine and colon, and its cells are continually replenished by differentiation from stem cells. The small intestine and colon are anatomically distinct organs that have distinct functions in digestion, have differential microbial load, and are morphologically divergent (Atuma *et al*, 2001; Donaldson *et al*, 2015; Mowat & Agace, 2014; Rubin, 2007). Yet, stem cells of both organs are known to reside within the crypts of Lieberkühn (Figure 1), which are regularly invaginated areas of the epithelium that intercalate regions of post-mitotic, differentiated cells. Two main populations of stem cells were proposed: the crypt base columnar (CBC) cells discovered by Cheng and Leblond (Cheng & Leblond, 1974a), and +4 label retaining cells discovered by Potten (Potten *et al*, 1974). Seminal work performed in the Clevers lab identified Leucine-rich-repeat-containing G-protein coupled receptor 5 (*Lgr5*) as a *bona fide* CBC marker (Barker *et al*, 2007). Since this influential study, a variety of markers have been identified to mark CBCs (van der Flier *et al*, 2009; Kayahara *et al*, 2003), +4 cells (Takeda *et al*, 2011; Sangiorgi & Capecchi, 2008; Yan *et al*, 2011; Li *et al*, 2016, 2014; Montgomery *et al*, 2011; Powell *et al*, 2012), or both populations (Muñoz *et al*, 2012; Wong *et al*, 2012). The existence of single or multiple stem cell populations and their overlap is a topic of intense debate in the intestinal stem cell field and has been extensively reviewed elsewhere (Koo & Clevers, 2014; Yousefi *et al*, 2017).

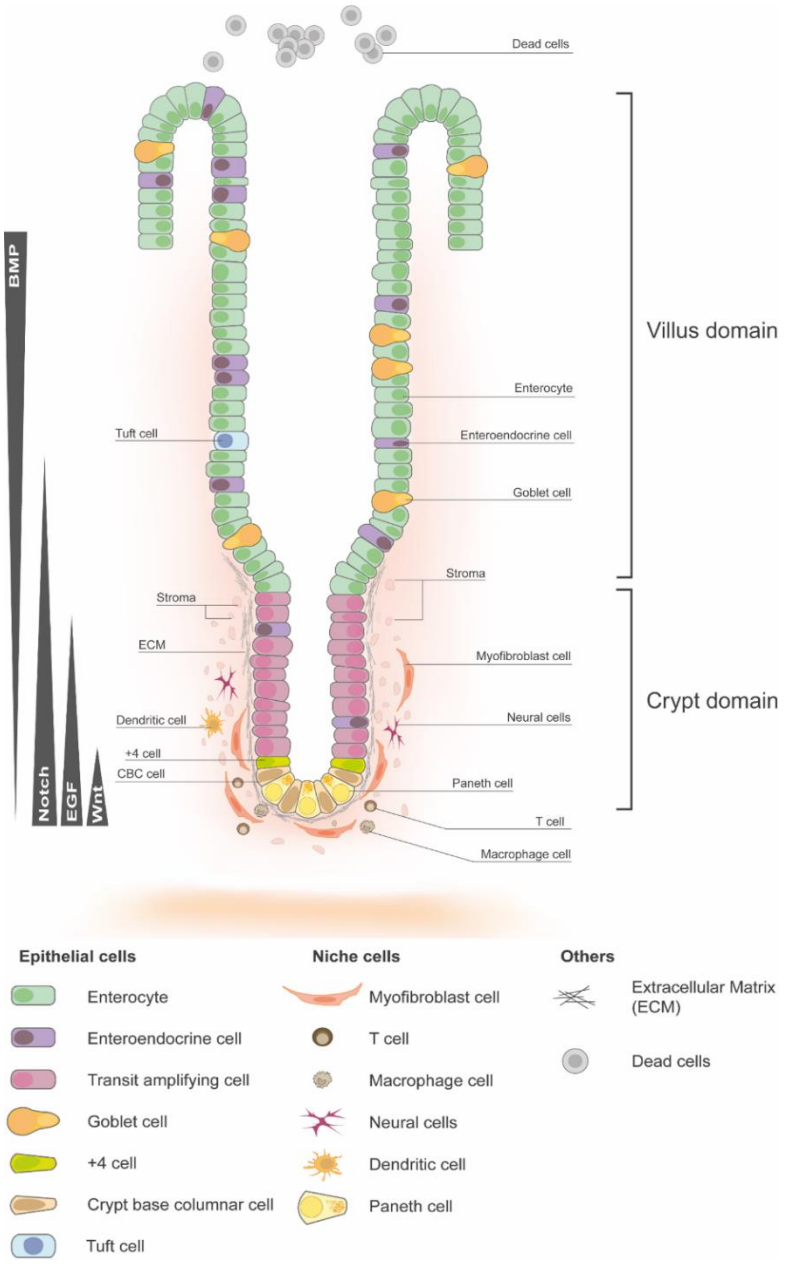

Figure 1. The stem cell niche of the small intestine. Two types of proposed intestinal stem cells the CBCs and +4 cells are located at the bottom of the crypt of Lieberkühn. Cells with committed fates migrate out of the stem cell niche into the transit-amplifying zone to eventually differentiate into the functional cell types of the intestine: the enterocytes, tuft cells, goblet cells, enteroendocrine cells, and Paneth cells. Cells on the villus domain are eventually shed off into the lumen. Stem cells at the crypt bottom reside within a niche comprised of various mesenchymal, neural, and immune cells, which provide an instructive signaling environment for stem cell fate decisions. Wnt ligands, EGF, and Notch ligands are highly expressed at the bottom of the crypt, whereas BMP gradually increases in the villus area than the crypt. The extracellular matrix physically and biochemically shapes the stem cell niche.

Two important properties, however, speak to the importance of the niche in directly controlling stem cell function. First, while there is evidence supporting asymmetric division of intestinal stem cells due to directional Wnt activation (Potten *et al*, 2002; Habib *et al*, 2013), it is now well-accepted that these stem cells divide symmetrically while population equilibrium is maintained by the process of neutral drift (Escobar *et al*, 2011; Snippert *et al*, 2010; Lopez-Garcia *et al*, 2010; Kozar *et al*, 2013). In this process, cells that are pushed out of the niche from mitotic pressure begin differentiation due to exposure to a differential signaling environment, while cells that remain in the center of the niche are more likely to maintain their stem cell states (Ritsma *et al*, 2014). This way, a stable number of stem cells is maintained while fueling the constant requirement of cells to replenish the epithelium. Second, several recent studies have pointed towards the plasticity of committed cells to regain stem cell identity when endogenous stem cells are perturbed by irradiation (Yan *et al*, 2011) or diphtheria toxin-based ablation (Tian *et al*, 2011). Potential Paneth, endocrine, and absorptive progenitor cells have been shown to demonstrate this activity thus far (Buczacki *et al*, 2013; Tetteh *et al*, 2016; Schonhoff *et al*, 2004; van Es *et al*, 2012; Yan *et al*, 2017a). What these studies speculate is that when space in the stem cell niche is made available from the loss of endogenous stem cells, cells with committed fates can migrate back to physically fill these empty spaces. Exposure of a stem cell signaling environment in the niche then allows these committed cells to re-adopt a stem cell identity. These studies highlight the importance of the signaling environment provided by the stem cell niche to instruct a stem cell to either maintain its identity or adopt a differentiated cell fate.

Paneth cell differentiation and function

Paneth cells, identified by the anatomist Josef Paneth in the late 1800s, are a pyramidal cell type intercalated between CBC stem cells at the base of the crypts of Lieberkühn in the small intestinal epithelium (Barker *et al*, 2007; Clevers & Bevins, 2013). Their role in intestinal innate immunity by their expression of anti-bacterial proteins has been well documented, but only

recently has their function as a “nurse cell” for neighboring stem cells been better appreciated. Paneth cells express critical components of key signal transduction pathways, including Notch ligands DLL1 and DLL4, WNT3a, and EGFR ligands TGF-α and EGF, along with the WNT receptor FZD5 (Sato *et al*, 2011a). These signaling pathways, discussed in the previous section, are essential in maintaining the balance between multipotency and differentiation within the stem cell zone. Stem cells strive to maximize cell-to-cell contact with neighboring Paneth cells since the ligands secreted from the latter have limited diffusion capacity (Farin *et al*, 2016; Gracz *et al*, 2015). *In vitro* experiments have confirmed this requirement, as increased organoid forming efficiency was observed when CD24+ Paneth cells were coupled to *Lgr5*+ stem cells compared to single cultured stem cells (Sato *et al*, 2011a).

While the other cell types of the intestinal epithelium migrate up through the crypt-lumen axis, Paneth cells reside in the crypt base and have a lifespan of thirty to forty days (Ireland *et al*, 2005; Clevers & Bevins, 2013). WNT-target genes ephrin type B receptor 2 (*EphB2*) and 3 (*EphB3*) have been shown to regulate Paneth cell localization to the crypt base, since Paneth cells in either *EphB2*- or *EphB3*-null mutants are dispersed throughout the crypt-to-lumen axis (Batlle *et al*, 2002; Genander *et al*, 2009). Transcriptional factors Atonal homolog 1 (*Atoh1*), downstream of Notch signaling, and *Sox9*, a Wnt target gene, are critical for Paneth cell differentiation(Shroyer *et al*, 2007; Bastide *et al*, 2007; Mori-Akiyama *et al*, 2007). Epithelial-specific deletion of either *Atoh1* or *Sox9* results in complete loss of the bactericidal enzyme and Paneth cell marker lysozyme from the crypt base (Vandussen & Samuelson, 2010; Bastide *et al*, 2007).

However, there has been some controversy regarding the necessity of Paneth cells in maintaining homeostasis in the stem cell niche. Numerous Paneth cell deletion models have been used to study the *in vivo* role of this cell type in supporting small intestinal stem cell function. In the CR2-tox176 model, diphtheria toxin A was activated by expression of Paneth cell-specific cryptidin-2 promoter (Garabedian *et al*, 1997). The vast majority of small intestinal crypts lacked

Paneth cells while some crypts retained lysozyme expression. In this incomplete model of Paneth cell ablation, Lgr5+ stem cells were reduced in number and the expression of multipotency marker Olfm4 also decreased (Sato *et al*, 2011a). A more complete and long-term model of Paneth cell deletion used the epithelial-specific *Villin*^{Cre} promoter to recombine *Sox9*$^{loxP/loxP}$ gene in small intestinal crypts. Following Paneth cell loss, numbers of Musashi-1-positive stem cells and Ki67+ proliferative cells increased (Bastide *et al*, 2007). Similar results were observed in *Atoh1*-null (*Villin*^{CreER}*; Atoh1*$^{flox/flox}$) crypts expressing a *Lgr5*^{GFP} construct where, despite the absence of Paneth cells, stem cells survived and produced the various cell types of the intestinal epithelium (Kim *et al*, 2012; Durand *et al*, 2012). These lines of evidence suggest that, while Paneth cells are a crucial component of the crypt niche, they are dispensable for stem cell function, as there appear to be compensatory cell types in the intestinal niche.

The commensal microbiome and microbial-derived metabolites

The gut is a nutrient-rich environment, where digested material from the alimentary tract is absorbed by absorptive cells. The anaerobic luminal environment is also home to trillions of microbes that must also metabolize macronutrients for survival. Host-microbiome interactions in the gastrointestinal tract shape intestinal architecture and function but can also drive disease pathogenesis (Sartor & Mazmanian, 2012; Donaldson *et al*, 2015). Epithelial goblet cells secrete the glycoprotein mucin 2 to create a semi-permeable matrix, separating the gut microbiome from the underlying mucosa (Turner, 2009). In the small intestine, this barrier consists of a single, porous mucus layer whereas, in the colon, which has a greater microbial biomass, there is a more complex double layer of mucin (Figure 2A-B) (Johansson *et al*, 2011; Hansson, 2012; Donaldson *et al*, 2015). The impermeability of the mucus layer establishes a concentration gradient of metabolites and oxygen throughout the villus-crypt architecture (Glover *et al*, 2016; Zheng *et al*, 2015). Maintenance of the anoxic environment of the lumen and the oxygenated environment of the crypt is critical to the function of epithelial stem cell populations.

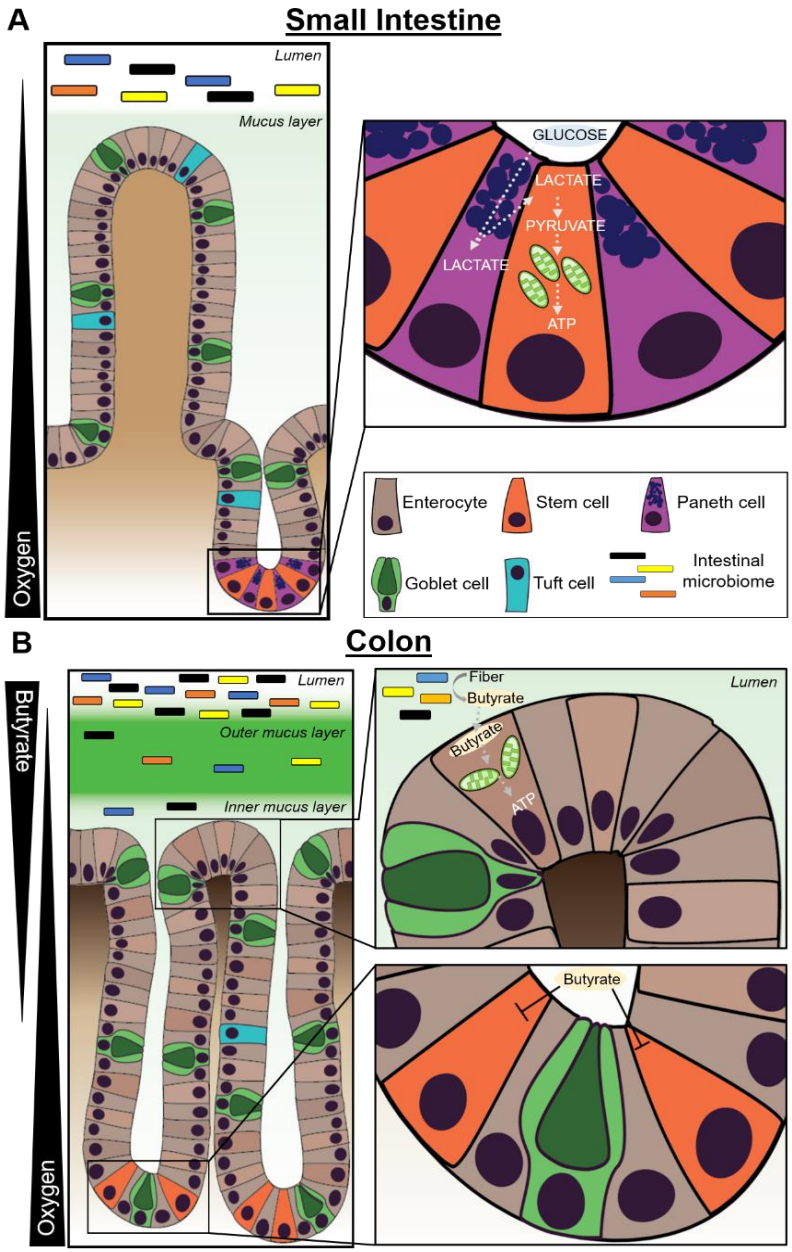

Figure 2. Distinct metabolic pathways drive epithelial cell function in the small and large intestine. (A) In the small intestine, anaerobic bacteria thrive in the anoxic environment of the gut lumen but are separated from the underlying mucosa and oxygen-rich crypt niche by a mucus barrier, primarily secreted by goblet cells. Increased glycolysis in Paneth cells and increased oxidative phosphorylation in stem cells maintain the balance between multipotency and differentiation in small intestinal crypts. **(B)** Due to the increased biomass residing in the lumen of the large intestine, a double layer of mucus prevents inappropriate interactions between commensal bacteria and host cells. Fiber fermentation by these bacterial species releases the short chain fatty acid butyrate into the lumen, which is transported and metabolized by absorptive colonocytes at the top of the crypt. By siphoning up butyrate, colonocytes mitigate its deleterious effect on proliferative stem cells at the base of the crypt. Animal systems which lack the crypt structure are particularly susceptible to stem cell dysfunction following exogenous butyrate administration.

Commensal obligate anaerobic bacteria largely ferment complex carbohydrates as their main energy source, leading to the release of short chain fatty acids, such as butyrate, as a metabolic byproduct (Guilloteau *et al*, 2010; Vanhoutvin *et al*, 2009). Short chain fatty acids are beneficial metabolites that regulate the immune system in the intestine (Furusawa *et al*, 2013; Smith *et al*, 2013; Arpaia *et al*, 2013). Butyrate serves as a nutrient source to normal cells, yet acts as a histone deacetylase inhibitor on cancer cells that depend on the Warburg effect for energy production (Donohoe *et al*, 2012). Thus, while absorptive colonocytes convert butyrate to acetyl-coA to enter the Krebs cycle, epithelial stem cell proliferation is significantly suppressed when exposed to butyrate (Kaiko *et al*, 2016). The Stappenbeck group hypothesized that the colonic crypt structure sequesters butyrate to the top of the crypt, where colonocytes act as a "sink" by metabolizing butyrate, thus mitigating its deleterious effects on stem cells at the base of the crypt (Figure 2B) (Kaiko *et al*, 2016). Critically, exogenous butyrate treatment had profound suppressive effects on intestinal stem cells of the zebrafish, whose intestine lacks the invaginated crypt structure (Kaiko *et al*, 2016).

Population-level microbiome analysis

In recent years, the improved cost and efficiency of next-generation sequencing platforms has greatly facilitated the study of the intestinal microbiome. Taxonomic analysis of microbiome constituents is facilitated by the sequencing of the variable 4 (V4) region in the bacterial 16s ribosomal RNA gene, which is comprised of alternating conserved and variable regions (Bhatt *et al*, 2013). Microbiome dysbiosis is a characteristic of various illnesses, including obesity, to gestational diabetes, to schizophrenia in human subjects (Karlsson *et al*, 2013; Schulz *et al*, 2014; Koren *et al*, 2012; Pyndt Jørgensen *et al*, 2015). The use of mice may help in identifying which segments of these pathogenic communities are directly causative of disease and the mechanisms by which they wield their effects. One of the key methods by which this can be accomplished is through transplantation of individual species in gnotobiotic mice maintained in germ-free

conditions (Turnbaugh *et al*, 2009; Martin *et al*, 2008). Through this method, population level structure of the microbiome is maintained, although there may be changes at the species or OTU (operational taxonomic unit) level (Turnbaugh *et al*, 2009). These mice have been used to assess the microbiome's effects on traits such as obesity and susceptibility to infection by pathogenic bacteria such as *Salmonella* (Chung *et al*, 2012). Recent research has shed light on the drastic influences of the microbiome on vertebrate organism physiology, including metabolism and immunity. The establishment of the microbiome is a function of not only inherent features such as genetics, but the environment where the organism is housed and raised as well. Mice from the same strain exhibit different biological behaviors if they are acquired from different sources. For example, C57BL/6 mice exhibit divergent T helper(Th) 17 differentiation in the gut depending on whether they originate from Taconic Farms, Jackson Laboratories or Charles River (Ivanov *et al*, 2008). Human studies suggest that the adult microbiome is relatively stable, and is established through a chaotic process during the first year of life when dietary richness and environmental exposures are increased (Wu *et al*, 2011). Importantly, dizygotic twins show significant similarity in early temporal profile gut microbiome development, demonstrating the importance of early fostering (Palmer *et al*, 2007). There has been evidence suggesting that the adult mouse microbiome is not as stable and can be changed within days (Carmody *et al*, 2015). Cage specific effects are strong and can account for up to 30% of variation. These effects can be reduced by mixing bedding and/or medium term co-housing for weeks, although these approaches may not result in perfect normalization (Hildebrand *et al*, 2013). A better strategy may be to begin with littermates or germ-free mice followed by co-housing, although only a limited number of mice can be studied by this strategy.

Host metabolites

Nutrient levels also mediate cellular function in the crypt niche as the intestine adapts to changes in energy availability. Caloric restriction was seen to expand stem cell numbers while

reducing the relative proportion of differentiated cell types (Yilmaz *et al*, 2012; Igarashi & Guarente, 2016). This suggests that, in response to nutrient deprivation, the intestine shuttles energy towards priming stem cells for preservation and/or expansion at the expense of differentiation. Moreover, caloric restriction enhanced Paneth cell function and, in *ex vivo* assays, the calorie restricted-Paneth cells demonstrated an increased in the organoid efficiency of intestinal stem cells (Yilmaz *et al*, 2012). Response to caloric restriction is mediated through a sirtuin1 (Sirt1)-dependent mechanism as mice deficient for Sirt1, a NAD-dependent deacetylase, in epithelial cells do not respond to nutrient deprivation (Igarashi & Guarente, 2016). Obesity and high fat diets are known to cause low grade inflammation and compromise barrier function in the intestine (Gruber *et al*, 2013). Animals fed with a high fat diet have reduced Paneth cells but increased number of ki67+ cells in the crypt niche (Gulhane *et al*, 2016). *In vitro,* these stem cells have increased regenerative capacity but these effects are abrogated by the deletion of the *Ppard* gene, suggesting that these effects are part of a Peroxisome proliferator-activated receptor (PPAR) signaling-dependent mechanism (Gulhane *et al*, 2016). Paneth cells, discussed earlier, are not solely suppliers of ligands activating key developmental pathways. Rodriguez-Colman *et al.* demonstrated a clear divergence in metabolic profiles between Paneth cells, which favor glycolytic activity, and *Lgr5*+ stem cells, which favor mitochondrial activity (Rodríguez-Colman *et al*, 2017). Paneth cells are a critical source of lactate in the stem cell crypt and support oxidative phosphorylation in neighboring stem cells (Figure 2A) (Rodríguez-Colman *et al*, 2017). Inhibition of glycolysis in organoids suppressed stem cell proliferation and induced crypt formation, implying that stem cells shift resources towards differentiation rather than self-renewal (Rodríguez-Colman *et al*, 2017). Energy metabolism therefore plays a critical role in maintaining the balance between plasticity and differentiation within the stem cell niche.

Organoid culture

The ability to culture stem cells *in vitro* and differentiate them into functional organs has been a fundamental goal of regenerative medicine (Lancaster & Knoblich, 2014). In 2009, Sato and Clevers reported the culturing conditions necessary to form “miniaturized intestines” from individual *Lgr5*+ stem cells isolated from the adult intestine (Sato *et al*, 2009). These miniguts, also termed intestinal organoids or enteroids (Stelzner *et al*, 2012), form proliferative, budding structures that represent the stem cell niche of the intestinal crypt and villus domains where differentiated cells reside and subsequently slough off into the lumen (Sato *et al*, 2009). Because of the spatial segregation of different functional domains into “crypt” and “villus”, stem cells are maintained via differential autocrine signaling within the niche, while cells that migrate out of the niche differentiate into the typical intestinal cell types (enterocytes, goblet, and endocrine cells), with the exception of Paneth cells which reside within the buds. The culturing conditions for intestinal organoids do not involve any mesenchymal feeder cells, but instead, comprise only of diffusible molecular factors. These components activate intestinal stem cell maintenance signaling pathways mentioned in the previous section, including EGF, Wnt3a, the Wnt agonist R-spondin, and the BMP antagonist noggin, together with laminin-rich Matrigel to provide extracellular matrix support (Figure 3). Notch agonist added to culture improved the survival and organoid-forming capabilities of single Lgr5+ stem cells, when juxtacrine Notch signaling from neighboring cells is unavailable (Sato *et al*, 2009). Importantly, intestinal organoid cultures can be maintained long-term through multiple passages without compromising genomic integrity (Behjati *et al*, 2014). Because of the stability and tractability of the intestinal organoid system, it has gained widespread use for investigating all aspects of intestinal biology (Sato & Clevers, 2013; Zachos *et al*, 2015; Drost & Clevers, 2017), and organoid forming conditions have since been determined for other organs of the gastrointestinal (GI) tract, including the large intestine (Sato *et al*, 2011b). There are currently many applications of intestinal organoids, including high-throughput screening studies (Gracz *et al*, 2015; Crespo *et al*, 2017; Pauli *et al*, 2017; Drost *et al*, 2017), investigation

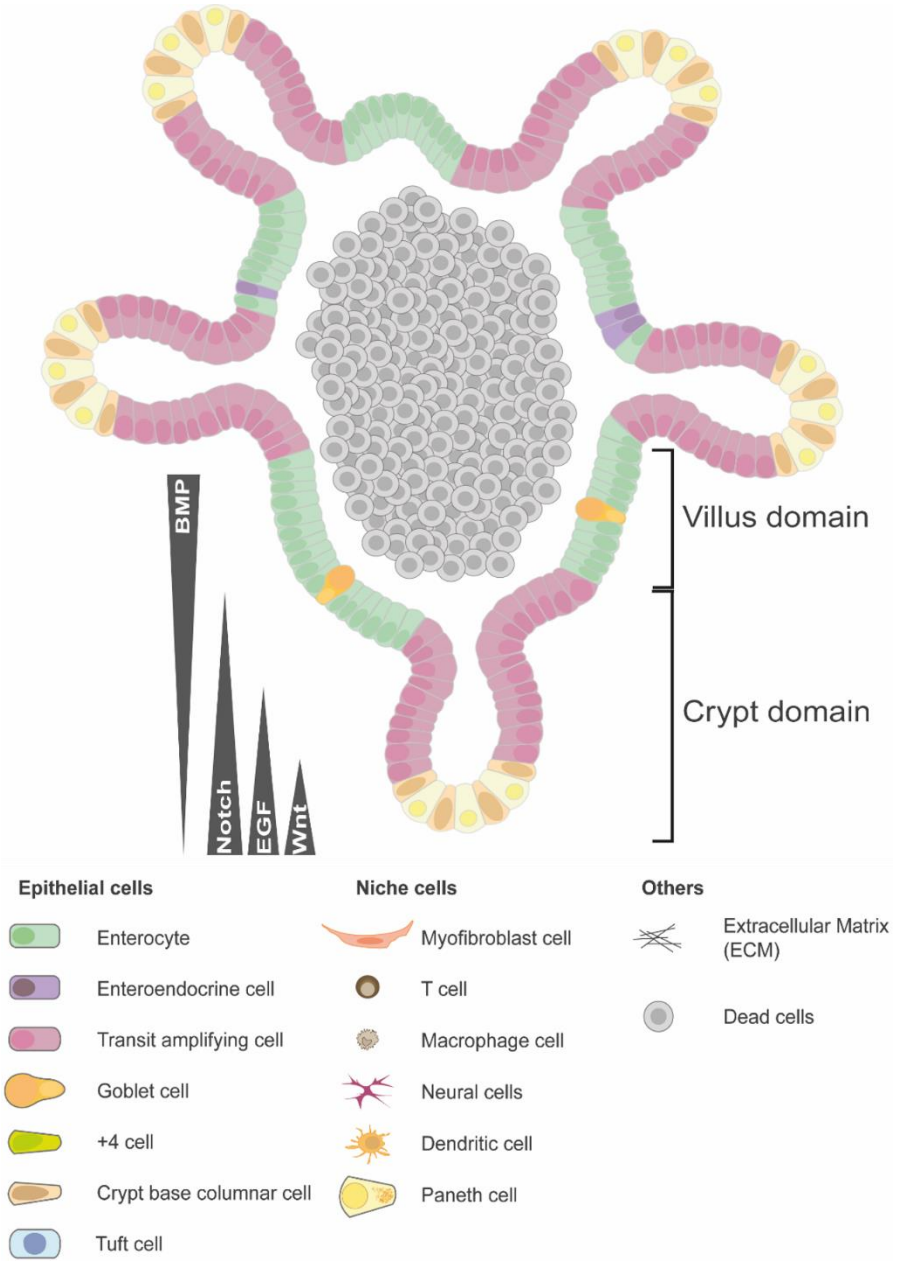

Figure 3. Recapitulation of the stem cell niche in organoid culture. Isolated intestinal stem cells are able to form organoids in conditions mimicking the intestinal stem cell niche. These conditions include supplementation with Noggin (BMP antagonist), R-spondin (Wnt agonist), WNT3a and EGF. Self-organization and localized signaling allows for spatial compartmentalization and differentiation, resulting in the formation of 3D budding structures. Similar to in vivo, Paneth cells and intestinal stem cell are located at the bottom of the buds (crypt domains), whereas enterocyte-like cells are located at the flattened area of organoids (villus domains).

of host-pathogen interactions (Foulke-Abel *et al*, 2014; Kovbasnjuk *et al*, 2013; In *et al*, 2016), and modeling the progression of sporadic colorectal cancer thorough sequential mutations engineered by Crispr/Cas9 (Drost *et al*, 2015; Matano *et al*, 2015).

Systems biology and single-cell analysis

Systems biology is an approach to studying biological and biomedical problems from an integrative perspective. An ideal outcome of a systems-level investigation would consist of a model that represents all of the species in a system and their interactions. Furthermore, it would describe how particular network states relate to given outcomes. By knowing how the pieces of the network relate to one another and how those relationships relate to particular outcomes, the network could be engineered in order to produce a desired outcome. This could be used for deriving combinations of therapies that target not just proteins or pathways, but entire network states, and by extension, phenotypic outcomes. While this represents the ideal outcome of systems-level analysis, in actual practice, researchers are still building the experimental and analytical tools that would enable the production of complete models. Spatial and biophysical constraints, the presence of other cell types, access to oxygen, and the presence of microbes are just a few of the additional factors that may drive cellular, organ and organismal behavior. This complexity provides one of the strongest arguments for the need for systems approaches in studying intestinal diseases, however, it is also one of the chief obstacles to creating meaningful, actionable models. Even comparatively simple *in vitro* systems cannot be mechanistically modeled at the scale of many thousands of molecular species. This difficulty is further compounded by the complexity of the *in vivo* tissue environment. While the ultimate goal of producing computable systems-level models at the tissue and organismal scale may be out of reach with current measurement and analytic techniques, systems-level correlative studies have already been powerful tools for hypothesis generation and have enhanced our knowledge of

human gastrointestinal function and disease (Lau *et al*, 2012, 2011). In the next sections, I will describe several measurement techniques and data analysis approaches used to integrate systems-scale data. Finally, I will touch on the use of mouse models, which have been an invaluable tool for generating hypotheses using systems-level measurement and analysis.

Background on DISSECT-CyTOF

A major hurdle in single-cell analysis of epithelial tissues is that the disruption of cell-to-cell connections inherently perturbs native signaling states (Simmons *et al*, 2015). To overcome this limitation, our lab developed Disaggregation for Intracellular Signaling in Single Epithelial Cells from Tissue (DISSECT), a novel strategy for dissociating epithelial tissues into single-cell suspensions for multi-analyte analysis by cytometry Time-of-Flight (CyTOF) and fluorescent flow applications (Simmons *et al*, 2015). Compared to a conventional single-cell dissociation method, DISSECT was better able to preserve native signal transduction by fixing antibodies to their respective targets prior to dissociation using collagenase and dispase (more detailed methods can be found in Chapter III). We paired our DISSECT technique with a 21-plex CyTOF metal-conjugated antibody panel, including common cell identity and signal transduction markers (Simmons *et al*, 2015). By analyzing single-cell suspensions following exogenous stimulation, we were able to determine differential responses to inflammatory signals, as will be discussed in Chapter III.

Background on droplet-based single-cell RNA-sequencing (scRNA-seq)

In previous years, a number of single-cell encapsulation platforms have been developed to capture the transcriptome of individual cells. For our studies, we utilize the microfluidics-based inDrops platform (Klein *et al*, 2015). Cells are encapsulated in individual droplets of lysis buffer, reverse transcription enzymes, and beads containing barcoded primers. Ultraviolet light cleavage post-encapsulation frees the barcode from the hydrogel beads and reverse transcription labels

the transcriptome with an unique cell-based barcode as well as an unique molecular identifier (UMI) sequence for each transcript. Post-sequencing data processing generates read count information based on UMI quantification on a per gene basis in every cell. Filtration of poor quality or dead cells is performed to eliminate low information data points (Klein *et al*, 2015). However, variations in sequencing runs or library preparation can result in batch effects, requiring batch correction and data alignment between biological replicates. Our approach utilizes Seurat alignment (Stuart *et al*, 2018) and the ComBat algorithm (Chen *et al*, 2011), originally developed for bulk RNA sequencing data, to correct for batch effects between scRNA-seq biological replicates. Further details are provided in the methods section from Chapter V.

Background on p-Creode

Putative (p)-Creode is a cell differentiation mapping algorithm capable of generating data topologies from single-cell data (Herring *et al*, 2018). Briefly, p-Creode identifies end states, which are typically stem or differentiated cell states, in the dataset and then connects cell states based upon closeness. End-states have fewer connections in comparison to progenitor cells, which are highly connected to other transitioning cell types. Cell clusters are represented by nodes and transitions by edges connecting nodes. An ensemble approach is applied to select the most representative graph and scoring of multiple maps is used to reliably identify the graph which best represents the data topology. In contrast to other algorithms, p-Creode can reliably identify bifurcations in cell differentiation by identifying branch points without prior knowledge of the landscape. Moreover, the algorithm was developed to analyze single-cell data regardless of the modality, including CyTOF, single-cell RNA sequencing, and multiplex immunofluorescence imaging (Herring *et al*, 2018). Furthermore, we can analyze gene or protein expression in different lineages as a function of pseudotime and classify analyte expression into different trends, as will be described in Chapter V. Comparison of p-Creode landscapes and lineage dynamics among

different conditions can reveal important insights regarding biological phenomenon, such as cancer or inflammation.

Mouse models

Every system used to understand human health and disease has its advantages and disadvantages. Though human subjects certainly provide the best reflection of human physiology, patient tissue is not always readily available or sufficiently robust for experimental purposes. On the other end of the spectrum, cell lines are far more readily available and provide some of the same network architecture observed in human beings. However, since they lack many of the critical features of physiological space, they are not always an ideal platform for simulating human disease. Model organisms, such as rodents or zebrafish, have long been used to model human disease (Conn, 2013). These animal models have provided the means for numerous breakthroughs yet there can be significant drawbacks in their use that should be kept in mind. Ultimately, given trade-offs in cost *versus* homology, the mouse still represents the best model system for addressing questions of intestinal disorder *via* systems approaches. Mouse models are relatively inexpensive, have a strong experimental tool kit, and reflect many aspects of human immune and gastrointestinal physiology. As later chapters will discuss the use of the $TNF^{\Delta ARE/+}$ model to study IBD, the next section will expand on this model in greater detail.

$TNF^{\Delta ARE/+}$ model of Crohn's-like ileitis

The $TNF^{\Delta ARE/+}$ mouse model, developed by George Kollias and colleagues, is a common platform for studying Crohn's-like ileitis (Kontoyiannis *et al*, 1999). Insertion of an AU-rich element (ΔARE) into the *Tnf-α* gene results in mRNA stabilization and systemic overproduction of the TNF-α protein (Kontoyiannis *et al*, 1999). Similar to CD patients, $TNF^{\Delta ARE/+}$ mice have severe ileal inflammation characterized by transmural infiltration and goblet cell hyperplasia (Kontoyiannis *et al*, 2002). Effects of TNF-α are facilitated by the TNF receptor I (TNFRI) given $TNF^{\Delta ARE/+};TNFRI^{-/-}$

mice are disease free (Kontoyiannis *et al*, 2002). Intestine-specific *TNF*$^{\Delta ARE/+}$ models, where the ΔARE sequence is activated by *Cre* recombinase under the control of a *Villin* or *Fabp* promoter, have demonstrated that epithelial production of TNF-α is sufficient to drive ileal disease (Roulis *et al*, 2011; Bamias *et al*, 2013). These epithelial-specific models develop significant villus blunting and ileitis but not extraintestinal manifestations, such as inflammatory arthritis (Roulis *et al*, 2011; Bamias *et al*, 2013). As in human CD patients, the microbiome is critical to disease development given that *TNF*$^{\Delta ARE/+}$ animals housed under germ-free conditions are disease free and have normal crypt-villus architecture (Roulis *et al*, 2016a; Schaubeck *et al*, 2015). Transfer of a dysbiotic microbiome from conventional *TNF*$^{\Delta ARE/+}$ animals is sufficient to induce disease and reduce barrier-regulating antimicrobial peptides in germ-free *TNF*$^{\Delta ARE/+}$ animals (Schaubeck *et al*, 2015). Additionally, high-fat diet-fed *TNF*$^{\Delta ARE/+}$ animals have worse disease and increased levels of inflammatory cytokines, implying that other environmental factors, including diet, play a role in disease pathogenesis (Gruber *et al*, 2013).

Chapter II

BACKGROUND

SPECIFICATION AND FUNCTION OF SMALL INTESTINAL TUFT CELLS

Recreated from **Amrita Banerjee**, Eliot T. McKinley, Jakob von Moltke, Robert J. Coffey, and Ken S. Lau. “Interpreting heterogeneity in intestinal tuft cell structure and function.” *JCI*. 128(5):1711-1719. May 2018.

Small intestinal tuft cells are a rare chemosensory cell type

For close to a century, tuft cells (also known as brush or caveolated cells) have been identified in numerous epithelial tissues, including the gallbladder (Luciano & Reale, 1979, 1990, 1997; Luciano *et al*, 2003; Gilloteaux *et al*, 1989), stomach (Kugler *et al*, 1994; Luciano *et al*, 1993; Johnson & Young, 1968; Luciano *et al*, 2003), lung alveolus (Meyrick & Reid, 1968; Foliguet & Grignon, 1980; Hijiya *et al*, 1977; Hijiya, 1978; DiMaio *et al*, 1988), and intestine (Trier *et al*, 1987; Isomaki & Isomäki, 1962; Isomaki, 1973; Henrik *et al*, 1976; McNabb & Sandborn, 1964; Okamoto *et al*, 2008). Decades of investigation revealed little regarding the function of this mysterious cell type, until recently (Grencis & Worthington, 2016; Sato, 2007; Gerbe *et al*, 2012; Gerbe & Jay, 2016; Middelhoff *et al*, 2017). This chapter focuses on recent breakthroughs into the biology and function of intestinal tuft cells (Höfer & Drenckhahn, 1992; Gerbe *et al*, 2011; Gebert *et al*, 2000; Silva, 1966). Tuft cells represent approximately 0.5-1% of epithelial cells in the murine small intestine and colon but are slightly more prevalent in the distal part of the small intestine, compared to the proximal (McKinley *et al*, 2017). Tuft cells originate from *Lgr5*+ stem cells, similar to other differentiated intestinal epithelial cells (Gerbe *et al*, 2011), and are marked by doublecortin-like kinase 1 (DCLK1) (Gerbe *et al*, 2009). As DCLK1+ tuft cells were often

observed in the quiescent “+4” position of the intestinal crypt, they were originally considered a reserve stem cell pool (May *et al*, 2008, 2009; Dekaney *et al*, 2009). However, Gerbe et al. demonstrated that DCLK1+ tuft cells were a separate and distinct fifth intestinal epithelial cell lineage (Gerbe *et al*, 2009).

This chapter will describe new insights into intestinal tuft cell structure enabled by advances in electron microscopy techniques. Furthermore, more sensitive, single-cell sequencing approaches have provided new understanding of the intestinal tuft cell gene signature, which may expand current knowledge regarding tuft cell heterogeneity and function. Finally, this chapter will summarize recent reports on the role of intestinal tuft cells in the 1) recovery of the intestinal epithelium from damage, and 2) induction of a type 2 immune response to eukaryotic intestinal colonization.

Tuft cell morphology

Early studies describing tuft cells in rodent models noted the distinctive apical “bristles” that formed a highly organized brush border, giving these cells their eponymous “tufted” morphology (Nabeyama & Leblond, 1974; Luciano & Reale, 1990; Hijiya *et al*, 1977; Luciano & Reale, 1979; Silva, 1966). The distribution and dimensions of tuft cell microvilli, summarized in Table 1, are profoundly different from those of neighboring enterocytes (Morroni *et al*, 2007; Hoover *et al*, 2017). Unlike enterocytes, tuft cells do not possess a terminal web at the base of apical microvilli and possess a thinner fucose-rich glycocalyx above their apical membrane (Isomaki & Isomäki, 1962; Silva, 1966; Sato, 2007). The shape of the main tuft cell body may vary depending on the organ (Luciano & Reale, 1979; Sato, 2007). Intestinal tuft cells have a cylindrical cell body that narrows at the apical and basal ends (Isomaki & Isomäki, 1962; Isomäki, 1973), whereas alveolar tuft cells are flatter (Meyrick & Reid, 1968; Hijiya *et al*, 1977; Foliguet & Grignon, 1980; DiMaio *et al*, 1988; Hijiya, 1978), and gallbladder tuft cells are cuboidal in shape (Luciano *et al*, 2003; Gilloteaux *et al*, 1989). These differences may reflect different environments or

Table 1. Dimensions of enterocyte and tuft cell microvilli in mouse and human small intestine.

Cell Type	Murine small intestine[A]	Human small intestine[B]
Enterocyte	0.132 µm (SD±0.010 µm) x 0.975 µm (SD±0.101 µm)	0.09 µm (25^{th}-75^{th} percentile: 0.09-0.10 µm) x 1.0 µm (25^{th}-75^{th} percentile: 0.8-1.1 µm)
Tuft cell	0.187 µm (SD±0.024 µm) x 2.289 µm (SD±0.222 µm)	0.12 µm (25^{th}-75^{th} percentile: 0.11-0.17 µm) x 1.7 µm (25^{th}-75^{th} percentile: 1.4-2.0 µm)

[A]Small intestinal tuft cells (*n* = 3 animals, 3 tuft cells/animal) analyzed using serial block-face scanning electron microscopy and automated tape-collecting ultramicrotome scanning electron microscopy. Width (thickness) and height (length) of microvilli from tuft cells and adjacent enterocytes were measured for comparison (Hoover et al. 2017). [B]Small intestinal tuft cells (*n* = 6) from more than 300 human biopsy specimens analyzed by transmission electron microscopy. Width (thickness) and height (length) of microvilli from tuft cells and adjacent enterocytes were measured using a micrometer (Morroni, Cangiotti, and Cinti 2007).

indicate organ-specific functions but may also be experimental artifacts due to varying sectioning or fixation techniques. Lateral projections from the tuft cell's basolateral membrane associate with neighboring cell nuclei (Luciano & Reale, 1979, 1990). As early as 1979, Luciano and Reale presented evidence of microvilli at the lateral cell border that appeared to continue into the cytoplasm of adjacent cells (Luciano & Reale, 1979). However, limitations of conventional transmission electron microscopy could not provide the resolution necessary to characterize these protrusions, recently termed "cytospinules" by Hoover et al. (Figure 4) (Hoover *et al*, 2017). Each tuft cell possesses 3-4 such projections, and a cytospinule can pierce the lateral membrane of a neighboring cell, making direct contact with its nuclear membrane (Hoover *et al*, 2017). While the point of connection appears electron-dense and its exact purpose remains unclear, it may be postulated that this tuft cell-to-neighboring cell contact serves as a direct means of communication or cargo transport.

Intracellular tuft cell structure

Transmission electron microscopy studies in the epithelial lining of the rat submandibular gland were among the first to characterize the tuft cell intracellular landscape(Sato *et al*, 2002; Sato & Miyoshi, 1997; Nevalainen, 1977; Sato *et al*, 2000). These studies identified a filamentous bundle emanating from the apical microvilli and terminating at the ER (Sato *et al*, 2002; Sato & Miyoshi, 1997; Sato, 2007). The filamentous bundle was interspersed with transparent vesicles and electron-dense spheres containing indeterminate cargo (Sato *et al*, 2002; Sato & Miyoshi, 1997; Sato, 2007). More recent studies using volumetric electron microscopy offered increased resolution into the cytoplasmic contents of intestinal tuft cells (Bohórquez *et al*, 2014; Hoover *et al*, 2017). Using a ChAT:GFP::Pyy-Cre:TdTomato transgenic mouse, Hoover et al. identified choline acetyltransferase (ChAT)+ tuft cells in the intestine (Schütz *et al*, 2015) that were distinguishable from peptide YY (PYY)-secreting enteroendocrine cells (Bohórquez *et al*, 2014; Hoover *et al*, 2017). Volumetric electron microscopy analysis of the filamentous bundle confirmed

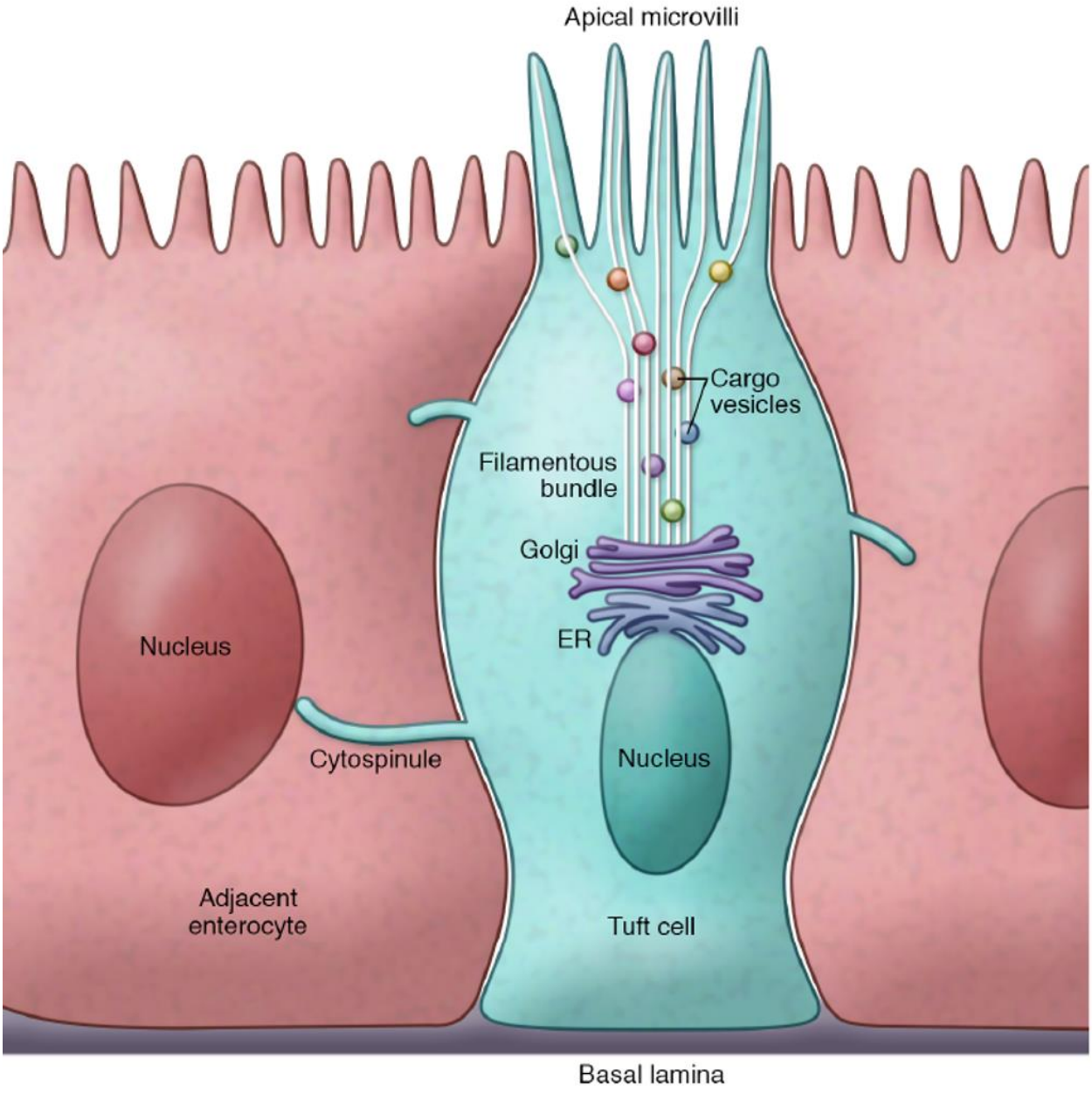

Figure 4. Structural characteristics of intestinal tuft or caveolated cells. Intestinal tuft cells are easily distinguishable from neighboring enterocytes by their unique apical brush border and oval-shaped cell body. The apical microvilli connect the extracellular environment of the lumen to the intracellular cytoplasm via a filamentous bundle. Vesicles carrying unknown cargo are interspersed within the filamentous bundle, which terminates at a tubular network at the apex of the tuft cell nucleus. Lateral membrane projections or cytospinules emanate from the tuft cell and pierce the membrane of adjacent enterocytes. Cytospinules have been shown to directly contact the nuclei of tuft cell neighbors, possibly serving as a means of cell-to-cell communication.

the presence of tubules running from the base of apical microvilli to the ER (Hoover *et al*, 2017).Electron-dense vesicular bodies of >30 nm were interspersed within the filamentous bundle, possibly serving as a means of cargo transport between the ER and apical membrane (Hoover *et al*, 2017). However, the cargo carried within those vesicles remain poorly characterized.

Tuft cells express chemosensory proteins, such as TRPM5 and α-gustducin, which suggests tuft cells are innervated by neighboring neurons. Structural studies have long attempted to characterize the relationship between these two cell types (Kaske *et al*, 2007; Sbarbati & Osculati, 2005; Bohórquez *et al*, 2014; Höfer & Drenckhahn, 1996; Bezençon *et al*, 2007, 2008; Hoover *et al*, 2017). Studies in the rat submandibular gland noted that terminal nerve processes were often in close contact with tuft cells (20-25 nm in separation) (Sato *et al*, 2002; Sato & Miyoshi, 1997). Several studies in the mouse intestine also demonstrated close proximity between tuft cells and nerve cells (Bezençon *et al*, 2008). However, volumetric electron microscopy analysis by Hoover et al. did not identify any direct point of contact between tuft cells and nearby nerve cells (Hoover *et al*, 2017). Transmission electron microscopy of human duodenojejunal tissue confirmed that human and mouse tuft cells share similar features, including the tufted microvillar morphology, filamentous core, and lateral membrane projections (Morroni *et al*, 2007). Interestingly, this human-based study observed direct contact between unmyelinated fibers of a mature neuron and the basolateral surface of a nearby tuft cell (Morroni *et al*, 2007). While synaptic vesicles containing electron-dense granules were clearly apparent in the terminal axons, no evidence of a synapse was observed (Morroni *et al*, 2007). However, in 300 human biopsy specimens, only six tuft cells were characterized and only a single tuft cell was associated with a naked terminal axon (Morroni *et al*, 2007). As tuft cell rarity limits many structural studies, whether direct tuft cell-to-nerve cell contacts are a critical component of tuft cell biology remains an open question.

Tuft cells have also been shown to share common structural features with chromogranin A (CHGA)-expressing, chemosensory enteroendocrine cells in the small and large intestine (Tsubouchi & Leblond, 1979; Yan *et al*, 2017a; Okamoto *et al*, 2008; Bellono *et al*, 2017; Bohórquez *et al*, 2014). Enteroendocrine cells regulate nutrient sensory functions in the intestine and secrete a wide variety of neuropeptides, including PYY and cholecystokinin (CCK) but, like tuft cells, are epithelial in origin (Bjerknes *et al*, 2012; Bjerknes & Cheng, 2006; Yan *et al*, 2017a). Like tuft cells, these cells are characterized by a tightly organized apical brush border but, unlike tuft cells, they possess a basal projection known as a neuropod (Bohórquez *et al*, 2014). Neuropod projections are thought to associate with processes from enteric glia in the lamina propria (Bohórquez *et al*, 2014), though direct contact is yet undocumented. Nonetheless, intestinal enterochromaffin cells were observed to form synaptic-like connections with nerve fibers (Bellono *et al*, 2017). Therefore, based on structural studies, tuft and enteroendocrine cells may share some common physical characteristics that implicate these cell types in a sensory role within the intestinal epithelium (Bellono *et al*, 2017; Bjerknes & Cheng, 2006; Gerbe *et al*, 2011; Bjerknes *et al*, 2012). As discussed below, tuft cells may also share a gene signature and progenitor cell with enteroendocrine cell subsets, further supporting the possibility of a relationship between the two cell types.

Small intestinal tuft cell specification

Investigations of intestinal epithelial specification initially classified tuft cells into the secretory lineage along with goblet, Paneth, and enteroendocrine cells (Durand *et al*, 2012; Shroyer *et al*, 2007; Kazanjian *et al*, 2010). Atonal homolog 1 (*Atoh1*) is a basic helix-loop-helix transcription factor known as the “master” transcription factor regulator for secretory lineage specification (Han *et al*, 2015; VanDussen *et al*, 2012; Shroyer *et al*, 2007). In one study, *Villin-Cre*-mediated intestine-specific knockout of *Atoh1* eliminated MUC2+ goblet, lysozyme+ Paneth cells, and DCLK1+ tuft cells (Gerbe *et al*, 2011). However, other groups utilizing similar *Villin-Cre*

drivers or a stem cell-driven *Lgr5*$^{eGFP;IRES;CreERT2}$ model, demonstrated that tuft cells are preserved after *Atoh1* loss (Westphalen *et al*, 2014; Bjerknes *et al*, 2012). In addition, a recent study further challenged the dependency of small intestinal tuft cell specification on *Atoh1*. Herring et al. used p-Creode, a novel computational trajectory-mapping algorithm, on single-cell data to determine that small intestinal tuft cells do not share a trajectory with the *Atoh1*-dependent secretory lineage (Herring *et al*, 2018). They further demonstrated that *Atoh1* knockout using a *Lrig1-CreERT2* stem cell-specific driver resulted in significantly increased small intestinal tuft cell numbers, despite the absence of secretory goblet and Paneth cells (Herring *et al*, 2018). These findings suggest that tuft cell specification may be more complex than previously supposed and could be driven by environmental factors.

Interestingly, tuft cell specification depends upon genes canonically involved in taste signaling (Table 2). Pou domain class 2 (*Pou2f3*) is a homeodomain transcription factor necessary for the specification of sweet, umami, and bitter taste cells (Matsumoto *et al*, 2011; Yamashita *et al*, 2017; Bezençon *et al*, 2007; Gerbe *et al*, 2016). *Pou2f3*-null mice have a deficient taste response but also lack tuft cells in epithelial tissues, including the intestine (Yamashita *et al*, 2017; Matsumoto *et al*, 2011; Gerbe *et al*, 2016). The taste signal transduction proteins TRPM5 (Oike *et al*, 2006; Gulbransen *et al*, 2008; Bezençon *et al*, 2008; Kaske *et al*, 2007; Bezençon *et al*, 2007; Howitt *et al*, 2016) and α-gustducin (Höfer *et al*, 1996; D. & Drenckhahn, 1998; Jang *et al*, 2007; Bezençon *et al*, 2007; Gulbransen *et al*, 2008) are expressed in DCLK1+ cells, and *Trpm5*-null mice have decreased number of intestinal tuft cells (Howitt *et al*, 2016). Numerous groups have demonstrated that DCLK1+ tuft cells express the Wnt target gene *Sox9,* though experiments in the *Villin*^{Cre}*;Sox9*$^{fl/f}$ model make little mention of the effect of *Sox9* loss on tuft cell distribution (Mori-Akiyama *et al*, 2007; Gerbe *et al*, 2011; Durand *et al*, 2012). Prostaglandin synthesis pathway members, cyclooxygenases COX-1 and COX-2, co-localize with tuft cell markers (Herring *et al*, 2018; McKinley *et al*, 2017b; Gerbe *et al*, 2011). Acetylated tubulin and phosphorylated-EGFR (pEGFR(Y1068)), are enriched at the apical tuft region

Table 2. Intestinal tuft cell markers and their proposed role in tuft cell function.

Marker [A]	Proposed function[B]	Reference
Acetylated tubulin	Structural	(Höfer and Drenckhahn 1996)
CK18	Structural	(Höfer and Drenckhahn 1996; Bjerknes et al. 2012)
ChAT	Chemosensory	(Bohórquez et al. 2014; Schütz et al. 2015)
Alpha-gustducin	Chemosensory	(Höfer, Püschel, and Drenckhahn 1996; Carole Bezençon, le Coutre, and Damak 2007)
TRPM5	Chemosensory, Type 2 immune response	(Carole Bezençon, le Coutre, and Damak 2007; C. Bezençon et al. 2008; Bjerknes et al. 2012; Howitt et al. 2016)
POU2F3	Chemosensory, Type 2 immune response	(Gerbe et al. 2016)
IL-25	Type 2 immune response	(von Moltke et al. 2016; Howitt et al. 2016; Gerbe et al. 2016; Haber et al. 2017)
pSTAT6	Type 2 immune response	(Howitt et al. 2016; Herring et al. 2018)
COX1, COX2	Prostaglandin synthesis, damage recovery	(C. Bezençon et al. 2008; Gerbe et al. 2011; May et al. 2014; Bjerknes et al. 2012; McKinley et al. 2017; Herring et al. 2018)
DCLK1	Quiescent stem cell, damage recovery	(May et al. 2008, 2009; Gerbe et al. 2009; Bjerknes et al. 2012)
HOPX	Unknown	(McKinley et al. 2017; Herring et al. 2018)
GFI1β	Unknown	(Bjerknes et al. 2012)
SOX9	Unknown	(Gerbe et al. 2011; McKinley et al. 2017; Herring et al. 2018)
pEGFR(Y1068)	Unknown	(McKinley et al. 2017; Herring et al. 2018)
[A]Based on antibody staining of intestinal tuft cells. [B]Proposed role of protein marker within intestinal tuft cells, based on recent published literature		

(Höfer & Drenckhahn, 1996; Herring *et al*, 2018; McKinley *et al*, 2017b). Expression of the *Lgr5* stem cell marker has been observed in tuft cells (Itzkovitz *et al*, 2011; McKinley *et al*, 2017b). Recent studies on small intestinal tuft cells during acute helminth infection in the intestine confirmed expression of multiple type 2 immunity-related proteins, such as IL-25 (von Moltke *et al*, 2016; Haber *et al*, 2017; Howitt *et al*, 2016; Yan *et al*, 2017a). Utilizing multiplex immunofluorescence, Herring et al. confirmed that pSTAT6, which is necessary for type 2 immunity (Allen & Sutherland, 2014; Ramanan *et al*, 2016; Howitt *et al*, 2016), and DCLK1 co-localize in the small intestine, whereas colonic tuft cells, which are not known to participate in type 2 immune responses, are pSTAT6-negative (Herring *et al*, 2018). McKinley et al. identified broad tuft cell heterogeneity between the small intestinal and colonic tuft cell population based on multiple marker expression (McKinley *et al*, 2017a). These results suggest that multiple tuft cell states can result in response to multiple, diverse environmental cues.

Tuft cell gene signature

Recent developments in single-cell RNA sequencing (scRNA-Seq) have revealed further insights into tuft cell heterogeneity. Haber et al. applied droplet-based scRNA-Seq to characterize the transcriptome of the mouse small intestinal epithelium. Clustering analysis of scRNA-Seq data identified two distinct populations of mature tuft cells, categorized as tuft-1 and tuft-2 (Haber *et al*, 2017). Whereas both groups expressed *Dclk1*, the tuft-2 cluster was enriched for immune-related genes, including *Ptprc*, which encodes the pan-immune marker CD45 (Haber *et al*, 2017). This unexpected finding was confirmed through single molecule FISH, where some DCLK1-expressing tuft cells co-expressed *Ptprc* mRNA (Haber *et al*, 2017). The tuft-1 cluster was enriched for neuronal genes, including *Ptgs1*, which is plausible since tuft cells express COX-1 and COX-2 (May *et al*, 2014; Herring *et al*, 2018; Haber *et al*, 2017; Gerbe *et al*, 2011; McKinley *et al*, 2017b). Perhaps indicative of their newly discovered role in mounting a type 2 immune response against parasitic helminths, tuft-1 and tuft-2 cells expressed the type 2 cytokine *Il25* and the type 2-related

cytokine receptors *Il17rb*, *Il4ra*, and *Il13ra* (Haber *et al*, 2017). In contrast, only tuft-2 expressed significant levels of the type 2-promoting cytokine *Tslp* (Haber *et al*, 2017).

While characterizing the transcriptome of *Bmi1*-GFP+ stem cells, Yan et al. utilized scRNA-Seq to reveal intriguing evidence regarding similarities between tuft cells and *Neurod1*- and *Prox1*-expressing enteroendocrine cells (Yan *et al*, 2017a). *In vivo* studies demonstrated that *Prox1*-expressing cells were capable of lineage-tracing entire crypts during homeostasis and following irradiation-induced injury (Yan *et al*, 2011, 2017a). *Prox1*-GFP+ cells are enriched for enteroendocrine secretory products, including *Cck* and *Pyy*, and tuft cell markers, *Dclk1* and *Trpm5* (Yan *et al*, 2017a). Immunostaining of small intestinal tissue confirmed that CHGA+ enteroendocrine cells and DCLK1+ tuft cells expressed *Prox1,* suggesting that some of these cells may act as a quiescent stem cell pool, activated following tissue damage (Westphalen *et al*, 2014; Yan *et al*, 2017a; Bjerknes & Cheng, 2006). However, while some DCLK1+ tuft cells expressed *Prox1*, a subset of tuft cells was *Prox1*-negative, indicating further heterogeneity in the tuft cell population, with some resembling enteroendocrine cells while others are less similar.

Colonic tuft cells

While the specification and function of small intestinal tuft cells have been extensively studied, colonic tuft cells have been less rigorously investigated, and it cannot be assumed that lessons learnt in the small intestine are transferrable to the large intestine. Accordingly, Herring et al. computationally determined that the specification programs controlling colonic and small intestinal tuft cells may vary. As previously discussed, while *Atoh1*-deficient mice developed tuft cell hyperplasia in the small intestine, the large intestine was largely absent of DCLK1+ tuft cells when *Atoh1* was ablated (Herring *et al*, 2018). This result suggests that *Atoh1* may be necessary for tuft cell specification in the colon, while its role in small intestinal specification is less clear. Colonic tuft cells may also be capable of responding to perturbation of the luminal environment, as McKinley et al. demonstrated that colonic tuft cells increased in germ-free mice upon

introduction of microorganisms, although the effect was transient (McKinley *et al*, 2017b). These lines of evidence suggest much remains to be understood regarding possible variation in specification and function of tuft cells in the small intestine versus the colon.

Tuft cells in intestinal epithelial damage response

Recent work has begun to shed light on tuft cell function, and I will focus primarily on the role of these cells in: 1) recovery of the intestinal epithelium from damage, and 2) induction of a type 2 immune response against eukaryotic intestinal colonization.

A well-established model of intestinal epithelial damage is total body irradiation of >8 Gy, which triggers double-stranded DNA breaks followed by destruction of crypt units and villus atrophy (Booth *et al*, 2012; Potten *et al*, 2002). During the recovery process, the small intestinal epithelium undergoes a tightly controlled program of cell death and proliferation, which occurs in two distinct waves 6 hours and 24 hours post-irradiation (May *et al*, 2014). The effects of high irradiation are non-lethal and reversible, with wildtype animals recovering normal intestinal morphology within 1-2 weeks through a stem cell-driven process (Booth *et al*, 2012; May *et al*, 2014).

Although deleting *Dclk1* using a *Villin*$^{Cre/+}$;*Dclk1*$^{fl/fl}$ model did not produce a discernible phenotype at homeostasis, irradiated animals without epithelial *Dclk1* rarely survived beyond five days, whereas irradiated control mice recovered as expected (May *et al*, 2014). In the intestine, *Villin*$^{Cre/+}$;*Dclk1*$^{fl/fl}$ animals failed to recover normal crypt-villus architecture and barrier function after irradiation, demonstrative of a defective regenerative process, although initial crypt proliferation was unimpaired, as determined by BrdU incorporation (May *et al*, 2014). Irradiated *Villin*$^{Cre/+}$;*Dclk1*$^{fl/fl}$ intestinal tissue showed time-dependent downregulation of the stem cell markers *Lgr5* and *Bmi1* compared with wildtype animals (May *et al*, 2014). Whereas the previous study investigated epithelial loss of *Dclk1*, Westphalen et al. interrogated the role of DCLK1+ tuft cells in epithelial regeneration, using a *Dclk1*$^{CreERT/+}$*;R26-DTA* model to specifically ablate *Dclk1*-

expressing cells (Westphalen *et al*, 2014). Similar to the previous study, total body irradiation induced significant morbidity in induced *Dclk1*$^{CreERT/+}$*;R26-DTA* animals within 7 days, with significant crypt aberration and increased number of apoptotic cells (Westphalen *et al*, 2014). However, DCLK1 expression is not limited to epithelial cells, as DCLK1 and a closely-related splice variant, DCX-like, play a role in neuronal migration during brain development (Koizumi *et al*, 2006b, 2006a; Verissimo *et al*, 2010). Therefore, ablating DCLK1-expressing neurons or neural progenitor cells in the intestinal stroma may have a deleterious effect on intestinal integrity, independent of tuft cell function. Using quantitative imaging, McKinley et al. demonstrated that tuft cells are resistant to mucosal atrophy after acute fasting, while the number of other intestinal epithelial cell types can be reduced by up to one-third of their original abundance (McKinley *et al*, 2017b). The persistence of tuft cells in this setting could indicate a potential functional relevance for this cell type in tissue recovery. Thus, DCLK1+ tuft cells have been shown to contribute to epithelial regeneration following damage. It was initially hypothesized that DCLK1+ tuft cells may act as a damage-activated reserve stem cell pool.

To verify if tuft cells exhibit a stem cell gene signature, Chandrakesan et al. developed a *Dclk1-CreER*;*Rosa26-YFP* mouse line, where YFP was a reliable marker for DCLK1+ tuft cells (Chandrakesan *et al*, 2015). Sequencing of sorted YFP+ cells showed enrichment of the stem cell gene *Bmi1* and pluripotency factors *Sox2* and *Klf4*, but not *Lgr5*, in comparison with non-YFP-expressing intestinal epithelial cells (Chandrakesan *et al*, 2015). These cells also expressed cell cycle inhibitors, including *Cdkn1a/p21*, but are de-enriched for the cell cycle driver *Cdk1*, suggesting that they may act as a quiescent stem cell population that is activated upon genotoxic insult (Chandrakesan *et al*, 2015). The Houchen group had previously demonstrated that individual, FACS-sorted DCLK1+ cells can produce spheroids in vitro (May *et al*, 2009). These spheroids, when implanted into immunocompromised mice, developed nodular structures, which expressed intestinal epithelial secretory and absorptive fate markers (May *et al*, 2009). While this would imply DCLK1+ crypt cells are capable of acting as stem cells, studies in the mammary

epithelium have demonstrated in vitro culture and transplantation may reprogram non-stem cells into a multipotent cell state, potentially confounding the *in vivo* relevance of this experiment (Prater *et al*, 2014; Keymeulen *et al*, 2011). Moreover, Westphalen et al., using a *Dclk1*^{CreERT}*;R26-LacZ* reporter mouse line, did not observe an increase in lineage-tracing events following irradiation- or DSS-induced small intestinal injury, arguing against a reserve stem cell role for DCLK1+ cells (Westphalen *et al*, 2014). Furthermore, Nakanishi et al. showed that postmitotic DCLK1+ tuft cells do not lineage-trace under homeostatic conditions, and only cancer cells that gain *Dclk1* expression can act as cancer stem cells (Nakanishi *et al*, 2013). Thus, while DCLK1+ tuft cells may modulate injury responses, they do not appear to be a damage-activated quiescent stem cell population.

Although DCLK1+ intestinal tuft cells may not act as stem cells upon epithelial injury, they may play a crucial role in mucosal recovery. Irradiated *Villin*$^{Cre/+}$;*Dclk1*$^{fl/fl}$ animals exhibited dramatic reduction in the expression of pluripotency factors, including *Oct4* and *Klf4*, and self-renewal pathways, including Notch and Akt/mTOR (Chandrakesan *et al*, 2016; May *et al*, 2014). However, bulk lysate analysis precluded a consensus of whether these factors are downregulated in DCLK1+ cells or in actual stem cells through a non-cell autonomous mechanism (May *et al*, 2014; Chandrakesan *et al*, 2016). In support of the latter, *Villin*$^{Cre/+}$;*Dclk1*$^{fl/fl}$ animals showed lower levels of epithelial COX-2 and serum prostaglandin E2 (PGE2) 24 hours post-irradiation (Chandrakesan *et al*, 2016). DCLK1+ tuft cells highly express COX-1 and COX-2, and these enzymes process arachidonic acid into secreted PGE2. *Dclk1* overexpression in colonic epithelial YAMC cells increased levels of intracellular COX-2 and secreted PGE2 (Chandrakesan *et al*, 2016). Myoshi et al. recently showed that PGE2 induces stem and progenitor cell proliferation, promoting tissue repair following epithelial damage (Miyoshi *et al*, 2017). Without *Dclk1*, epithelial cells were de-enriched for cell cycle regulators cyclin E1 and cyclin D1 after damage (Chandrakesan *et al*, 2016). While the evidence remains circumstantial, tuft cells may be a major source of PGE2 and, thereby, involved in inducing stem cell proliferation and promoting post-

irradiation tissue recovery in a non-cell autonomous manner (Cohn *et al*, 1997; Booth *et al*, 2012; Westphalen *et al*, 2014).

In addition to stem cell-driven epithelial recovery, *Dclk1* may also play a critical role in the damage response phase. *Villin*$^{Cre/+}$;*Dclk1*$^{fl/fl}$ crypts had a significantly higher number of TUNEL+ cells and were positive for the apoptotic markers caspase-3 and -9 (Chandrakesan *et al*, 2016). While there are multiple mechanisms of cell survival post-irradiation, DNA double-stranded break repair is predominantly mediated by the ATM serine/threonine kinase (Booth *et al*, 2012). In support of this mechanism, markers of the ATM-dependent repair pathway, including phosphorylated-ATM, gamma-H2AX, and BRCA1, decreased in the small intestine of irradiated *Villin*$^{Cre/+}$;*Dclk1*$^{fl/fl}$ (Chandrakesan *et al*, 2016). Co-immunoprecipitation using an anti-DCLK1 antibody as bait demonstrated a direct protein-protein interaction between DCLK1 and ATM (Chandrakesan *et al*, 2016). *Dclk1*-overexpressing YAMC cells exposed to irradiation showed increased phosphorylation of ATM and H2AX, suggesting an enhanced DNA damage response, as well as increased colony formation, a metric of cell survival (Booth *et al*, 2012; Chandrakesan *et al*, 2016). Thus, *Dclk1*-expressing cells may be important in both initial DNA damage-associated crypt loss and subsequent stem-cell driven recovery. However, it remains to be seen whether and how DCLK1+ tuft cells categorically orchestrate each of these processes. While Westphalen et al. used a diphtheria toxin-based strategy to induce DCLK1+ tuft cell loss, Chandrakesan et al. relied on a *Villin-Cre* system to ablate *Dclk1* in all intestinal epithelial cells, including stem and progenitor cells. Furthermore, impaired barrier function in the *Villin*^{Cre}*;Dclk1*$^{fl/fl}$ model may exacerbate the effects of irradiation-induced damage, independent of DCLK1+ tuft cells, thus complicating the interpretation of these results (May *et al*, 2014; Chandrakesan *et al*, 2016). The use of more targeted cell ablation strategies may provide more definitive evidence of tuft cell-specific functions.

Tuft cells in gastrointestinal helminth infection

In 2016, three separate publications demonstrated that tuft cells play a critical role in mounting a type 2 immune response against parasitic worm colonization of the intestine. Parasitic worms, or helminths, are multicellular metazoans and present a significant global infectious burden (Allen & Sutherland, 2014; von Moltke *et al*, 2016; Howitt *et al*, 2016; Gerbe *et al*, 2016). Helminth eggs or infectious larvae pass into human hosts via contaminated soil or water sources and often colonize the proximal small intestine, namely the duodenum and jejunum (von Moltke *et al*, 2016; Allen & Sutherland, 2014). The rodent metazoan parasite *Nippostrongylus brasiliensis* (*N. brasiliensis*) is a robust model for studying helminth infection. *N. brasiliensis* are delivered via subcutaneous injection in larval form and migrate through the circulatory system to the lung, where they molt (Allen & Sutherland, 2014; Gerbe *et al*, 2016). Eventually, they migrate to the trachea and are coughed up, only to be swallowed by the mouse host and delivered to the intestine. In the gastrointestinal tract, the parasite reaches sexual maturity and produces eggs that develop into the adult form within a short period of time (Allen & Sutherland, 2014). Adult worms are expelled from the intestine 1-2 weeks following the initial infection. Host detection of parasitic worms induces a rapid type 2 immune response and subsequent remodeling of the intestinal epithelium via goblet cell hyperplasia (von Moltke *et al*, 2016; Howitt *et al*, 2016; Gerbe *et al*, 2016). Goblet cells produce the anti-helminth molecule resistin-like 1 beta (RETN1β) in a type 2-dependent manner which, together with increased mucus production and smooth muscle hypercontractility, contributes to worm expulsion (Allen & Sutherland, 2014; Gerbe & Jay, 2016; Gerbe *et al*, 2016).

Each of the three groups independently detected expansion of the intestinal tuft cell population following helminth colonization. Gerbe et al. and von Moltke et al. utilized *N. brasiliensis* and *H. polygyrus*, which are cleared by a type 2 immune response. Howitt et al. observed the same phenotype with these two worm types as well as *Trichinella spiralis* (*T. spiralis*) and the mouse protist *Tritrichomonas muris* (*T. muris*) In all three studies, hyperplastic tuft cells

in infected mice expressed canonical tuft cell markers, including DCLK1, SOX9, and COX-1, confirming that these were bona fide tuft cells and not an alternative, damage-induced cell type (Howitt *et al*, 2016; Gerbe *et al*, 2016; von Moltke *et al*, 2016). The investigators tested the necessity of intestinal tuft cells in driving worm expulsion using animal models deficient in tuft cell number or function (von Moltke *et al*, 2016; Howitt *et al*, 2016; Gerbe *et al*, 2016). As previously mentioned, *Pou2f3*-null mice lack intestinal tuft cells and tuft cell hyperplasia was absent in *Pou2f3*-null mice following *N. brasiliensis* infection (Gerbe *et al*, 2012). While wildtype animals recovered by day 9 or 10 post-infection, *Pou2f3*-null mice had significant worm burden at day 42 post-infection and worms were detected in distal regions of the intestine, beyond their normal areas of adherence (Gerbe *et al*, 2016). Neither gustducin- nor *Trpm5*-null mice exhibited significant tuft cell expansion in the presence of *T. muris* compared to infected wildtype animals (Howitt *et al*, 2016). Therefore, functional chemosensation within intestinal tuft cells appears necessary for detecting eukaryotic infection and mounting an effective immune response.

The type 2 cytokine IL-25 plays a critical role in the tuft cell response to eukaryotic infection. Gerbe et al. identified an increase in mucosal IL-25 by RNA-sequencing and its tuft cell-specific expression by immunohistochemistry at day 9 post-infection. von Moltke et al. utilized a knockin IL-25-RFP-expressing mouse and showed constitutive IL-25 expression in intestinal tuft cells but not in other intestinal epithelial cell types. Similarly, Howitt et al. performed RT-qPCR on sorted tuft cells and showed *Il25* enrichment compared to other epithelial subpopulations. All three groups confirmed that tuft cells are not a critical source of either TSLP or IL-33, two other type 2 cytokines known to be important in helminth response, although bulk analysis of tuft cells may have masked the subset-specific expression of *Tslp* revealed by single-cell analysis (Yan *et al*, 2017a). A $Villin^{Cre/+};Il25^{F25/F25}$ model enabled IL-25 ablation from epithelial cells and these mice lacked tuft cell hyperplasia on day 7 post-*N. brasiliensis* infection (von Moltke *et al*, 2016). Furthermore, IL-25 did not act directly on epithelial cells to promote tuft cell expansion, based upon in vitro intestinal organoid experiments (Gerbe *et al*, 2016). While von Moltke et al. showed

similar results in in vitro studies, exogenously applied IL-25 increased tuft cell numbers *in vivo*, confirming that IL-25 must indirectly stimulate tuft cell hyperplasia, likely via immune cell subpopulations.

Previous literature confirmed that the type 2 cytokines IL-4 and IL-13 are involved in parasitic worm expulsion (Allen & Sutherland, 2014). von Moltke et al. demonstrated that exogenous administration of IL-4 *in vivo* and in *ex vivo* enteroid culture induces tuft cell expansion. However, $Il4^{KN2/KN2}$ animals, which are IL-4 deficient, still have a hyperplastic tuft cell phenotype following worm infection (von Moltke *et al*, 2016). Furthermore, Gerbe et al. observed that IL-4 levels were not significantly different between *N. brasiliensis*-infected wildtype and *Pou2f3*-null mice, despite the absence of tuft cells in the latter condition. These results implied that IL-4 is sufficient but not necessary for tuft cell expansion and its downstream immune response. In contrast, when Gerbe et al. and von Moltke et al. examined the effects of worm infection in an *Il4ra*-null model, which displays disrupted IL-4 and IL-13 signaling, they observed no tuft cell expansion (von Moltke *et al*, 2016; Gerbe *et al*, 2016). Similarly, $Il13^{Cre/Cre};GT(ROSA)26^{STOP\text{-}Flox::DTA/+}$ animals, which have disrupted IL-13 signaling, do not have tuft cell hyperplasia upon infection (von Moltke *et al*, 2016). In contrast to IL-4 levels, IL-13 levels decreased in *N. brasiliensis*-infected *Pou2f3*-null animals, compared to infected wildtype mice (Gerbe *et al*, 2016). Furthermore, *in vivo* and *ex vivo* addition of IL-13 was sufficient to induce tuft cell expansion (von Moltke *et al*, 2016; Howitt *et al*, 2016; Gerbe *et al*, 2016), implying IL-13 is necessary and sufficient for inducing tuft cell expansion by acting directly on the epithelium. Lineage-tracing experiments by von Moltke et al. indicated that, similar to homeostatic conditions, infection-induced hyperplastic tuft cells are still specified via the *Lgr5*+ stem cell population rather than by clonal expansion of the existing tuft cells or by transdifferentiation (von Moltke *et al*, 2016). These results suggest IL-13 acts upon stem or progenitor cell populations to drive tuft cell lineage expansion.

Th2 lymphocytes and innate lymphoid cells type 2 (ILC2s) both secrete IL-13, so that either or both cell populations could be the primary mediator of tuft cell expansion in response to

eukaryotic infection (Allen & Sutherland, 2014). Th2 and ILC2 cell specification is controlled by transcription factor *Gata3* but, unlike Th2 cells, ILC2s lack antigen receptors (Allen & Sutherland, 2014; Gerbe & Jay, 2016; Gerbe *et al*, 2016). Elimination of both cell populations in immunodeficient RAG2;IL2Rγ-null mice attenuated tuft cell hyperplasia following *T. muris* infection (Howitt *et al*, 2016). *T. muris*-infected *Rag2*-null and *N. brasiliensis*-infected *Rag*-null mice, which lack Th2s but not ILC2s, had significant tuft cell expansion, confirming that Th2 cells are largely dispensable for this phenotype (Howitt *et al*, 2016; Gerbe *et al*, 2016). Tuft cell hyperplasia was not observed in infected *Il17ra*-null and *Il2rg*-null mice, which lack all innate lymphoid cells, or infected $Il5^{Cre/Cre}$;$GT(ROSA)26^{STOP\text{-}Flox::DTA/\ STOP\text{-}Flox::DTA}$ mice, which lack IL-5+ ILC2s, confirming that ILC2s are necessary to facilitate IL-25-induced tuft cell expansion, at least in these models of acute eukaryotic infection (von Moltke *et al*, 2016). Together these studies established a feedback model, summarized in Figure 5, in which tuft cells, through the release of IL-25, induce ILC2 recruitment or expansion and IL-13 release, stimulating tuft and goblet cell hyperplasia.

While tuft cell taste receptors have been proposed to sense luminal infection, it is unclear how these signals are transduced *in vivo*, either through intracellular or intercellular means, to induce tuft cell hyperplasia. A recent report suggested a possible role for the mTOR complex 1 (mTORC1), a critical nutrient sensing protein complex that drives cell proliferation and growth (Laplante & Sabatini, 2012; Aladegbami *et al*, 2017). The mTORC1 complex includes the proteins mTOR, mLST8/GβL, PRAS40, DEPTOR, and Raptor, a scaffold protein necessary for mTORC1 activation. Epithelial-specific *Raptor* ablation using $Villin^{CreER/+}$;$Raptor^{fl/fl}$ animals resulted in intestinal tuft cell loss, indicating that mTORC1 is necessary for homeostatic tuft cell lineage commitment (Aladegbami *et al*, 2017). Previous publications have demonstrated that mTORC1 plays a role in specification of other intestinal epithelial cell types, as mTORC1 activation promotes goblet and Paneth cell specification (Zhou *et al*, 2015; van Es *et al*, 2005). Furthermore,

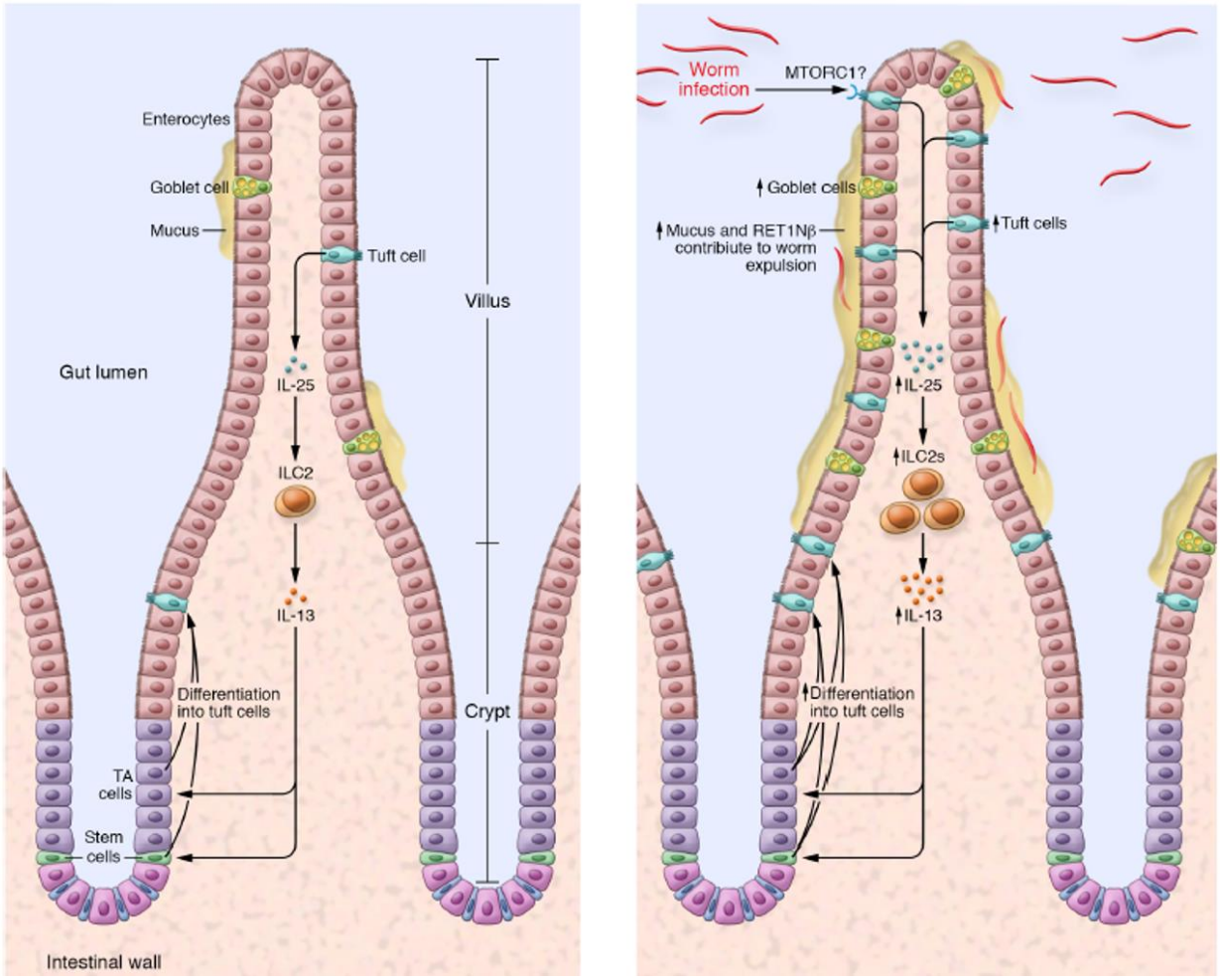

Figure 5. Small intestinal tuft cells induce a type 2 immune response following eukaryotic colonization of the gut. (A) At homeostasis, DCLK1^{+} cells promote their own specification through release of IL-25, which stimulates ILC2s to produce IL-13. By an unknown mechanism, IL-13 stimulates stem cells and/or transit-amplifying progenitors to differentiate into tuft cells. **(B)** During eukaryotic colonization of the small intestine, tuft cells sense pathogens through an ill-defined mechanism, possibly involving the mTORC1 complex and Raptor. Increased IL-25 release by tuft cells drives IL-13–dependent expansion of the tuft cell lineage. Goblet cell hyperplasia and increased release of mucus as well as the anti-helminth molecule RETN1β contribute to worm expulsion from the proximal gut.

tuft cell loss is accompanied by decreased epithelial *IL-25* mRNA and stromal *IL-13* mRNA expression, and lack of tuft cell expansion and type 2 immune response to *T. muris* infection (Aladegbami *et al*, 2017). pSTAT6, which is required for type 2 immunity (Allen & Sutherland, 2014; Ramanan *et al*, 2016), was decreased in infected *Villin$^{CreER/+}$;Raptor$^{fl/fl}$* animals, likely due to inadequate IL-13 levels (Aladegbami *et al*, 2017). Consequently, worm burden was significantly higher in infected *Villin$^{CreER/+}$;Raptor$^{fl/fl}$* mice versus wildtype animals (Aladegbami *et al*, 2017). In contrast to *in vivo* findings, *ex vivo* enteroids generated from *Villin$^{CreER/+}$;Raptor$^{fl/fl}$* mice lacked a tuft cell defect or difference in IL-4 signaling (Aladegbami *et al*, 2017). Thus, Raptor is unlikely to act in a cell autonomous fashion to direct tuft cell differentiation but might be involved in intercellular communication. Thus, the direct mechanism linking luminal sensing to tuft cell response still remains an important unanswered question for understanding how this chemosensory cell directs the clearance of eukaryotic parasites from the intestine.

Chapter III

SINGLE-CELL ANALYSIS OF DIFFERENTIAL RESPONSE TO INFLAMMATORY STIMULI

Recreated from: Alan J. Simmons*, **Amrita Banerjee***, et al. "Cytometry-based Single-cell Analysis of Intact Epithelial Signaling Reveals MAPK Activation Divergent from TNFα-induced Apoptosis in Vivo." *Molecular Systems Biology:* 835. 2015. Print. (*Co-first author)

Introduction

Characterization of protein signaling networks for systems-level analysis of cellular behavior requires the quantification of multiple signaling pathway activities in a multiplex fashion. Previous and current studies of multi-pathway epithelial signaling rely on bulk assays that hinge on the assumption of cell homogeneity in, for example, *in vitro* cell culture systems. Although useful in revealing coarse-grain biological insights into behaviors exhibited by a majority of cells (Lau *et al*, 2013, 2012, 2011), these technologies fail to address the complexities exhibited by heterogeneous cell types *in vivo*. Flow cytometry is a tractable method for detecting and quantifying signal transduction information at single-cell resolution (Krutzik *et al*, 2004; Irish *et al*, 2004). CyTOF, where the limitation of fluorescence spectral overlap is overcome by the resolution of metal-labeled reagents by mass spectrometry, allows for multiplex sampling of protein signals at a network scale and at single-cell resolution (Bendall *et al*, 2014, 2011). In parallel, newly developed fluorescent dyes and compensation algorithms allow 15-20 parameters to be measured simultaneously using multicolor fluorescent flow cytometry (O'Donnell *et al*, 2013). A tremendous opportunity for single-cell studies lies in expanding quantitative cytometric approaches to epithelial tissues, from which many diseases arise. A significant challenge, however, is the preparation of single-cell suspensions from these tissues while maintaining intact

cell signaling states. Disruption of epithelial cell junctions during cell detachment perturbs native cell signaling networks (Baum & Georgiou, 2011; Pieters *et al*, 2012) and can create experimental artifacts that overwhelm native signaling. To date, strategies to quantify epithelial protein signal transduction by cytometry approaches without confounding dissociation artifacts have not been developed.

We present a novel method, DISSECT, for preparing single-cell suspensions from epithelial tissues for single-cell, cytometry-based signaling analyses. We use DISSECT followed by CyTOF to characterize multiple signaling pathway responses in the murine intestinal epithelium following *in vivo* exposure to TNF-α, a pleiotropic cytokine that plays significant roles in the pathogenesis of IBD (Colombel *et al*, 2010), celiac disease (Chaudhary & Ghosh, 2005), and necrotizing enterocolitis (Halpern *et al*, 2006). In the villus of the duodenum, TNF-α triggers caspase-dependent cell death, creating an epithelial barrier defect that increases exposure of nutrient and microbial antigen to the underlying immune system (Williams *et al*, 2013; Lau *et al*, 2011). Remarkably, only a fraction of villus cells undergo apoptosis, and higher levels of cell death cannot be induced by a higher TNF-α dose (Lau *et al*, 2011). The existence of heterogeneous responses provides a unique opportunity to leverage the natural variation of cells for identifying perturbations that result in desirable cellular outcomes. To decipher heterogeneous responses at single-cell resolution, we first provide rigorous, quantitative validation of our single-cell approach in comparison to gold-standard lysate-based methods for evaluating both cellular identity and signaling. We then use DISSECT-CyTOF to quantify 21 protein and phospho-protein analytes across core signaling pathways at single-cell resolution. Quantitative modeling of single-cell datasets reveals that a subset of the presumably homogeneous enterocyte population exhibits combinations of signaling responses that confer sensitivity to TNF-α-induced cell death. Our results reveal novel insights into the intricacies of *in vivo* epithelial cell populations that exhibit significant complexity when perturbed and then observed at single-cell resolution. Our approach

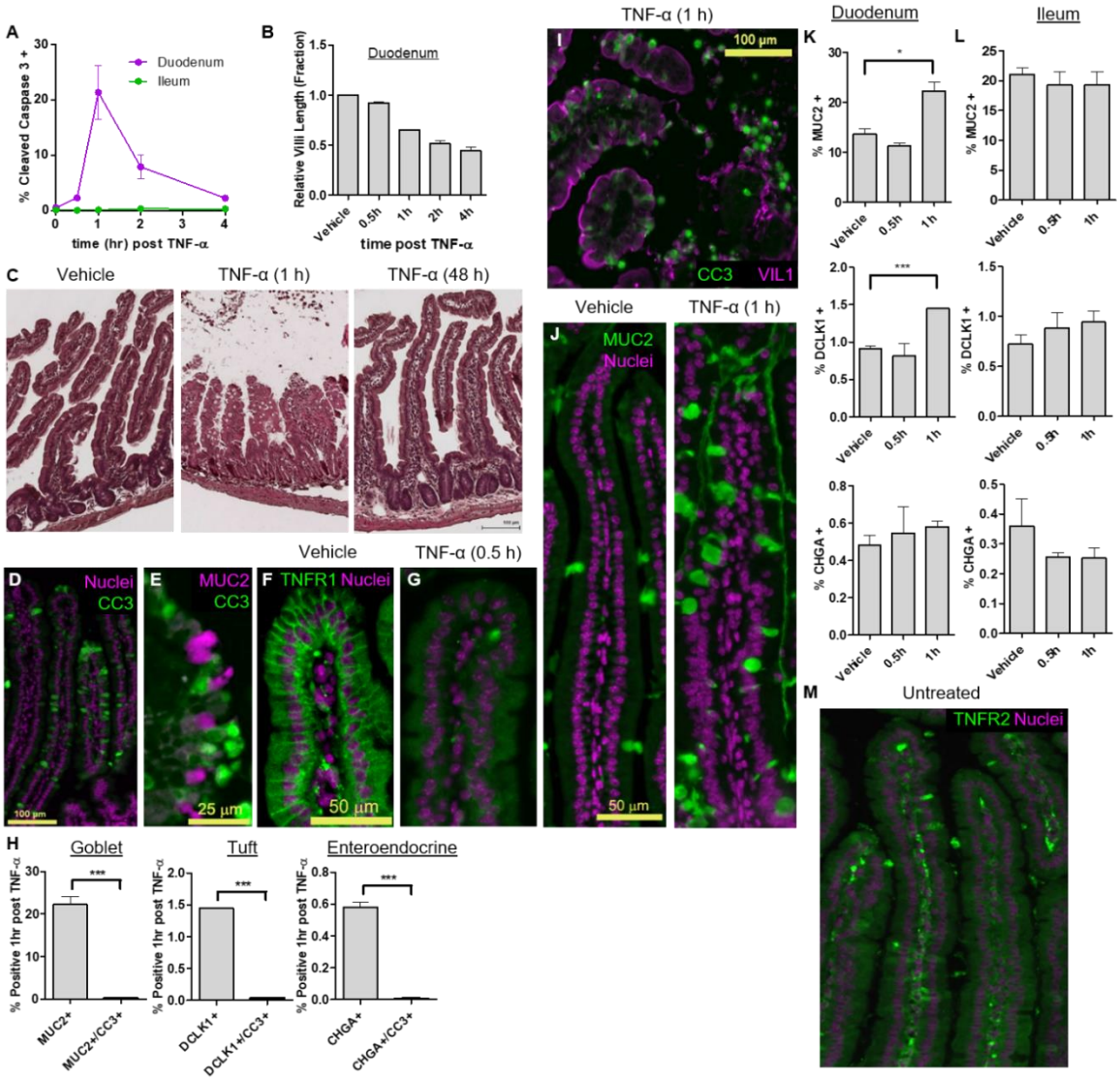

Figure 6. TNF-α induces heterogeneous villus epithelial cell death. (A) The fraction of CC3-positive cells identified by immunofluorescence (IF) image analysis over a time course of TNF-α induction. Error bars represent the standard error of the mean (SEM) from n=3 mice per time point. Cell death percentage integrated over time is 34.25 +/- 0.05 %. (B) Villi length quantified by image analysis, normalized to vehicle control. Error bars represent SEM from n=3 animals. (C) Morphology of villi 48 hours post TNF-α administration compared to vehicle control and 1 hour post TNF-α that exhibits severe villus blunting. (D) Representative immunofluorescence imaging (IF) of cells undergoing heterogeneous, position-independent TNF-α-induced apoptosis in the villus as marked by CC3. (E) Non-overlapping localization between MUC2 (marking goblet cells) and CC3 at 1-hour post TNF-α administration. Extrusion of cells does not necessarily occur at the villus tips. (F-G) Expression of TNFR1 at basolateral cell membranes of villus epithelial cells in (F) vehicle-treated tissues and (G) loss of the receptor following TNF-α exposure. (H) IF quantification of cells expressing villus epithelial cell markers only (MUC2 – goblet cells, DCLK1 – tuft cells, CHGA – enteroendocrine cells), or their co-expression with CC3 1hr post TNF-α administration. Error bars represent SEM from n=3 animals. (I) IF of VIL1 co-localization with CC3 1hr post TNF-α administration. (J) Increased density of MUC2-positive cells detected by IF as cell death occurs. (K-L) Quantification of mature villus cell types over time by IF image analysis using stereotypic markers (MUC2 – goblet, DCLK1 – tuft, CHGA – enteroendocrine), for both (K) duodenum and (L) ileum. Error bars represent SEM from n=3 animals. (M) IF for expression of TNFR2 in the villus. * P ≤ 0.05, ** P ≤ 0.01, *** P ≤ 0.001, **** P ≤ 0.0001

can be extended to a broad range of complex, heterogeneous epithelial tissues that can be studied via the use of either multiparameter flow cytometry or CyTOF.

Results

A novel disaggregation procedure for investigating epithelial signaling heterogeneity

Tissues *in vivo* present substantial heterogeneity at the cellular level, as exemplified by the different responses of individual cells to exogenous perturbations. We modeled heterogeneous response *in vivo* by inducing villus epithelial cell death by systemic TNF-α administration. TNF-α triggered apoptosis only in a third of duodenal villus epithelial cells over a 4-hour time course (Figure 6A-B). The remaining cells were not in the process of cell death, as evidenced by the full recovery of intestinal morphology 48 hours after TNF-α exposure (Figure 6C). Heterogeneous, TNF-α-induced apoptosis occurred intermittently throughout the length of the villus, and not only at the villus tip as observed in homeostatic cell shedding (Figure 6D). Furthermore, TNF-α-induced apoptosis appeared to occur solely in a subset of villus enterocytes, as cleaved caspase-3 (CC3) did not co-localize with other epithelial cell type markers (goblet- MUC2: Mucin2, tuft- DCLK1: doublecortin-like kinase 1, enteroendocrine- CHGA: Chromagranin A) (Figure 6E,H). However, CC3 was co-localized in cells positive for Villin, a protein of enterocyte brush borders, both within the villus epithelium (dying cells) and in the gut lumen (dead cells) (Figure 6I). The notion of enterocyte-specific cell death was further supported by increased goblet and tuft cell fractions over time, indicating enrichment of these cell types compared to the remaining enterocytes (Figure 6J-L). Although enterocyte cell death occurred heterogeneously in response to TNF-α, the sensing of TNF-α ligand by TNF receptor (TNFR) appeared uniform in these cells (Figure 6F). TNFR1 expression was observed on the basolateral membranes of all villus epithelial cells, and was reduced in all cells uniformly upon TNF-α stimulation (Figure 6G), consistent with internalization of the receptor in direct response to TNF-α binding (Schütze *et al*, 2008). TNFR2 was expressed at very low levels in the villus epithelium (Figure 6M), supporting

previous reports of its minimal role in the villus compartment (Lau *et al*, 2011). Since TNF-α sensing appeared uniform in all villus epithelial cells, we surmise that heterogeneous TNF-α responses in enterocytes may depend upon differences in signal transduction downstream of receptor binding.

DISSECT application of CyTOF identifies a differentially signaling enterocyte subpopulation that is sensitized to TNF-α-induced cell death

A 21-analyte CyTOF panel of heavy-metal labeled reagents specific for epithelial signaling was generated (Table 3). Twenty-one-plex CyTOF analysis was performed on three cohorts of mice subjected to a time course of acute TNF-α exposure, giving rise to average early and late signaling results that matched with flow cytometry, imaging, and quantitative immunoblotting (Figure 7A). We used single-cell CyTOF data to first reaffirm TNF-α-induction of cell death strictly within the duodenal enterocyte population. Indeed, CC3 did not colocalize with other epithelial cell type-specific markers (CK18: cytokeratin 18 – secretory subset, CLCA1 - goblet, CHGA-enteroendocrine, CD45 - leukocytes) (Fig. 7B-C compared to Fig. 6). The few double positive cells are not cell clusters. The fraction of differentiated cell types detected again matched published results (Gerbe *et al*, 2011; Rojanapo *et al*, 1980; Paulus *et al*, 1993; Imajo *et al*, 2014; van der Flier & Clevers, 2009; Wright & Alison, 1984; Gunawardene *et al*, 2011; Cheng & Leblond, 1974b), as well as flow and imaging data we obtained previously (Figure 7B). To identify subpopulations of enterocytes with distinct signaling activities indicative of cell death, we used t-SNE (t-Distributed Stochastic Neighbor Embedding) to visualize multiplex single-cell data in 2 dimensions while maintaining dissimilarities between cells in multidimensional data space (Figure 7D) (Amir *et al*, 2013). We again focused on the one-hour time point to characterize active signaling cells undergoing cell death. t-SNE analysis allowed groupings of different functional cell types based on combinations of signaling and cell identity markers. In addition, a distinct population of CC3+ enterocytes was identified. We used manual gating on t-SNE space to

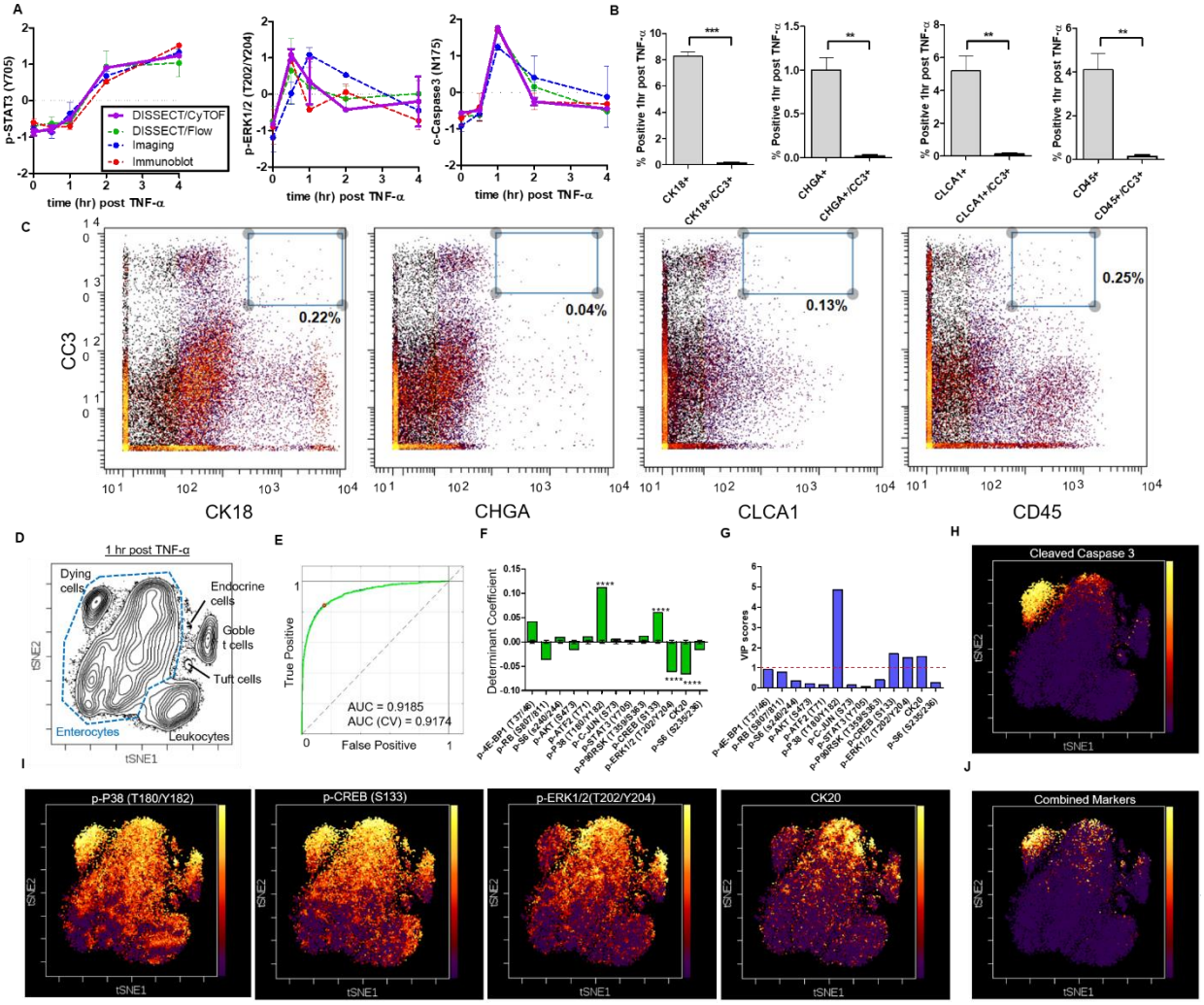

Figure 7. DISSECT disaggregation applied to CyTOF to investigate TNF-α signaling heterogeneity at single-cell resolution. (A) A sample of CyTOF signaling data generated from DISSECT in the intestinal epithelium as a TNF-α stimulation time course compared to other quantitative approaches. Data scales are normalized as in Figure 3. **(B)** CyTOF quantification of cells expressing villus epithelial cell markers only (CLCA1 – goblet cells, CK18 – subset of secretory cells, CHGA – enteroendocrine cells, CD45 –leukocytes), or their co-expression with CC3. Error bars represent SEM from n=3 animals. **(C)** Bi-plots generated by CyTOF demonstrating B for one sample. **(D)** t-SNE analysis of 21-dimensional single-cell data demonstrating the segregation of cell types by signaling and cell identity marker expression. **(E)** The ROC curve of a 2-dimensional PLSDA model used for selecting features classifying enterocytes undergoing cell death against those that do not. Blue line represents the calibration model built with all data, while the green line represents the average of cross validation models built with partial data. **(F)** Determinant coefficients of the model with error bars representing the standard deviation around 0 over 10000 permuted runs. Stars denote the four most statistically significant coefficients. **(G)** VIP scores of the model, with scores greater than 1 representing importance in classification. **(H)** t-SNE map with heat representing CC3 expression, **(I)** p-P38, p-CREB, p-ERK1/2, CK20, and (J) combination of the four markers.

supervise a partial least squares discriminant (PLSDA) model to categorize enterocytes undergoing cell death against living enterocytes. Classification based upon calibration signaling data in 2-latent variable PLSDA space to predict CC3 expression resulted in an area (AUC) of 0.92 under the receiver of operating characteristic (ROC) curve, indicative of high sensitivity and specificity (Figure 7E). We then cross-validated our model by repeatedly withholding 10% of the data using random, venetian blind, and block selection. Our cross-validation model yielded similar prediction power (ROC AUC = 0.92) compared to our calibration model due to the high number of data points used for fitting a model with a relatively limited set of parameters, which dramatically lowers the prospects of overfitting. We used the discriminant coefficients (β) of our PLSDA model to select signaling features that were informative for classification. Using 10000-fold permutation testing, we generated β distributions around zero and determined the probability for obtaining our model coefficients. The four coefficients with the lowest p–values were p-P38, p-CREB, p-ERK, and CK20 (Figure 7F). Another method for feature selection using Variable Importance in Projection (VIP) scores also identified the same four variables (Figure 7G). We overlaid these four variables onto t-SNE plots to determine their ability to predict CC3 expression (Figure 7H). While individual variables positively or negatively correlated with the CC3+ population, they were incapable of clearly discerning this population from other cellular populations (Figure 7I). Linearly combining these four variables without scaling allowed for clear identification of CC3+ enterocytes (Figure 7J), indicating that combinatory activities of multiple signaling pathways contribute to a “signaling code” that implicate cell death. More importantly, the same experimental and computational analysis applied to three different cohorts of mice selected the same set of four variables that identify CC3+ enterocytes (Figure 8A-B). In addition, other β coefficients besides the top four variables also followed the same trend of positive or negative correlation with CC3 in different mouse cohorts. These results indicate that DISSECT followed by CyTOF is a highly reproducible method to accurately characterize single-cell behavior using multi-pathway signaling parameters.

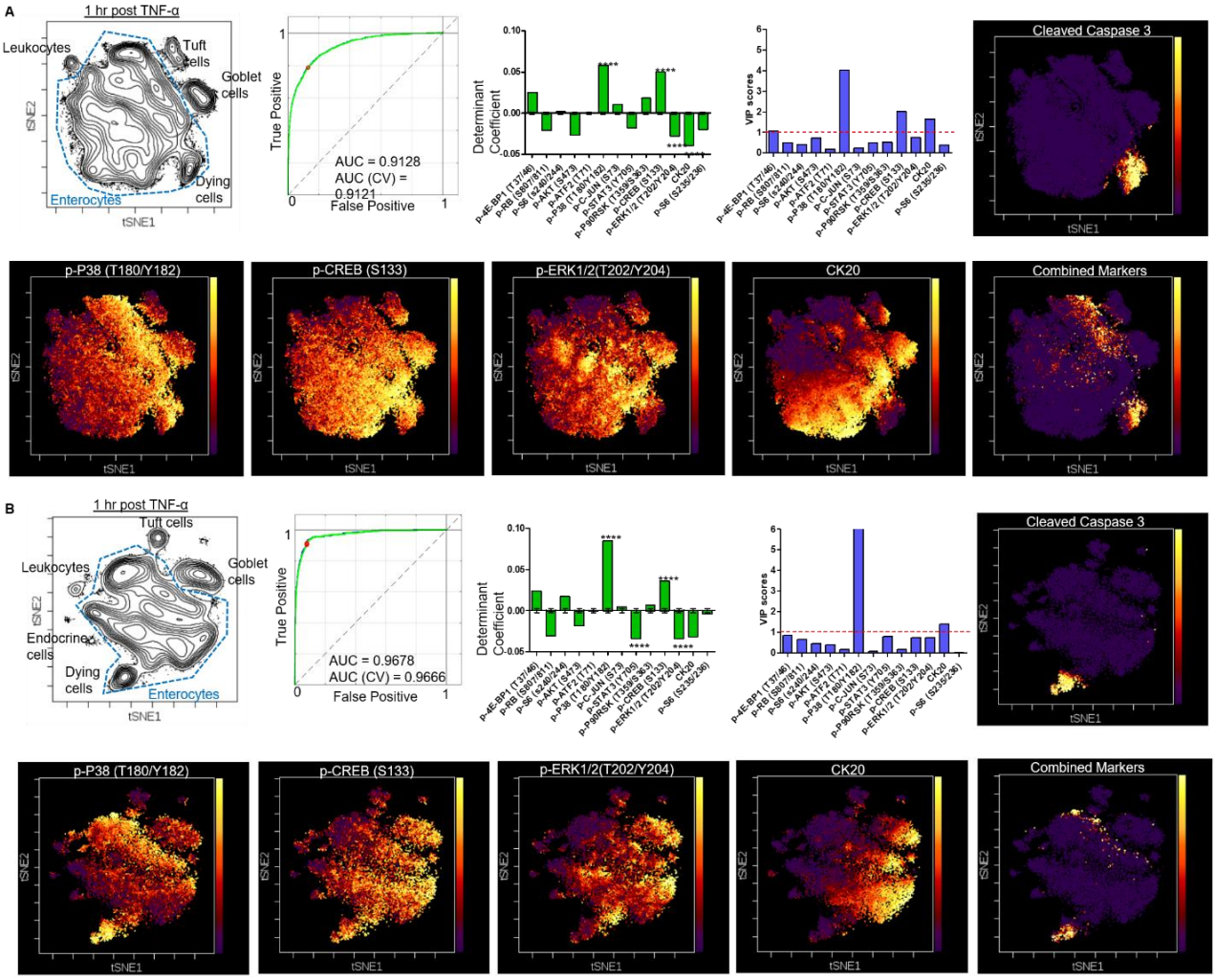

Figure 8. Analysis and modeling of 21-dimensional data over multiple biological replicates (A-B) Analyses were performed as described in **Figure 7 (D-J)**. The same set of features was statistically identified to drive classification of enterocytes undergoing apoptosis over independent experiments.

Divergently responding enterocytes are neighbors within the intestinal epithelium

Having a signaling fingerprint that classifies dying and non-dying enterocytes allows us to identify divergent signaling mechanisms that significantly affect intestinal physiology. Specifically, we chose to investigate divergent p-ERK signaling in the intestinal epithelium, which occurred in the surviving, but not in the dying, cell population. p-ERK activation in surviving enterocytes was also heterogeneous, which prompted us to envision spatial patterns of p-ERK activity that conferred survival. Whole-mount imaging of whole villus at 1-hour post TNF-α exposure revealed a “flower petal” ring-like pattern of epithelial p-ERK signaling, with five or six p-ERK positive cells surrounding a p-ERK negative area (Figure 9A, yellow arrows). Co-staining with CC3 revealed that in many cases, the dying CC3+ cells occupied the central area surrounded by p-ERK+ neighbors (Figure 9B, yellow arrows). In other cases, the dying CC3+ cell has already been extruded from the epithelium, leaving an apoptotic rosette surrounded by p-ERK+ cells undergoing contraction-dependent closure (red arrow). Furthermore, the ratios of CC3+ dying cells and p-ERK+ enterocytes in 3 cohorts of mice were 1:4.56, 1:6.04, 1:4.73, respectively, supporting that the immediate neighbors of the dying cell activated p-ERK signaling (Figure 9C-D). We surmise that the dying cell signals to neighboring cells non-autonomously to activate a cell survival program, in order to prevent large swaths of contiguous epithelium from dying and to prevent unrecoverable barrier defects. Thus, we tested the effect of inhibiting p-ERK signaling using the allosteric MEK inhibitor PD0325901 (Figure 9G). Inhibition of p-ERK signaling affected the latency of the cell survival program such that epithelial apoptosis occurred immediately following TNF-α exposure, which resulted in a higher number of dying cells in total (Figure 9I). Inhibition of P38 alone minimally affected TNF-α induced apoptosis (Figure 9H) but was able to partially normalize early apoptosis due to MEK inhibition (Figure 9I), consistent with P38’s pro-apoptotic role that is context-dependent. To our knowledge, this is the first reported observation of this “flower petal” pattern of p-ERK activation in response to TNF-α-induced cell death in epithelial tissue. This new finding demonstrates the applicability of our single-cell signaling

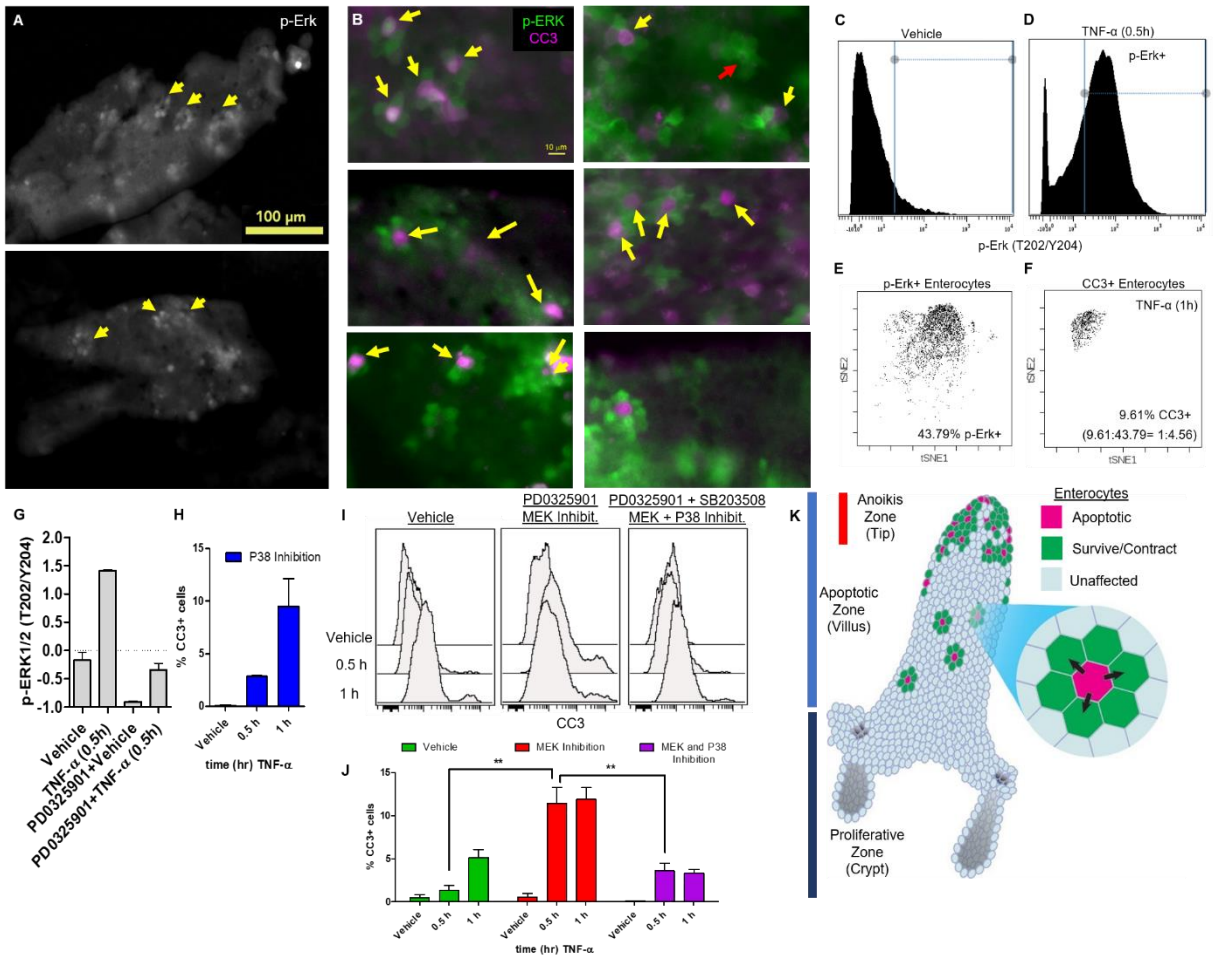

Figure 9. p-ERK activated in cells neighboring the dying cell promotes survival. (A) Whole villus imaging of p-ERK "flower petal" ring pattern surrounding a dying cell, as indicated by the yellow arrows. **(B)** $CC3^+$ cells surrounded directly by clusters of p-ERK^+ neighbors (yellow arrows); an example of contraction-dependent closure by p-ERK^+ cells after dying cell has been extruded (red arrow). **(C-D)** Gating of p-ERK+ cells from CyTOF data. A vehicle control **(C)** and a TNF-a-treated sample **(D)** were used to gate for cells with homeostatic p-ERK levels versus activated p-ERK levels, respectively. **(E-F)** p-ERK+ cells **(E)** and dying cells **(F)** plotted in t-SNE space for cohort 1. The percentages of dying and p-ERK+ cells were used to calculate ratio of dying to p-ERK+ cells. **(G)** The efficacy of MEK inhibition assessed by p-ERK stimulation by TNF-a in the duodenum at 0.5 h. Error bars represent SEM of biological duplicates. **(H)** Percentage of CC3+ cells by flow cytometry in the context of P38 inhibition. Error bars represent SEM of biological duplicates. **(I)** Flow cytometry of $CC3^+$ cells induced by TNF-α under conditions of control, MEK inhibition, and MEK and P38 inhibition. **(J)** Quantification of flow cytometry with error bars representing SEM from $n = 3$ animals. Unpaired *t*-test was used to determine statistical significance. $^{**}P \leq 0.01$. **(K)** Model of cell death-dependent activation of survival signaling in neighboring cells. Direct neighbors to the dying cell are instructed to survive to prevent contiguous patches of cell death unrecoverable by simple contraction-dependent closure.

experimental platform, in conjunction with data analysis, to reveal novel, non-cell autonomous responses in complex heterogeneous epithelia.

Discussion

A longstanding challenge for the expansion of multi-parameter cytometric analyses into epithelial signaling is the disruption of native signaling during single-cell disaggregation. While techniques have been derived to detect epithelial structural proteins by single-cell cytometric approaches (Yamashita, 2007), activated signaling components have never been shown to be quantifiable. The DISSECT procedure precisely overcomes this limitation by preserving native signaling states in single epithelial cells. The quantitative yield of single cells recovered is demonstrated to be higher than that of conventional dissociation methods for cytometric applications. Application of multiplex single-cell analyses enables the investigation of tissue heterogeneity that is characterized at the functional level by protein signaling. Natural variation of single cells, if accurately quantified, can be leveraged to generate tens of thousands of data points for building highly powered mathematical models. Our approach can reproducibly generate quantitative results, as supported by repeatable, robust conclusions drawn from mathematical modeling over multiple independent experiments in different animals. Furthermore, DISSECT has wide applications for either fluorescent flow cytometry or mass cytometry, and has demonstrated effectiveness in a broad range of epithelial tissues for interrogating *in vivo* signal transduction at single-cell resolution or in a cell type-specific fashion.

Our approach to interrogate single-cell signaling in epithelial tissues has several advantages over other single-cell assays. Common single-cell isolation approaches such as the Fluidigm C4 platform allow collection of only hundreds of cells, which limits the statistical power of downstream analyses (Trapnell *et al*, 2014). *In situ* approaches that require tissue sectioning result in inaccuracies in single-cell quantification, since it is very difficult to control how much of each cell is retained during tissue sectioning. Specifically, for intestinal epithelial cells that have

diameters of ~ 10 to 40 μm (depending on the axis measurement), 5 μm tissue sections result in partial analyses of cells that contribute to measurement noise. Multiplex imaging techniques, either iterative (Gerdes *et al*, 2013) or heavy-metal based (Giesen *et al*, 2014; Angelo *et al*, 2014), are relatively low throughput and can takes many hours of imaging for one sample, compared to 15 minutes per sample on the CyTOF. Arraying tissues on a slide can increase the throughput of imaging but at the expense of whole tissue sampling of large numbers of cells, since a small region of the tissue will be the focus of a particular array core. Similarly, sectioning can only provide a very localized representation of whole tissue unless comprehensive serial sectioning and analysis are performed, a proposal only practical for small scale studies. However, compared to *in situ* methods such as RNA *in situ* hybridization (Itzkovitz *et al*, 2011), disaggregation into single-cell suspensions eliminates all spatial context information. We can overcome this limitation by coupling cytometric analyses with imaging-based analyses such as MultiOmyx microscopy (Gerdes *et al*, 2013). Cell positions in cytometric analyses can then be cross-referenced to multiple markers characteristic of a cell's location determined by imaging. These marker-cell location relationships can be used for building "geographical maps", where independent cytometric datasets can be projected onto a spatial context.

Certain protein markers correlated much better than others when comparing the three experimental approaches. Partly, this is a reagent issue common in antibody-based detection assays, given that the access to a particular antigen is different under different denaturing and fixation conditions. Consequently, comparison between even the two traditional signaling analysis approaches, immunofluorescence imaging and immunoblotting, does not yield perfect correlation (Appendix Fig. S10). Our cytometric approach uses a different procedure to expose antigens and is expected to exhibit some differences. Due to this reason, a specific advantage of our approach is its ability to detect a wider variety of antigens inaccessible to traditional immunohistochemistry. For example, the stem cell marker LRIG1 can only be detected in fresh or frozen tissues but not in paraffin embedded fixed tissues, but it is accessible to DISSECT-cytometry (Poulin *et al*, 2014).

Other sources of noise that can dampen the correlations include differences by which the average signal is quantified between the different methods (via median intensity in cytometry, the integrated intensity of an immunoblot band, and the mean pixel intensity in imaging). Because of our limitations in defining intestinal cell borders in a confident manner using conventional imaging, we chose a highly reliable, unbiased way to establish nuclear and cytoplasmic masks for measuring signals in those subcellular compartments (Lau *et al*, 2007). This method, although simple, gives repeatable results especially with manual input, but comes with the added caveat that nuclear signals are fully represented whereas cytoplasmic signals represent a sampling of the perinuclear region. This may explain the sole discord in p-P90Rsk quantification given that this signal exists solely in the cytoplasm. Furthermore, quantification of tissue section images relies on microscope/camera-dependent pixel intensities in slivers of partial cells that are 5 μm thick, whereas flow cytometry quantifies the integrated voltage pulse generated by whole fluorescent particles. These differences in data generation were further amplified by our normalization procedure that can be affected by obvious outliers. Given these conditions, the high significance resulting from our correlation analyses is a testament to the robustness of DISSECT for generating quantitative results.

We previously published a model that selected features of TNF-α-induced cell death in the murine small intestine using lysate-based ELISA assays (Lau *et al*, 2011). Data variation was generated by examining different regions of the gut, which exhibit differential responses, or by using genetic mutations that affect TNF-α sensitivity (Lau *et al*, 2013, 2012). Our current approach to leverage natural variation in the same tissue can more accurately identify direct effectors of cellular behavior, since analyses of drastically different experimental contexts tend to select for secondary correlates. For instance, the duodenum and ileum are markedly distinct tissues (Bates *et al*, 2002), and features selected by modeling these variations may exaggerate the inherent differences between the tissues rather than actual modulators of TNF-α responses.

Our analysis identified that combinations of p-P38 and p-ERK MAP kinase pathway activities are critical determinants of TNF-α-induced cell death in the intestinal epithelium. A large body of literature over the past two decades has described P38 and ERK activation as responses to TNF-α-induced inflammatory stress in epithelial cells (Bian *et al*, 2001; Ho *et al*, 2008; Jijon *et al*, 2005; Kim *et al*, 2005; Saez-Rodriguez *et al*, 2009; Song *et al*, 2003). In these bulk cell studies, p-P38 and p-ERK are implied to be co-regulated in the same cells as stress signals. P38 activation has been shown to be required for cell death downstream of TNF-α in a variety of contexts (Yu *et al*, 2014; Wu *et al*, 2015); co-activation of ERK by TNF-α has also been shown to be required (Qi *et al*, 2014). Our previous analyses of bulk lysate data also identified the MEK-ERK pathway to be positively correlated with cell death (Lau *et al*, 2011). However, our current results demonstrate that ERK is not activated in the relatively small fraction of dying enterocytes, but is activated heterogeneously in the remaining cells as a secondary response, resulting in its overall up-regulation at a whole tissue level. Activation of p-ERK occurs in direct neighbors surrounding the dying cell, forming a “flower petal” ring-like pattern. We propose that dying cells send signals to neighboring cells to activate a survival program, in order to prevent large swaths of neighboring cells from dying. Previous studies have demonstrated that an epithelial cell in the apoptotic process can signal to its neighbors to initiate purse-string contraction, generating enough force for cell extrusion (Rosenblatt *et al*, 2001; Monier *et al*, 2015). We reason that when more than one contiguous cell undergoes apoptosis, contraction-dependent wound closure by surrounding cells becomes suboptimal, which leads to loss of epithelial integrity. Thus, epithelia have evolved intercellular communication programs for cells neighboring dying cells to survive. The molecular mechanisms responsible for this novel survival phenomenon remain to be identified, but may involve ATP released from the apoptotic cell, secretion of RTK ligands, or secondary responses downstream of cytoskeleton-dependent contraction (Patel *et al*, 2015; Boyd-Tressler *et al*, 2014; Kawamura *et al*, 2003; Xing *et al*, 2015). Consequently, inhibiting this survival mechanism both accelerated and increased TNF-α-induced cell death. Because of the complex *in vivo* regulation

of intact epithelium, there are most likely other redundant, MEK-independent mechanisms in place to prevent wholescale cell death. Our study is distinct from other epithelial wound healing studies that focus on local cell targeting (e.g., by laser ablation). Instead, divergent outcomes arise from epithelial cells exposed to the same apoptotic stimulus. This phenomena is also different from compensatory proliferation (Li *et al*, 2010), as cell death-driven proliferation in our system takes place in the crypt proliferative zone and not in the villus (Lau *et al*, 2011). Our novel epithelial cell-based CyTOF analysis allows us to identify heterogeneous signaling responses at the individual cell level with novel intercellular implications. Our epithelial application of cytometry-based technologies is useful for high-resolution dissection of heterogeneous responses in a complex tissue, and will have broad applicability to disease modeling, therapeutic design, and regenerative medicine.

Methods

Animal experiments and tissue collection

Female C57BL6/J Mice (Jackson Laboratory) were administered 0.4mg/kg TNF-α in PBS via retro-orbital injection and sacrificed at time points ranging from 30 minutes and 4 hours post injection. Control mice were injected with PBS and sacrificed at 30 minutes post-injection. These mice (and their microbiomes) were acclimatized to Vanderbilt's mouse facility for at least 4 weeks. Upon sacrifice, 5 cm sections of duodenum and ileum were removed, washed using PBS, and spread longitudinally onto Whatman paper. Epithelial tissue was then separated from the muscle layers using a razor blade and transferred to a fixative solution of 4% paraformaldehyde (PFA) (Affymetrix) with protease (Roche) and phosphatase inhibitors (Sigma). After 30 minutes fixation at room temperature, tissues were washed twice in PBS and re-suspended in a solution of 1% BSA and 0.005% sodium azide in PBS for storage of up to 2 months. The number of animals used to generate data for each experimental time point/condition is indicated in Figure Legends, but most were of n=3. As required, tissues from the same mice were either directly lysed in lysis

(RIPA) buffer supplemented with protease and phosphatase inhibitors for immunoblotting analysis, or fixed in 4% PFA overnight for histological and imaging analysis. Histological samples were transferred to 70% ethanol and embedded in paraffin.

Declaration of approval for animal experiments

All animal experiments were performed under protocols approved by the Vanderbilt University Animal Care and Use Committee and in accordance with NIH guidelines.

Cytometry analyses

For both flow cytometry and CyTOF, cells were initially gated from debris using DNA content (Hoescht/Iridium). This was followed by size gating to eliminate cell clusters to obtain mostly cells with 2n/4n DNA content (Appendix Fig. S2). Single cells were then analyzed for intensities of antibody conjugates. Flow cytometry was performed on a BD LSRII with 5 lasers and CyTOF was performed on a Fluidigm-DVS CyTOF 1 instrument.

Quantitative immunoblotting

Immunoblotting was performed using standard procedures and quantified using a LICOR Odyssey Fc imaging system. The top and bottom of the bounding box were used for background subtraction. Integrated intensity of immunoblot bands were taken after background subtraction (Appendix Fig. S8).

Quantitative immunofluorescence imaging

Mouse intestinal tissues were processed using standard immunohistological techniques and sectioned at 5 μm. Quantitative imaging was performed on an Olympus IX-81 inverted fluorescent microscope with a robotic stage for automated imaging of multiple fields of view. All images were first manually processed to eliminate stromal components. Automated image processing was then

performed using custom ImageJ scripts. For determining cell fractions, masks were generated from the marker of interest and then quantified. Quantification was then normalized to the mask generated by nuclear staining with Hoescht. For co-localization, the intersecting mask from two sets of masks was obtained and then quantified as above. For signaling quantification, a nuclear mask was made from the nuclear channel and a 2 pixel thick cytoplasmic mask was made 5 pixels away from the nuclear mask. The target signal channel was quantified within the nuclear or cytoplasmic mask depending on if the signal was nuclear or cytoplasmic. The mean pixel intensity of the target signal was used for comparing between methods (Appendix Fig. S8). A single time course was stained, imaged and quantified per slide, and multiple technical replicates from serial section were performed. Villi lengths were measured by the pixel lengths from tips of villi to bases of crypts at 2x magnification.

Data analysis

t-SNE analysis was performed using the viSNE implementation on Cytobank.org (Amir *et al*, 2013). Manual gating on t-SNE was performed by drawing contour lines based on density with 10% of the least dense data points excluded from the contours. The contours of the remaining cells represented cell populations grouped by their densities. PLSDA modeling, permutation testing, and feature selection were performed on Matlab (Mathworks). Unpaired t-tests were performed using Prism (Graphpad). Analyzed datasets are publicly available.

Antibody reagents

See Table 3 for antibodies used in immunofluorescence imaging, a detailed procedure is documented in the Antibody Validation section in (Gerdes *et al*, 2013). Briefly, the procedure includes an antibody titration to determine the concentration range for optimal signal-to-noise detection. Further specificity testing included, but not limited to, immunogen peptide blocking, phosphatase treatment of samples to verify phospho-specificity, and visual inspection of expected

localization patterns. The same antibody reagents were used across all experimental platforms. For optimization of antibodies for DISSECT-cytometry, similar titration studies were performed. Because the DISSECT procedure entails dissociation after staining, the localization of staining (crypt-villus/subcellular localization) was verified.

Table 3. Antibodies utilized for immunofluorescence imaging and flow cytometry.

Epitope	Clone
p-C-JUN (Ser73)	D47G9
p-STAT3 (Tyr705)	D3A7
p-CREB (Ser133)	87G3
p-ERK1/2 (Thr202/Tyr204)	D13.14.4E
p-S6 (Ser240/244)	N7-548
p-S6 (Ser235/236)	D3F9
p-P90RSK (Thr359/Ser363)	D1E9
p-MTOR (Ser2448)	D9C2
p-RB (Ser807/811)	J112-906
p-4E-BP1 (Thr37/46)	236B4
p-AKT (Ser473)	D9E
p-ATF2 (Thr71)	11G2
Cleaved Caspase 3 (Asp175)	Polyclonal CS9661
DCLK1	EPR6085
p-EGFR (Tyr1068)	D7A5
Cytokeratin 20	D9Z1Z
CLCA1	EPR12554-88
Chromogranin A	Polyclonal SC1488
Cytokeratin 18	C-04
CD45	30-F11
Iκβα	L35A5
TNFR1	Polyclonal SC7859
TNFR2	D-2
LRIG1	Polyclonal AF3688
Na+/K+ ATPase	EP1845Y

Chapter IV

TRAJECTORY MAPPING OF SINGLE-CELL DATA REVEALS AN ALTERNATE ORIGIN FOR SMALL INTESTINAL TUFT CELLS

Recreated from: Charles A. Herring, **Amrita Banerjee**, et al. “Unsupervised Trajectory Analysis of Single-Cell RNA-Seq and Imaging Data Reveals Alternative Tuft Cell Origins in the Gut.” *Cell Systems.* 6(1):37–51. Jan 2018.

Introduction

Multi-cellular organ function emerges from heterogeneous collectives of individual cells with distinct phenotypes and behaviors. Integral to understanding organ function are the different routes from which distinct cell types arise. Multipotent cells transition towards mature states through continuous, intermediary steps with increasingly restricted access to other cell states (Waddington, 1957). A stem cell can be identified by lineage tracing, a method whereby continuous generation and differentiation of cells from a labeled source results in permanently labeled organ units (Barker *et al*, 2007). Seminal studies have determined the relationship between stem and differentiated cells by focusing on the effects of genetic and epigenetic perturbations on terminal cell states (Noah *et al*, 2011). While the behaviors of intermediate states such as progenitor cells remain to be fully elucidated, modern single-cell technologies have enabled the interrogation of transitional cell states that contain information regarding branching cell fate decisions across entire developmental continuums (Gerdes *et al*, 2013; Giesen *et al*, 2014; Grun *et al*, 2015; Klein *et al*, 2015; Simmons *et al*, 2016; Treutlein *et al*, 2014; Paul *et al*,

2015). Despite experimental tools to generate data at single-cell resolution, resolving cellular relationships from large volumes of data remains a challenge.

Various computational approaches have been developed for tracking cell transition trajectories when temporal datasets are available (Marco *et al*, 2014; Zunder *et al*, 2015). However, for most adult and human tissues, *in vivo* cell transitions have to be inferred from data collected at a snapshot in time. A major push in the field of single-cell biology is to enable data-driven arrangement of cell states into pseudo-progression trajectories to infer cellular transitions. These algorithms fall broadly into two categories: Minimum Spanning Tree (MST)-based approaches (Anchang *et al*, 2016; Ji & Ji, 2016; Qiu *et al*, 2011; Shin *et al*, 2015; Trapnell *et al*, 2014) and non-linear data-embedding approaches (Haghverdi *et al*, 2015; Welch *et al*, 2016). MST algorithms are widely known to be unstable with large datasets, such that multiple distinct solutions are obtained given the same dataset (Giecold *et al*, 2016). MST algorithms also tend to overfit smaller datasets, producing topologies with superfluous branches (Setty *et al*, 2016; Zunder *et al*, 2015). While MST-based tools have shown utility when applied to well-defined systems such as hematopoiesis, they do not provide a direct means to assess solutions for determining the correct topologies of less-defined systems. Non-linear embedding algorithms, such as Diffusion Map, are sensitive to the distribution of data such that local resolution may be gained or lost. Thus, they are largely used for depicting simple topologies that can be derived from the largest variation in the data, with less emphasis on sub-branches (Haghverdi *et al*, 2015; Setty *et al*, 2016; Welch *et al*, 2016). While a large amount of effort has focused on visualization strategies (Zunder *et al*, 2015) solutions to statistically assess computed results remain to be developed and formalized. A class of algorithms developed by Dana Pe'er's group using supervised-random walk over a cellular network produce robust results that can be statistically scored (Bendall *et al*, 2014; Setty *et al*, 2016). The most recent advance, named Wishbone, can identify bifurcations in a topology, but is limited to cases with a single, known branch point (Setty

et al, 2016). There is a paucity of data-driven, unsupervised approaches that generate cell transition hierarchies *de novo* to map multiple branching decisions in a statistically verifiable way.

Tuft cells, also known as brush or caveolated cells, in the gut are a rare population of chemosensory cells that remains poorly understood (Gerbe & Jay, 2016). They originate from epithelial stem cells (Gerbe *et al*, 2011), and express taste receptors such as α-gustducin (Höfer *et al*, 1996) and TRPM5(Bezençon *et al*, 2007, 2008; Höfer *et al*, 1996), which implicate their function in chemoreception similar to lingual taste cells. Recently, a number of important studies have demonstrated their role in immune responses against helminth infection by establishing an IL25-IL13 circuit with innate lymphoid cells type 2 (ILC2s) (Gerbe *et al*, 2016; Howitt *et al*, 2016; von Moltke *et al*, 2016). Thus, understanding the development of tuft cells is important in intestinal disease contexts. Tuft cells are commonly thought to be specified from the secretory lineage (Gerbe *et al*, 2011) along with goblet, Paneth, and enteroendocrine cells (VanDussen *et al*, 2012), although their origins have recently been disputed (Bjerknes *et al*, 2012).

We sought to clarify the lineage origin of tuft cells with single-cell analysis. We present p-Creode, a novel algorithm to derive multi-branching transition trajectories with a unique method to statistically score each result. After rigorous validation of p-Creode, we used this tool, along with validation experiments in the mouse, to demonstrate that tuft cells may be specified outside the *Atoh1*-dependent secretory lineage in the small intestine but are regulated by *Atoh1* in the colon. Our findings highlight important physiological differences between the small intestine and the colon, which directly impact the development and function of tuft cells in these two anatomically distinct regions.

Results

p-Creode analysis of MxIF data generates robust topologies depicting intestinal cell specification

An unresolved issue in single-cell data analysis is the applicability of various algorithms across experimental platforms, such as flow-based or imaging-based methods, that generate data with different distributions. Therefore, we applied p-Creode to derive biological insights from data generated on a different technological platform, MxIF, to analyze intestinal cell transition relationships using single-cell data. MxIF is an iterative fluorescence staining procedure that dramatically increases the number of protein analytes that can be analyzed in a single tissue section (Gerdes *et al*, 2013). We applied MxIF to generate single-cell data depicting cell specification at homeostasis of the murine intestinal and colonic epithelia, which are continuously renewing tissues fueled by a stem cell-driven process (van der Flier & Clevers, 2009). Similar to hematopoiesis in the bone marrow, transitioning cell states (known as transit-amplifying or TA cells in the gut) are present at any snapshot in time, but they are poorly characterized and lack specific markers (Buczacki *et al*, 2013; van Es *et al*, 2012; Tetteh *et al*, 2016). We used MxIF with an 18-marker panel that broadly covers the stem-to-differentiated cell spectrum (Hopx, PCNA, Lgr5(GFP), Sox9, Survivin, CK20, Chromogranin A, DCLK1, Lysozyme, Muc2, p-EGFR(Y1068), Ki67, Villin, β-Catenin, NaKATPase, pan-Cytokeratin-PCK26, CD44v6, S6), with the assumption that multiple marker combinations can delineate transitioning cell states.

Mature cell types can be identified by canonical markers, such as Muc2 marking goblet cells, DCLK1 marking tuft cells, Villin marking enterocytes, Chromogranin A marking enteroendocrine cells, and Lysozyme marking Paneth cells. Combinations of p-EGFR, Hopx, and Sox9 marked distinct TA cells (Figure 10A-B). More importantly, the spatial resolution afforded by MxIF allowed the direct visualization of transitioning cells above the bottom of the crypt. For example, Lgr5(GFP) from a reporter mouse marked thin, wedge-shaped stem cells (crypt-based columnar cells or CBCs) (Barker *et al*, 2007) intercalating Paneth and Paneth-like cells at the crypt base, while Survivin marked CBCs and also transitioning cells in the mid-crypt (Figure 10A-B). A full depiction of all markers throughout the crypt-luminal axis of the small intestine and colon

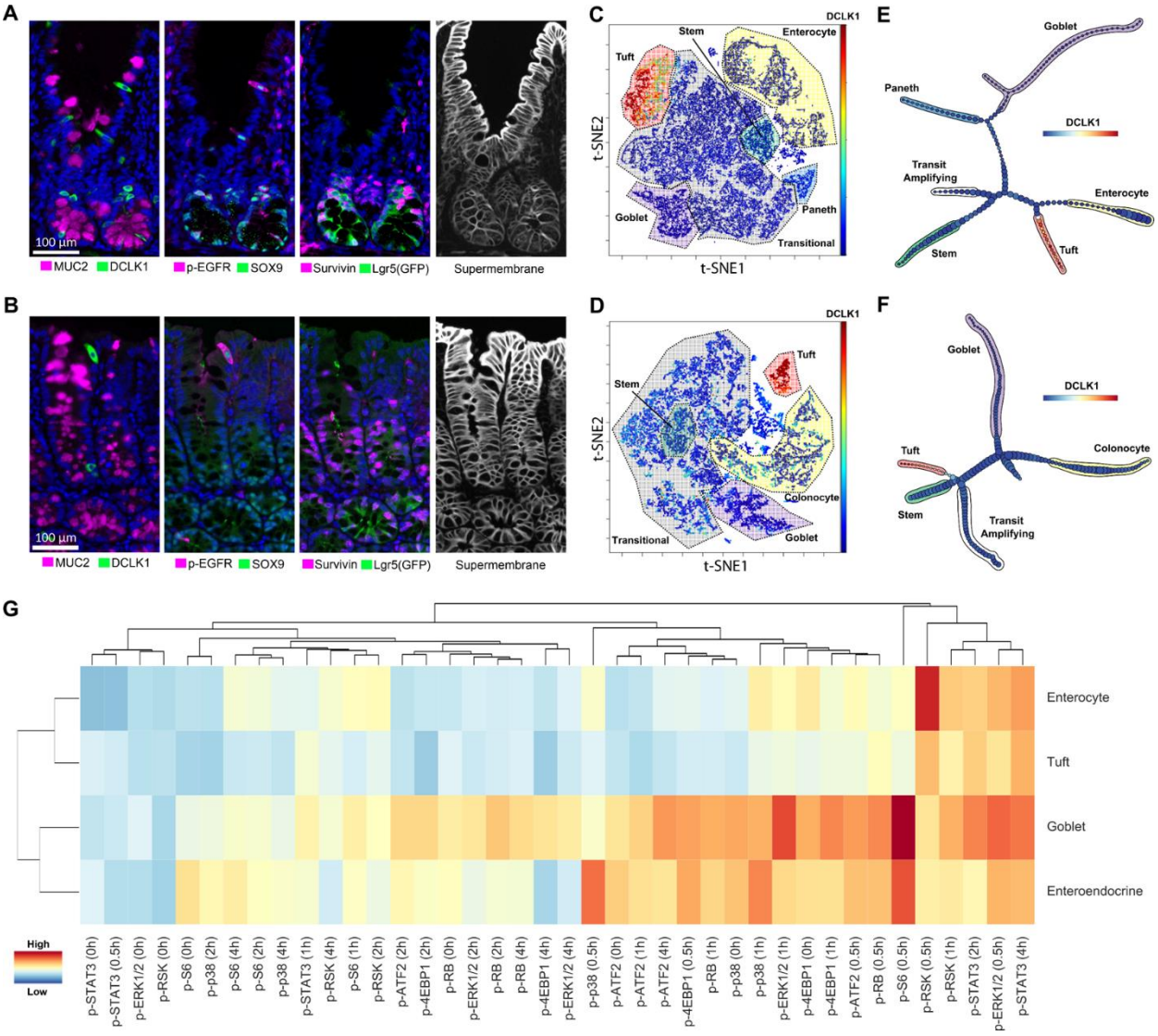

Figure 10. p-Creode analysis of single-cell multiplex immunofluorescence (MxIF) data reveals an alternate origin for tuft cells in small intestine versus colon. (A-B) MxIF images where quantitative single-cell data are derived by extracting segmented cell objects using a combined, "supermembrane" mask. Example staining for differentiated, transit-amplifying (TA), and stem cell markers in the **(A)** small intestinal and the **(B)** colonic epithelium. **(C-D)** t-SNE analysis on 19-marker MxIF datasets of the **(C)** small intestinal and the **(D)** colonic epithelium. Cell types, as defined by clusters on the t-SNE map, were manually annotated. Overlay represents DCLK1 levels. **(E-F)** p-Creode analysis of datasets in E and F with the most representative graphs over N=100 runs, for **(E)** small intestine and **(F)** colon. Overlay represents DCLK1 levels. **(G)** Hierarchical clustering of major epithelial cell types by their response to *in vivo* stimulation by TNF. Clustering on all normalized signals (indicated by heat map) measured by DISSECT-CyTOF.

is presented in Herring et al. Object segmentation with a super-membrane mask (β-Catenin, NaKATPase, PCK26, CD44v6), preprocessing to remove non-cells, and quantification of single cells were performed as previously described (McKinley *et al*, 2017a). We also applied an additional filter to remove data points (cells) that were gated negative for all markers and, therefore, uninformative to the analysis. Overall, data from 39,000 and 17,000 individual cells acquired from the small intestine and colon, respectively, were analyzed.

t-SNE and manual gating applied to the small intestine and colon datasets revealed several groupings of well-known intestinal epithelial cell types, as well as a large portion of unidentified, potentially transitioning cell states in both tissues (Figure 10C-D). p-Creode analysis of these datasets with N=100 resampled runs generated topologies with the same terminal cell types identified by t-SNE analysis (Figure 10E-F). Furthermore, the topologies connecting these terminal cell types through transitional cells largely resembled the known differentiation hierarchy of the small intestinal and colonic epithelium (Kim *et al*, 2014). At N=100 runs, robust results were obtained with most of the individual runs generating similar topologies (Figure 11). In the small intestine, Lgr5(GFP)+ stem cells were depicted to transit through cell states with variable expression of Survivin, Ki67, PCNA, Sox9, p-EGFR, and Hopx in cells largely residing outside the stem cell zone, as indicated by imaging (Figure 12). The topology implied a decision between secretory and absorptive lineages in this transitioning zone with secretory progenitors biased towards Hopx and Sox9 (Paneth and goblet progenitors), and absorptive progenitors biased towards proliferative markers (Ki67 and Survivin) (Figure 12). This bias is supported by studies of Notch activation and inhibition, which controls secretory versus absorptive cell specification associated with proliferation (Fre *et al*, 2005; Tsai *et al*, 2014). Secretory progenitors further branched into goblet and Paneth cells in the intestine, which are known to share a common origin.

Two possible abnormalities were identified from these topologies. First, Chromogranin A+ enteroendocrine cells were not identified, stemming from the extreme rarity of this cell type in our

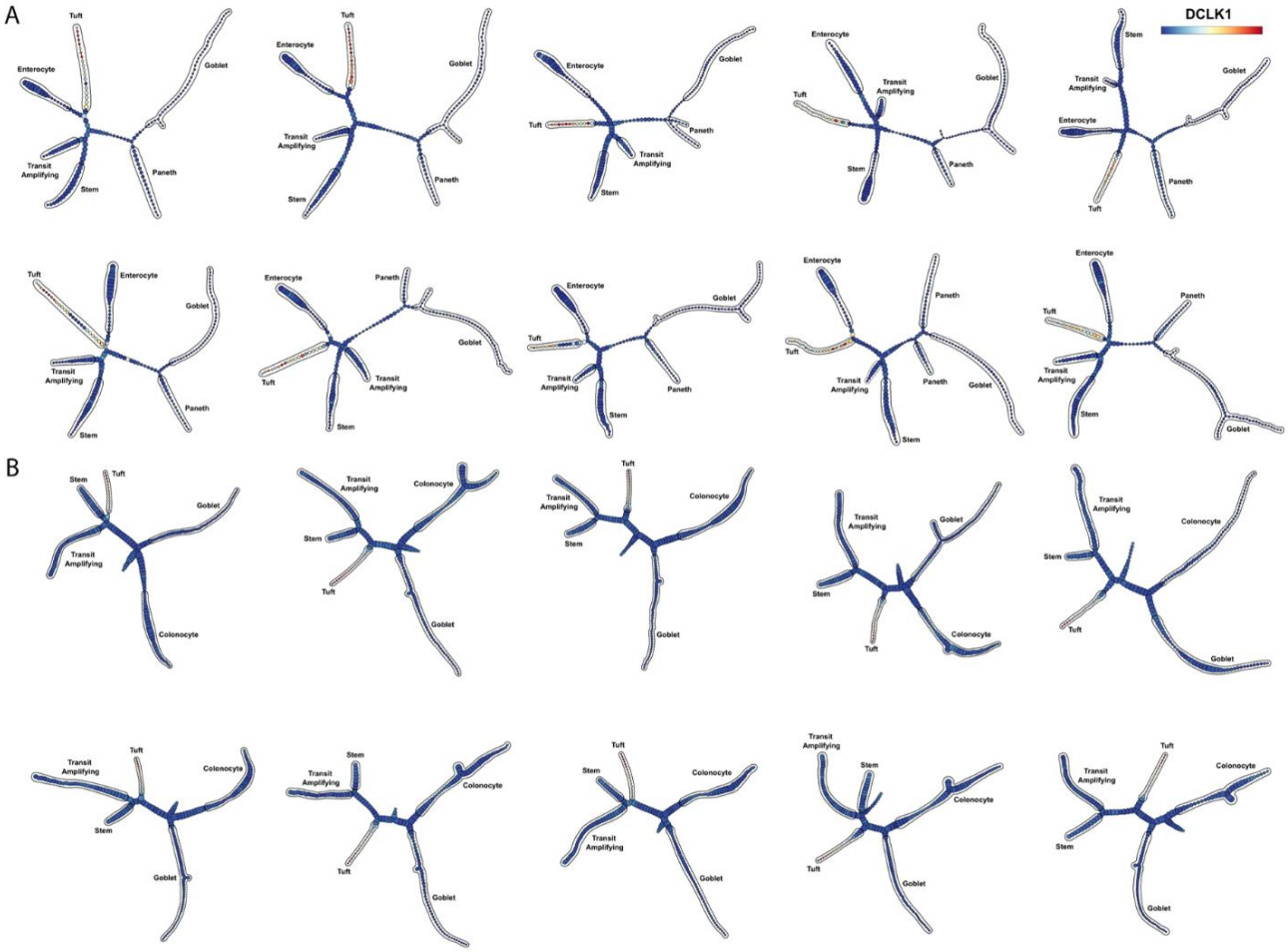

Figure 11. Robust sampling of p-Creode results from the gut epithelium. Ten resampled runs of p-Creode on MxIF datasets from **(A)** small intestine and **(B)** colon. Overlay represents *Dclk1* levels.

dataset (<0.2%), which makes them indistinguishable from technical noise in down-sampling. The rarity of Chromogranin A+ endocrine cells is supported by a recent study using a Chromogranin A-GFP reporter mouse (Engelstoft *et al*, 2015). Tuft cells, also relatively rare, make up ~ 1% of all epithelial cells in our datasets and thus were differentiated from noise. Second, cycling cells (Ki67/PCNA+) were identified as an end-state with its own branch, although the location of the branch in the topology was correct (in the TA population close to stem cells) (Figure 10E-F). Appearance of additional branches can result from using markers denoting cells in other states (such as in the cell cycle) distinct from the process of interest (cell specification). When we eliminated proliferative markers from the analysis, p-Creode was able to align TA cells, which express Survivin, Ki67, and PCNA, into the correct transition trajectory between stem cells and differentiated cells (Figure 13). Thus, markers selected for the analysis of a specific cell transition process must be considered since a complex biological system engages multiple processes simultaneously. Overall, p-Creode analysis on single-cell MxIF data was able to generate cell transition topologies of the gut that are supported by the literature.

Tuft cells are specified outside the Atoh1-dependent secretory lineage in the small intestine in contrast to the colon

Tuft cells are luminal-sensing epithelial cells recognized as a secretory cell type akin to goblet and Paneth cells. In the p-Creode analysis, tuft cells in the small intestine appeared distinct from the secretory lineage consisting of goblet and Paneth cells, and instead shared a common trajectory with enterocytes (Figure 10E). In the colon, however, tuft cells exhibited an alternative trajectory close to stem cells (Figure 10F). These results suggest alternate routes for tuft cell development between the small intestine and the colon.

To determine if tuft cells in the small intestine behave more similarly to secretory or

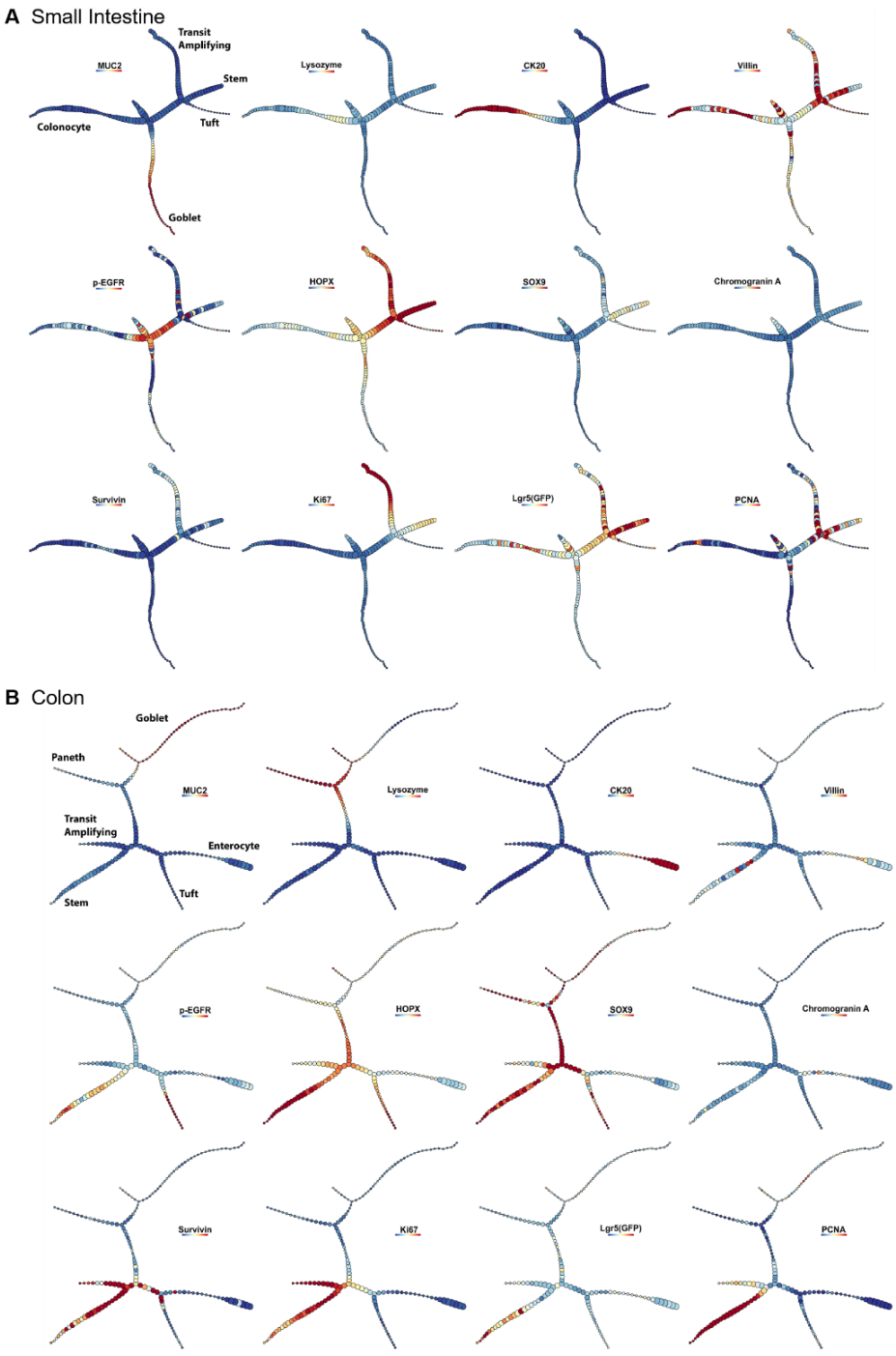

Figure 12. Overlay of different epithelial cell-specific protein markers on p-Creode topologies. (A) Overlays represent relative protein expression by MxIF in the small intestine. **(B)** Overlays represent relative protein expression by MxIF in the colon.

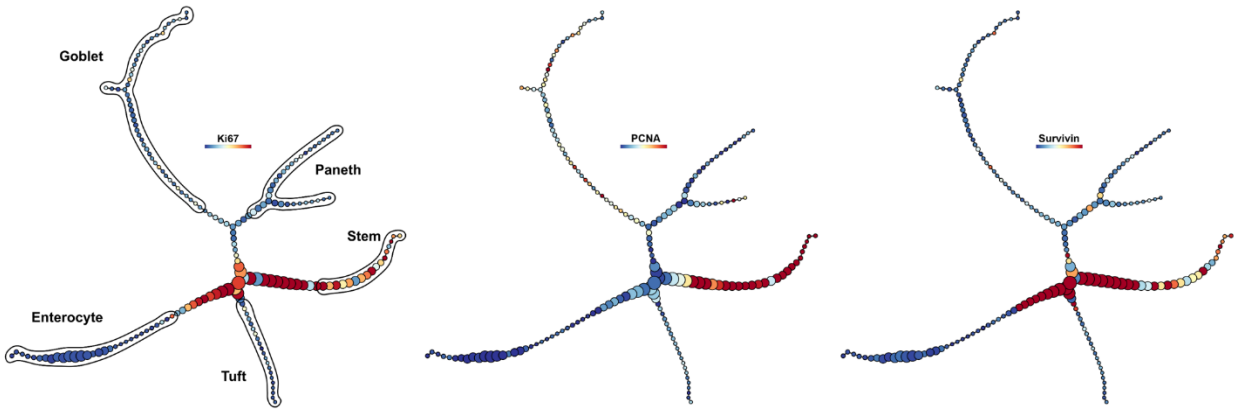

Figure 13. p-Creode analysis of small intestinal cell trajectories without proliferative markers. p-Creode analysis constructed without proliferative markers but overlaid with such markers and Survivin (a TA cell marker).

absorptive cells, we evaluated epithelial cell type-specific responses to TNF-α stimulation. Using the DISSECT approach (Simmons et al., 2015), intestinal epithelial tissues were collected over specific time points over a four-hour time course after systemic administration of TNF, disaggregated, evaluated by mass cytometry, and data were gated into different villus cell populations (Figure 14A). From these populations, 8 signaling proteins previously determined to respond to TNF were measured.

As previously shown (Simmons et al., 2016), TNF-α elicited stronger signaling responses in secretory cells compared to enterocytes (p-S6, p-ATF2, p-RB, p-p38, p-4EBP1, p-ERK1/2) (Figure 14B). Tuft cells shared low signaling amplitudes with enterocytes, as well as similar transient p-ERK and p-RSK dynamics (Figure 14B). Summarizing these observations, we used hierarchical clustering on all signaling parameters to determine similarities among cell types. Secretory cells clustered together, as expected, whereas enterocytes and tuft cells clustered together in contrast to their established lineages (Figure 10G). These results demonstrate that the signaling behaviors of small intestinal tuft cells over multiple pathways do not resemble secretory cells, consistent with p-Creode results of their origins.

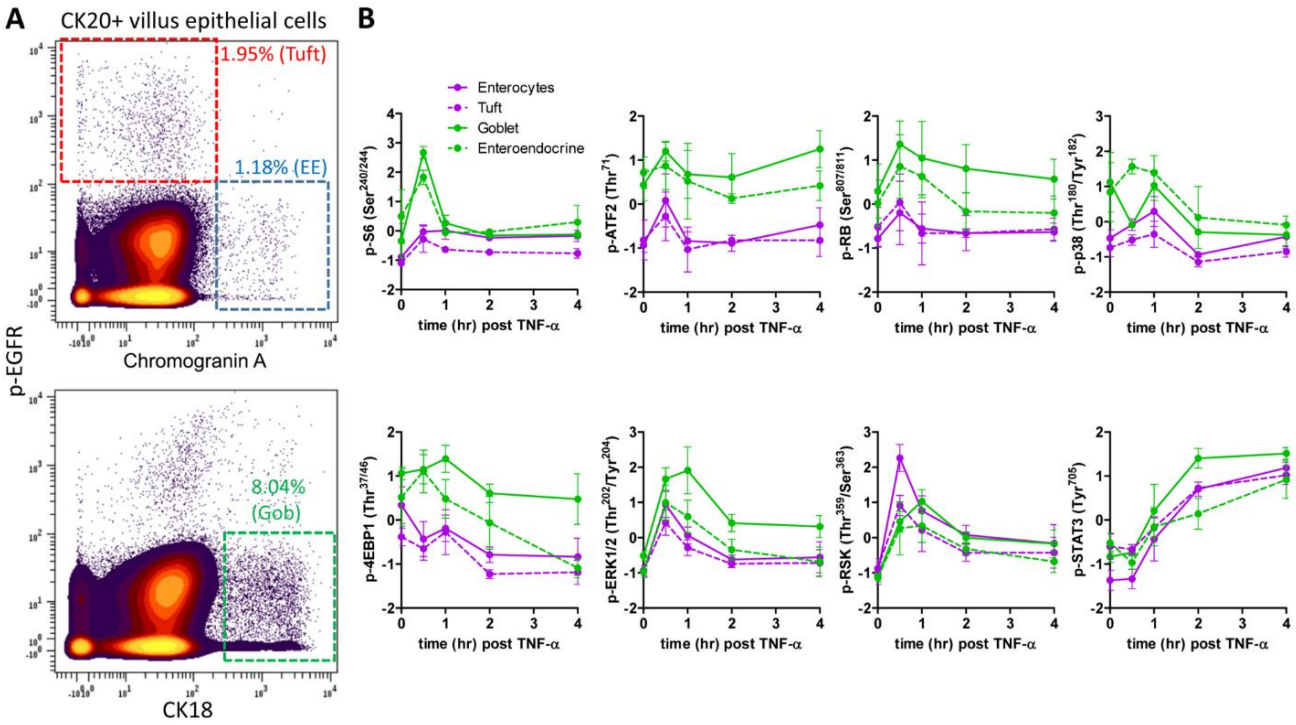

Figure 14. Tuft cells respond to exogenous stimulus in a different way compared to other secretory epithelial cells. (A) Gating scheme for differentiated (CK20+ villus) tuft, enteroendocrince (EE) and goblet (Gob) cells in the small intestinal epithelium from DISSECT-CyTOF data. **(B)** Epithelial cell type-specific time courses of different (8) signaling proteins in response to in vivo TNF stimulation. Cell types were gated as described in **A**, and multiplex data were collected from DISSECT-CyTOF. Error bars represent SEM from n=3 animals. Data scales are Z-score values derived from mean centering and variance scaling of each time course experiment after ArcSinh scaling.

To further validate p-Creode-generated results, we selectively ablated *Atoh1*, a master transcription factor that regulates the secretory lineage in the intestinal epithelium (VanDussen and Samuelson, 2010). We used the *Lrig1*$^{CreERT2/+}$ driver to induce excision of the *Atoh1* floxed allele in intestinal epithelial stem and progenitor cells (Powell et al., 2012), generating *Lrig1*$^{CreERT2/+}$*;Atoh1*$^{flox/flox}$ mice. Tamoxifen administration in adult mice resulted in complete ablation of CLCA1+ goblet and Lysozyme+ Paneth cells in the small intestine and CLCA1+ goblet cells in the colon (Figure 15A-D, Figure 16A-B). In contrast to previous findings (Gerbe et al., 2011), tuft cells, as marked by DCLK1, increased in the small intestine, rather than being suppressed (Figures 15A-B, 5E, 16A-C). These DCLK1 cells are *bona fide* tuft cells and not stem-like cells, as evidenced by their villus localization, candle-like "tufted" morphologies, and multi-marker protein signature (McKinley et al., 2017) (Figures 15B, 15E, Figure 16B). Because previous work has used a *Villin*$^{CreERT2/+}$ driver to induce recombination, we repeated our experiment using *Villin*$^{CreERT2/+}$*;Atoh1*$^{flox/flox}$ tissue, which again resulted in the increase of DCLK1+ cells (Figure 16D). In contrast, dibenzazepine (DBZ), a γ-secretase inhibitor known to inhibit Notch signaling, resulted in complete conversion of the epithelium into secretory cells, yet showed only a slight increase in numbers of tuft cells (Figure 16E) (VanDussen et al., 2012). Since *Atoh1* is the most proximal inducer of intestinal secretory progenitors (Buczacki et al., 2013; Kim et al., 2014, 2016; Li et al., 2016; Shroyer et al., 2005), these results again suggest that tuft cells do not descend from the established secretory lineage in the small intestine.

Contrary to the small intestine, tuft cells in the colon, marked by DCLK1 expression, were absent when *Atoh1* was ablated, responding to *Atoh1* loss in a similar fashion to CLCA1+ goblet cells (Figures 15C-D, 15F). This result suggested that colonic tuft cell specification was indeed controlled by the master secretory cell transcription factor *Atoh1*, whereas this was not the case in the small intestine. These experiments corroborated our p-Creode assessment of tuft cell specification differences between the small intestine and colon.

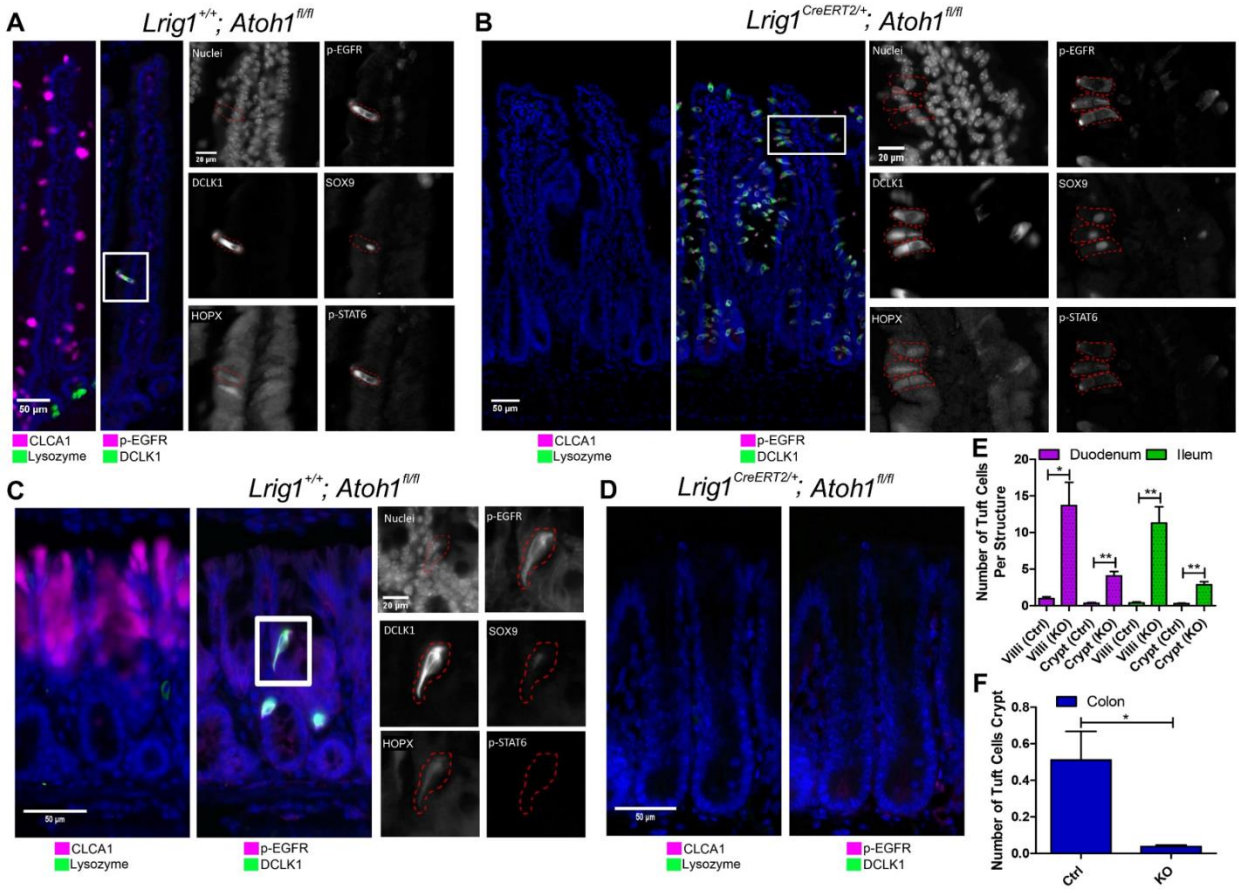

Figure 15. Tuft cells have alternative specification requirements in small intestine versus the colon. (A) Control (*Lrig1*$^{+/+}$*;Atoh1*$^{fl/fl}$ + tamoxifen) and **(B)** epithelial-specific Atoh1 ablated (*Lrig1*$^{CreERT2/+}$*;Atoh1*$^{fl/fl}$ + tamoxifen) duodenum, with acute ablation of *Atoh1* at 8 weeks of age and analysis performed 2 weeks later. Analysis of Paneth (Lysozyme+), goblet (CLCA1+), and tuft (DCLK1+; p-EGFR+) cells. Inset represents a multi-marker tuft cell signature of cells on the villi with certain markers (p-STAT6, p-EGFR) demonstrating an apical tuft staining pattern. **(C)** Control and **(D)** epithelial-specific *Atoh1* ablated colon, analyzed the same way as in **A-B**. **(E-F)** Quantitative analysis of DCLK1+ cells from images per crypt or villus in the **(E)** small intestine and **(F)** colon (F). Error bars represent SEM from n=3 animals. **P<0.01, *P<0.05 by *t*-test.

p-Creode application on scRNA-seq data generated from mouse colon reveals additional cell transition relationships

We then generated scRNA-seq data on the mouse colon with the inDrops platform, which uses droplet-based encapsulation in conjunction with a barcoding strategy to query thousands of cells (Klein et al., 2015). Using an epithelial enrichment procedure (Sato *et al*, 2011b), single cells were isolated with at least 85% viability (Leelatian et al., 2017). After additional viability enrichment (see Methods) to >99% viability, ~1900 and ~700 colonic cells from two replicates were encapsulated and sequenced. After sequence mapping, barcode deconvolution, and filtering by reads (Klein et al., 2015), 2402 (92%) colonic cells with an average of 49,680 reads per cell were recovered. In line with previous results with inDrops, the doublet rate appeared close to 0% (Figure 17A). We then performed t-SNE analysis and observed that the data from the two replicates were largely interspersed within each other, signifying minimal batch effects (Figure 17B). t-SNE analysis on these data revealed the presence of progenitor cells, secretory cells, absorptive cells, and immune cells identified by lineage-specific markers (Figure 17C-D, Figure 18). Immune cells, presumably intraepithelial lymphocytes, were gated out such that only epithelial cells were further analyzed.

p-Creode analysis on colonic scRNA-seq data revealed a characteristic cell transition pattern with a stem/progenitor branch (Lgr5+/Lrig1+/Sox9+), an absorptive colonocyte branch (Slc26a3+/ Car1+), and a secretory goblet cell branch (Muc2+/Clca1+) (Figure 17E-F). Progenitor to differentiated cell relationships can be clearly delineated with the pan-differentiation marker Krt20 (CK20). Unlike MxIF which is candidate-based, scRNA-seq afforded additional details regarding cell trajectories. For instance, a Reg4+ goblet cell branch can be seen arising from the secretory lineage (Figure 17F). Reg4+ goblet cells were recently identified as deep crypt secretory cells that exhibit niche roles in the colon analogous to Paneth cells in the small intestine (Rothenberg *et al*, 2012; Sasaki *et al*, 2016). Similar to Paneth cells, they share a trajectory with

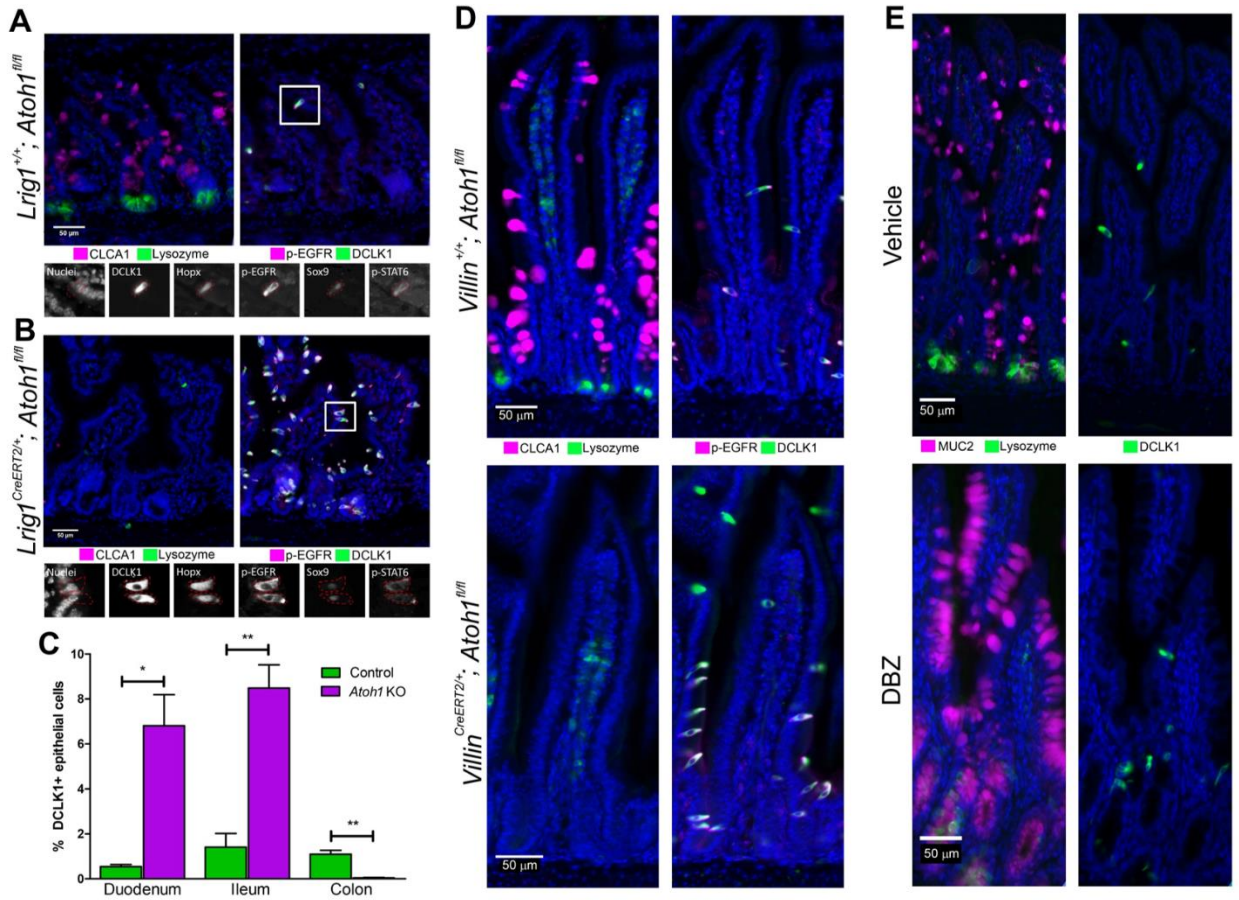

Figure 16. Tuft cells specification as a function of *Atoh1*. (A) Control (*Lrig1+/+;Atoh1fl/fl* + tamoxifen) and **(B)** epithelial-specific *Atoh1* ablated (*Lrig1CreERT2/+;Atoh1fl/fl* + tamoxifen) ileum, with acute ablation of *Atoh1* at 8 weeks of age and analysis performed two weeks later. Analysis of Paneth (Lysozyme+), goblet (CLCA1+), and tuft (DCLK1+; p-EGFR+) cells. Inset represents a multi-marker tuft cell signature of cells on the villi with certain markers (p-STAT6, p-EGFR) demonstrating an apical tuft staining pattern. **(C)** Automated image analysis to quantify tuft cell percentage by DCLK1. Approximately 100,000 cells analyzed for each sample over entire Swiss rolls. Error bars represent SEM from n=3 animals. **P<0.01,*P<0.05 by t-test. **(D)** Representative image of control (*Villin+/+;Atoh1fl/fl*) and epithelial-specific Atoh1-ablated (*VillinCreERT2/+;Atoh1fl/fl*) duodenum. Analysis of Paneth (Lysozyme+), goblet (CLCA1+), and tuft (DCLK1+; p-EGFR+) cells. **(E)** Vehicle and DBZ-treated duodenum. Analysis of Paneth (Lysozyme+), goblet (Muc2+), and tuft (DCLK1+) cells.

goblet cells in the colon in our analysis. These cells appear to arise from a Sox9+ progenitor, and Sox9 is a known transcription factor required for Paneth cell differentiation (Mori-Akiyama et al., 2007). In addition, *Atoh1*, the master transcription factor for the secretory lineage, was also mapped to secretory cell progenitors.

While p-Creode has the potential to contribute to the ongoing debate on the existence of multiple reserve stem cell populations or whether reserve stem cells are dedifferentiated committed cells (Buczacki *et al*, 2013; Li *et al*, 2016; Yan *et al*, 2017b), our limited dataset does not allow us to reach a definitive conclusion. Because of the overrepresentation of committed cell states, the resolution required to depict the more nuanced relationships among rare populations of reserve stem cells (~5 cells in a set of >2000 cells) was lacking. To refine these relationships, it will be necessary to enrich these populations prior to encapsulation in a more targeted analysis. Similar to stem cells, tuft cells were also underrepresented in our dataset (Figure 17B). They expressed tuft cell markers, including Dclk1 and Nrgn (Middelhoff *et al*, 2017), and also Il25 (data not shown), a cytokine recently identified to be expressed in tuft cells to modulate type 2 immune responses (Gerbe *et al*, 2016; von Moltke *et al*, 2016) (Figure 17F). Similar to analysis derived from MxIF data, both t-SNE and p-Creode analysis placed the tuft cell lineage close to the stem cell lineage in the colon (Figure 17B, E). These results reveal the global structure of cell-state transitions from unbiased scRNA-seq data of the colonic epithelium.

Discussion

We have developed a new single-cell data analysis platform, called p-Creode, for the unsupervised mapping of multi-branching topologies from high-dimensional single-cell data. Importantly, a metric for scoring graph structures comprised of both changing nodes and edges was derived to statistically evaluate the quality of computed results. To the authors' knowledge,

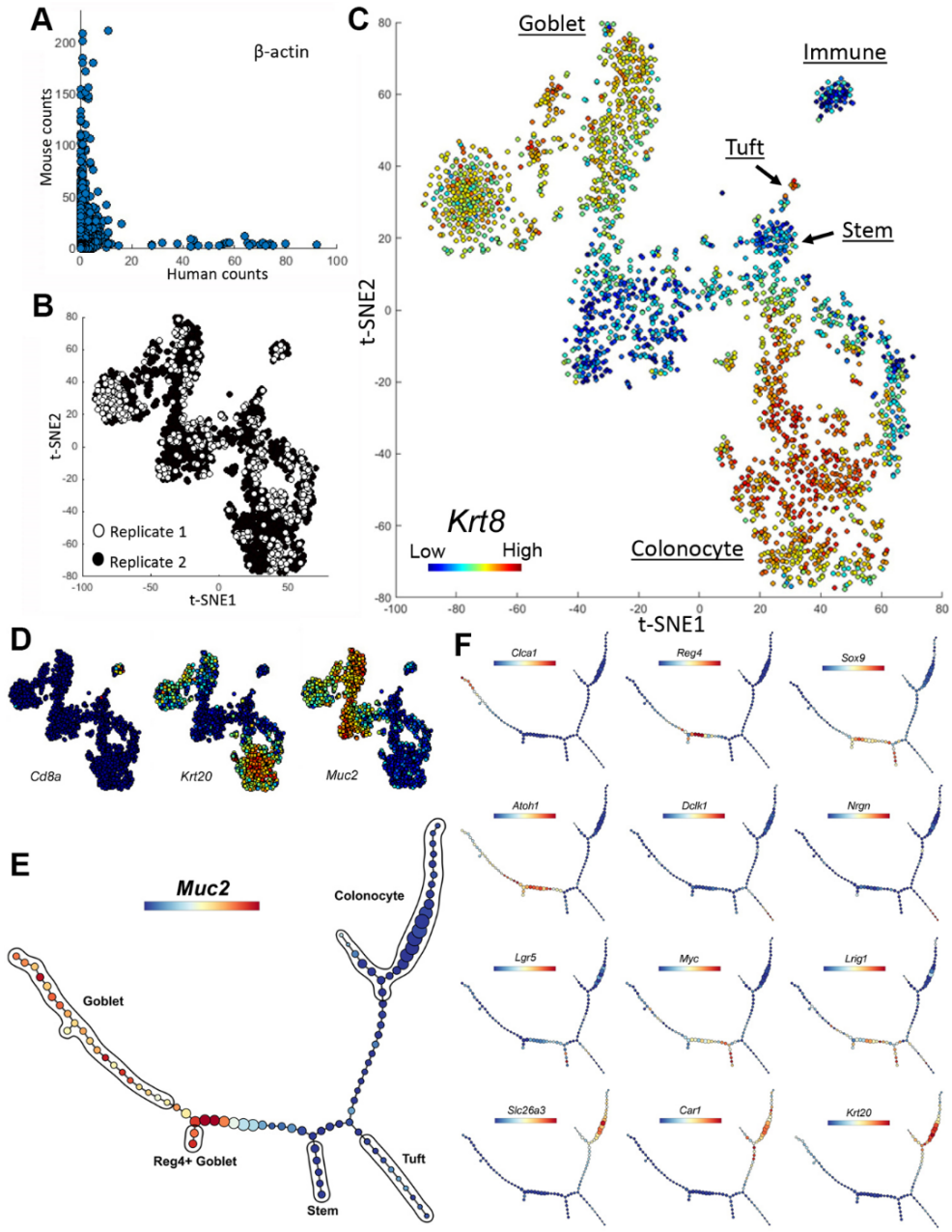

Figure 17. inDrops scRNA-seq reveals the developmental trajectory of Reg4+ secretory cells in the murine colon. (A) Human versus mouse β-actin transcript count by mapping to human and mouse reference genomes, respectively. Each data point represents a single cell. **(B)** t-SNE analysis of scRNA-seq data demonstrating the absence of segregation of data points from 2 replicates. **(C)** t-SNE analysis of murine colonic cells using scRNA-seq data. Cell types, as defined by clusters corresponding to specific cell type markers on the t-SNE map, were manually annotated. Overlay represents *Krt8* transcript levels. **(D)** Overlay of selected transcripts depicting colonic cell lineages on the t-SNE map generated in **C**. **(E)** p-Creode analysis of scRNA-seq data generated by inDrops from colonic epithelial cells, most representative graph over n =100 runs. Overlay represents Muc2 transcript levels. **(F)** Overlay of selected transcripts depicting colonic epithelial cell differentiation on the p-Creode topology generated in **E**. Overlays represent ArcSinh-scaled gene expression data.

this metric is the first of its kind in the field of graph theory and can be applied to a variety of graphs such as signal transduction networks or phylogenetic trees. We have applied p-Creode on a variety of datasets from mass cytometry, MxIF, and scRNA-seq. Specifically, important is the ability of p-Creode to generate multi-branching trajectories in each of these cases to recapitulate the complexity of cell-state transitions, which is a significant step forward in the single-cell biology field.

We uncovered alternative routes of tuft cell ontogeny between the small intestine and the colon from our analysis. Tuft cells were originally found to be specified in the secretory lineage (Gerbe *et al*, 2011), but their origins have since been contested (Bjerknes *et al*, 2012; Westphalen *et al*, 2014). Both our computational and experimental analyses indicate an *Atoh1*-independent, and possibly, non-secretory cell origin of tuft cells in the small intestine, and an alternative origin of tuft cells in the colon. These observations support recent speculations by Gerbe and Jay regarding the potential functional differences among tuft cells at different anatomical sites (Gerbe & Jay, 2016), as well as our previous observations of different tuft cell distributions between the small intestine and the colon (McKinley *et al*, 2017a). The discrepancies in phenotypes among studies and organ systems may arise due to the secondary effects of the microbiome. It has been shown that tuft cells can be regulated by luminal parasites, such as helminths (Gerbe *et al*, 2016; Howitt *et al*, 2016; von Moltke *et al*, 2016), and commensal bacteria (McKinley *et al*, 2017a). As such, knockout of *Atoh1* ablates microbiome-regulating goblet and Paneth cells, which can subsequently affect tuft cells as a secondary effect. It should be noted that the small intestine and colon are characterized by large differences in microbial content and load, and we observe differential dependence of *Atoh1* on tuft cell development between the two regions. A recent study also suggested that tuft cells may share a common progenitor with subsets of enteroendocrine cells in the small intestine (Yan et al., 2017). Because of the importance of the microbiome in various ailments, modulating luminal-sensing tuft cell may be important in controlling allergic and

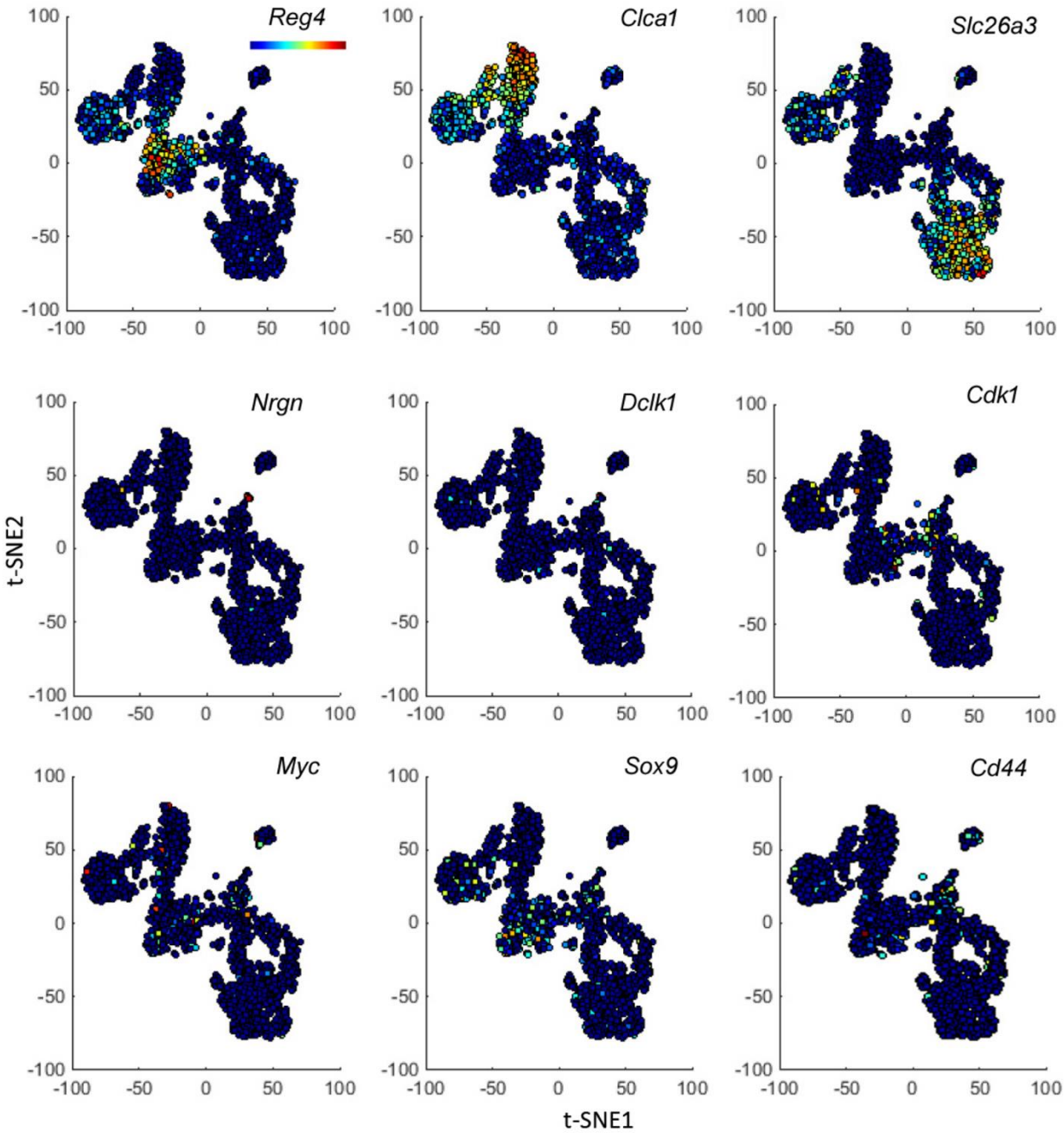

Figure 18. scRNA-seq data generated from the colonic epithelium by inDrops. Overlay of selected transcripts depicting colonic epithelial differentiation and cell type markers on a t-SNE map generated from inDrops scRNA-seq data. Overlays represent ArcSinh-scaled gene expression data.

inflammatory diseases.

p-Creode analysis of single-cell, tissue-level data generates hypotheses regarding cellular transitions. Specifically, p-Creode can be used to provide insights as to how the structures of transitional topologies change upon external perturbations such as in disease or wound repair. Our scoring metric provides a rigorous way to quantify the probabilistic nature of cell transitions where we expect a diverse ensemble of computed topologies in more stochastic transition processes. Overall, broad advances in single-cell data analysis, such as p-Creode, may have significant potential in a range of biomedical applications.

Methods

Mouse experiments

Animal experiments were performed under protocols approved by the Vanderbilt University Animal Care and Use Committee and in accordance with NIH guidelines. Mice were stimulated with TNF-α as a time course, and their duodena (proximal small intestine) were collected for analysis as previously described (Lau et al., 2012). For DISSECT, a previously published protocol was used (Simmons et al., 2015). For FFPE embedding for MxIF imaging, tissues were fixed in 4% formaldehyde for 24 hours and then were subjected to standard embedding procedures. For Cre-induced recombination experiments, 2 mg of tamoxifen (Sigma) was administered intraperitoneally at 2 months of age for 4 consecutive days, and animals were sacrificed, and their tissues harvested 14 days after the first injection. Both Cre and wildtype mice were administered tamoxifen to control for its effects. *Lrig1*^{CreERT2} and *Atoh1*^{fl} strains were purchased from the Jackson Laboratory in a C57BL/6 background. *Villin*^{CreERT2} and DBZ experiments were performed as previously described (Kim *et al*, 2014).

Mass cytometry analysis

Mass cytometry was performed on a Fluidigm-DVS CyTOF1 instrument with elemental calibration bead spike-ins (Finck *et al*, 2013). Cells were gated using intercalator (Iridium) following established procedures to identify intact single cells and eliminate cell doublets and clusters from analysis (Simmons *et al*, 2015). Single cells were then analyzed for intensity of multiple antibody conjugates. Further reagent information can be found in Herring et al.

MxIF analysis

FFPE tissues were sectioned at 4μm and processed using standard immunohistological and antigen-retrieval techniques. MxIF was performed by using a sequential staining and fluorescence-inactivation protocol as previously described (Gerdes *et al*, 2013). Imaging was performed on an Olympus X81 inverted microscope with a motorized stage and acquired at 20x magnification. Antibody staining was performed overnight at 4°C. At each round, images were computationally registered, and corrected for illumination and autofluorescence. Processed images were then segmented using a multi-marker supermembrane mask, and individual cells were quantified, as described (Gerdes *et al*, 2013). Partial and poorly segmented cells were removed. The mean, standard deviation, median, and maximum staining intensity for each protein was quantified with respect to the whole cell, cell membrane, cytoplasm, and nucleus, as well as cell location, area, and shape. Image processing was performed on the Amazon Cloud through the KNIME parallel architecture.

Single-cell RNA-sequencing

Colonic epithelium was enriched by incubating and shaking colonic issues in a 2mM EDTA/EGTA chelation buffer, as previously described (Sato *et al*, 2011b). The epithelium was then dissociated

into single cells with a collagenase/DNAse enzyme cocktail (2mg/ml Collagenase I, 2.5mg/ml DNAse1) in a modified protocol that maintains high cell viability (Leelatian *et al*, 2017). Cell viability was determined by counting Trypan Blue positive cells. The cell suspension was further enriched with a MACS dead cell removal kit (Miltenyi) prior to encapsulation, and the density of cells were calculated by counting. Before encapsulation ~10% human K562 cells were spiked into the suspension to evaluate the doublet rate. Single cells were encapsulated and barcoded using the inDrops platform (1CellBio) with an in vitro transcription library preparation protocol (Klein et al., 2015). The number of cells encapsulated was calculated by the density of cells arriving at the device multiplied by the duration of encapsulation. After library preparation, the samples were sequenced using Nextseq 500 (Illumina) using a 150bp paired-end sequencing kit in a customized sequencing run (50 cycles read 2, 6 for the index read, rest for read 1). The two replicates were multiplexed in a single sequencing run. After sequencing, reads were filtered, sorted by their barcode of origin and aligned to the reference transcriptome using inDrops pipeline (https://github.com/indrops/indrops). Mapped reads were quantified into UMI-filtered counts per gene, and barcodes that correspond to cells were retrieved based on previously established methods (Klein et al., 2015). Overall, out of ~2600 cells encapsulated, 2402 cells (92%) were retrieved.

scRNA-seq data analysis

For inDrops data, which consisted of raw transcript count, mitochondrial genes and genes where the maximal counts are one (noise) were filtered out, resulting in ~15,000 genes remaining. Transcript counts for each gene were normalized to the total transcript count per cell multiplied by the median total transcript count across all cells, as previously described (Setty et al., 2016). Data generated for inDrops were then ArcSinh normalized to stabilize the variance with a cofactor of 5, noting that the outcomes were not sensitive to the cofactor being used. From these

normalized data table, the same select gene procedure was applied as previously described (https://github.com/jw156605/SLICER) (Welch et al., 2016). Briefly, the procedure selects monotonically increasing genes using a neighborhood variance approach. These data were then analyzed by p-Creode.

p-Creode overview

The purpose of p-Creode is take inherently noisy single-cell data and reveal the robust, underlying structure under such data with *n* cells in *N* dimensional analyte space. The inherent technical variabilities generated by single-cell approaches conceal this structure to varying degrees. This is dependent on the process of study and the technology applied. Each of p-Creode algorithm's 6 steps is geared towards managing this issue: i) Down-sampling, ii) Graph construction, iii) End-state identification, iv) Topology reconstruction, v) Consensus alignment, vi) Scoring. Further information can be found in Herring et al.

Chapter V

SMALL INTESTINAL TUFT CELL SPECIFICATION AND FUNCTION IN ILEAL INFLAMMATORY DISEASE

Appear as: **Amrita Banerjee**, Charles A. Herring, et al. “Using scRNA-seq and microbiome analysis to decipher tuft cell specification and function in the small intestine.” (Manuscript in preparation).

Introduction

Crohn’s disease (CD) is a relapsing-remitting Inflammatory Bowel Disease (IBD) characterized by chronic inflammation of the small intestine, with 60% of CD patients developing disease in the terminal ileum (Caprilli, 2008; Goulart *et al*, 2016). Despite the rising rate of IBD diagnoses, the etiology of CD remains unclear, but is thought to be partially driven by a combination of a compromised barrier, a dysbiotic microbiome, and an altered immune response (Spalinger *et al*, 2014; Molodecky *et al*, 2012). Genome-wide association studies have clearly implicated epithelial-specific genes regulating microbial tolerance and clearance in IBD pathogenesis (Liu & Stappenbeck, 2016; de Lange *et al*, 2017; Liu *et al*, 2015; Barrett *et al*, 2009). In light of this, therapeutic strategies to manipulate the microbiome for ameliorating disease activity have been attempted with limited success. Broad spectrum and targeted antibiotic therapy have both had limited efficacy in treating active CD, and long-term remission is often not achieved with patients developing intolerance and other side effects to prolonged antibiotic regimens (Nitzan *et al*, 2016). Similarly, probiotics, such as VSL3 which consists of eight lactic acid-

producing bacterial species, and fecal microbiome transplants have demonstrated the ability to induce response and remission in small cohort of IBD patients with no significant adverse effects (Bibiloni *et al*, 2005; Lopez & Grinspan, 2016). Since non-targeted therapies have had limited efficacy in achieving remission in CD, the development of personalized microbiome therapies may benefit CD treatment (Nitzan *et al*, 2016; Bibiloni *et al*, 2005).

Longitudinal analysis of global IBD incidence has identified an inverse correlation between the rates of communicable disease and autoimmune disorders (Molodecky *et al*, 2012; Saidel-Odes & Odes, 2014; Koloski *et al*, 2008). Known as the "hygiene hypothesis," this phenomenon is thought to result from improved hygiene practices associated with decreased tolerance to environmental antigens (Saidel-Odes & Odes, 2014; Spalinger *et al*, 2014; de Silva MBBS & Korzenik, 2015). This paradoxical effect has led to emerging interest in the use of parasitic worms, or helminths, for the treatment of IBD (Helmby, 2015; Summers *et al*, 2003, 2005b, 2005a). Studies of the gut mucosa in IBD patients have demonstrated an increase in proinflammatory cytokines related to T-helper (Th)1 and Th17 cells, including interferon-γ and interleukin (IL)-17 as well as a commensurate decrease in Th2-associated cytokines, such as IL-25 and IL-13 (Su *et al*, 2013; Annunziato *et al*, 2015). An enhanced type 2 immune response, such as that seen in helminth infection, has been shown to suppress Th1 and Th17 activity (Su *et al*, 2013; Broadhurst *et al*, 2010). Clinical trial data in CD and ulcerative colitis (UC) patients has been inconclusive, as some trials have demonstrated decreased disease activity while others have been discontinued due to lack of efficacy (Summers *et al*, 2003, 2005b, 2005a). However, helminth therapy has its drawbacks given prolonged infection can cause complications and, therefore, precision therapy using excretory products may circumvent the majority of these issues (Summers *et al*, 2005a; Helmby, 2015).

Upon infection, helminths colonize the proximal small intestine and provoke a type 2 immune response orchestrated by doublecortin-like kinase 1 (DCLK1)-positive epithelial tuft cells

(Gerbe *et al*, 2016; von Moltke *et al*, 2016; Howitt *et al*, 2016). Through the release of IL-25, tuft cells promote their own specification via a positive feedback loop and tuft cell hyperplasia mediated by innate lymphoid type 2 cells (ILC2s) is critical for driving pathogen clearance (Gerbe *et al*, 2016; von Moltke *et al*, 2016; Howitt *et al*, 2016). Tuft cell specification depends upon genes, such as *Trpm5* and *Pou2f3*, which are canonical regulators of taste signal transduction (Gerbe *et al*, 2016; Howitt *et al*, 2016). Initially, studies of intestinal epithelial cell specification categorized DCLK1+ tuft cells within the secretory lineage, along with barrier-promoting goblet and Paneth cells, regulated by the master secretory transcription factor Atonal homolog 1 (*Atoh1*) (Gerbe *et al*, 2009, 2011). Recent studies have demonstrated that small intestinal tuft cells may have an alternative lineage specification route (Herring *et al*, 2018; Gracz *et al*, 2018) that may depend on cues from luminal microorganisms (Wilen *et al*, 2018). Despite the inverse relationship between incidence of parasitic infections and rates of IBD diagnoses, there is very little known about the functional role of tuft cells in human disease. In this study, we demonstrate that tuft cell specification is decreased in the inflamed small intestine of both human and mouse. By analyzing molecular pathway alterations in a lineage-specific manner during tuft cell hyperplasia, we identified commensal microbial-driven changes in metabolic pathways that promote tuft cell specification. Finally, metabolite-induced tuft cell hyperplasia in a mouse model of Crohn's-like ileitis suppressed disease symptoms and restored epithelial architecture.

Results

Reduced tuft cell numbers are correlated to areas of ileal inflammation in human and mouse

Numerous studies have elucidated the critical role of tuft cells in driving a type 2 immune

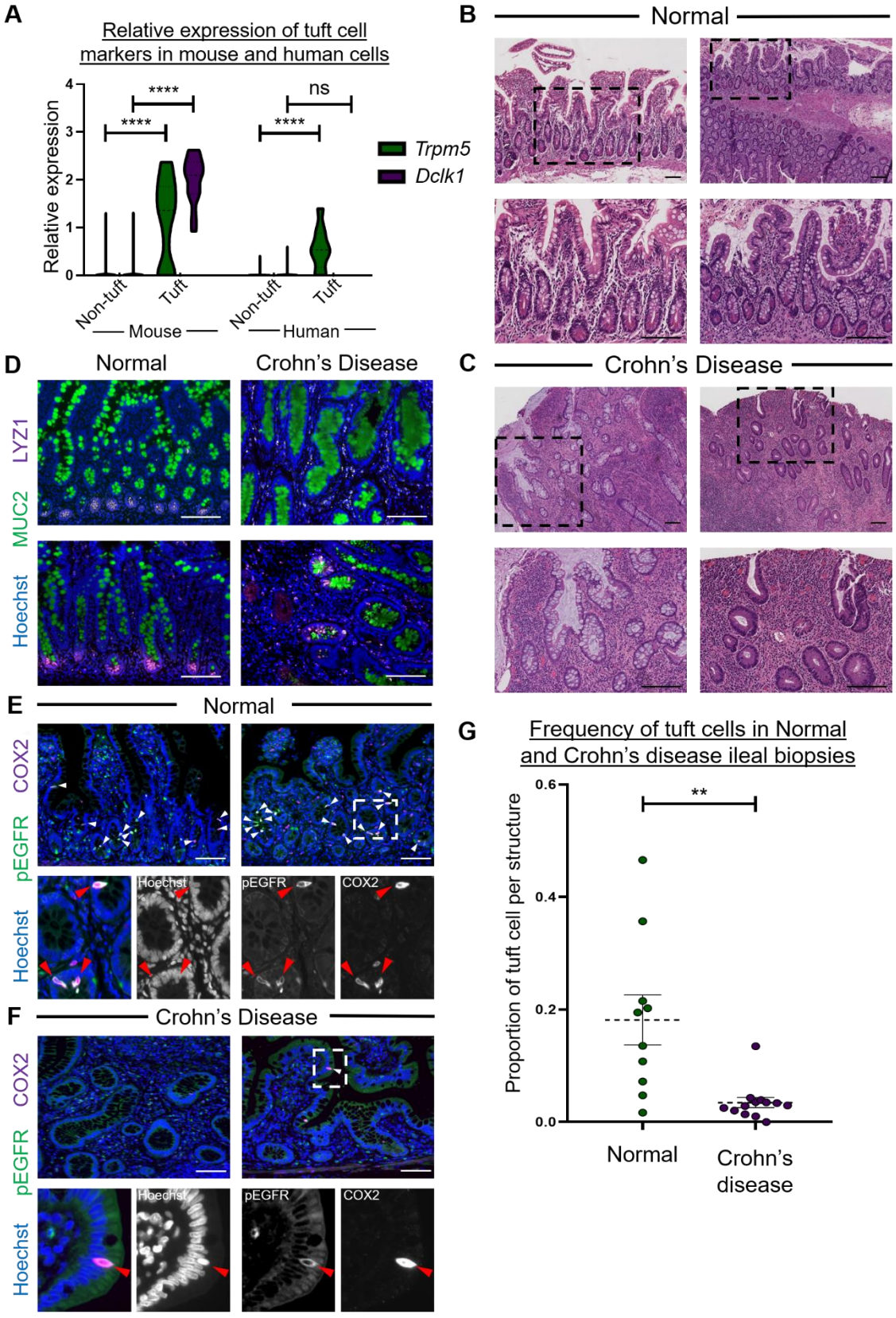
A
Relative expression of tuft cell markers in mouse and human cells
Relative expression
****
****
ns
****
Trpm5
Dclk1
Non-tuft
Tuft
Non-tuft
Tuft
Mouse
Human
B
Normal
C
Crohn's Disease
D
Normal
Crohn's Disease
LYZ1
MUC2
Hoechst
E
Normal
COX2
pEGFR
Hoechst
Hoechst
pEGFR
COX2
F
Crohn's Disease
COX2
pEGFR
Hoechst
Hoechst
pEGFR
COX2
G
Frequency of tuft cells in Normal and Crohn's disease ileal biopsies
Proportion of tuft cell per structure
**
Normal
Crohn's disease

Figure 19. Human tuft cells are decreased in patients with ileal Crohn's disease. (A) Quantification of relative gene expression of *Dclk1* (green) and *Trpm5* (magenta) in mouse and human non-tuft (n = 1166 and 1942 cells, respectively) and tuft cell (n = 13 and 9, respectively) populations from single-cell RNA sequencing. ****p < 0.0001 by t-test. **(B-C)** Histology of the distal small intestine from **(B)** normal and **(C)** Crohn's disease patients. Dotted square shows magnified inset. Representative images are shown from two separate normal or Crohn's disease patients, respectively. Scale bar = 100 μm. **(D)** Immunofluorescence staining of MUC2 (green) and LYZ1 (magenta) in normal and Crohn's disease ileal biopsies. Representative images are shown from two separate normal or Crohn's disease patients, respectively. Hoechst (blue) denotes nuclei, scale bar = 100 μm. **(E-F)** Immunofluorescence staining of pEGFR(Y1068) (green) and COX2 (magenta) in human ileum biopsies from **(E)** normal and **(F)** Crohn's disease patients**.** Co-localization of pEGFR and COX2 labeled small intestinal tuft cells, denoted by white arrows. Magnified inset of the epithelium shows that both markers are expressed in individual tuft cells, demarcated by red arrows. Representative images are shown from two separate normal or Crohn's disease patients, respectively. Hoechst (blue) denotes nuclei, scale bar = 100 μm. **(G)** Quantification of pEGFR and COX2 double-positive tuft cells in normal (green) and Crohn's disease (magenta) ileal biopsies. Each dot represents a separate patient. Error bars represent SEM for n = 10 normal and n = 13 Crohn's disease samples, respectively. **p < 0.01 by t-test.

response against helminth infection (Helmby, 2015; Summers *et al*, 2005b, 2003; von Moltke *et al*, 2016; Howitt *et al*, 2016; Gerbe *et al*, 2016). Activation of the type 2 immune response has been implicated in the suppression of the proinflammatory environment in IBD patients (Helmby, 2015; Summers *et al*, 2005b, 2003). Thus, we first wanted to investigate the correlation between tuft cell number and local tissue inflammation in ileal specimens from CD patients, a study whichto our knowledge has not been performed. Tuft cell hyperplasia following acute helminth infection has been studied in the small intestine but not the colon (Howitt *et al*, 2016; von Moltke *et al*, 2016; Gerbe *et al*, 2016), Therefore, we restricted the inclusion criteria for CD patients to those with ileal involvement (n = 19) compared with healthy distal ileal regions from controls (n = 14) in order to limit our analysis to small intestinal tuft cells.

One of the major reasons for the absence of studies on human tuft cells is the lack of validated markers. Previous attempts to use antibodies against DCLK1, a tuft cell-specific marker validated in the mouse intestine, to identify human tuft cells have not been successful (Gerbe *et al*, 2012). While others argue that current DCLK1 antibodies lack specificity against the human DCLK1 protein versus the mouse homolog, our scRNA-seq data of human ileum showed that the

DCLK1 gene was not significantly expressed in human tuft cells compared to murine tuft cells (Figure 19A). We have previously identified a double staining strategy of pEGFR(Y1068) and COX2 to specifically mark tuft cells in both mouse and human intestine (McKinley *et al*, 2017a; Herring *et al*, 2018). Using this strategy, we observed double-positive pEGFR and COX2 cells in both the villi and crypts of Lieberkühn of the normal ileal epithelium (Figure 19B, 19E), that are distinct from single-positive pEGFR or COX2 cells in the lamina propria. Moreover, many of the double-positive cells possessed a prominent pEGFR-positive apical "tuft," increasing the likelihood that these were genuine small intestinal tuft cells (Figure 19E).

We applied this strategy to detect tuft cells from ileal tissues of CD patients. As previously observed, inflammation was heterogenous within ileal regions from CD samples and was characterized by severe blunting and distortion of the crypt-villus architecture (Figure 19C). Consistent with previous reports, MUC2+ goblet cells were increased in the inflamed epithelium while LYZ1+ Paneth cells were decreased (Figure 19D) (VanDussen *et al*, 2014; Antoni *et al*, 2014; Wehkamp *et al*, 2007, 2016; Erben *et al*, 2016). The few Paneth cells remaining in inflamed regions contained more diffuse apical, lysozyme-positive granules (Figure 19D), consistent with known Paneth cell phenotypes in CD (VanDussen *et al*, 2014). However, LYZ1 expression was increased in the lamina propria in inflamed tissue, most likely from active immune cells (Figure 19C). Tuft cells, detected by co-staining of pEGFR and COX2, were significantly reduced in ileal sections from CD patients (Figure 19F, 19G). In certain CD specimens, particularly in regions with less disease involvement and more organized tissue architecture, tuft cells could be detected by pEGFR and COX2 staining (Figure 19F). From these results, we speculate that suppression of tuft cell specification may contribute to the loss of inflammation control in CD and thus may be associated with disease development and/or progression.

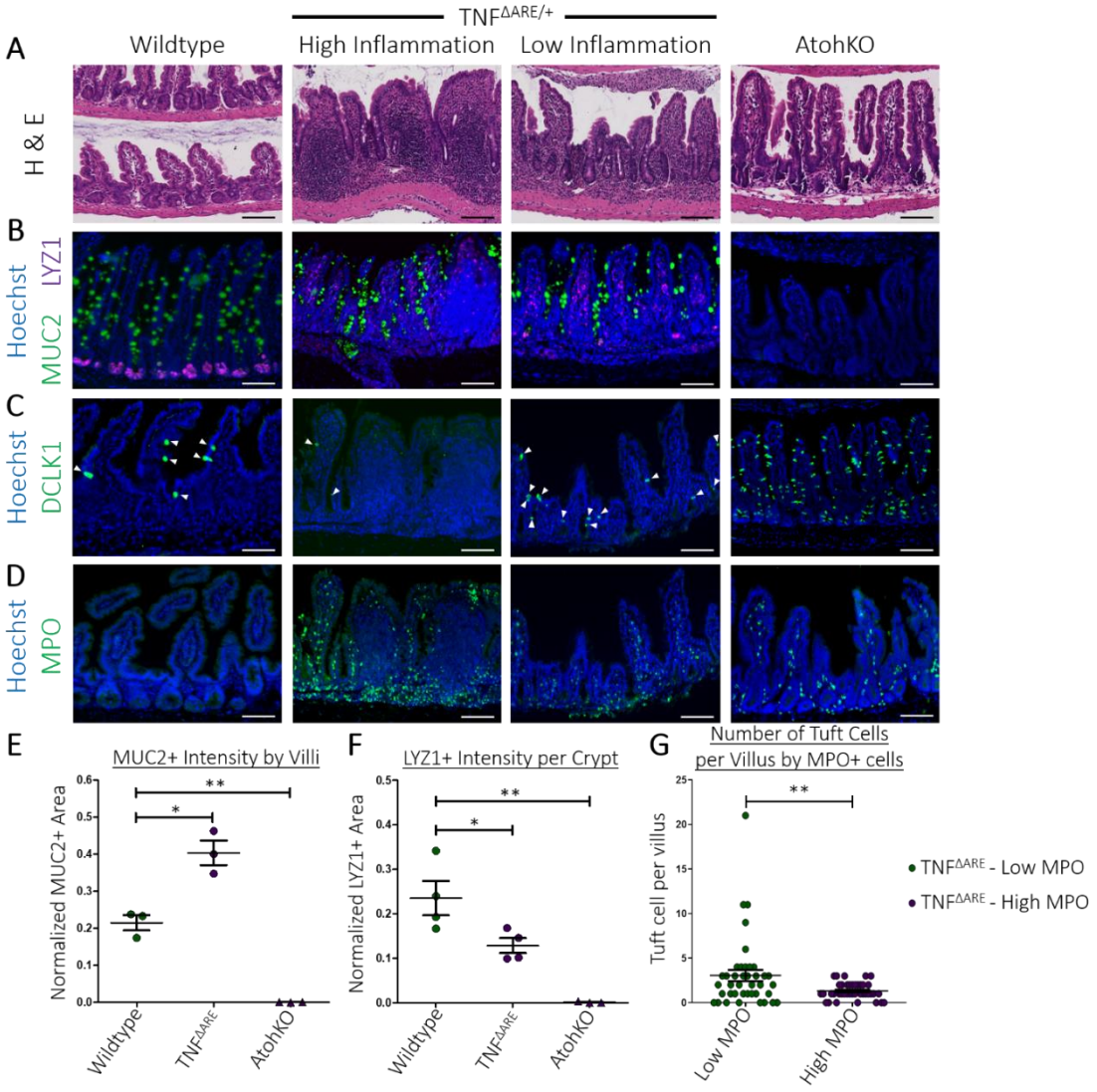

Figure 20. Decreased tuft cell number is correlated to high inflammation in the *TNF$^{\Delta ARE/+}$* model. (A) Histology of distal ileum from wildtype, low and high inflammation regions in *TNF$^{\Delta ARE/+}$*, and AtohKO animals. Scale bar = 100 µm. **(B)** Immunofluorescence imaging of MUC2 and LYZ1. Hoechst (blue) denotes nuclei, scale bar = 100 µm. **(C)** Immunofluorescence imaging of DCLK1 (green) and Hoechst (blue) in wildtype, low and high inflammation regions in *TNF$^{\Delta ARE/+}$*, and AtohKO ileum. White arrows indicate DCLK1+ tuft cells. Scale bar = 100 µm. **(D)** Immunofluorescence imaging of myeloperoxidase (MPO) (green) and Hoechst (blue) in wildtype, low and high inflammation regions in *TNF$^{\Delta ARE/+}$*, and AtohKO ileum. Scale bar = 100 µm. **(E)** Quantification of MUC2 staining normalized by Hoechst area in villi. Error bars represent SEM from n = 3 mice per condition. **p < 0.01, *p < 0.05 by t-test. **(F)** Quantification of LYZ1 staining normalized by Hoechst area per crypt. Error bars represent SEM from n = 4 wildtype and *TNF$^{\Delta ARE/+}$* mice and n = 3 AtohKO animals. **p < 0.01, *p < 0.05 by t-test. **(G)** Tuft cell number per villi in the *TNF$^{\Delta ARE/+}$* ileum stratified by MPO+ neutrophils. Low MPO < 35 neutrophils and High MPO ≥ 36 neutrophils. Error bars represent SEM for n = 40 villi per condition across 8 *TNF$^{\Delta ARE/+}$* animals. **p < 0.01 by t-test.

To assess tuft cell specification in a more controlled manner, we used the *TNF*$^{\Delta ARE/+}$ mouse model (see Chapter I), which, by the deletion of an AU rich element (ΔARE) in the gene encoding the proinflammatory cytokine tumor necrosis factor alpha (TNF-α), has increased levels of the TNF-α mRNA and develops Crohn's-like ileitis by two to three months of age (Kontoyiannis *et al*, 2002, 1999; Erben *et al*, 2016). The *TNF*$^{\Delta ARE/+}$ model mimics many features of human ileal CD, including dependence on TNF-α and microbiome dysbiosis (Roulis *et al*, 2016b; Goulart *et al*, 2016). We observed histological changes in the terminal ileum of four-month-old *TNF*$^{\Delta ARE/+}$ animals, characterized by distorted crypt structure and blunted villi in comparison to wildtype littermates (Figure 20A). The number of LYZ1+ Paneth cells was decreased while the remaining ones exhibited diffuse LYZ1 staining, suggesting impaired Paneth cell function (Figure 20B, 20F) (VanDussen *et al*, 2014; Wehkamp *et al*, 2005). The numbers of LYZ1+ cells in the lamina propria and MUC2+ goblet cells in the epithelium were increased, which bear resemblance to the ilea of human CD patients (Figure 19C, Figure 20B, 20E) (Wehkamp *et al*, 2005; Erben *et al*, 2016). Increased immune cell infiltration can be observed by myeloperoxidase (MPO)-positive neutrophils in the lamina propria of inflamed tissues when compared to uninflamed controls (Figure 20D, 20G).

Similar to the heterogeneity observed in specimens from CD patients, we were able to identify both highly inflamed and less inflamed regions within the ilea of *TNF*$^{\Delta ARE/+}$ mice. We performed spatially-resolved analysis to determine the relationship between tuft cell numbers and inflammation by quantifying the number of DCLK1+ tuft cells in the epithelium and infiltrating MPO+ neutrophils in the lamina propria on a per-villus basis (Figure 21). Consistent with human intestinal phenotypes, regions classified as highly inflamed with >35 MPO+ cells/villus were characterized by severe villus blunting and distortion, while less inflamed regions (0-35 MPO+ cells/villus) possessed normal crypt-villus architecture resembling healthy wildtype controls (<10 MPO+ cells/villus) (Figure 21C). Within the same *TNF*$^{\Delta ARE/+}$ animal, tuft cell numbers were

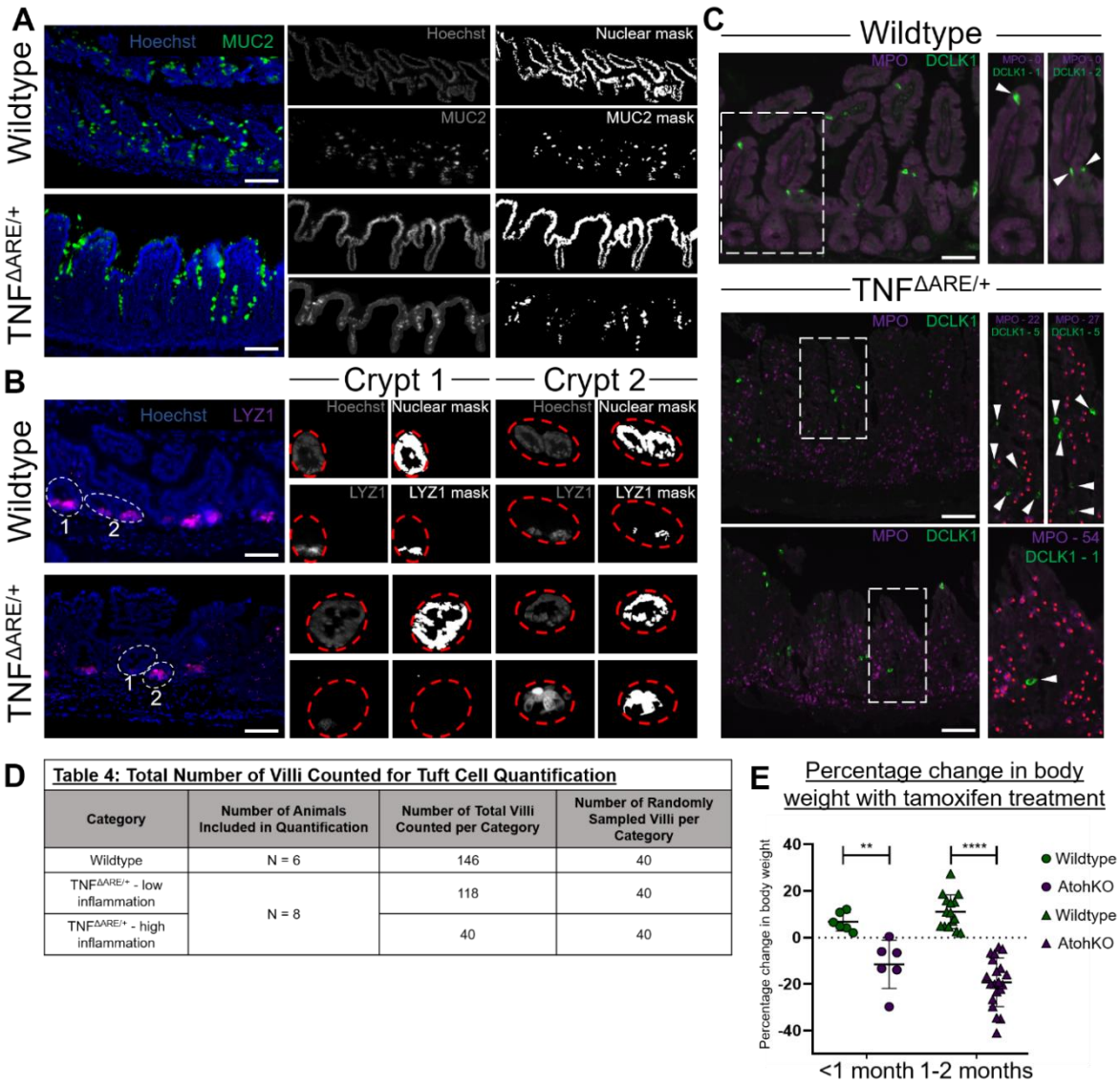

Table 4: Total Number of Villi Counted for Tuft Cell Quantification

Category	Number of Animals Included in Quantification	Number of Total Villi Counted per Category	Number of Randomly Sampled Villi per Category
Wildtype	N = 6	146	40
$TNF^{\Delta ARE/+}$ - low inflammation	N = 8	118	40
$TNF^{\Delta ARE/+}$ - high inflammation		40	40

Figure 21. Image processing of immunofluorescence staining was used to quantify DCLK1+ tuft cell number versus severity of inflammation. (A) Image analysis of Hoechst (blue) and MUC2 (green) staining were used to manually demarcate the epithelial monolayer and generate a nuclear and MUC2 mask, respectively, from wildtype, *$TNF^{\Delta ARE/+}$*, and AtohKO (not pictured) images. MUC2 levels were normalized to total Hoechst area to quantify staining intensity between conditions. Scale bar = 100 µm. **(B)** Image analysis of Hoechst (blue) and LYZ1 (magenta) staining were used to manually demarcate individual crypts (white dashed line) and generate a nuclear and LYZ1 mask (red dashed line), respectively, from wildtype, *$TNF^{\Delta ARE/+}$*, and AtohKO (not pictured) images. LYZ1 levels were normalized to total Hoechst area to quantity staining intensity. Scale bar = 100 µm. **(C)** Immunofluorescence imaging of MPO (magenta) and DCLK1 (green) was used to manually quantify severity of inflammation and tuft cell number, respectively. Within the magnified inset, white arrows indicate DCLK1+ tuft cells and red dots indicate MPO+ neutrophils. Scale bar = 100 µm. **(D)** Table 4 shows the total number of villi counted for DCLK1+ quantification. 40 villi were randomly selected for final quantification. **(E)** Percentage change in starting body weight following tamoxifen treatment in wildtype (green) and AtohKO (magenta) animals stratified by short-term (<1 month, circles) and long-term (1-2 months, triangles) treatment. Each data point represents a single animal (<1 month, wildtype and AtohKO n = 6; 1-2 mo. wildtype n = 15 and AtohKO n = 20). ****p < 0.0001, **p < 0.01 by t-test.

significantly decreased in highly inflamed regions compared to less inflamed regions (Figure 20G). The number of tuft cells in less inflamed regions is increased beyond the normal number of tuft cells found in the normal ileum (Figure 20C). These results are consistent with observations in human ileal specimens and imply that a feedback response for increasing tuft cell specification in the early stages of disease may suppress ileal inflammation.

Tuft cells are specified outside of the secretory lineage in the small intestine

Based on our observations in human and mouse inflammation, we hypothesized that increasing tuft cell specification may potentially mitigate CD symptoms. Therefore, we sought to better understand the mechanisms regulating tuft cell specification, specifically in the context of perturbed microbiome-epithelium interaction in IBD (Boyapati *et al*, 2015; Roulis *et al*, 2016a). However, the regional heterogeneity of inflammation and tuft cell specification in the $TNF^{\Delta ARE/+}$ model precludes most systematic analysis. To uncover the signals governing tuft cell specification in a more tractable manner, we generated a genetically inducible model of tuft cell hyperplasia that is homogeneous throughout the entire ileum. The $Lrig1^{CreERT2}$ driver was crossed to $Atoh1^{loxP/loxP}$ mice to generate $Lrig1^{CreERT2/+}; Atoh1^{fl/fl}$ (AtohKO) animals, where the administration of tamoxifen drove recombination of *Atoh1* in *Lrig1*-expressing stem cells (Herring *et al*, 2018). AtohKO animals exhibit relatively normal crypt-villus architecture, as seen by H&E staining (Figure 20A). Quantification of immunofluorescence staining confirmed that AtohKO animals lack MUC2+ goblet cells and LYZ1+ Paneth cells (Figure 20B, 20E-F), consistent with these cells belonging to the *Atoh1*-dependent secretory lineage (Vandussen & Samuelson, 2010; Shroyer *et al*, 2007; Noah *et al*, 2011). However, contrary to the established paradigm, we observed a significant increase in DCLK1+ tuft cells throughout the small intestine, which supports more recent studies suggesting tuft cells can be specified outside the *Atoh1*-dependent secretory lineage (Figure 20)

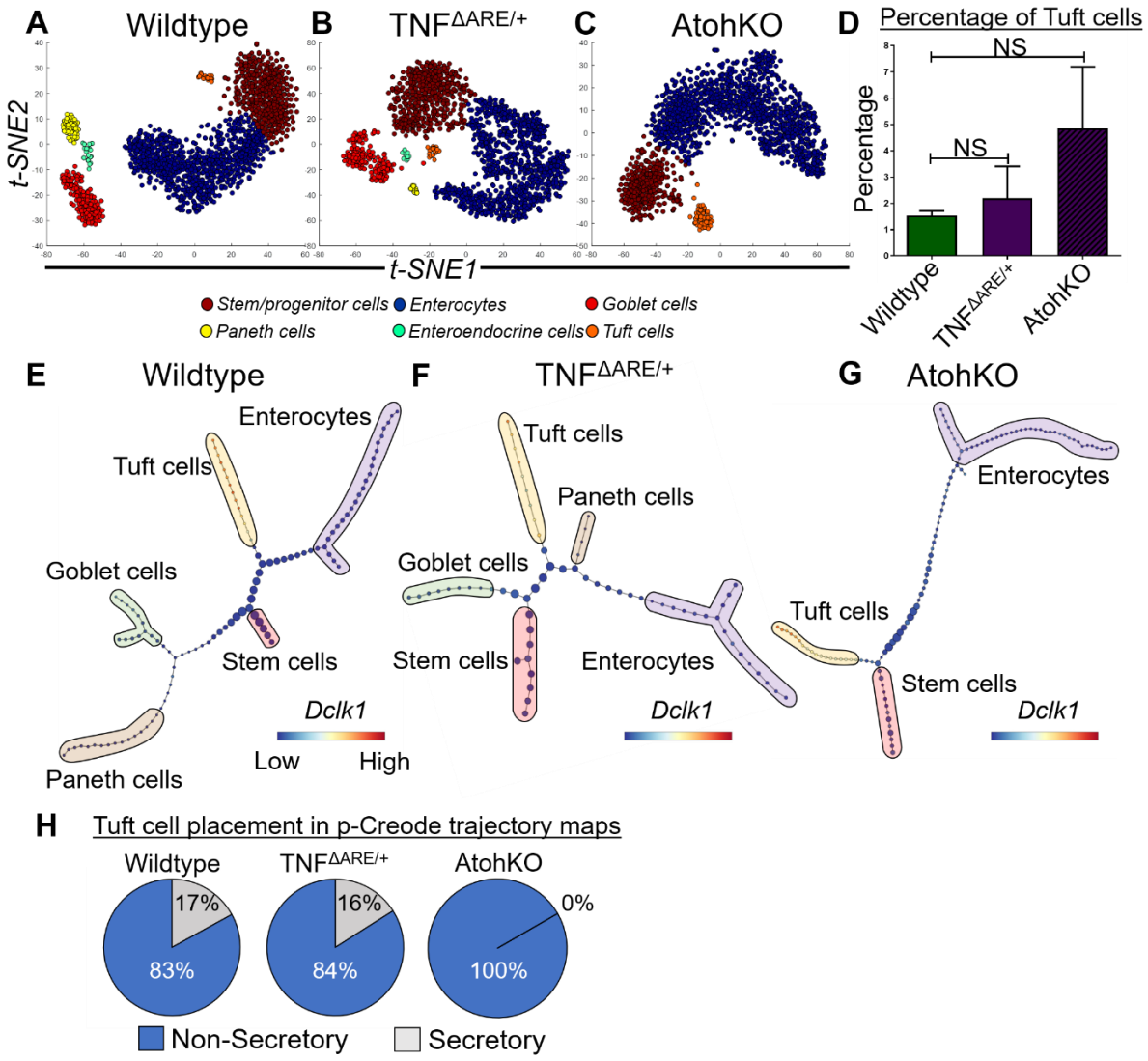

Figure 22. p-Creode trajectory analysis of ileal epithelial scRNA-seq data supports an alternate origin for small intestinal tuft cells. **(A-C)** t-SNE analysis of scRNA-seq data generated from **(A)** wildtype, **(B)** *TNF*$^{\Delta ARE/+}$, and **(C)** AtohKO ileal epithelium. Cell type clusters, including goblet cells (red), Paneth cells (yellow), enteroendocrine cells (green), tuft cells (orange), enterocytes (dark blue), and stem/progenitor cells (brown), were identified by k-means clustering and manually annotated. Each t-SNE plot depicts 1,450 randomly selected datapoints from their corresponding complete dataset and each datapoint represents a single cell. **(D)** Quantification of tuft cell percentage within the scRNA-seq datasets of wildtype, *TNF*$^{\Delta ARE/+}$, and AtohKO ileal epithelium. Error bars are generated from n = 4 wildtype replicates, n = 3 *TNF*$^{\Delta ARE/+}$ replicates, and n = 3 AtohKO replicates. **p < 0.01, *p < 0.05, and ns (not significant) by t-test. **(E-G)** p-Creode analysis of scRNA-seq datasets shown in A-C, depicting the most representative topology map over n = 100 runs for **(E)** wildtype, **(F)** *TNF*$^{\Delta ARE/+}$, and **(G)** AtohKO datasets. Graph overlay depicts *Dclk1* levels. Cell lineages, including goblet cells (green), Paneth cells (purple), tuft cells (orange), enterocytes (blue), and stem cells (red), were manually labelled. Node size represents cell state density and each edge represents cell state transitions. **(H)** Quantification of n = 100 p-Creode maps for wildtype, *TNF*$^{\Delta ARE/+}$, and AtohKO datasets, respectively. Tuft cell placement was classified as secretory (grey) when the tuft cell lineage shared a trajectory with goblet cells and as non-secretory (blue) when the tuft cells and absorptive enterocytes shared a trajectory.

(Herring *et al*, 2018; Gracz *et al*, 2017). In addition, we observed an increased presence of MPO+ neutrophils in the villi of AtohKO animals, reflecting a baseline level of inflammation, similar to the less inflamed regions of $TNF^{\Delta ARE/+}$ animals, potentially due to goblet and Paneth cell loss (Figure 20D). The uniformity of these phenotypes throughout the ilea of AtohKO mice allows us to investigate inflammation-induced tuft cell specification in an *in vivo* model with a physiologically intact microbiome and immune system.

In order to decipher lineage-specific alterations that drive tuft cell specification, we generated single-cell RNA sequencing (scRNA-seq) data from wildtype, $TNF^{\Delta ARE/+}$, and AtohKO ilea using the inDrops platform (Klein *et al*, 2015), by enriching for epithelial crypts and generating single-cell suspensions via a cold protease dissociation protocol (Adam *et al*, 2017). Following data processing and quality control, we obtained a 4,598-cell wildtype scRNA-seq dataset from four biological replicates and performed t-SNE analysis on 1,450 randomly selected cells from the entire complement of datapoints (Figure 22A, Figure 23D-E). Population analysis demonstrated that the wildtype scRNA-seq dataset contained the correct proportion of expected cell types, including stem and progenitor cells (brown), enterocytes (blue), goblet cells (red), Paneth cells (yellow), enteroendocrine cells (teal), and tuft cells (orange) (Figure 22A, Figure 23A, Figure 24A). To compare across conditions, 1,450 datapoints from the $TNF^{\Delta ARE/+}$ and AtohKO scRNA-seq datasets were randomly selected for further analysis. In the $TNF^{\Delta ARE/+}$ dataset, while all the cell types were represented, the Paneth cell population was greatly diminished, consistent with results observed by immunofluorescence imaging (Figure 22B, Figure 23B, Figure 24B).

Quantification of DCLK1-expressing cells indicated that the tuft cell population is slightly expanded in the $TNF^{\Delta ARE/+}$ dataset, which may be accounted for by less inflamed regions of the $TNF^{\Delta ARE/+}$ ileum having more tuft cells, and highly inflamed regions having fewer tuft cells (Figure 23B, 23D, Figure 24B). Given the loss of spatial resolution subsequent to single-cell dissociation, it is reasonable that a global approach such as scRNA-seq cannot accurately capture the spatial

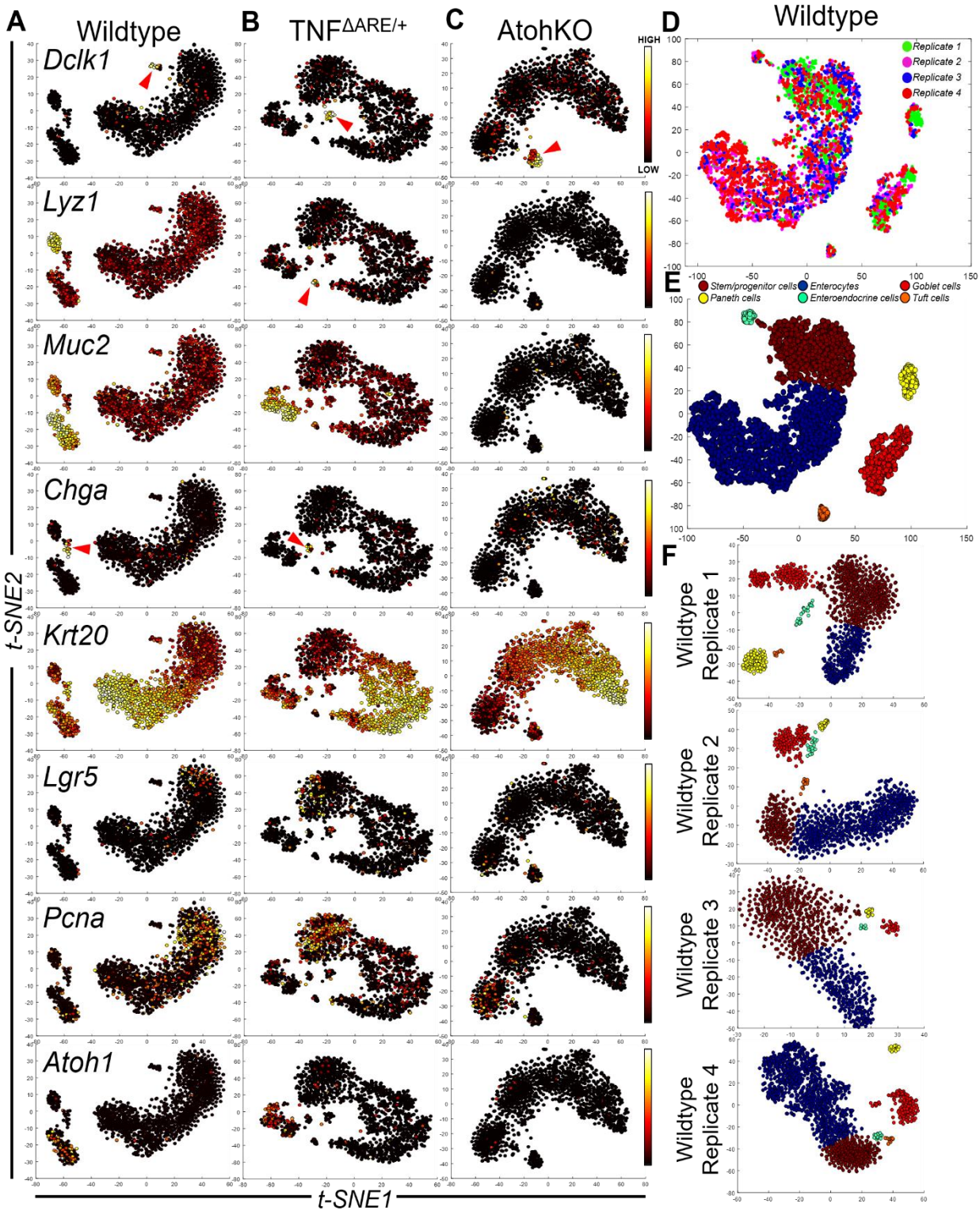

Figure 23. t-SNE analysis of scRNA-seq of cell identity genes. (A-C) t-SNE plots of scRNA-seq data generated from **(A)** wildtype, **(B)** TNF$^{\Delta ARE/+}$, and **(C)** AtohKO ileal epithelium. Selected cell identity genes, including *Dclk1*, *Lyz1*, *Muc2*, *Chga*, *Krt20*, *Lgr5*, *Pcna*, and *Atoh1*, are overlaid

on the t-SNE plots. Red arrows indicate smaller cell clusters, such as tuft and enteroendocrine populations. Each t-SNE plot depicts 1,450 randomly selected datapoints from their corresponding complete dataset and each datapoint represents a single cell. Overlay represents ArcSinh-scaled gene expression data. **(D)** t-SNE analysis of the complete wildtype scRNA-seq dataset consisting of 4,598 datapoints. Manual annotation of the t-SNE plot demonstrates the absence of segregation in datapoints from four biological replicates (Rep. 1 – green, Rep. 2 – magenta, Rep. 3 – blue, and Rep. 4 – red). Each datapoint represents a single cell. **(E)** Clustering analysis of the complete wildtype scRNA-seq dataset shows stem/progenitor cells (brown), enterocytes (blue), goblet cells (red), Paneth cells (yellow), enteroendocrine cells (green), and tuft cells (orange). **(F)** Clustering analysis of separate wildtype replicates shows each dataset contains the expected cell populations. Rep. 1 consists of 1,179 cells, Rep. 2 consists of 1,099 cells, Rep. 3 consists of 877 cells, and Rep. 4 consists of 1,443 cells.

heterogeneity of the *TNF*$^{\Delta ARE/+}$ model. The AtohKO scRNA-seq data confirmed the absence of goblet, Paneth, and enteroendocrine lineages following *Atoh1* recombination, consistent with their *Atoh1*-dependent secretory origins (Figure 22C, Figure 23C, Figure 24C). Compared to the wildtype tuft cell cluster, the AtohKO tuft cell population was expanded (Figure 23D, Figure 24C).

We analyzed tuft cell specification pathways using the p-Creode algorithm to produce trajectory representations of our scRNA-seq datasets (Herring *et al*, 2018). The wildtype p-Creode map originated from the stem cell lineage and bifurcated into the secretory and absorptive lineages (Figure 23E, Figure 25A). As expected, goblet and Paneth cells originated from a common secretory progenitor before diverging into two distinct lineages (Figure 25A). In contrast, the tuft cell lineage shared a specification trajectory with absorptive cells, rather than secretory cells (Figure 23E, Figure 25A). In order to evaluate the robustness of this map, we generated 100 p-Creode graphs by randomly sampling the wildtype scRNA-seq dataset and quantified tuft cell placement. p-Creode maps were classified as “secretory” when the tuft cells were grouped with lineages containing goblet cells and as “non-secretory” otherwise (Figure 24D). Tuft cell placement was non-secretory in 83% of wildtype trajectories and secretory in the remaining 17% (Figure 22H). These results supported recent findings regarding an alternative origin of small intestinal tuft cells that is separate from the *Atoh1*-dependent secretory lineages (Herring *et al*,

2018; Gracz *et al*, 2018). p-Creode analysis of the *TNF*$^{\Delta ARE/+}$ scRNA-seq dataset illustrated that, even in inflammatory conditions, tuft cells share a trajectory with the absorptive cells (Figure 22F, Figure 24E, Figure 25B). Quantification of 100 p-Creode runs showed that tuft cell placement was non-secretory in 84% of *TNF*$^{\Delta ARE/+}$ maps and secretory in 16% of maps (Figure 22H, Figure 24E). Finally, due to the loss of the secretory lineages in the AtohKO model, all 100 p-Creode graphs generated from the corresponding scRNA-seq data depicted tuft cells and absorptive cells originating from a common progenitor (Figure 22G, 22H, Figure 24F, Figure 25C). Gene expression of tuft cell regulators, including *Pou2f3*, *Ptgs1*, *Ptgs2*, *Sox4*, *Sox9*, and *Trpm5*, was confirmed to be expressed in the tuft cell lineage in wildtype, *TNF*$^{\Delta ARE/+}$, and AtohKO p-Creode topologies (Figure 25A-C, Figure 26A-C). We performed a similar analysis by including rare enteroendocrine cells in the wildtype p-Creode topology and observed that, while enteroendocrine cells segregate with secretory cells, tuft cells still by-and-large share a trajectory with the absorptive cells (Figure 27A-C).

To confirm these results with an alternative dataset, we re-analyzed a 7,000+-cell scRNA-seq dataset generated using 10X Genomics by Aviv Regev's group (GSE92332), from which we were able to reproduce the expected distribution of cell types (Figure 28A-C) (Haber *et al*, 2017). p-Creode analysis demonstrated cell differentiation originated from stem cells, and bifurcated into the absorptive and secretory cells, which further diverged into the Paneth and goblet cell lineages (Figure 28D). In addition, we observed non-secretory placement of the tuft cell lineage with the absorptive enterocytes in 68% of p-Creode topologies and 32% placement with the secretory lineages (Figure 28E-F). Slight discrepancies in the results of the two analyses may be accounted for by technical differences between the datasets in regard to cell isolation, library preparation, and/or data processing procedures. Nevertheless, tuft cell specification from a non-secretory lineage was a robust and consistent feature of the wildtype small intestine across multiple datasets.

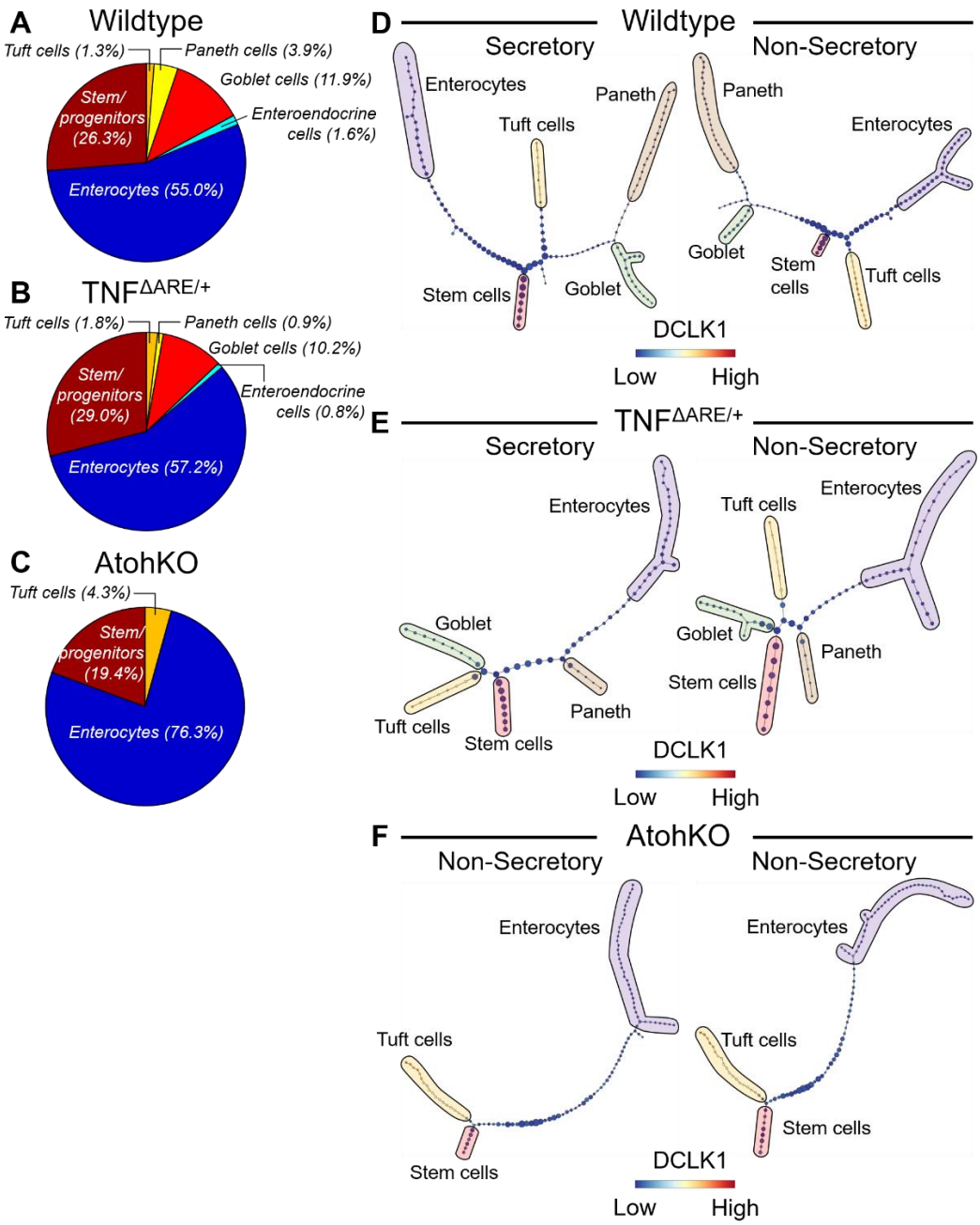

Figure 24. Classification of p-Creode topology maps based upon tuft cell placement within absorptive or secretory lineage. (A-C) Quantification of cell populations within the **(A)** wildtype, **(B)** *TNF*$^{\Delta ARE/+}$, and **(C)** AtohKO scRNA-seq data. **(D-E)** Representative **(D)** wildtype and **(E)** *TNF*$^{\Delta ARE/+}$ of either "Secretory," when tuft cells share a trajectory with goblet and Paneth cells, and "Non-Secretory," when tuft cells share a trajectory with absorptive enterocytes, classification. **(F)** Examples of Non-Secretory AtohKO p-Creode maps. Graph overlay depicts *Dclk1* levels. Cell lineages, including goblet cells (green), Paneth cells (purple), tuft cells (orange), enterocytes (blue), and stem cells (red), were manually labelled. Node size represents cell state density and each edge represents cell state transitions. Overlay represents ArcSinh-scaled gene expression data.

Alterations in TCA metabolic pathways along the tuft cell trajectory are associated with induced tuft cell specification

p-Creode trajectory mapping enables analysis of gene expression changes in a lineage-specific manner (Liu *et al*, 2018; Herring *et al*, 2018). Within the intestinal epithelium, expression of *Dclk1* gradually increased in the tuft cell lineage but was undetectable in the enterocyte and goblet cell lineage (Figure 30A). Conversely, *Muc2* and *Krt20* expression gradually increased as goblet cells and enterocytes differentiate in their respective lineages (Figure 30A). To identify pathways that induce tuft cell differentiation, we focused our analysis on dynamic alterations in gene expression along the tuft cell lineage between the wildtype and AtohKO intestinal epithelium using this framework. This approach circumvented any batch effects since the dynamics of gene expression along a trajectory is self-contained within individual biological replicates.

We aimed to identify genes that switch their expression dynamics between wildtype and AtohKO conditions to determine functional perturbations in tuft cells from the latter. Firstly, gene dynamics in the wildtype tuft cell lineage were first classified into four broad categories (Figure 29A). Group 1 genes, such as *Soux*, trend upward along pseudotime of the stem-to-tuft cell trajectory, while group 4 genes, including *Rps6*, trend downwards (Figure 30B). Group 1 genes included known tuft cell marker genes that are upregulated during differentiation (for instance, *Ptgs1* and *Sox9*) (McKinley *et al*, 2017a), while group 4 genes included stem cell markers that are downregulated (Figure 30B). Intermediate genes that trend upwards but return to a lower baseline or those that trend downwards but return to a higher baseline are categorized into groups 2 and 3, respectively (Figure 30B). When all expressed genes between the wildtype and AtohKO were visualized within these categories, a broad expansion of group 2 genes was observed upon loss of *Atoh1*, implicating changes in lineage-specific gene expression dynamics (Figure 29A). To identify pathways that induce tuft cell specification in an unbiased manner, we extracted 1,532 genes that were positively enriched in the AtohKO group, that is, those that switched categories

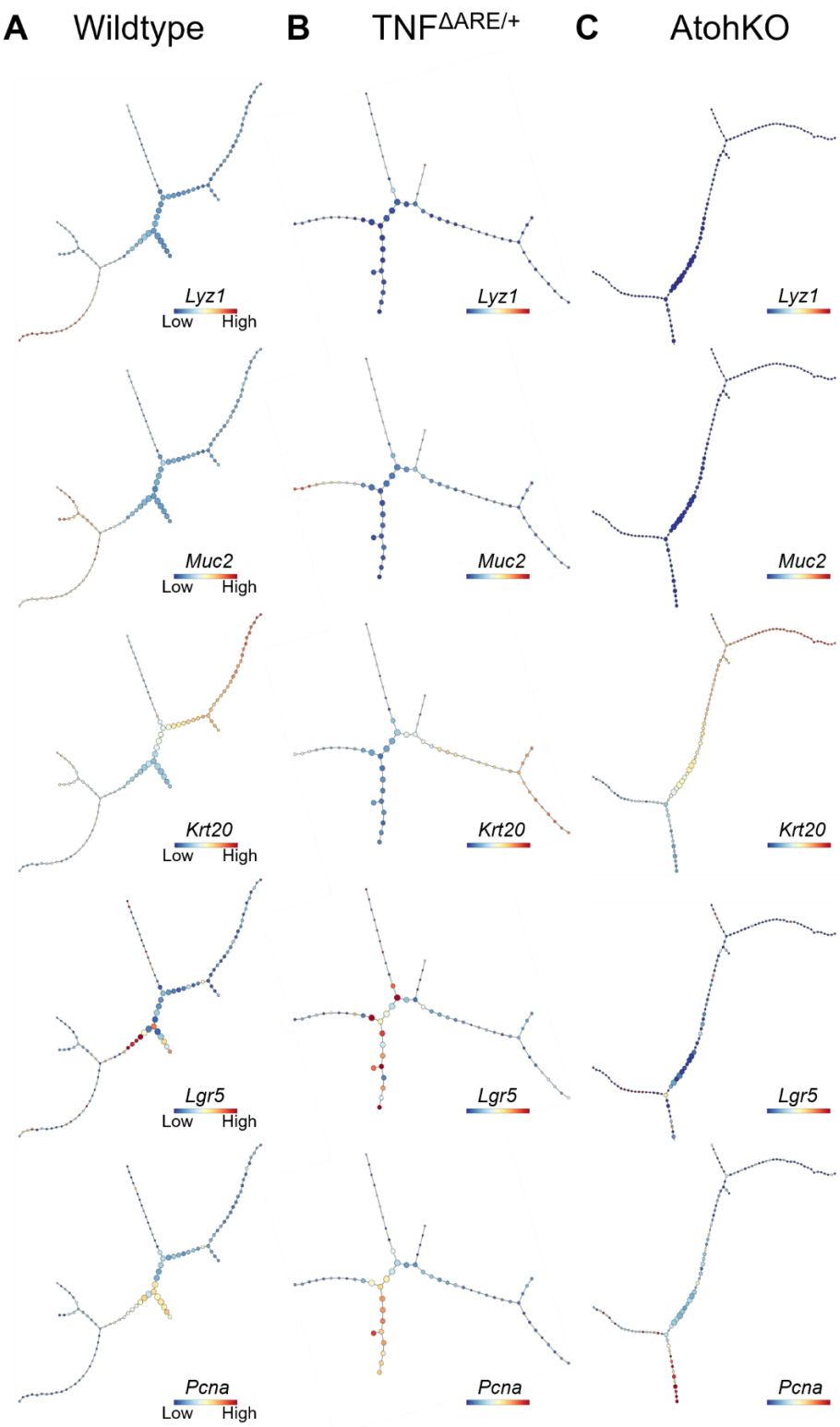

Figure 25. Cell identity gene overlay on p-Creode graphs. (A-C) Overlay of selected cell identity genes, including *Lyz1*, *Muc2*, *Krt20*, *Lgr5*, and *Pcna*, on **(A)** wildtype, **(B)** *TNF*$^{\Delta ARE/+}$, and **(C)** AtohKO p-Creode maps. Overlays represent ArcSinh-scaled gene expression data.

from a lower group in the wildtype data to a higher group in AtohKO (Figure 30C). Over-representation analysis of positively enriched genes in the AtohKO epithelium identified pathways related to the tricarboxylic acid (TCA) cycle and oxidative phosphorylation based on KEGG (Figure 29B), Wiki pathways (Figure 30E), and Reactome analyses (Figure 30F). We repeated this analysis by grouping the dynamic trends into 2 categories (up or down) and again identified genes that were positively enriched in the AtohKO trajectory. This coarse grain analysis produced similar results as before, as over-representation analysis identified enrichment for metabolic-associated processes, such as the TCA cycle and electron transport chain (Figure 30E-I).

The TCA or citrate acid cycle converts glycolysis products into NADH+, which is then shuttled to the electron transport chain for ATP production (Mills & O'neill, 2014). Alterations in selected pathway genes between wildtype (green) and AtohKO (magenta), respectively, can be directly visualized by plotting expression trends fit to raw data from ten representative p-Creode maps (Figure 29C-H). As benchmarks, we observed that canonical tuft cell genes, including *Dclk1* and *Trpm5*, trended upward, while stem or progenitor cell genes, *Myc* and *Pcna*, trended downward; neither set of genes switched dynamics between wildtype and AtohKO trajectories (Figure 30D). In contrast, the TCA cycle enzyme malate dehydrogenase (*Mdh2*) trended down along the wildtype tuft cell differentiation trajectory, while its expression remained constant in the AtohKO tuft cell trajectory (Figure 29C). Similarly, other TCA enzymes, such as *Sdha*, *Sdhb*, and *Sdhd*, all switched to more positive dynamic trends along the AtohKO tuft cell trajectory compared with the wildtype tuft cell trajectory (Figure 29F-H). Additional downstream pathway genes, including those coding NADH dehydrogenases and ATP synthases also switched to more positive dynamic trends in the AtohKO tuft cell lineage (Figure 29D-E, Figure 31). Analysis of altered dynamics suggest that tuft cell hyperplasia in the AtohKO model is accompanied by increased TCA cycle and downstream metabolic activities along the tuft cell specification trajectory.

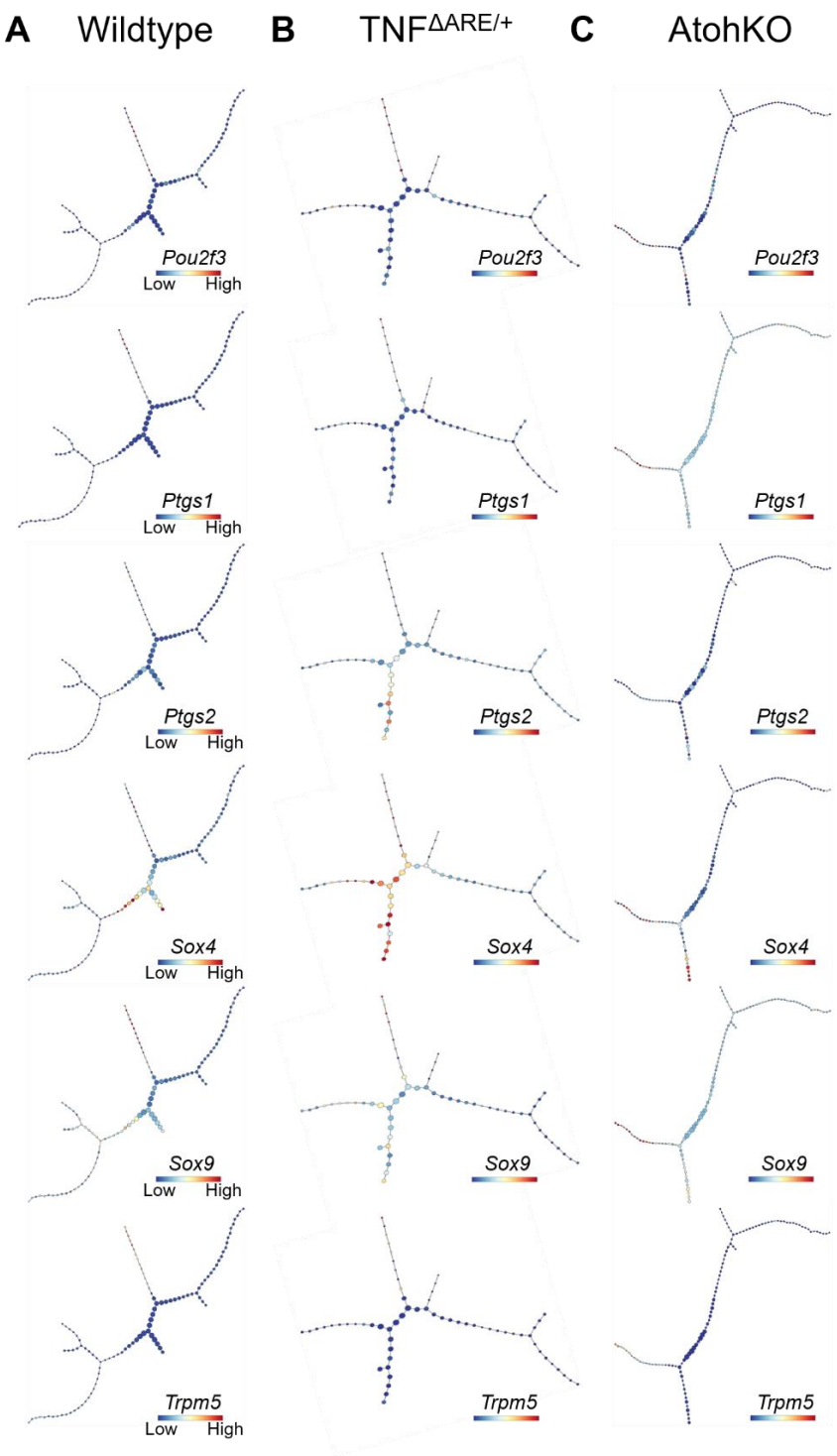

Figure 26. Gene expression overlay of tuft cell-specific genes on p-Creode graphs. (A-C) Overlay of selected tuft cell-specific genes, including *Pou2f3*, *Ptgs1*, *Ptgs2*, *Sox4*, *Sox9*, and *Trpm5*, on **(A)** wildtype, **(B)** *TNF*$^{\Delta ARE/+}$, and **(C)** AtohKO p-Creode maps. Overlays represent ArcSinh-scaled gene expression data.

As a confirmatory method, we grouped cells within the tuft cell trajectory and performed standard bulk differential expression analysis between wildtype and AtohKO cell populations. Standard gene set enrichment analysis (GSEA) (Subramanian *et al*, 2005) performed on genes upregulated in AtohKO tuft cells identified positive enrichment for TCA cycle genes (Figure 29I, Figure 32A). Enrichment plots for the two gene sets with the highest normalized enrichment score (NES) based on GSEA, "Reactome_Citric_Acid_Cycle_TCA_Cycle" and "Mootha_TCA" are shown (Figure 29J-K). The expression of selected genes highly enriched in these gene sets was compared between wildtype and AtohKO cells (Figure 32F). TCA-related enzymes *Idh3b*, *Mdh2*, *Sdha*, *Sdhb,* and *Sdhd,* as well as the ribosomal protein gene *Rpl18a,* were all significantly higher in AtohKO (magenta) tuft cells compared to wildtype tuft cells (green) (Figure 29N-S). While the expression of other TCA cycle enzymes, including *Cs (Citrate synthase), Idh3a*, *Idh3g*, *Ogdh*, and *Sdhc*, were not statistically significant, they trended upward in AtohKO tuft cells (Figure 32H). Additional GSEA over PANTHER (Figure 32B), Gene ontology (Figure 29L, Figure 32C), Wiki pathways (Figure 32D), and KEGG (Figure 29M, Figure 32E) datasets also identified TCA cycle-associated genes were upregulated in the AtohKO tuft cells, confirming activated metabolism in this cell population.

In addition to metabolism-associated genes, GSEA identified hypoxia and hypoxia inducible factor 1 alpha (HIF1-α)-related gene sets to be positively enriched in the AtohKO cell population. Top enriched genes included the ubiquitin ligase *Ube2d3* and *Rbx1,* which regulates turnover of cellular proteins (Figure 32G) (Colgan, 2016; Mills & O'neill, 2014). *Hif1-α* was included in the list of highly enriched genes, though it did not contribute to of the gene set's NES (Figure 32G). Relative expression of *Tceb2* and *Rps27a* was significantly higher in AtohKO tuft cells, while *Ube2d3*, *Rbx1*, and *Hif1a* trended upward (Figure 32I).

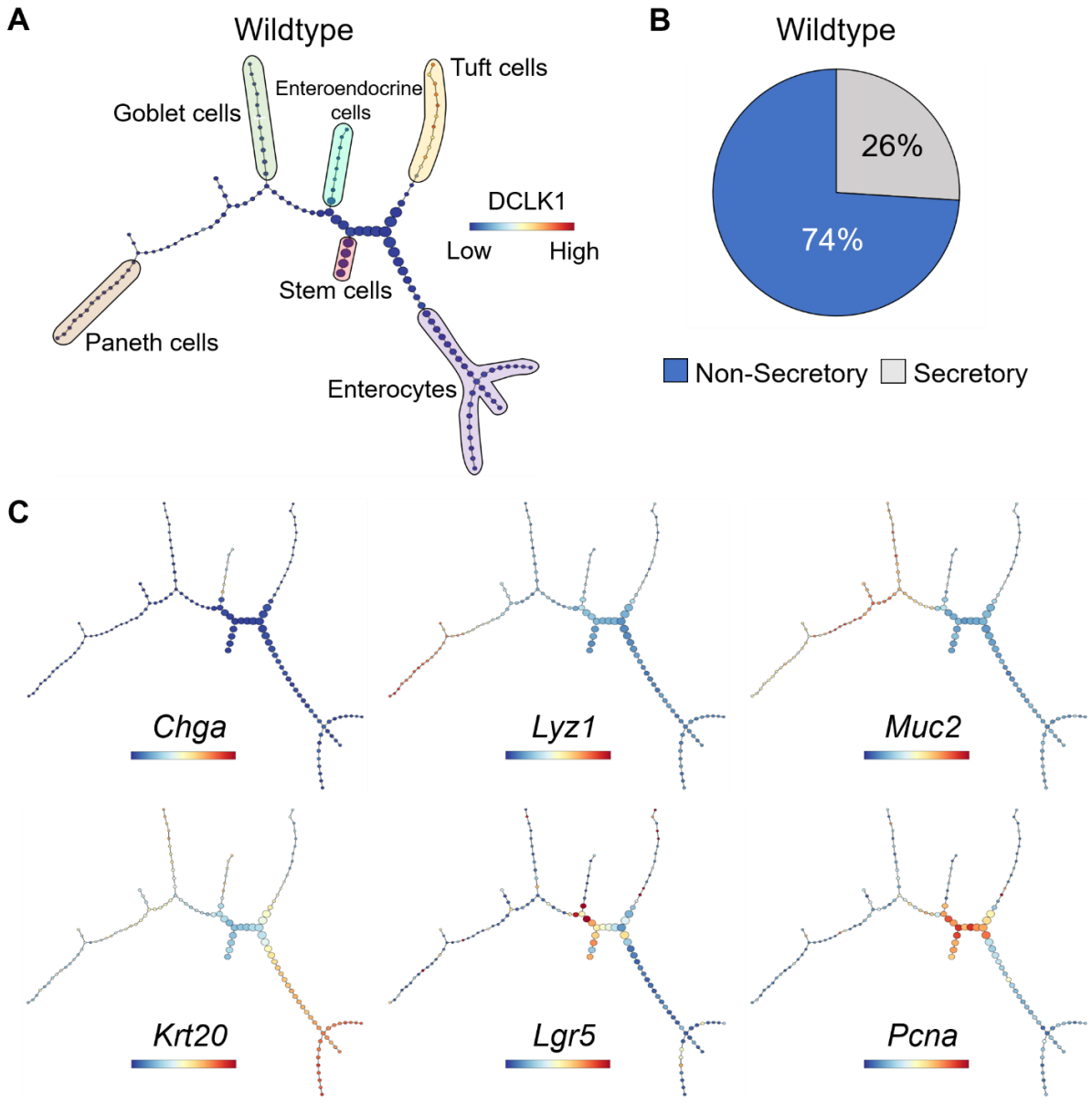

Figure 27. p-Creode analysis of small intestinal epithelium with enteroendocrine cells. (A) Representative p-Creode map of wildtype scRNA-seq dataset, including enteroendocrine cells. Graph overlay depicts *Dclk1* levels. Cell lineages, including enteroendocrine cells (teal), goblet cells (green), Paneth cells (purple), tuft cells (orange), enterocytes (blue), and stem cells (red), were manually labelled. Node size represents cell state density and each edge represents cell state transitions. Overlays represent ArcSinh-scaled gene expression data. **(B)** Quantification of wildtype maps (n = 100) indicating 74% of graphs were classified as non-secretory and 26% as secretory. **(C)** Overlay of selected cell identity genes, including *Chga*, *Lyz1*, *Muc2*, *Krt20*, *Lgr5*, and *Pcna*, depicting epithelial cell differentiation in the wildtype topology. Overlays represent ArcSinh-scaled gene expression data.

Our multi-way analysis of tuft cell lineage-specific gene expression demonstrates TCA cycle metabolic activities to be correlated with tuft cell numbers and proposes and proposes that this pathway can be leveraged to induce tuft cell specification.

Non-parasite-derived sources of succinate drive tuft cell specification

While metabolic pathways were upregulated in the AtohKO tuft cell lineage, it was unclear whether these changes arose from epithelial cell-intrinsic function of ATOH1 as a transcription factor or other non-cell autonomous mechanisms. The AtohKO epithelium lacks barrier-regulating goblet and Paneth cells, which may lead to changes in the microbiome and an influx of tuft cell-promoting commensal-derived metabolites. To test the necessity of the microbiome in driving tuft cell hyperplasia, we induced *Atoh1* recombination in *ex vivo* enteroid cultures in a sterile environment (Sato *et al*, 2011b). Vehicle-treated enteroids have robust expression of LYZ1+ Paneth cells, MUC2+ goblet cells, and DCLK1+ tuft cells, as expected (Figure 33A-B). Similar to the *in vivo* condition, loss of *Atoh1* via Cre recombination induced loss of Paneth and goblet cells (Figure 33C-D). However, tuft cell hyperplasia was not observed in sterile enteroids (Figure 33C-D), which suggests that tuft cell hyperplasia in the AtohKO model may arise via a microbiome-dependent mechanism *in vivo*.

To assess the necessity of the microbiome for inducing tuft cell hyperplasia *in vivo*, we used an antibiotic cocktail, consisting of kanamycin, metronidazole, gentamicin, colistin sulfate, and vancomycin, to deplete a broad range of gram-positive and gram-negative bacteria with minimal impact on overall health (Meng *et al*, 2007; Julia *et al*, 2000) (Figure 33G). Loss of *Atoh1* in this context resulted in depletion of LYZ1+ Paneth cells (Figure 33E I-IV), but antibiotic administration significantly suppressed the resulting tuft cell hyperplasia (Figure 33F I-IV). The

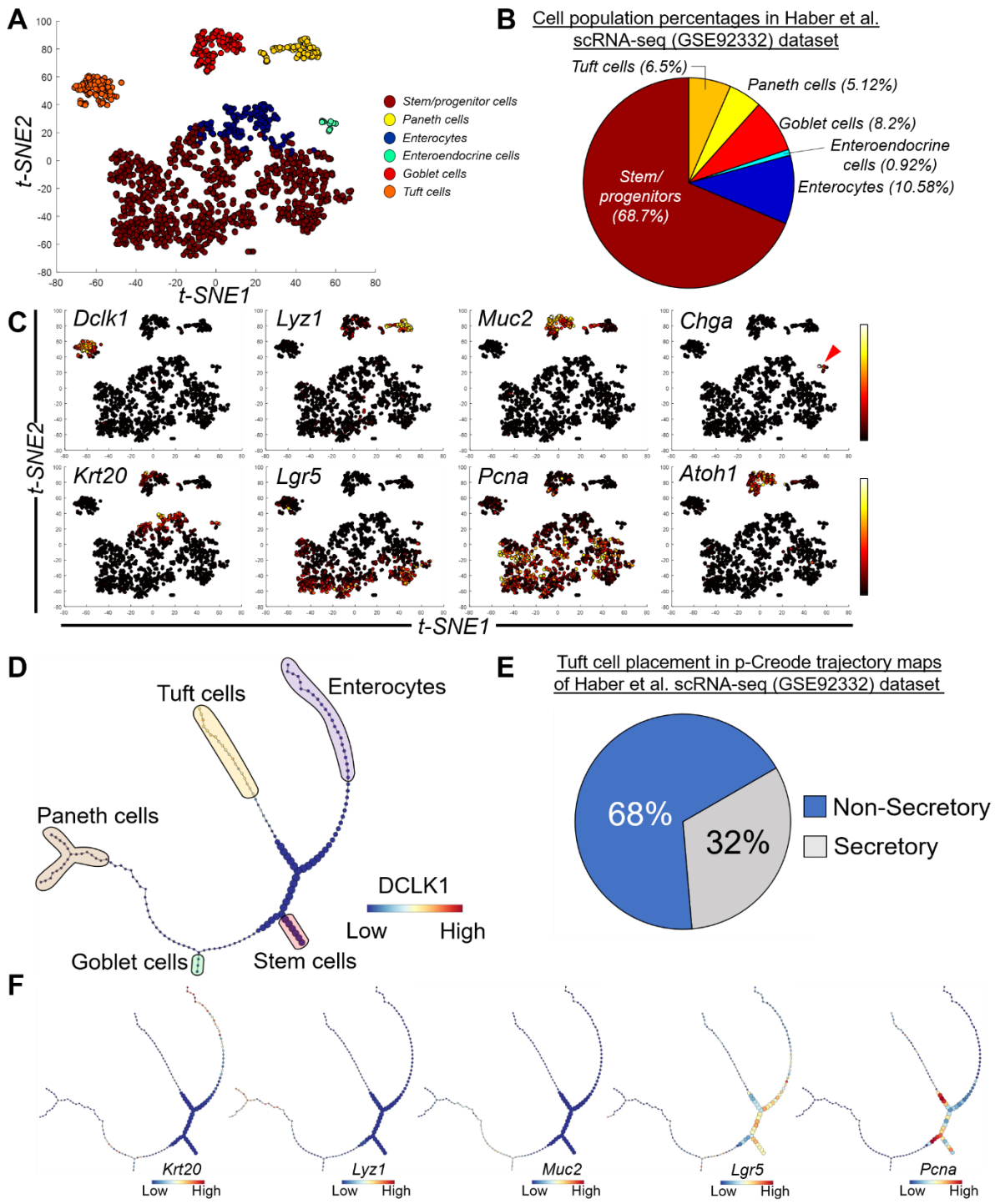

Figure 28. p-Creode analysis of GSE92332 scRNA-seq dataset. (A) t-SNE analysis of the GSE92332 scRNA-seq dataset generated from the wildtype ileal epithelium. Cell type clusters, including goblet cells (red), Paneth cells (yellow), enteroendocrine cells (green), tuft cells (orange), enterocytes (dark blue), and stem/progenitor cells (brown), were identified by k-means clustering and manually annotated. Each datapoint represents a single cell from a 1,522 cell-dataset. **(B)** Quantification of cell populations within the GSE92332 datasets. Tuft cell (orange)

percentage is 6.5% of the 1,522 cell-dataset. **(C)** Overlay of selected cell identity genes, including, including *Dclk1*, *Lyz1*, *Muc2*, *Chga*, *Krt20*, *Lgr5*, *Pcna*, and *Atoh1*, on the wildtype t-SNE plot. Red arrows in the *Chga* plot denote the enteroendocrine cluster. **(D)** Representative p-Creode map of GSE92332 scRNA-seq dataset. Graph overlay depicts *Dclk1*. Cell lineages, including goblet cells (green), Paneth cells (purple), tuft cells (orange), enterocytes (blue), and stem cells (red), were manually labelled. Node size represents cell state density and each edge represents cell state transitions. Overlay represents ArcSinh-scaled gene expression data. **(E)** Quantification of n = 100 p-Creode maps show that 68% of graphs are classified as non-secretory and 32% as secretory. **(F)** Overlay of selected cell identity genes, including *Chga*, *Lyz1*, *Muc2*, *Krt20*, *Lgr5*, and *Pcna*, depicting epithelial cell differentiation in the wildtype topology. Overlays represent ArcSinh-scaled gene expression data.

effects of antibiotics-based microbiome depletion were dose-dependent, with a general suppression of tuft cell hyperplasia correlated to increasing antibiotics concentration. To identify the pathways associated with this suppression, we generated scRNA-seq datasets from AtohKO intestine treated with low and mid dose antibiotics, where tuft cells are still present, albeit at a lower level (Figure 33 F II-III). Again, clustering analysis confirmed the presence of enterocytes, stem cells, and tuft cells (Figure 33H). Based on genes gleaned from prior GSEA analysis, we compared the expression of TCA cycle- and hypoxia-related genes in the AtohKO tuft cells from vehicle and antibiotics-treated mice. TCA cycle enzymes *Idh3b, Mdh2*, *Shda, Sdhb,* and *Sdhd*, which were upregulated in AtohKO tuft cells, were significantly decreased following antibiotics treatment (Figure 33I-J, 33L-N). Additionally, *Cs* and *Ogdh* which trended upward in the AtohKO tuft cells, were also significantly decreased in the antibiotics-treated AtohKO condition (Figure 34A). Lastly TCA-related gene *Rpl18a* and hypoxia-related genes *Rps27a* and *Tceb2,* which were all highly enriched in the AtohKO tuft cells, were decreased in the antibiotics-treated datasets (Figure 33K, Figure 34B). These results indicated that extrinsic signals from the intestinal microbiome drive gene expression changes in the AtohKO tuft cell lineage that result in hyperplasia *in vivo*.

In order to investigate the microbial-derived signals driving the increased tuft cell specification, we sought to characterize the differences in (1) commensal-derived metabolites and

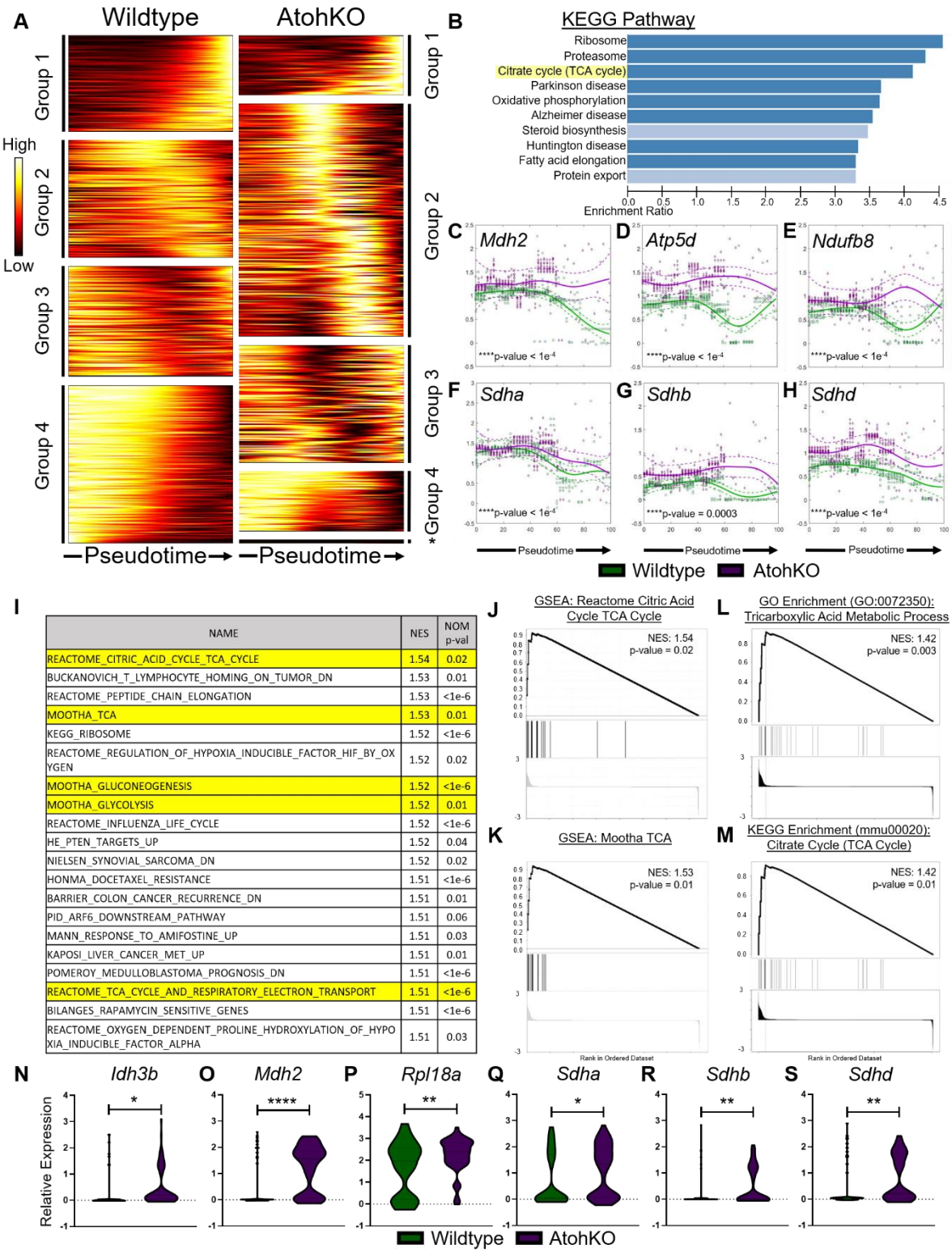

NAME	NES	NOM p-val
REACTOME_CITRIC_ACID_CYCLE_TCA_CYCLE	1.54	0.02
BUCKANOVICH_T_LYMPHOCYTE_HOMING_ON_TUMOR_DN	1.53	0.01
REACTOME_PEPTIDE_CHAIN_ELONGATION	1.53	<1e-6
MOOTHA_TCA	1.53	0.01
KEGG_RIBOSOME	1.52	<1e-6
REACTOME_REGULATION_OF_HYPOXIA_INDUCIBLE_FACTOR_HIF_BY_OXYGEN	1.52	0.02
MOOTHA_GLUCONEOGENESIS	1.52	<1e-6
MOOTHA_GLYCOLYSIS	1.52	0.01
REACTOME_INFLUENZA_LIFE_CYCLE	1.52	<1e-6
HE_PTEN_TARGETS_UP	1.52	0.04
NIELSEN_SYNOVIAL_SARCOMA_DN	1.52	0.02
HONMA_DOCETAXEL_RESISTANCE	1.51	<1e-6
BARRIER_COLON_CANCER_RECURRENCE_DN	1.51	0.01
PID_ARF6_DOWNSTREAM_PATHWAY	1.51	0.06
MANN_RESPONSE_TO_AMIFOSTINE_UP	1.51	0.03
KAPOSI_LIVER_CANCER_MET_UP	1.51	0.01
POMEROY_MEDULLOBLASTOMA_PROGNOSIS_DN	1.51	<1e-6
REACTOME_TCA_CYCLE_AND_RESPIRATORY_ELECTRON_TRANSPORT	1.51	<1e-6
BILANGES_RAPAMYCIN_SENSITIVE_GENES	1.51	<1e-6
REACTOME_OXYGEN_DEPENDENT_PROLINE_HYDROXYLATION_OF_HYPOXIA_INDUCIBLE_FACTOR_ALPHA	1.51	0.03

Figure 29. Analysis of AtohKO tuft cell gene expression identified upregulation in metabolic pathways. (A) Heatmap of gene expression trends across pseudotime in tuft cell lineage from wildtype and AtohKO p-Creode topologies. Genes were clustered by their dynamics

– Group 1-2 included upregulated genes and Groups 3-4 included downregulated genes. Group 5 (*****) in AtohKO consisted of genes that were 0 expression. **(B)** KEGG enrichment bar plots for genes that class switch from lower order in wildtype tuft cells to higher order in AtohKO tuft cells. Functional groups were ordered by NES. **(C-H)** Trend dynamics along pseudotime of citrate cycle-related genes for the wildtype (green) and AtohKO (magenta) tuft cell lineages. Solid lines represent wildtype (green) and AtohKO (magenta) gene expression trends from 10 representative p-Creode graphs. Raw data is shown for wildtype (green circles) and AtohKO (magenta diamonds). Confidence interval of raw data was depicted by dashed lines for wildtype (green) and AtohKO (magenta). Dynamic time warping was used to fit the wildtype and AtohKO tuft cell data to the same scale. Statistical analysis of trend differences and consensus alignment was performed between conditions, ****$p < 0.0001$ by t-test. **(I)** Gene set enrichment analysis of median difference between wildtype (n = 58 cells) and AtohKO (n = 64) tuft cell populations. Top 20 gene sets from positive gene enrichment are ranked by the normalized enrichment score (NES) and p-value. Yellow highlighted gene sets are related to the citric acid cycle and metabolism pathways. **(J-K)** Positive enrichment plots for the gene sets “Reactome Citric Acid Cycle TCA Cycle” and “Mootha TCA.” **(L-M)** Pathway analysis between wildtype and AtohKO tuft cells for **(L)** gene ontology and **(M)** KEGG enrichment shows positive enrichment for the Tricarboxylic or citrate acid cycle Metabolic Process. **(N-S)** Relative expression of citrate acid cycle genes in wildtype (green) and AtohKO (magenta) tuft cells. ****$p < 0.0001$, < 0.001, **$p < 0.01$, and *$p < 0.05$ by t-test.

(2) relative microbial abundance between wildtype and AtohKO animals. We used light chromatography-mass spectrometry to analyze metabolite levels in cecal luminal contents and cecal tissue. This analysis revealed that the relative concentration of succinate was significantly increased in the AtohKO cecal luminal contents but not in cecal tissue, compared to the wildtype condition (Figure 34C). Succinate or succinic acid is a metabolic intermediate in the TCA cycle and is converted into fumarate by the enzyme succinate dehydrogenase (SDH) (Mills & O’neill, 2014; Ryan *et al*, 2019). SDH-encoding genes were increased in AtohKO tuft cells suggesting that intracellular uptake of succinate by tuft cells was followed by metabolic processing of this metabolite into its downstream product. Moreover, the disparity in succinate concentration between luminal contents and whole tissue suggest a commensal microbiome rather than a host-derived origin for succinate. To support this hypothesis, we repeated the analysis in the AtohKO condition following microbiome depletion. Succinate levels were significantly decreased in the antibiotic-treated AtohKO cecal luminal contents, confirming that the commensal microbiome was primarily responsible for succinate production (Figure 34D). Previously published work has

demonstrated that parasite-derived succinate, downstream of helminth infection, can drive tuft cell hyperplasia and induce the type 2 immune response necessary for worm extrusion (Nadjsombati *et al*, 2018; Lei *et al*, 2018; Schneider *et al*, 2018). We confirmed that succinate administration induces tuft cell hyperplasia and activates the type 2 immune response, characterized by an increase in major basic protein (MBP)-positive eosinophils (Figure 34E-F) (Schneider *et al*, 2018; Lei *et al*, 2018; Nadjsombati *et al*, 2018; Allen & Sutherland, 2014).We also observed infiltration of MBP+ eosinophils in the AtohKO small intestine, suggesting an activation of the type 2 immune response may be responsible for the tuft cell hyperplasia observed in this model (Figure 34E-F). While it remains to be seen whether ILC2s are increased in the AtohKO small intestine, our work demonstrates that commensal bacteria-derived succinate is capable of inducing tuft cell hyperplasia, even in the absence of helminth infection or eukaryotic colonization.

Microbiome sequencing identified expansion of Firmicutes in the AtohKO ileum

As the microbiome was necessary for *in vivo* tuft cell hyperplasia, we used sequencing of the V4 region in the 16s rRNA gene to assess changes in microbiome distribution in the AtohKO model (Goodrich *et al*, 2014). DNA extraction and 16s sequencing were performed from the ileal luminal contents of co-housed wildtype and AtohKO littermates. Principal component analysis of the Bray-Curtis dissimilarity index, a measure of inter-sample relatedness (Goodrich *et al*, 2014), demonstrated that wildtype and AtohKO replicates clustered together based on biological phenotype rather than due to cage effects (Figure 35A-B). Average relative abundance from the wildtype replicates revealed that the family *Bacteroidaceae*, members of phylum Bacteroidetes,

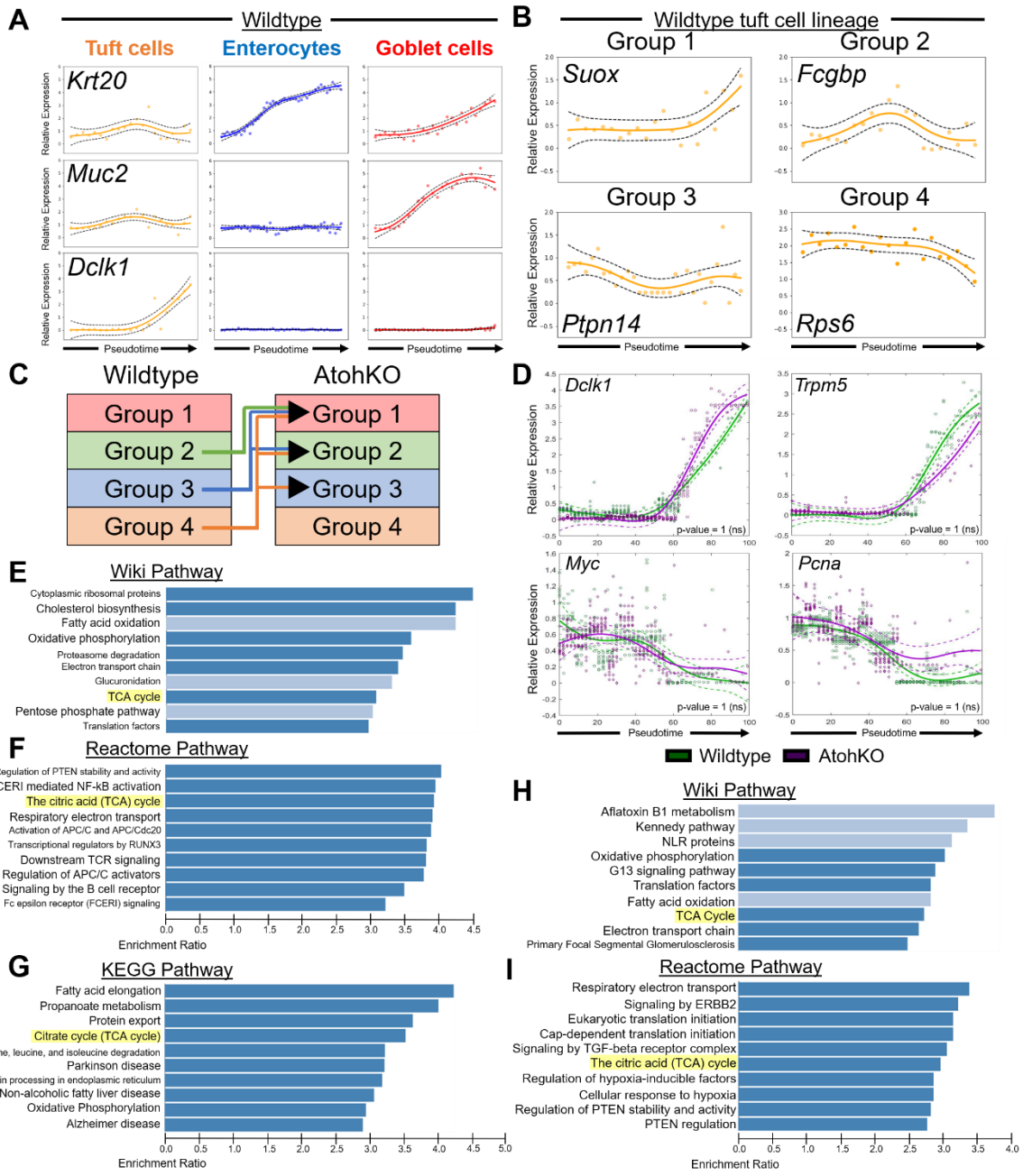

Figure 30. Trend dynamic analysis for p-Creode cell lineages. (A) Relative expression of cell identity genes, *Krt20, Muc2,* and *Dclk1,* along the wildtype tuft cell (orange), enterocyte (blue), and goblet cell (red) lineages along pseudotime. Gene expression is represented by ArcSinh scaled data. **(B)** Representative gene trends (solid orange line) across pseudotime from Groups 1 (e.g. *Suox*), 2 (e.g. *Fcgbp*), 3 (e.g. *Ptpn14*), and 4 (e.g. *Rps6*) of trend dynamic clustering of the tuft cell lineage. Solid circles depict raw data from single representative p-Creode graph and dashed black line represents the confidence interval for gene expression. **(C)** Schematic depicting the comparison between wildtype and AtohKO gene clusters. We identified 3,420 genes that class switched from wildtype groups 2-4 to AtohKO groups 1-3. **(D)** Trend dynamics along pseudotime of non-class switching tuft cell-expressing genes, *Dclk1* and *Trpm5*, and stem cell-expressing

genes, *Myc* and *Pcna*, between wildtype (green) and AtohKO (magenta). Solid line represents wildtype (green) and AtohKO (magenta) gene expression trends from 10 representative p-Creode graphs. Raw data is shown for wildtype (green circles) and AtohKO (magenta diamonds). Confidence interval of raw data was depicted by dashed lines for wildtype (green) and AtohKO (magenta). Dynamic time warping was used to fit wildtype and AtohKO tuft cell data to the same scale. Statistical analysis of trend differences and consensus alignment was performed between conditions, p-value = 1 (ns) by t-test. **(E-F)** Over-representation analysis using **(E)** Wiki and **(F)** Reactome Pathway datasets of 5-trend analysis. **(G-I)** Over-representation analysis using **(G)** KEGG, **(H)** Wiki Pathway, and **(I)** Reactome Pathway datasets of 3-trend analysis.

comprised the vast majority of the luminal microbiome in the normal ileum (Figure 35C). Firmicutes, such as *Lachnospiraceae* and *Bacillaceae*, were also well-represented though in lower abundance, as expected from a healthy intestinal microbiome (Figure 35C) (Roulis *et al*, 2016a). In the four wildtype replicates, relative abundance of *Bacteroidaceae* and Firmicutes, such as class *Bacilli* and family *Lachnospiraceae*, were consistent and at the expected ratios (Figure 35E).

As anticipated, the microbiome distribution of the AtohKO lumen was significant altered compared to wildtype littermates. While *Bacteroidaceae* abundance decreased, Firmicutes, especially *Bacilli* and *Lacobacillaceae*, were expanded (Figure 35D). Moreover, class *Gammaproteobacteria*, members of phylum Proteobacteria, did not comprise a substantial share of the wildtype ileal microbial biomass but was a far greater percentage of the AtohKO ileal microbiome (Figure 35D). Unlike the wildtype replicates, the AtohKO replicates had more sample-to-sample differences. For instance, *Lactobacillaceae* comprised a negligible share of AtohKO replicates 1, 2 ,and 3 but comprised about 80% of the total biomass in AtohKO replicate 4. While *Gammaproteobacteria* comprised 13-21% of AtohKO replicates 1- 3, this class was almost undetectable in replicate 4 (Figure 35F). These differences may explain why replicate 4 did not cluster with the other AtohKO replicates based on the Bray-Curtis dissimilarity index. Deeper analysis, closer to the species level, of operational taxonomic units (OTUs) is necessary to determine whether any of these overall differences are linked to the metabolic phenotypes

observed in the AtohKO model. It remains to be seen whether there are changes in the distribution of OTUs associated with succinate-consuming or succinate-producing bacterial species. Future experiments could monocolonize succinate producers in germ-free animals to categorically demonstrate that commensal-derived succinate can induce tuft cell hyperplasia.

Succinate treatment ameliorates inflammation in the $TNF^{\Delta ARE/+}$ model

Given the decreased frequency of tuft cells in highly inflamed regions of the $TNF^{\Delta ARE/+}$ and human ilea, we hypothesized that increasing tuft cell specification may suppress inflammation. In ten-week-old $TNF^{\Delta ARE/+}$ mice that had already developed disease, we therapeutically administered succinate (120mM) in the drinking water for short-term (5 days) and long-term (one month) treatment. While succinate-treated $TNF^{\Delta ARE/+}$ mice failed to gain as much weight as untreated controls, this was consistent with succinate treatment in wildtype controls (Figure 36A). Histology from treated $TNF^{\Delta ARE/+}$ animals demonstrated improved intestinal tissue organization compared to age-matched, untreated $TNF^{\Delta ARE/+}$ controls, based on restored crypt-villus architecture and minimized villus distortion (Figure 36B). Expression of epithelial LYZ1 was increased starting at five days of treatment and appeared to be completely restored at one month (Figure 36C). Importantly, LYZ1 expressing cells were restricted to the bottom of the epithelial crypts and exhibited the typical Paneth cell morphology, comparable to healthy controls. DCLK1+ tuft cells were increased in one month-treated animals, consistent with succinate's ability to induce tuft cell specification (Figure 36D). In line with improved histology, inflammation as assessed by MPO+ neutrophil infiltration was decreased with prolonged succinate exposure (Figure 36E). Overall, these experiments demonstrated that enhanced tuft cell specification was able to dampen ileal inflammation in the $TNF^{\Delta ARE/+}$ model.

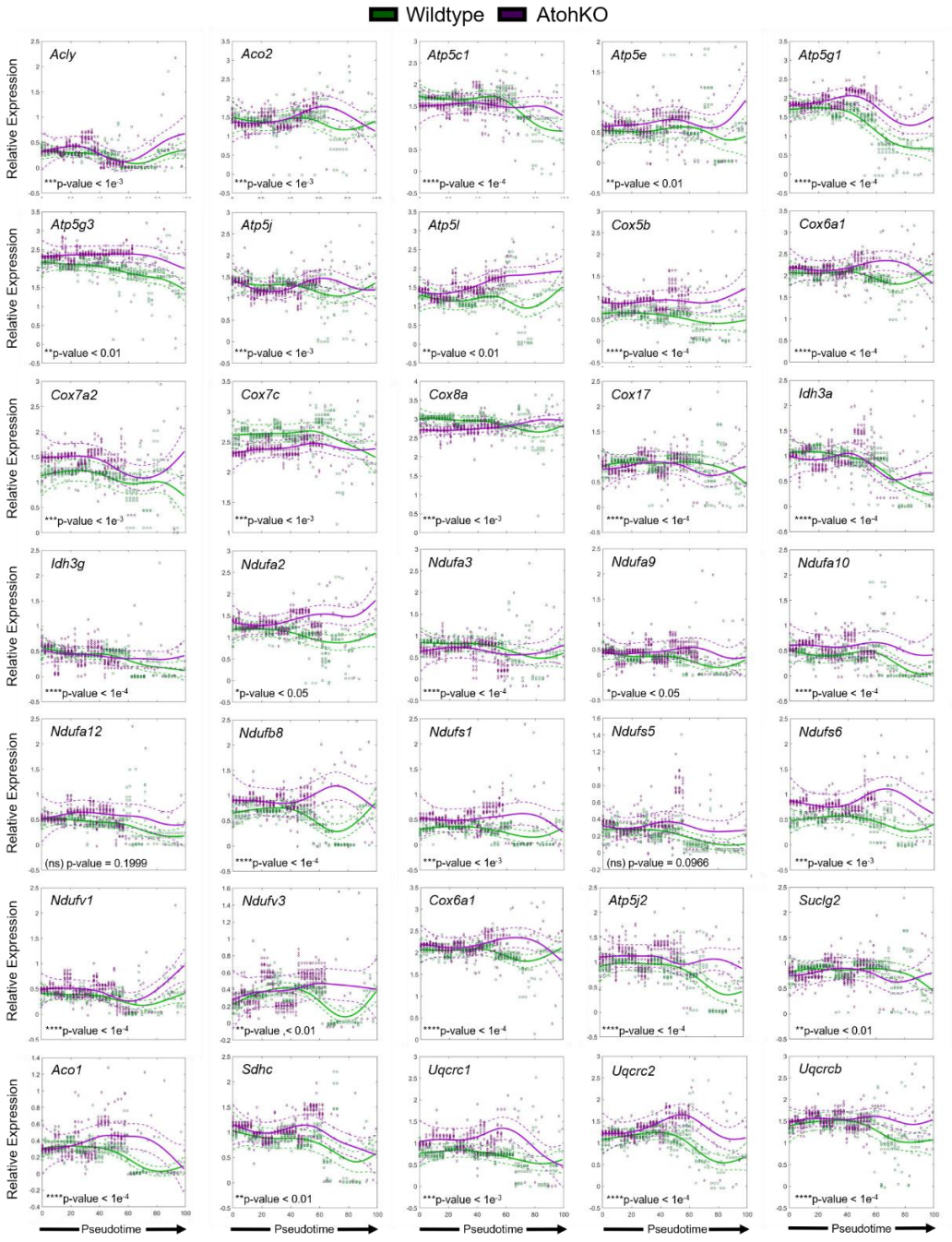

Figure 31. **TCA cycle genes in the wildtype and AtohKO tuft cell lineages.** Trend dynamics along pseudotime of TCA cycle-associated genes between wildtype (green) and AtohKO (magenta). Solid line represents wildtype (green) and AtohKO (magenta) gene expression trends from 10 representative p-Creode graphs. Raw data is shown for wildtype (green circles) and AtohKO (magenta diamonds). Confidence interval of raw data was depicted by dashed lines for wildtype (green) and AtohKO (magenta). Dynamic time warping was used to fit wildtype and AtohKO tuft cell data to the same scale. Statistical analysis of trend differences and consensus alignment was performed between conditions, *p-value < 0.05, **p-value < 0.01, ***p-value < 0.001, ****p-value < 0.0001 by t-test.

Discussion

This study presents the first evidence showing that tuft cell specification is decreased in intestinal inflammation. We observed decreased numbers of tuft cells, labeled with pEGFR and COX2, in ileal tissues acquired from CD patients. These results were confirmed in the *TNF*$^{\Delta ARE/+}$ model of Crohn's-like ileitis where frequency of DCLK1+ tuft cells was inversely correlated with inflammation severity. Highly inflamed regions had lower DCLK1+ tuft cell numbers while less inflamed regions in the *TNF*$^{\Delta ARE/+}$ ileum had increased tuft cell presence. This suggests that tuft cell presence may act to suppress inflammation and increasing tuft cell specification may potentially counteract proinflammatory signals in the intestinal tract. To identify mechanisms driving increased specification of tuft cells, we utilized a novel, genetically-inducible model of tuft cell hyperplasia, the AtohKO model. We generated single-cell RNA sequencing from wildtype, *TNF*$^{\Delta ARE/+}$, and AtohKO animals to examine gene expression changes in small intestinal tuft cells. Analysis of wildtype and *TNF*$^{\Delta ARE/+}$ scRNA-seq datasets using the p-Creode algorithm confirmed a non-secretory origin for epithelial tuft cells, independent of the *Atoh1*-regulated secretory lineage. In the AtohKO model, we used both population and trend analysis to demonstrate that expression of TCA cycle genes was upregulated. This suggests that tuft cells in the AtohKO were more metabolically active than their wildtype counterparts.

Given the chemosensory role associated with tuft cells, we asked whether these changes were the consequence of intrinsic or extrinsic mechanisms. Analysis of the intestinal microbiome between wildtype and AtohKO littermates showed the latter has significant changes in the distribution of bacterial species such as *Gammaproteobacteria* and *Lactobacilliaceae.* Microbiome depletion in AtohKO animals suppressed tuft cell hyperplasia and decreased expression of TCA cycle genes. This implicates the microbiome as a critical driver of tuft cell specification in the AtohKO model. We then performed metabolite analysis of luminal contents to query the signals transmitted by the microbiome to drive epithelial specification. We found that

A

NAME	NES	NOM p-val
BARRIER_COLON_CANCER_RECURRENCE_DN	1.54	0.008
REACTOME_PEPTIDE_CHAIN_ELONGATION	1.54	0
SA_TRKA_RECEPTOR	1.54	0.039
BANDRES_RESPONSE_TO_CARMUSTIN_MGMT_24HR_DN	1.53	0.013
HAHTOLA_CTCL_CUTANEOUS	1.53	0.012
MOOTHA_TCA	1.52	0.011
HE_PTEN_TARGETS_UP	1.52	0.03
VERRECCHIA_RESPONSE_TO_TGFB1_C5	1.52	0.019
KEGG_RIBOSOME	1.52	0
REACTOME_NONSENSE_MEDIATED_DECAY_ENHANCED_BY_THE_EXON_JUNCTION_COMPLEX	1.52	0
WANG_BARRETTS_ESOPHAGUS_DN	1.52	0.018
REACTOME_INFLUENZA_LIFE_CYCLE	1.52	0
MOOTHA_GLYCOLYSIS	1.51	0.007
BUCKANOVICH_T_LYMPHOCYTE_HOMING_ON_TUMOR_DN	1.51	0.011
REACTOME_OXYGEN_DEPENDENT_PROLINE_HYDROXYLATION_OF_HYPOXIA_INDUCIBLE_FACTOR_ALPHA	1.51	0.023
CHEN_LUNG_CANCER_SURVIVAL	1.51	0.016
REACTOME_REGULATION_OF_HYPOXIA_INDUCIBLE_FACTOR_HIF_BY_OXYGEN	1.5	0.026
REACTOME_INTERACTION_BETWEEN_L1_AND_ANKYRINS	1.5	0.035
BIOCARTA_TFF_PATHWAY	1.5	0.009
REACTOME_SRP_DEPENDENT_COTRANSLATIONAL_PROTEIN_TARGETING_TO_MEMBRANE	1.5	0

NAME	NES	NOM p-val
MOOTHA_GLYCOLYSIS	1.55	0.00
BARRIER_COLON_CANCER_RECURRENCE_DN	1.55	0.01
BARIS_THYROID_CANCER_UP	1.53	0.02
REACTOME_INTERACTION_BETWEEN_L1_AND_ANKYRINS	1.53	0.02
MOOTHA_TCA	1.53	0.01
VERRECCHIA_RESPONSE_TO_TGFB1_C5	1.53	0.02
REACTOME_OXYGEN_DEPENDENT_PROLINE_HYDROXYLATION_OF_HYPOXIA_INDUCIBLE_FACTOR_ALPHA	1.53	0.02
REACTOME_GLUTATHIONE_CONJUGATION	1.52	0.01
BUCKANOVICH_T_LYMPHOCYTE_HOMING_ON_TUMOR_DN	1.52	0.01
REACTOME_INFLUENZA_LIFE_CYCLE	1.52	0.00
REACTOME_INFLUENZA_VIRAL_RNA_TRANSCRIPTION_AND_REPLICATION	1.51	0.00
KAPOSI_LIVER_CANCER_MET_UP	1.51	0.01
BILANGES_SERUM_RESPONSE_TRANSLATION	1.51	0.00
NIELSEN_SYNOVIAL_SARCOMA_DN	1.51	0.03
REACTOME_PEPTIDE_CHAIN_ELONGATION	1.51	0.00
REACTOME_SRP_DEPENDENT_COTRANSLATIONAL_PROTEIN_TARGETING_TO_MEMBRANE	1.51	0.00
KEGG_RIBOSOME	1.50	0.00
REACTOME_CITRIC_ACID_CYCLE_TCA_CYCLE	1.50	0.01
REACTOME_GLUCONEOGENESIS	1.50	0.02
BIOCARTA_IGF1MTOR_PATHWAY	1.50	0.04

B

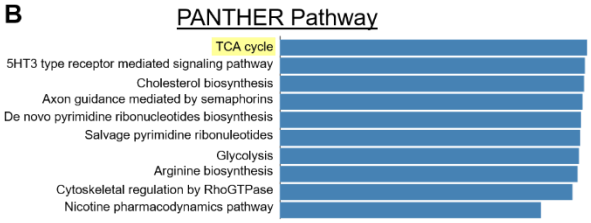

C

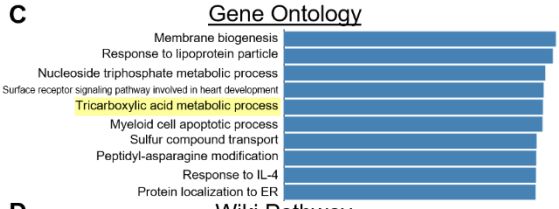

D

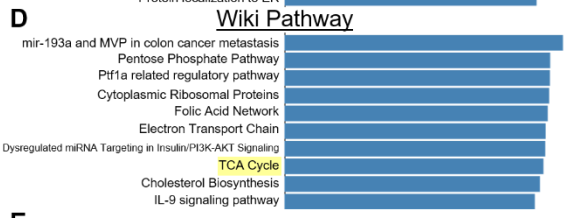

E

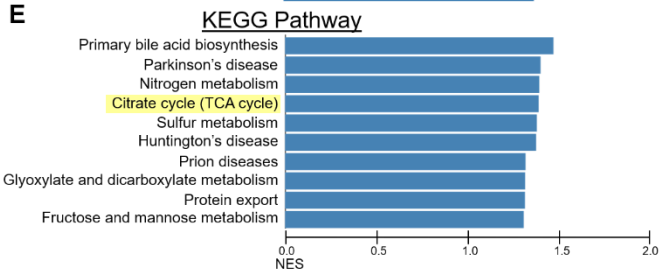

F

Table 2: Top Genes from GSEA: Reactome_Citric_Acid_Cycle_TCA_Cycle

Rank in Gene List	Gene Name	Running ES	Core Enrichment
28	*Mdh2*	0.23	Yes
88	*Sdha*	0.42	Yes
164	*Cs*	0.58	Yes
242	*Sdhc*	0.72	Yes
257	*Ogdh*	0.85	Yes
539	*Idh3b*	0.86	Yes
571	*Idh3g*	0.89	Yes
576	*Sdhd*	0.91	Yes
614	*Idh3a*	0.93	Yes

G

Table 3: Top Genes from GSEA: Reactome Regulation of Hypoxia Inducible Factor HIF_by_Oxygen

Rank in Gene List	Gene Name	Running ES	Core Enrichment
139	*Ube2d3*	0.32	Yes
182	*Tceb2*	0.62	Yes
298	*Rbx1*	0.83	Yes
443	*Rps27a*	0.92	Yes
978	*Hif1a*	0.91	No

H

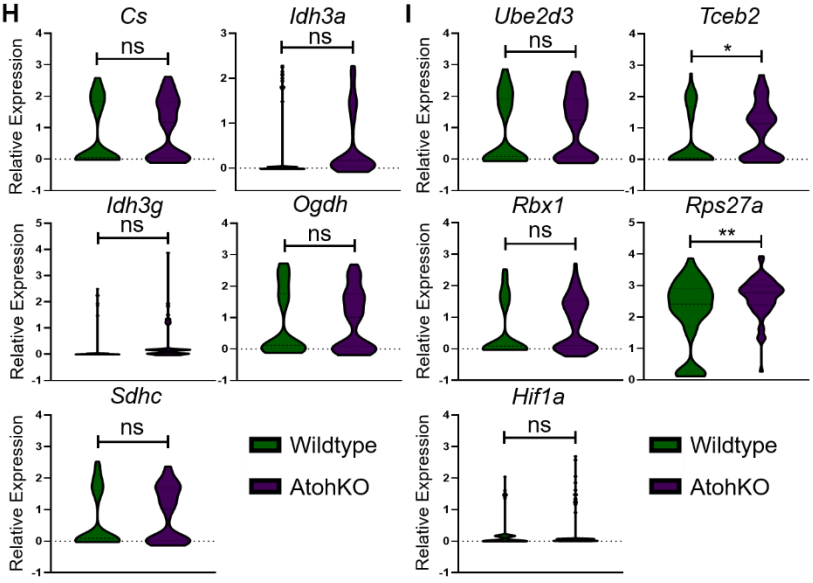

I

Figure 32. Gene expression analysis of wildtype and AtohKO tuft cells. (A) Two separate iterations of gene set enrichment analysis of median difference in gene expression between wildtype and AtohKO tuft cells. Top 20 gene sets from positive gene enrichment are ranked by the normalized enrichment score (NES) and p-value. Yellow highlighted gene sets are related to the citric acid cycle and metabolism pathways. Blue highlighted gene sets are related to the

hypoxia pathway. **(B-E)** Functional analysis between wildtype and AtohKO tuft cells for **(B)** PANTHER pathway, **(C)** Gene Ontology, and **(D)** Wiki Pathway, and **(E)** KEGG pathway analysis shows positive enrichment for the Tricarboxylic or citrate acid cycle (yellow highlighted). **(F-G)** Ranked gene list from the metabolism-related and hypoxia-related gene set with the highest NES, **(F)** "Reactome Citric Acid Cycle TCA Cycle" and **(G)** "Reactome Regulation of Hypoxia Inducible Factor HIF by Oxygen," respectively. Genes contributing to the Running enrichment score (ES) are labeled "Yes" for Core Enrichment. **(H)** Relative expression of citrate acid cycle genes in wildtype (green) and AtohKO (magenta) tuft cells. $^{**}p < 0.01$, $^{*}p < 0.05$, and not significant (ns) by t-test. **(I)** Relative expression of hypoxia pathway-associated genes in wildtype (green) and AtohKO (magenta) tuft cells. $^{**}p < 0.01$, $^{*}p < 0.05$, and not significant (ns) by t-test.

the TCA cycle intermediate succinate is significantly increased in the AtohKO lumen (but not the tissue) and is decreased under microbiome depletion, confirming its origins from the commensal microbiome. Helminth-derived succinate is known to signal to tuft cells and triggers tuft cell hyperplasia in acute infection models. However, our findings are the first to show that commensal-derived succinate can also induce tuft cell hyperplasia. Succinate administration, absent of helminth infection, is relatively harmless to wildtype animals and results in increased numbers of intestinal tuft cells.

In order to investigate the effect of increased tuft cell specification in inflammation, we therapeutically administered succinate to $TNF^{\Delta ARE/+}$ animals following onset of disease. We observed that succinate-treated $TNF^{\Delta ARE/+}$ animals had less villus blunting and improved tissue organization. LYZ1+ Paneth cells and DCLK1+ tuft cells were increased in the succinate condition, indicating decrease in inflammation severity. Future experiments will investigate the precise mechanism of tuft cell-induced suppression of intestinal inflammation. These studies highlight the potential of intestinal tuft cells to be leveraged therapeutically in inflammatory disease.

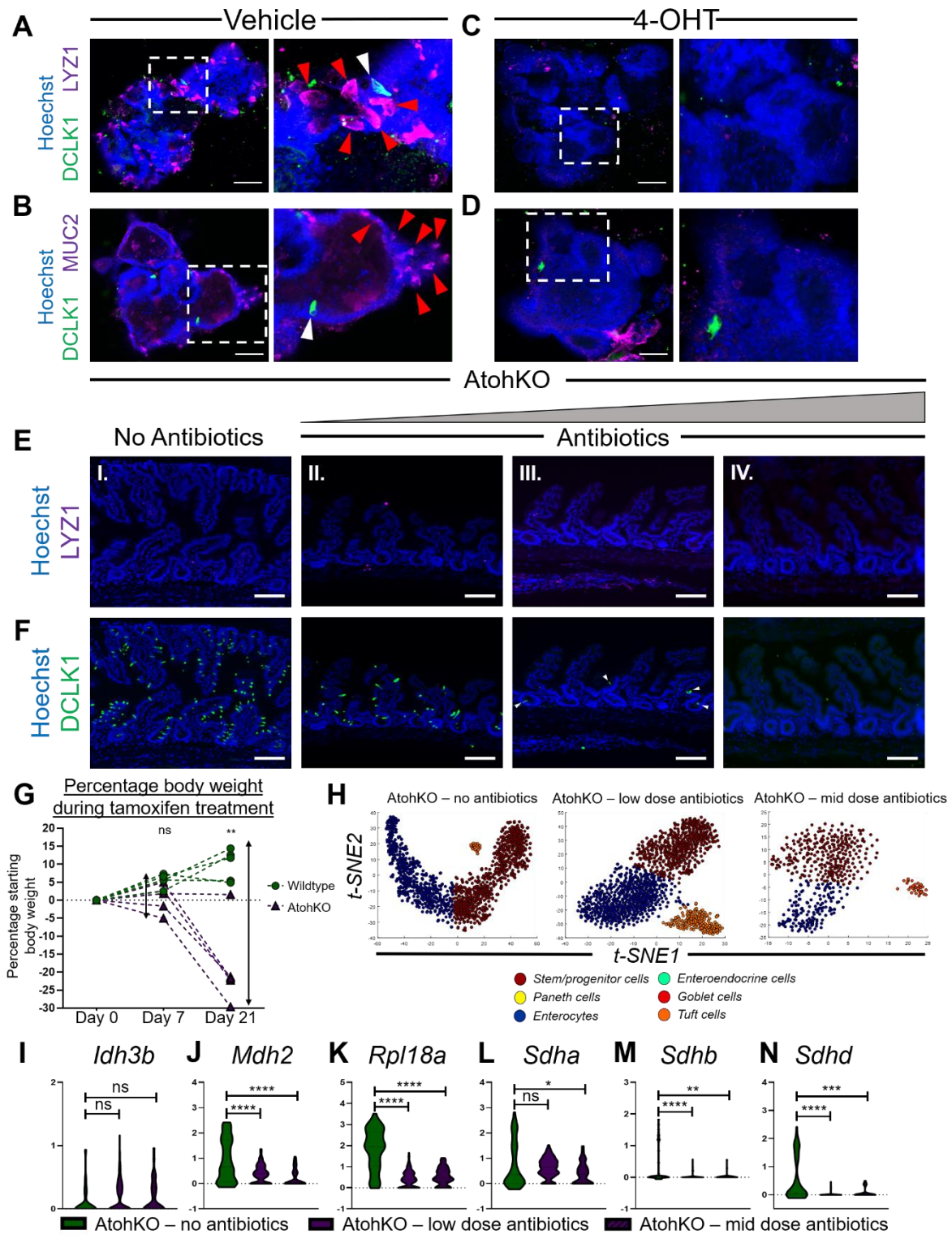

Figure 33. Tuft cell hyperplasia is microbiome-dependent. (A) Vehicle-treated *Lrig1*$^{CreERT2/+}$*;Atoh1*$^{fl/fl}$ small intestinal enteroids are positive for DCLK1+ tuft cells (green) and LYZ1+ Paneth cells (magenta). Magnified inset (white dashed box) shows LYZ1-positive Paneth cells (red arrows) and DCLK1+ tuft cell (white arrow). Hoechst (blue) denotes nuclei, scale bar =

50 µm. **(B)** Vehicle-treated *Lrig1*$^{CreERT2/+}$*;Atoh1*$^{fl/fl}$ small intestinal enteroids are positive for DCLK1+ tuft cells (green) and MUC2+ goblet cells (magenta). Magnified inset (white dashed box) shows MUC2-positive Paneth cells (red arrows) and DCLK1+ tuft cell (white arrow). Hoechst (blue) denotes nuclei, scale bar = 50 µm. **(C-D)** 4-OHT-treated *Lrig1*$^{CreERT2/+}$*;Atoh1*$^{fl/fl}$ small intestinal enteroids lack DCLK1+ and both **(C)** LYZ1+ Paneth (magenta) and **(D)** MUC2+ goblet cells (magenta). Hoechst (blue) denotes nuclei, scale bar = 50 µm. **(E-F)** Representative immunofluorescence staining of **(E)** LYZ1 (magenta) and **(F)** DCLK1 (green) in the AtohKO ileum, **(I)** without antibiotics and with antibiotics, **(II)** low dose, **(III)** mid dose, and **(IV)** high dose. Hoechst (blue) denotes nuclei, scale bar = 100 µm. **(G)** Change in percentage body weight during antibiotic and tamoxifen treatment. Day 0 – start of antibiotic treatment, Day 7 – start of tamoxifen treatment (antibiotics continued), and Day 21 – cessation of tamoxifen (and antibiotic treatment). Wildtype (green) (n = 5 replicates) and AtohKO (magenta) (n = 5 replicates). **p < 0.01, ns (not significant) by t-test. **(C)** Relative gene expression of tricarboxylic acid cycle-related genes, identified by GSEA, among untreated AtohKO – no antibiotics (green), AtohKO – low dose antibiotics (magenta), and AtohKO – mid dose antibiotics (magenta, dashed) tuft cell populations. **(H)** Clustering analysis in t-SNE of scRNA-seq data from AtohKO – no antibiotics (n = 1 replicate, x cells), AtohKO – mid dose antibiotics (n = 1 replicate, x cells), and AtohKO – mid dose antibiotics (n = 1 replicate, 488 cells). Stem/progenitor cells (brown), enterocytes (blue), goblet cells (red), Paneth cells (yellow), enteroendocrine cells (green), and tuft cells (orange). Each data point represents a single cell. **(G)** Relative expression of tricarboxylic acid cycle-related genes in AtohKO – no antibiotics (green), AtohKO – low dose antibiotics (magenta), and AtohKO – mid dose antibiotics (magenta, dashed) tuft cells. ****p < 0.001, *p < 0.05, and not significant (ns) by t-test. **(I-N)** Relative expression of hypoxia pathway-related genes in AtohKO – no antibiotics (green), AtohKO – low dose antibiotics (magenta), and AtohKO – mid dose antibiotics (magenta, dashed) tuft cells. ***p < 0.001, *p < 0.05, and not significant (ns) by t-test.

Methods

Human tissue

Formalin-fixed, paraffin-embedded blocks of ileum surgical resections were obtained from the Vanderbilt Cooperative Human Tissue Network (CHTN) Western Division, along with deidentified patient data and pathology reports. All procedures and studies were performed according to protocols approved by the Vanderbilt University Institutional Review Board (Protocol No. 182138). Pathological examination was utilized to classify samples as “normal” (n = 14) or “diseased” (n = 19). Samples from patients with Crohn’s disease were included only if inflammation was evident in the distal ileum. Tissue samples were prepared for histology or immunofluorescence staining as described below.

Mouse experiments

All animal protocols were approved by the Vanderbilt University Animal Care and Use Committee and in accordance with NIH guidelines. *Lrig1*^{CreERT2} and *Atoh1*$^{flox/flox}$ strains, each in a C57BL/6 background, were purchased from Jackson Laboratory to generate *Lrig1*$^{CreERT2/+}$*;Atoh1*$^{fl/fl}$ (AtohKO) animals. Cre recombinase activity was induced in 2- or 3-month-old *Lrig1*$^{CreERT2/+}$*;Atoh1*$^{fl/fl}$ and *Lrig1*$^{+/+}$*;Atoh1*$^{fl/fl}$ males via intraperitoneal administration of 2mg of tamoxifen (Sigma-Aldrich) for 4 consecutive days. Animals were weighed prior to treatment and at time of sacrifice as specified elsewhere. *TNF*$^{\Delta ARE/+}$ and wildtype littermates were sacrificed at 4 months of age. For microbiome depletion experiments, *Lrig1*$^{CreERT2/+}$*;Atoh1*$^{fl/fl}$ animals were pre-treated with either a broad-spectrum antibiotic cocktail containing kanamycin (4.0mg/ml), metronidazole (2.15mg/ml), gentamicin (0.35mg/ml), colistin sulfate (8500U/ml), and vancomycin (0.45mg/ml) or ampicillin (1mg/ml) in their drinking water for 7 days prior to tamoxifen treatment. Mid-dose antibiotics and low-dose antibiotics were 0.75x and 0.25x of the original 1x concentration, respectively. Following tamoxifen administration, *Lrig1*$^{CreERT2/+}$*;Atoh1*$^{fl/fl}$ received either standard or antibiotic-supplemented drinking water for an additional 14 days. For microbiome experiments, co-housed male *Lrig1*$^{CreERT2/+}$*;Atoh1*$^{fl/fl}$ littermates received either vehicle (corn oil) or tamoxifen for 1 month. For succinate treatment, *TNF*$^{\Delta ARE/+}$ received either sodium succinate hexahydrate (120 mM; Alfa Aesar) or standard drinking water following disease onset (3- to 4-months-old) for 5 days or 1 month (Lei *et al*, 2018; Schneider *et al*, 2018).

Immunofluorescence staining and imaging

Paraffin-embedded ileal tissues were section (5µm) prior to deparaffinization, rehydration, and antigen retrieval using a citrate buffer (pH 6.0) for 20min in a pressure cooker at 105°C, followed by a 20-min cool down at room temperature (RT). Endogenous background signal was quenched

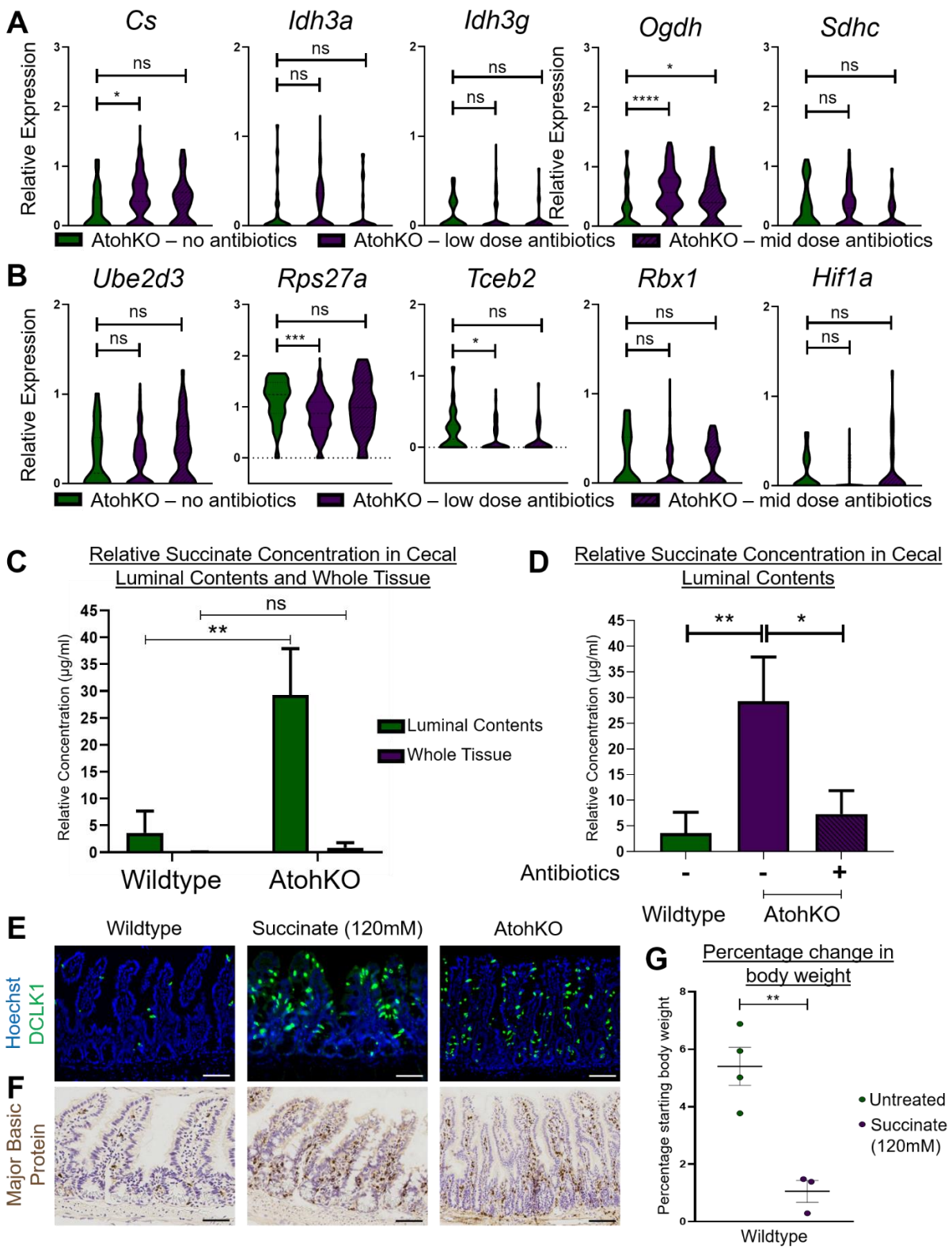

Figure 34. Luminal succinate is increased in the AtohKO model. (A) Relative expression of tricarboxylic acid cycle-related genes in AtohKO – no antibiotics (green), AtohKO – low dose

antibiotics (magenta), and AtohKO – mid dose antibiotics (magenta, dashed) tuft cells. ****p < 0.001, *p < 0.05, and not significant (ns) by t-test. **(B)** Relative expression of hypoxia pathway-related genes in AtohKO – no antibiotics (green), AtohKO – low dose antibiotics (magenta), and AtohKO – mid dose antibiotics (magenta, dashed) tuft cells. ***p < 0.001, *p < 0.05, and not significant (ns) by t-test. **(C)** Relative concentration (µg/ml) of succinate in the cecal lumen and whole cecal tissue from wildtype (green) and AtohKO (magenta) animals. Error bars represent SEM across 4 wildtype and AtohKO replicates. **p < 0.01 and not significant (ns) by t-test. **(D)** Relative succinate concentration (µg/ml) from the lumen of wildtype (green), AtohKO (magenta), and antibiotic-treated AtohKO (magenta, dashed) animals. Error bars represent SEM across n = 4 wildtype and untreated AtohKO replicates and n = 3 antibiotic treated-AtohKO replicates. **p < 0.01 and *p < 0.05 by t-test. **(E)** Immunohistochemistry staining of major basic protein in wildtype, succinate-treated, and AtohKO small intestine. Blue denotes nuclei and brown represents the counterstain. Scale bar = 100µm. **(F)** Immunofluorescence staining of DCLK1 (green) in wildtype, succinate-treated, and AtohKO small intestine. Hoechst (blue) denotes nuclei, scale bar = 100 µm. **(G)** Percentage change in body weight in untreated and succinate-treated (120mM) wildtype animals. Error bars represent SEM across n = 4 untreated and n = 3 succinate-treated replicates. **p < 0.01 by t-test.

by incubating tissue slides in 3% hydrogen peroxide for 10min at RT. Tissue sections were blocked in staining buffer (3% bovine serum albumin/ 10% normal donkey serum) for 1hr at RT prior to incubation with primary antibody overnight at RT. Antibodies used for immunofluorescence included, LYZ1 (DAKO, 1:100, rabbit), MUC2 (Santa Cruz, 1:100, rabbit), Myeloperoxidase (DAKO, 1:100, rabbit), DCLK1 (Santa Cruz, 1:100, goat). Tissues were then incubated with AF-555- or AF-647-conjugated secondary antibodies (Life Technologies, 1:500) for 1hr at RT and Hoecsht (1:10,000, Life Technologies) for 10min at RT. For human tuft cell labeling, Ax488-conjugated pEGFR (Abcam, 1:100) and unconjugated COX2 (CST, 1:100, rabbit) were used. Slides were incubated with anti-rabbit AF-647-conjugated secondary antibody and stained with Hoecsht. Imaging was performed using a Zeiss Axio Imager M2 microscope with Axiovision digital imaging system (Zeiss, Jena GmBH, Germany).

Image quantification

To quantify human tuft cell numbers, first the number of crypt and villus structures were counted in each field of view (FOV) for each subject (approximately 15-20 FOVs per sample). Tuft cell number, as identified by pEGFR and COX co-labeling, was manually counted per FOV in a blinded fashion. Quantification of tuft cell number per epithelial structure (crypt and villus) was generated for each subject and then stratified by disease state ("normal" or "Crohn's disease") using the pathology report. Results were analyzed by t-test using Prism GraphPad. For MUC2 quantification, manual demarcation of the epithelial villi was performed in each FOV and a nuclear mask was generated based on Hoescht staining. In the same region, a MUC2 mask was generated using immunofluorescence staining of MUC2. Total area of both masks was calculated to generate a normalized ratio of MUC2 intensity to nuclear staining. This process was repeated for LYZ1 quantification, except that only crypts were manually demarcated in the FOVs. Finally, for MPO and DCLK1 quantification, each villus was considered a separate unit and number of MPO+ neutrophils and DCLK1+ tuft cells were counted in a blinded fashion. Tuft cell number per villi was stratified based on MPO staining as either "low inflammation" (<35 neutrophils per villi) or "high inflammation" (≥ 35 neutrophils per villi). Total number of villi counted, and total number used for significance testing can be found in Figure 21.

Immunohistochemistry staining

Paraffin-embedded ileal tissue from wildtype and succinate-treated slides were retrieved as described above and standard H&E staining was performed for histology. To identify eosinophils, tissues were incubated with major basic protein (Mayo Clinic Arizona) followed by anti-rat HRP and counterstained with hematoxylin. Immunohistochemistry was performed by the Vanderbilt Translational Pathology Shared Resource and 20x brightfield scanning of immunohistochemistry

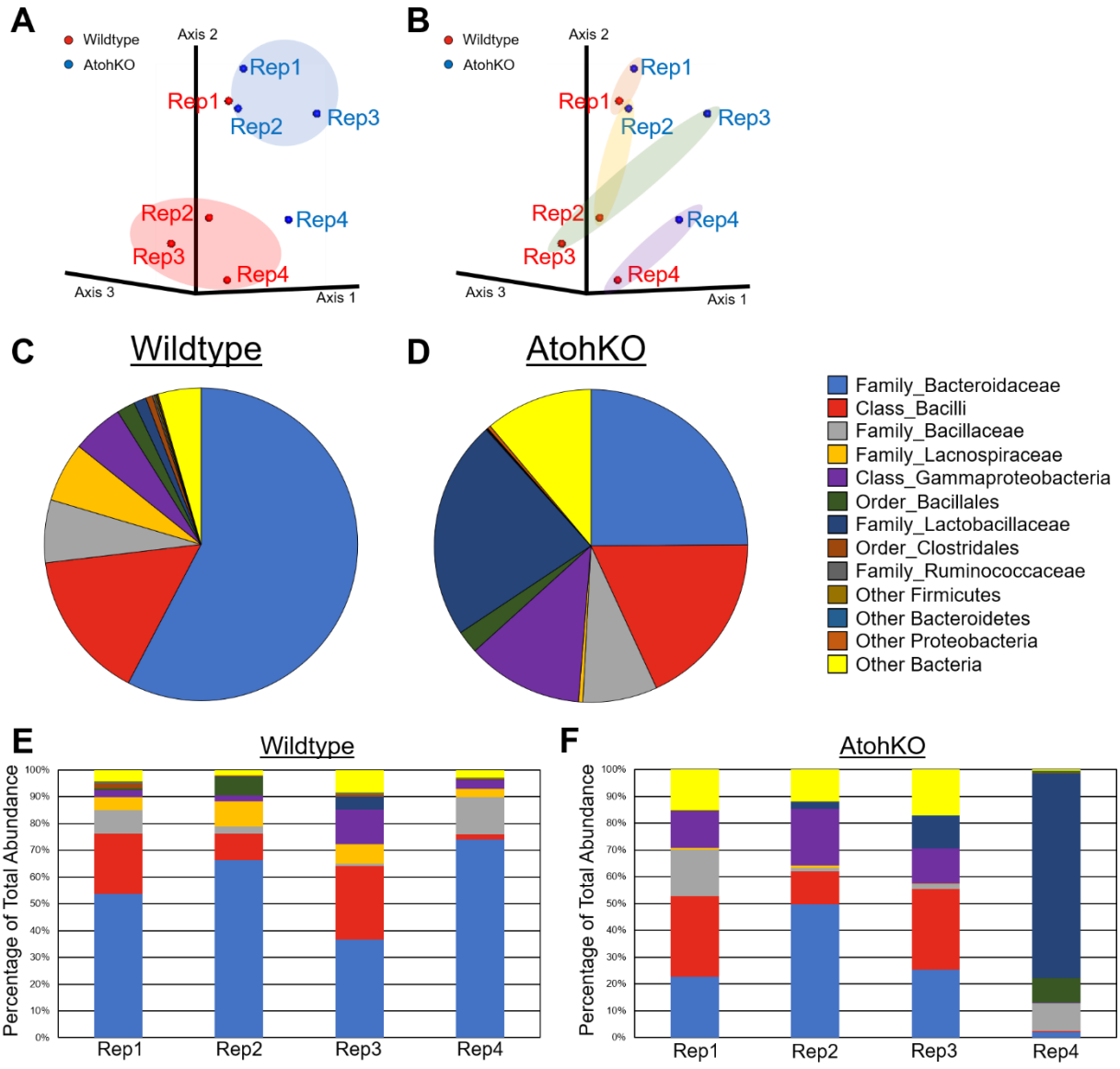

Figure 35. Ileal microbiome distribution is altered in the AtohKO ileum. (A) Principal component analysis of ileal microbiota as determined by Bray-Curtis dissimilarity index based on 16s rRNA amplicon sequencing. Annotation of PCA plot indicates clustering of wildtype (n = 4, red) and AtohKO (n = 4, blue) biological replicates by phenotype. **(B)** Principal component analysis of ileal microbiota as determined by Bray-Curtis dissimilarity index based on 16s rRNA amplicon sequencing. Annotation of PCA plot based on littermate pairs indicates dissimilarity between wildtype and AtohKO animals. **(C-D)** Pie chart show the average relative microbial abundance in the distal ileum over 4 **(C)** wildtype and **(D)** AtohKO samples, respectively. **(E)** Stacked bar plots showing relative abundance of microbial DNA from the wildtype ileal lumen (n = 4). Annotation reflects bacterial taxonomy. **(F)** Stacked bar plots showing relative abundance of microbial DNA from the AtohKO ileal lumen (n = 4). Annotation reflects bacterial taxonomy.

slides was performed by a Leica SCN400 Slide Scanner in the Vanderbilt Digital Histology Shared Resource.

Enteroid experiments

Ileal tissue was dissected and incubated in chelation buffer (3mM EDTA/EGTA, 0.5mM DTT, 1% P/S) at 4°C for 45 minutes. The tissue was shaken in PBS and filtered through a 100µm filter to isolate individual ileal crypts. The crypt suspension was centrifuged at 2.8 x 1000 RPM for 1 ½ minutes at 4°C following which 10µl of crypt pellet was resuspended in 300µl of reduced growth factor Matrigel and embedded in a 24-well dish. Enteroids were cultured initially in IntestiCult Organoid Growth Medium (StemCell Technologies) supplemented with Primocin antimicrobial reagent (InvivoGen, 1:1000) for 4 days before being changed to Primocin-supplemented differentiation media, as previously described (Sato *et al*, 2009). For *ex vivo* Cre-activation, *Lrig1*$^{CreERT2/+}$*;Atoh1*$^{fl/fl}$ enteroids were treated overnight at 37°C with either 1µM 4-hydroxytamoxifen (Sigma-Aldrich) or vehicle (ethanol) in differentiation media. Enteroids were passaged the following day into 8-well chamber slides and, after 5 days, were fixed on ice using 4% PFA for immunofluorescence staining.

Enteroid immunofluorescence staining

Fixed enteroids were permeabilized with Triton X-100 for 30min and blocked with 1% normal donkey serum (PBS) for 30min at RT. Enteroids were stained with primary antibodies including LYZ1 (DAKO, 1:100, rabbit), MUC2 (Santa Cruz, 1:100, rabbit), and DCLK1 (Santa Cruz, 1:100, goat). Enteroids were then incubated with AF-555- or AF-647-conjugated secondary antibodies (Life Technologies, 1:500) for and Hoecsht (1:10,000, Life Technologies) 1hr at RT. Vectashield

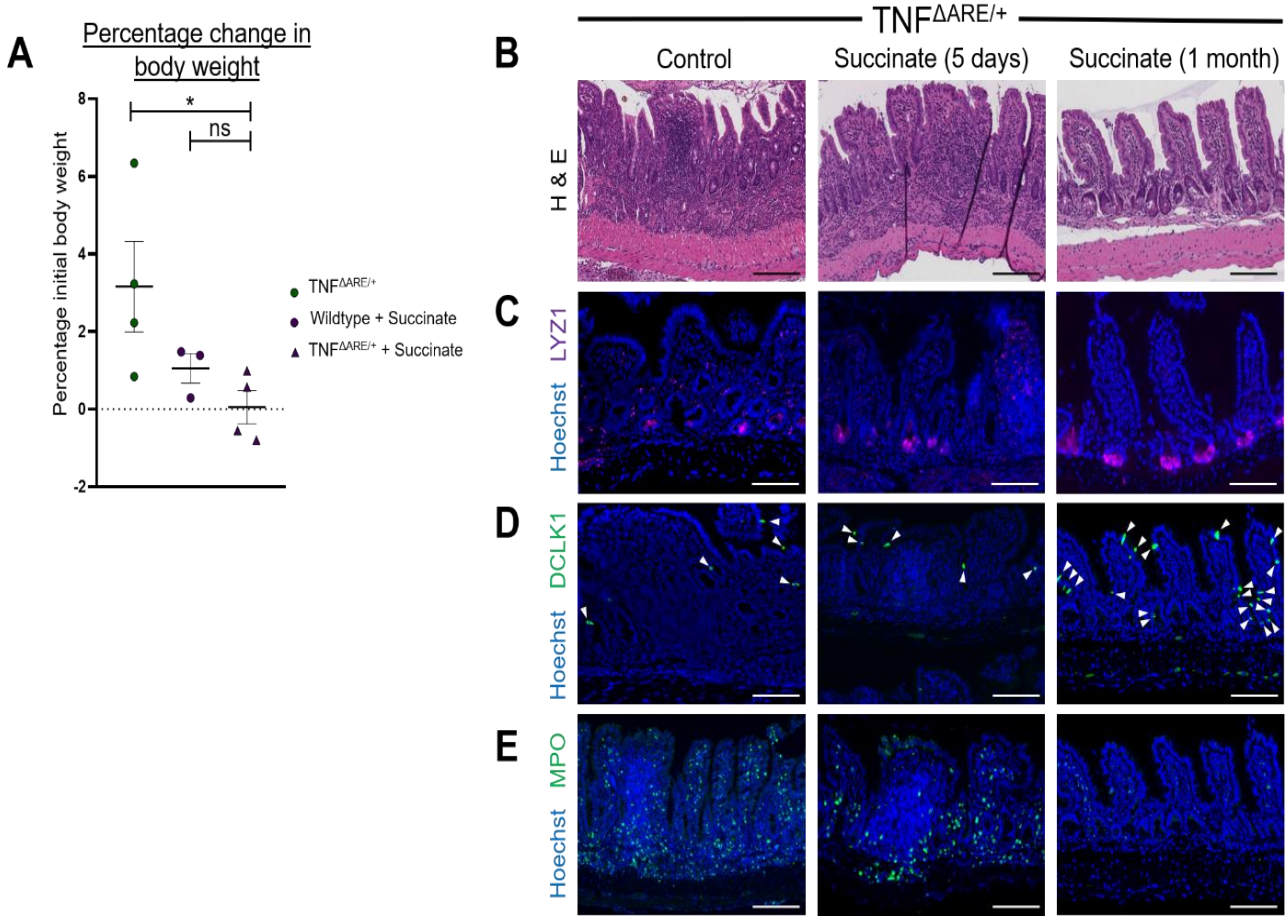

Figure 36. Succinate treatment mitigates inflammation in the TNF$^{\Delta ARE/+}$ model. (A) Percentage change in body weight in untreated TNF$^{\Delta ARE/+}$ (green circles) and succinate-treated wildtype (magenta circles) and TNF$^{\Delta ARE/+}$ animals (magenta triangles). Error bars represent SEM across n = 4 wildtype replicates, n = 3 succinate-treated wildtype replicates, and n = 4 succinate treated-TNF$^{\Delta ARE/+}$ replicates. *p < 0.05 and not significant (ns) by t-test. **(B)** Histology from untreated and succinate-treated 4-month-old TNF$^{\Delta ARE/+}$ ileum. Scale bar = 100µm. **(C)** Immunofluorescence imaging of LYZ1 (magenta) in the ileal epithelium of untreated and succinate-treated TNF$^{\Delta ARE/+}$ ileum. Scale bar = 100µm. **(D)** Immunofluorescence imaging of DCLK1 (green) in the untreated and succinate-treated TNF$^{\Delta ARE/+}$ ileum. White arrows indicate epithelial tuft cells. Hoechst (blue) denotes nuclei, scale bar = 100 µm. **(E)** Immunofluorescence imaging of MPO (green) in the ileum of untreated and succinate-treated TNF$^{\Delta ARE/+}$ ileum. Hoechst (blue) denotes nuclei, scale bar = 100 µm.

Antifade Mounting Medium (Vectorlabs) was applied to enteroids before imaging with a Nikon Spinning Disk Confocal microscope.

inDrops single-cell RNA sequencing

Ileal crypts from human and mouse tissue were isolated as described above. Crypts were dissociated into single cells using a cold-activated protease (1mg/ml)/ DNAseI (2.5mg/ml) enzymatic cocktail in a modified protocol that maintains high cell viability (Adam *et al*, 2017). Dissociation was performed at 4°C for 15mins followed by trituration to mechanically disaggregate cell clusters. Cell viability was assessed by counting Trypan Blue positive cells. The cell suspension was enriched for live cells with a MACS dead cell removal kit (Miltenyi) prior to encapsulation. Single cells were encapsulated and barcoded using the inDrops platform (1CellBio) with an *in vitro* transcription library preparation protocol (Klein *et al*, 2015). Briefly, the CEL-Seq work flow entailed (1) reverse transcription (RT), (2) ExoI digestion, (3) SPRI purification (SPRIP), (4) Single strand synthesis, (5) T7 *in vitro* transcription linear Amplification, (7) SPRIP, (8) RNA Fragmentation, (9) SPRIP, (10) primer ligation, (11) RT, and (12) library enrichment PCR (Herring *et al*, 2018). Each sample was estimated to contain approximately 2,500 encapsulated cells. Following library preparation, the samples were sequenced using Nextseq 500 (Illumina) using a 150bp paired-end sequencing kit in a customized sequencing run (Herring *et al*, 2018). After sequencing, reads were filtered, sorted by their barcode of origin, and aligned to the reference transcriptome using the inDrops pipeline. Mapped reads were quantified into UMI-filtered counts per gene, and barcodes that correspond to cells were retrieved based on previously established methods (Klein *et al*, 2015). Overall, from approximately 2,500 encapsulated cells, approximately 1,800-2,000 cells were retrieved per sample.

Pre-processing and batch correction of scRNA-seq data

Datasets were filtered for cells with low library size or high mitochondrial gene expression (Klein *et al*, 2015). Filtered datasets for each replicate were analyzed using the Seurat pipeline (Stuart *et al*, 2018). Briefly, count matrices were log scale normalized followed by feature selection of highly variable genes. Canonical correlation analysis (CCA) was used to align replicates based on biological condition using dynamic time warping. Following subspace alignment, modularity optimization (0.8 resolution) was used to identify cell clusters. The ComBat algorithm (Chen *et al*, 2011) was then used to batch correct each gene on a per cluster basis. Visual assessment of alignment between replicates was performed using t-SNE analysis.

p-Creode mapping and trajectory analysis

The wildtype dataset, as well as the GSE92332 ileum dataset (Haber *et al*, 2017), were feature selected using the binned variance method and these gene features were used for all other conditions. Feature selected datasets were analyzed using the p-Creode algorithm (https://github.com/KenLauLab/pCreode) (Herring *et al*, 2018). For graph scoring, 100 independent runs were generated from each combined dataset. Overlay of normalized data was used to identify cell lineages and quantify tuft cell placement as “secretory” or “non-secretory.”

Trend analysis overview

Trend analysis was performed to identify gene expression changes in the AtohKO tuft cell lineage compared to the wildtype tuft cell lineage. 10 p-Creode resampled runs were used from the wildtype and AtohKO dataset. The following steps were performed for each p-Creode map:

(i) 2500 top genes over the tuft cell trajectory ranked by variance were selected from each of the wildtype and AtohKO datasets. The union of these gene sets was used for downstream analysis (3420 genes).

(ii) The dynamic trend of gene expression for each gene over the tuft cell trajectory was obtained by fitting a linear Generalized Additive Model (GAM) with a normal distribution and an identity link function using 10 splines (Servén & Brummitt, 2018). The fitted curves were then normalized between 0 and 1 for comparison between datasets.

(iii) For each gene trend, classification of its dynamics was performed by calculating its dynamic time warping distances to 12 reference trends. These categories were then broadly combined into 5 classes: (1) upward, (2) upward transitory, (3) downward transitory, (4) downward, and (5) flat.

(iv) For the coarse grain analysis, 3 trend classes were formed by combining (1) group 1 and 2 genes into “upward,” (2) group 3 and 4 genes into “downward,” and (3) flat.

(v) We scored the trend classification by consensus over 10 resampled runs (Herring *et al*, 2018) for both the (A) 5-trend and (B) 3-trend analysis. Genes with high consensus are those with a cumulative sum of 16 between the two classifications (for instance, a gene being grouped in the same trend in 8 out of 10 p-Creode replicates in the 5-trend analysis and in 8 out of 10 p-Creode replicates in the 3-trend analysis). This resulted in 2,004 high-consensus genes being used for downstream over-representation analysis

(vi) From the list of high consensus genes, we identified genes which switched from (A) wildtype group 4 to AtohKO group 1, 2, or 3, (B) wildtype group 3 to AtohKO group 1 or 2, or (C) wildtype group 2 to AtohKO group 1. Over-representation analysis, based on KEGG, Reactome pathway, and Wiki pathway datasets, of upregulated genes was performed in WebGestalt (http://www.webgestalt.org/).

(vii) Using 3-trend analysis, we identified genes that switched from wildtype group 2 (downward) to AtohKO group 1 (upward) and performed over-representation analysis.

Visualization and significance testing of trend analysis

Trend dynamics were plotted for enriched genes from the Reactome Pathway “Citric acid cycle (TCA cycle)” (https://reactome.org/content/detail/R-HSA-71403) gene list using Matlab software. Each gene plot included raw expression data from each wildtype or AtohKO p-Creode map and the trend line as an average of raw expression data aligned by dynamic time warping across all 10 resampled runs for each respective condition. For significance testing between wildtype and AtohKO trends, randomized classifications were generated for each gene in the wildtype and AtohKO condition. The null hypothesis stated that there was no consensus across the wildtype classifications or that there was no upward class switching from wildtype to AtohKO trajectories. Simulations comparing the randomized and observed classifications were performed 10,000 times to obtain a p-value score.

Gene set enrichment analysis (GSEA) of differential expression

Median difference in gene expression was calculated between wildtype and AtohKO tuft cells. GSEA (http://software.broadinstitute.org/gsea/index.jsp) of differential gene expression was performed to identify positively enriched pathways. Top 20 gene sets with the highest NES and most significant p-value were used for the further analysis. Relative expression in wildtype and AtohKO tuft cells of highly enriched genes was plotted using Prism Graphpad. GSEA and over-representation analysis for specific gene sets (KEGG, Reactome pathway, and Wiki pathways) was performed using WebGestalt (http://www.webgestalt.org/).

DNA extraction and 16s rRNA sequencing

Ileal luminal contents were collected fresh from tamoxifen- or vehicle-treated *Lrig1*$^{CreERT2/+}$*;Atoh1*$^{fl/fl}$ animals, as described above. All samples were collected on the same day and frozen in 2ml Eppendorf tubes (DNAse and RNAse free) at -80°C. Microbial genomic DNA extraction was performed using the PowerSoil DNA Isolation Kit (MO BIO Laboratories) (Zackular *et al*, 2016). Briefly, luminal contents were added to PowerBead Tubes and homogenized twice in a Bead Beater machine for 3 minutes with a 2min cool down in between homogenization. Samples were then processed as per the kit instructions and DNA was eluted into a sterile buffer. The V4 region of the 16s rRNA gene from each sample was amplified and sequenced by Georgia Genomics and Bioinformatics Core (http://dna.uga.edu) using the Illumina MiSeq Personal Sequencing platform (Zackular *et al*, 2014). Bioinformatics analysis of forward reads from 16s rRNA sequencing was performed using the Qiime2 software package (https://qiime2.org/).

Light chromatography-mass spectrometry (LC-MS) analysis of cecal luminal contents and whole cecal tissue

Tandem LC-MS analysis was performed by the Vanderbilt Mass Spectrometry Service Laboratory. Briefly, luminal contents were mixed in 1:1 MeOH/H_2O with 0.1% Formic acid per mg of content. Samples were processed as described previously prior to reconstitution in 2:1 ACN/H_2O with 250µM Tyr$^{13}C_2$/1mM Lactate ^{13}C (Marcobal *et al*, 2013). Cecal tissues were mixed in 10mM NH_4OAc in 9:1 H_2O/MeOH per mg of tissue and sonicated before being processed as previously described. An aliquot of PBS was processed and reconstituted as a negative control. O-benzylhydroxylamine (O-BHA) derivatization of common tricarboxylic acid intermediates was performed from both cecal luminal contents and tissues (Tan *et al*, 2014). Briefly, luminal filtrate was mixed in MeOH/H_2O with 0.1% Formic acid and added to Pyr $^{13}C_3$ (327µg/ml), EDC, and O-

BHA as described in the Sherwood protocol (Fensterheim *et al*, 2018). Tissue homogenates were processed similarly, and both were incubated at room temperature for 1hr prior to extraction with ethyl acetate. 100µl of luminal content sample (200mg/ml) or tissue sample (250mg/ml) was analyzed for specified metabolites and analyte response ratios were calculated using validated standards (Zhu *et al*, 2014).

Chapter VI

DISCUSSION AND FUTURE DIRECTIONS

Summary

This dissertation has shown that the application of single-cell approaches in examining cellular heterogeneity can be used to understand tissue-level function. In Chapter II, DISSECT-CyTOF, was used to demonstrate that acute TNF-α stimulation induced significant cell death in absorptive enterocytes but not secretory cell types, indicating that intestinal epithelial cells signal differentially to proinflammatory stimuli. Moreover, in the enterocyte population, there was an increase in both cell death and cell survival pathways, which might not have been identified using standard bulk analysis. Direct visualization of TNF-α-stimulated tissue showed that the divergent signaling behavior occurred in neighboring cells, such that dying cells were surrounded by pro-survival cells, creating a “rosette” pattern in the villi. This observation has broad impact on understanding how the intestinal epithelial tissue maintains its critical barrier function in response to inflammatory insult and, consequently, how it may be restored in chronic inflammatory disease.

Single-cell approaches can also be used to reveal new insights into fundamental cell development questions. In Chapter III, we performed multiplexed immunofluorescence (MxIF) imaging which allows us to preserve spatial resolution while querying multiple analytes in intestinal tissue, both in the epithelial (Herring *et al*, 2018) and immune (Maseda *et al*, 2018) compartment. To analyze the large datasets generated from this technique, our lab developed the novel cell differentiation mapping algorithm, p-Creode. Trajectory maps from the small intestinal epithelium demonstrated that chemosensory tuft cells do not originate from the same lineage as secretory goblet and Paneth cells. Instead small intestinal tuft cells share a lineage trajectory with the absorptive enterocytes. In the colon, however, we observed the reverse,

namely that tuft cells share a trajectory with secretory goblet cells rather than colonocytes. Computational analysis of single-cell data revealed an alternative route of differentiation for epithelial tuft cells and also highlighted regional differences in cell specification. To experimentally test this finding, we developed a genetic knockout model for *Atoh1*, the master secretory regulator, using the *Lrig1*^{CreERT2} driver. Unlike published models of intestinal epithelial cell specification, we observed that recombination of *Atoh1* increased tuft cell number throughout the small intestine; whereas, in the colon, tuft cells were lost, confirming our findings from p-Creode analysis. We confirmed using multiple markers that the small intestinal tuft cells in the AtohKO model expressed the same protein markers as wildtype tuft cells. We further validated our results by inducing *Atoh1* recombination with the more widely-used *Villin*^{CreERT2} driver (VilAtohKO). In VilAtohKO tissues, generated both by our lab and others, secretory Paneth and goblet cells were lost but tuft cell hyperplasia was observed in the small intestine (Herring *et al*, 2018), contrary to what had been published by other groups (Gerbe *et al*, 2009, 2011). We hypothesized that given the loss of barrier-regulating cells, the microbiome may play a role in inducing tuft cell hyperplasia in the AtohKO model and microbiome differences between facilities may have contributed to the original observation of tuft cell loss in the VilAtohKO model.

In the fourth chapter, we focused on the role of small intestinal tuft cells in inflammatory disease. We observed that, in the both human and mouse ileum, tuft cell specification was decreased in inflamed regions. Therefore, we hypothesized that increasing tuft cell numbers may ameliorate inflammation and we examined our AtohKO model to identify pathways that might drive tuft cell hyperplasia. For these studies, we elected to using scRNA-seq, rather than candidate-based approaches, such as CyTOF or MxIF. scRNA-seq allows for unsupervised analysis of gene expression changes between different conditions and does not require prior knowledge to build a marker panel. We confirmed that wildtype and AtohKO tuft cells expressed the canonical transcriptional signature, including *Trpm5*, *Gfi1β, Gnat3*, and *Alox5ap*, based on

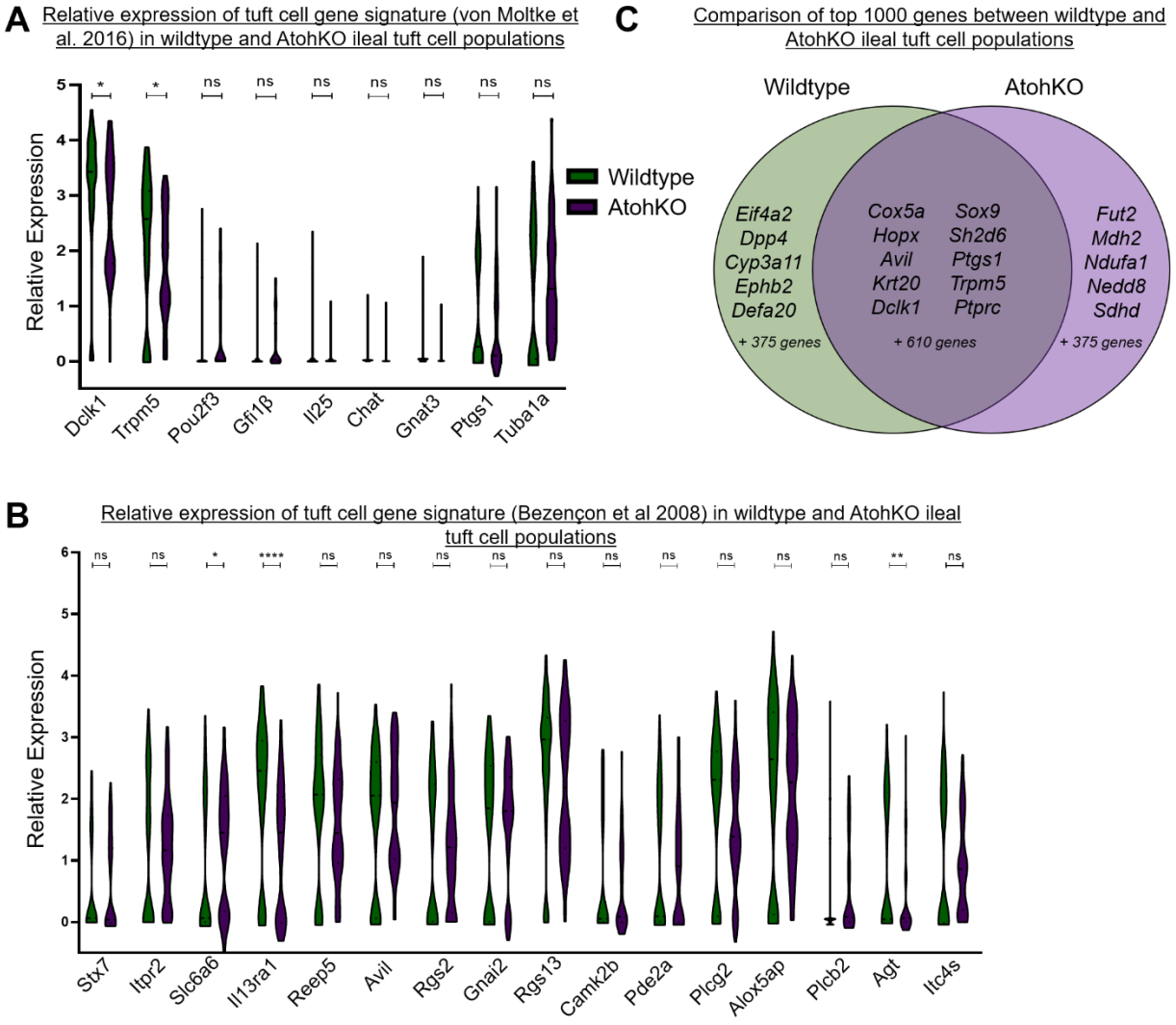

Figure 37. AtohKO tuft cells express a similar transcriptional signature as wildtype tuft cells. (A-B) Relative expression of tuft cell gene signature in small intestinal wildtype and AtohKO tuft cells. Selected genes were curated from published datasets. Expression data is generated from 58 wildtype (green) tuft cells (n = 4 replicates) and 64 AtohKO (magenta) tuft cells wildtype colonic tuft cells (n = 2 replicates). *p < 0.05, **p < 0.01, ****p < 0.001, and not significant (ns) by t-test. **(C)** Venn diagram depicting overlap between top 1,000 highly expressed genes in wildtype (green) and AtohKO (magenta) tuft cells.

previously published tuft cell studies (Figure 37A-B) (von Moltke *et al*, 2016; Bezençon *et al*, 2008). Moreover, there is significant overlap between the highest expressed genes between wildtype and AtohKO tuft cells (Figure 37C). Genes expressed in both datasets include known regulators of tuft cell specification while genes expressed in AtohKO but not wildtype tuft cells include TCA cycle genes (Figure 37C). We confirmed this finding by using p-Creode trend analysis and bulk differential analysis to demonstrate an increase in TCA cycle-related genes in AtohKO tuft cells, suggesting increased metabolic activity in this population. When we examined the microbiome of AtohKO animals, we confirmed that there were significant differences in various bacterial populations compared to wildtype littermates. Metabolite analysis demonstrated that the TCA cycle intermediate succinate was increased in the AtohKO lumen. Other publications had linked helminth-derived succinate to tuft cell hyperplasia in mouse models of acute parasitic infection. However, our work is the first demonstration of the commensal microbiome's ability to induce tuft cell hyperplasia through the release of succinate. Microbiome depletion decreased tuft cell hyperplasia as well as succinate levels in the AtohKO intestine, confirming that this phenotype was regulated through extrinsic, microbial-derived cues.

Finally, we wanted to therapeutically leverage tuft cell specification in the $TNF^{\Delta ARE/+}$ model of Crohn's-like ileitis by therapeutically administering succinate in animals with ileal disease. Prolonged succinate treatment in $TNF^{\Delta ARE/+}$animals resulted in increased tuft cell numbers and improved tissue organization compared to untreated controls. Immune cell infiltration and villus blunting were also decreased with succinate treatment while Paneth cell morphology was restored in epithelial crypts, indicative of decreased disease severity. Future work will expand on the mechanisms by which increased tuft cell specification can suppress inflammatory disease. In conclusion, this dissertation demonstrates that there is significant potential for the use of single-cell approaches, particularly scRNA-seq, to answer fundamental questions of cell differentiation and tissue biology. Moreover, single-cell approaches can provide a greater understanding of the

disease heterogeneity inherent within individual patients with CD and between different CD patients. Elucidating the molecular mechanisms driving CD may significantly impact clinical diagnostic and disease management practices allowing physicians to prescribe therapies based on a deeper understanding of the patient's unique disease. Ultimately, we hope that this leads to more effective treatments and better quality of care for CD patients. In the next section, I will expand on the future directions of the work described in this dissertation.

Future Directions

Elucidating the mechanism of tuft cell hyperplasia in the AtohKO model

In acute helminth infection models, tuft cell hyperplasia is dependent on ILC2s, which are activated by tuft cell-derived IL-25 (Howitt *et al*, 2016; von Moltke *et al*, 2016). Genetic knockout (Howitt *et al*, 2016) and antibody-based strategies (Hams *et al*, 2014) can be used to ablate or deplete ILC2s to determine whether this immune cell type is necessary for driving tuft cell hyperplasia in the AtohKO model. Based on the increased eosinophilia observed in the AtohKO small intestine (Figure 34F), we hypothesize activation of a type 2 immune response mediated by ILC2s could be a conserved mechanism for inducing tuft cell hyperplasia, even in the absence of helminth or eukaryotic infection. However, cytokine profiling can be used to determine whether type 2 cytokines are increased in the lamina propria of the AtohKO small intestine.

Additionally, it remains to be seen precisely what role the microbiome plays in the AtohKO model. We have confirmed that there is microbiome perturbation which is necessary for succinate production and tuft cell hyperplasia. However, our microbiome analysis has not linked increased production or decreased consumption of succinate to particular species differences in the AtohKO small intestine. Future studies could monocolonize germ-free AtohKO animals, which presumably lack tuft cells, with individual species to determine whether the bacteria alone can increase

succinate levels and induce tuft cell hyperplasia (Schneider *et al*, 2018). Furthermore, genetic approaches could be used to impair the bacterial mechanism controlling succinate production. We hypothesize that monocolonization with the null bacterial strain should block the ability to trigger tuft cell hyperplasia in a germ-free AtohKO animal. This series of experiments would more definitively demonstrate that commensal-derived succinate can drive increased tuft cell number. In the future, monocolonization of known succinate producers could be an effective therapy in IBD, similar to the effects of succinate in $TNF^{\Delta ARE/+}$ model.

In addition to microbiome sequencing, we can directly image the small intestine biomass using 16s FISH to characterize changes between luminal and mucosal adherent populations in the AtohKO compared to wildtype littermates (Vaishnava *et al*, 2012; Tomas *et al*, 2016). MUC2 staining confirmed the absence of goblet cells in AtohKO animals but histological examination has confirmed that this model does not develop spontaneous enteritis or colitis, unlike MUC2-deficient animals (Van der Sluis *et al*, 2006). This implies that compensatory mechanisms could substitute for barrier-promoting Paneth and goblet cells and imaging of the microbiome-epithelial interface could be used to determine whether the localization or abundance of bacterial species has altered with the loss of secretory cells. This would be an important question to answer in order to understand how microbe-host crosstalk impacts intestinal differentiation and function in the AtohKO model.

Succinate-induced suppression of inflammation in the $TNF^{\Delta ARE/+}$ model

Previous studies have shown that $TNF^{\Delta ARE/+}$ animals typically develop severe ileal inflammation by eight to ten weeks. Our work demonstrates that the therapeutic administration of succinate in $TNF^{\Delta ARE/+}$ mice post-disease onset can markedly improve tissue architecture in the distal ileum. We validated our histological analysis by staining for epithelial cell markers including

LYZ1+ Paneth cells, which are correlated to increased inflammation severity in the *TNF*$^{\Delta ARE/+}$ model as well as human disease (Schaubeck *et al*, 2015; VanDussen *et al*, 2014). Expression of epithelial LYZ1 is increased with succinate treatment as the normal intestinal crypt-villus axis is restored. Tuft cells, which we have shown in both human and mouse intestine to be inversely correlated to inflammation, are increased in *TNF*$^{\Delta ARE/+}$ animals treated with succinate. Future experiments are necessary to understand inflammation reversal in succinate-treated animals.

Inflammation in the *TNF*$^{\Delta ARE/+}$ ileum is characterized by an increase in type 1- and type 17-associated cytokines (Kontoyiannis *et al*, 2002; Roulis *et al*, 2011). In human IBD patients, helminth treatment and activation of a type 2 immune response can counteract type 1/type17 proinflammatory signaling (Broadhurst *et al*, 2010; Summers *et al*, 2005a, 2005b, 2003). Helminth infection models have demonstrated that the ILC2-tuft cell axis is activated by tuft cell chemosensation of parasitic-derived succinate (Lei *et al*, 2018; Nadjsombati *et al*, 2018; Schneider *et al*, 2018). Therefore, we hypothesized that exogenously administered succinate could induce tuft cell hyperplasia and trigger an anti-inflammatory immune response to counteract proinflammatory signaling in the *TNF*$^{\Delta ARE/+}$ mouse. Succinate administration markedly decreased immune cell infiltration and improved epithelial cell identity in the treated *TNF*$^{\Delta ARE/+}$ ileum. To investigate the mechanism of inflammation reversal, we will perform multiplexed cytokine profiling to query different classes of cytokines, including those associated with type 1 immunity, including TNF-α, type 17 immunity, such as IL-17, and type 2 immunity, such as IL-4 and IL-13 (Annunziato *et al*, 2015). We anticipate that untreated *TNF*$^{\Delta ARE/+}$ mice will have increased levels of type 1 and type 17 cytokines in comparison to wildtype littermates, indicative of increased disease severity (Schulz *et al*, 2014; Su *et al*, 2013). In succinate-treated *TNF*$^{\Delta ARE/+}$ animals we expect to observe a reduction in type 1 and type 17 cytokines and an increase in type 2 cytokines. We will confirm that succinate is responsible for increasing levels of type 2 cytokines by using succinate-treated wildtype animals as a positive control. However, additional experiments would be needed to more

conclusively show the interplay between the three classes of cytokines and how precisely type 2 immune cells and cytokines act to suppress type 1 and type 17 responses.

In addition, we will need to demonstrate that tuft cells are necessary for the observed effects of succinate treatment in *TNF*$^{\Delta ARE/+}$ animals. One approach to answering this question would be to generate a *TNF*$^{\Delta ARE/+}$ model which lacks tuft cells, for instance, by crossing these animals with *Pou2f3*$^{-/-}$ mice (Yamashita *et al*, 2017). As described in Chapter II, the *Pou2f3* transcription factor is a critical regulator of tuft cell specification in multiple epithelial tissues, including the small intestinal epithelium. In the absence of ileal tuft cells, *Pou2f3*$^{-/-}$;*TNF*$^{\Delta ARE/+}$ compound knockout mice may have worse disease than *Pou2f3*$^{+/+}$;*TNF*$^{\Delta ARE/+}$ littermates. Moreover, we hypothesize that compound knockout animals will be unresponsive to succinate due to the lack of tuft cell expression of *Sucnr1*, the gene encoding the succinate receptor (Schneider *et al*, 2018). In this model, succinate should neither increase tuft cell specification nor ameliorate symptoms of ileal inflammation. Alternatively, if our hypothesis is incorrect and these compound knockout mice are responsive to succinate, this may indicate that succinate can signal through a different receptor on a different cell type. However, we believe this to be unlikely, since others have demonstrated that SUCNR1 is the critical succinate sensor (Lei *et al*, 2018) and our own scRNA-seq confirms that *Sucnr1* is significantly enriched in tuft cells (Figure 38A) (Bezençon *et al*, 2008). Nevertheless, compensatory mechanisms may exist and allow succinate to act through succinate consuming bacterial species or otherwise shift the *TNF*$^{\Delta ARE/+}$ microbiome towards a less dysbiotic state and dampen inflammation even in the absence of tuft cells (Spiga *et al*, 2017). While we believe this outcome to be unlikely, ultimately, this experiment might help determine if tuft cell increase is a viable option to decrease inflammation in the *TNF*$^{\Delta ARE/+}$ model.

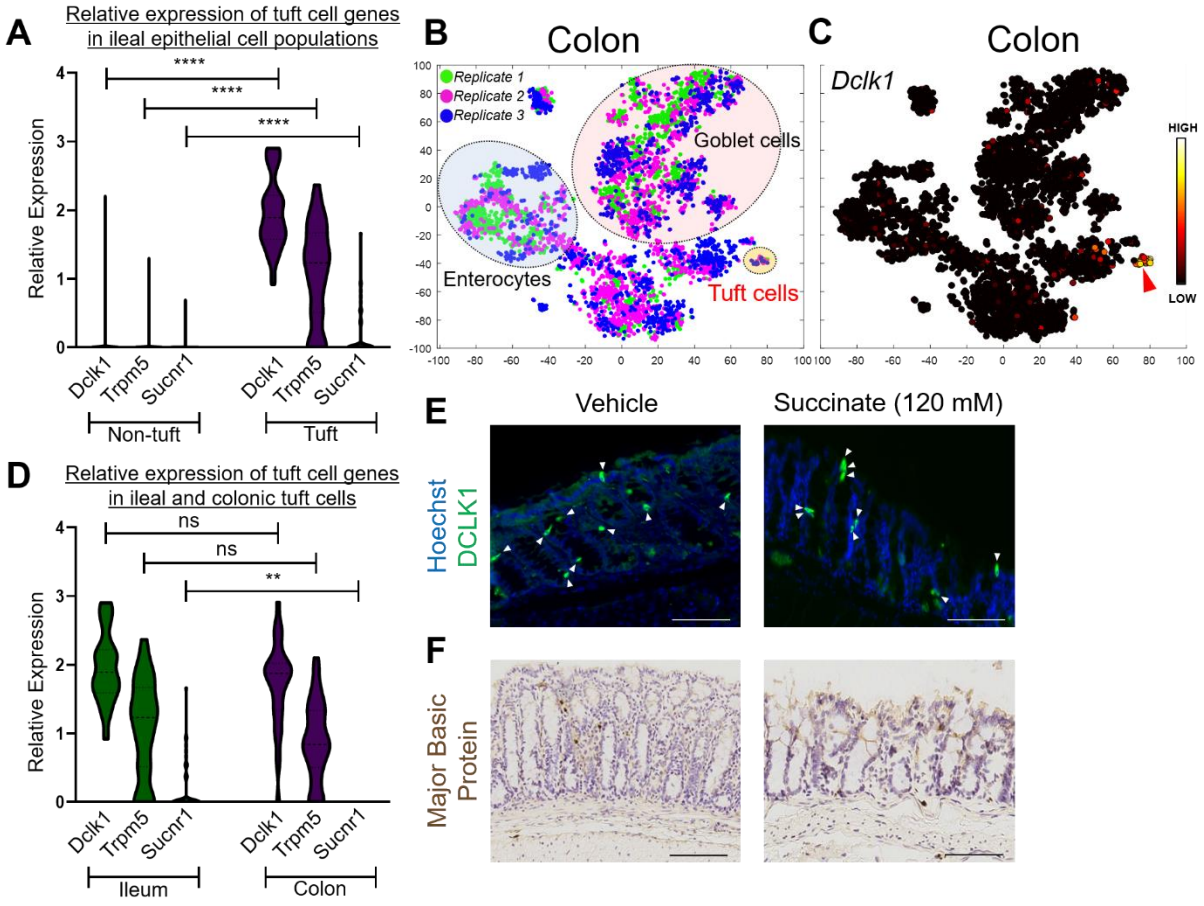

Figure 38. Colonic tuft cells do not express the succinate-sensing receptor, *Sucnr1*. (A) Quantification of relative expression of *Dclk1*, *Trpm5,* and *Sucnr1* in non-tuft (green) and tuft (magenta) cells from the wildtype ileal epithelium. Expression data is generated from 4,550 non-tuft cells and 58 tuft cells (n = 4 wildtype replicates). **(B)** t-SNE analysis of wildtype colonic scRNA-seq dataset consisting of 4,124 datapoints. Manual annotation of the t-SNE plot demonstrates the absence of segregation in datapoints from three biological replicates (Rep. 1 – green, Rep. 2 – magenta, and Rep. 3 – blue). Each datapoint represents a single cell. The enterocyte (blue), goblet cell (red), and tuft cell (orange) populations are manually annotated. **(C)** Overlay of ArcSinh-scaled *Dclk1* expression data on t-SNE plot of scRNA-seq data generated from the wildtype colonic epithelium. **(D)** Quantification of relative expression of *Dclk1*, *Trpm5*, and *Sucnr1* in ileal (green) and colonic (magenta) tuft cells. Expression data is generated from 58 wildtype tuft cells (n = 4 ileal replicates) and 32 wildtype colonic tuft cells (n = 3 colonic replicates). **p < 0.01, not significant (ns) by t-test. **(E)** Immunofluorescence imaging of DCLK1 (green) vehicle and succinate-treated colonic epithelium. Hoechst (blue) denotes nuclei and white arrows denote tuft cells. Scale bar = 100 µm. **(F)** Immunohistochemistry staining of major basic protein in vehicle and succinate-treated colonic epithelium. Blue denotes nuclei and brown represents the counterstain. Scale bar = 100µm.

Leveraging tuft cells therapeutically in the treatment of Crohn's disease

While we have observed that succinate can suppress inflammation in the *TNF*$^{\Delta ARE/+}$ model, there is still a certain level of heterogeneity in response. Some succinate-treated *TNF*$^{\Delta ARE/+}$ animals have uniform decrease in inflammation, while others have regions of response with increased tuft cell number and improved tissue organization as well as non-response with few tuft cells and characteristic villus blunting. While this finding further supports the correlation between inflammation and tuft cell number, it also demonstrates that there is a degree of stochasticity in succinate dosage and efficacy. To control for dosing effects, it would be better to develop a compound or small molecule which can be delivered uniformly with minimal variation between biological replicates. Furthermore, succinate-driven tuft cell hyperplasia relies on the immune population to drive tuft cell specification (Schneider *et al*, 2018; Lei *et al*, 2018; Nadjsombati *et al*, 2018). To avoid off-target effects, it may be beneficial to develop a compound that relies on cell intrinsic or epithelial-driven mechanisms to induce tuft cell hyperplasia.

Therefore, we could use human-derived enteroids, grown in a Matrigel scaffold, to screen compound libraries for molecules that can increase tuft cell number. We have robust markers for human tuft cells, including pEGFR and COX2, that can be used to assay for changes in tuft cell numbers. Potential drug candidates can be validated in AtohKO enteroids, which lack tuft cells, to verify their ability to intrinsically drive tuft cell specification, independent of any microbiome or immune contribution. Further validation could be performed by treating ileal enteroids grown from CD patients and observing the effects on epithelial morphology and cell identity markers. Similar approaches have been employed in the cancer therapeutics field via patient-derived xenografts and tumoroids with considerable success (Finnberg *et al*, 2017). Succinate treatment of *TNF*$^{\Delta ARE/+}$ animals serves as a robust positive control for what pathways could be modulated to increase tuft cell number and, potentially, suppress disease development.

Thus far, we have only looked at the effects of succinate in the *TNF*$^{\Delta ARE/+}$ model and we plan to replicate our findings in other models of intestinal inflammation but, as discussed in Chapter I, selecting the correct animal model is an important consideration. Besides the *TNF*$^{\Delta ARE/+}$model, the only other well-established model of small intestinal inflammation is the SAMP1/YitFC animal developed by Fabio Cominelli's group (Pizarro *et al*, 2011; Bamias *et al*, 2005). This animal develops spontaneous enteritis at ten weeks of age and is characterized by increased Th1 and Th2 signaling (Bamias *et al*, 2005). Experiments in this mouse are complicated by the difficulty in maintaining a colony and differing disease etiology from the *TNF*$^{\Delta ARE/+}$ model. Inflammation can also be induced via chemical means, such as dextran sulfate sodium (DSS) (Okayasu *et al*, 1990), or T-cell blockade using anti-CD3e (Miura *et al*, 2005; Farin *et al*, 2014) or anti-CD40 (Kumar *et al*, 2017) antibodies, which can cause severe diarrhea, weight loss, and immune cell response. However, these strategies are more akin to short-term injury models and are not comparable to long-term models of chronic inflammation (Kumar *et al*, 2017). Therefore, succinate treatment in these models may not be able to suppress inflammation in the timespan of injury and inflammation development. Furthermore, DSS and anti-CD40 damage the colon mucosa and are better suited to model colitis rather than ileitis (Okayasu *et al*, 1990; Kumar *et al*, 2017). Moreover, succinate may not be able to ameliorate colitis symptoms in the aforementioned model since published work from our group and others have demonstrated that small and large intestinal tuft cells may have different modes of specification, leading to differing function (Herring *et al*, 2018; McKinley *et al*, 2017a). Thus far, tuft cell hyperplasia in response to helminth infection appears to be specific to the small intestine (Howitt *et al*, 2016; von Moltke *et al*, 2016; Gerbe *et al*, 2016), although *Trichuris suis*, a helminth endemic to developing countries, has been proposed as a therapy for ulcerative colitis (Summers *et al*, 2005b). We examined scRNA-seq data from the murine colonic epithelium to investigate gene expression differences between ileal and colonic tuft cells (Figure 38B-C). As in the ileal tuft cells, colonic tuft cells express high levels of *Dclk1* and *Trpm5* (Figure 38D). However, unlike ileal tuft cells, the succinate receptor gene *Sucnr1* was

not highly expressed in colonic tuft cells (Figure 38D). When we administered succinate to wildtype animals, we did not observe a significant difference in colonic tuft cell number (Figure 38E), compared to ileal tissue (Figure 34G). MBP+ staining was not increased in succinate-treated colonic tissue (Figure 38F). This suggests that colonic tuft cells, unlike their small intestinal counterparts, cannot sense succinate, indicating that the latter may not be capable of ameliorating colonic inflammation.

Tuft cells connect the epithelial, immune, and microbiome systems in the intestine and, therefore, present an intriguing target for novel CD diagnostic or therapeutic approaches. Chemosensory mechanisms enable tuft cells to sense luminal perturbation and induce an immune response, which means that modulation of this cell type could shift the balance between health and disease. There is also a benefit in leveraging the patient's own immune response to act in an anti-inflammatory manner rather than relying on externally administered biologics to suppress inflammation. In theory, we may observe fewer off-target effects or complications from treatment. While this remains speculative, there is great potential in the tuft cell field to significantly impact both our basic understanding of host-microbiome crosstalk and also improve CD care.

REFERENCES

1. Adam M, Potter AS & Potter SS (2017) Psychrophilic proteases dramatically reduce single-cell RNA-seq artifacts: a molecular atlas of kidney development.
2. Adolph TE, Tomczak MF, Niederreiter L, Ko H-J, Bock J, Martinez-Naves E, Glickman JN, Tschurtschenthaler M, Hartwig J, Shuhei H, Flak MB, Cusick JL, Kohno K, Iwawaki T, Billmann-born S, Raine T, Bharti R, Lucius R, Kweon M, Marciniak SJ, et al (2014) Paneth cells as a site of origin for intestinal inflammation. *Nature* **503:** 272–276
3. Aladegbami B, Barron L, Bao J, Colasanti J, Erwin CR, Warner BW & Guo J (2017) Epithelial cell specific Raptor is required for initiation of type 2 mucosal immunity in small intestine. *Sci. Rep.* **7:** 5580
4. Allen JE & Sutherland TE (2014) Host protective roles of type 2 immunity: parasite killing and tissue repair, flip sides of the same coin. *Semin. Immunol.* **26:** 329–340
5. Amir E-AD, Davis KL, Tadmor MD, Simonds EF, Levine JH, Bendall SC, Shenfeld DK, Krishnaswamy S, Nolan GP & Pe'er D (2013) viSNE enables visualization of high dimensional single-cell data and reveals phenotypic heterogeneity of leukemia. *Nat. Biotechnol.* **31:** 545–52
6. Anchang B, Hart TDP, Bendall SC, Qiu P, Bjornson Z, Linderman M, Nolan GP & Plevritis SK (2016) Visualization and cellular hierarchy inference of single-cell data using SPADE. *Nat. Protoc.* **11:** 1264–1279
7. Angelo M, Bendall SC, Finck R, Hale MB, Hitzman C, Borowsky AD, Levenson RM, Lowe JB, Liu SD, Zhao S, Natkunam Y & Nolan GP (2014) Multiplexed ion beam imaging of human breast tumors. *Nat. Med.* **20:** 436–42
8. Annunziato F, Romagnani C & Romagnani S (2015) The 3 major types of innate and adaptive cell-mediated effector immunity. *J. Allergy Clin. Immunol.* **135:** 626–635
9. Antoni L, Nuding S, Wehkamp J & Stange EF (2014) Intestinal barrier in inflammatory bowel disease. *World J. Gastroenterol.* **20:** 1165–79
10. Arpaia N, Campbell C, Fan X, Dikiy S, van der Veeken J, deRoos P, Liu H, Cross JR, Pfeffer K, Coffer PJ & Rudensky AY (2013) Metabolites produced by commensal bacteria promote peripheral regulatory T-cell generation. *Nature* **504:** 451–5
11. Atuma C, Strugala V, Allen a & Holm L (2001) The adherent gastrointestinal mucus gel layer: thickness and physical state in vivo. *Am. J. Physiol. Gastrointest. Liver Physiol.* **280:** G922-9
12. Bamias G, Dahman MI, Arseneau KO, Guanzon M, Gruska D, Pizarro TT & Cominelli F (2013) Intestinal-specific TNFα overexpression induces Crohn's-like ileitis in mice. *PLoS One* **8:** e72594
13. Bamias G, Martin C, Mishina M, Ross WG, Rivera-Nieves J, Marini M & Cominelli F (2005) Proinflammatory effects of TH2 cytokines in a murine model of chronic small intestinal inflammation. *Gastroenterology* **128:** 654–66
14. Barker N, van Es JH, Kuipers J, Kujala P, van den Born M, Cozijnsen M, Haegebarth A, Korving J, Begthel H, Peters PJ & Clevers H (2007) Identification of stem cells in small intestine and colon by marker gene Lgr5. *Nature* **449:** 1003–1007
15. Barrett JC, Hansoul S, Nicolae DL, Cho JH, Duerr RH, Rioux JD, Brant SR, Silverberg MS, Taylor KD, Michael M, Bitton A, Dassopoulos T, Datta LW, Green T, Griffiths M, Kistner EO, Murtha MT, Regueiro MD, Jerome I, Schumm LP, et al (2009) Genome-wide association defines more than 30 distinct susceptibility loci for CD. **40:** 955–962
16. Barthel C, Spalinger MR, Brunner J, Lang S, Fried M, Rogler G & Scharl M (2014) A distinct pattern of disease-associated single nucleotide polymorphisms in IBD risk genes in a family with Crohn's disease. *Eur. J. Gastroenterol. Hepatol.* **26:** 803–6
17. Bastide P, Darido C, Pannequin J, Kist R, Robine S, Marty-Double C, Bibeau F, Scherer G, Joubert D, Hollande F, Blache P & Jay P (2007) Sox9 regulates cell proliferation and is required for Paneth cell differentiation in the intestinal epithelium. *J. Cell Biol.* **178:** 635–648

18. Bates MD, Erwin CR, Sanford LP, Wiginton D, Bezerra JA, Schatzman LC, Jegga AG, Ley-Ebert C, Williams SS, Steinbrecher KA, Warner BW, Cohen MB & Aronow BJ (2002) Novel genes and functional relationships in the adult mouse gastrointestinal tract identified by microarray analysis. *Gastroenterology* **122:** 1467–1482
19. Batlle E, Henderson JT, Beghtel H, van den Born MMW, Sancho E, Huls G, Meeldijk J, Robertson J, van de Wetering M, Pawson T & Clevers H (2002) Beta-catenin and TCF mediate cell positioning in the intestinal epithelium by controlling the expression of EphB/ephrinB. *Cell* **111:** 251–63
20. Baum B & Georgiou M (2011) Dynamics of adherens junctions in epithelial establishment, maintenance, and remodeling. *J. Cell Biol.* **192:** 907–917
21. Behjati S, Huch M, van Boxtel R, Karthaus W, Wedge DC, Tamuri AU, Martincorena I, Petljak M, Alexandrov LB, Gundem G, Tarpey PS, Roerink S, Blokker J, Maddison M, Mudie L, Robinson B, Nik-Zainal S, Campbell P, Goldman N, van de Wetering M, et al (2014) Genome sequencing of normal cells reveals developmental lineages and mutational processes. *Nature* **513:** 422–425
22. Bellono NW, Bayrer JR, Leitch DB, Brierley SM, Ingraham HA, Julius D, Castro J, Zhang C & O 'donnell TA (2017) Enterochromaffin Cells Are Gut Chemosensors that Couple to Sensory Neural Pathways. *Cell* **170:** 185–198.e16
23. Bendall SC, Davis KL, Amir EAD, Tadmor MD, Simonds EF, Chen TJ, Shenfeld DK, Nolan GP & Pe'Er D (2014) Single-cell trajectory detection uncovers progression and regulatory coordination in human b cell development. *Cell* **157:** 714–725
24. Bendall SC, Simonds EF, Qiu P, Amir ED, Krutzik PO, Finck R, Bruggner R V, Melamed R, Trejo A, Ornatsky OI, Balderas RS, Plevritis SK, Sachs K, Pe'er D, Tanner SD & Nolan GP (2011) Single-cell mass cytometry of differential immune and drug responses across a human hematopoietic continuum. *Science* **332:** 687–96
25. Bezençon C, le Coutre J & Damak S (2007) Taste-signaling proteins are coexpressed in solitary intestinal epithelial cells. *Chem. Senses* **32:** 41–49
26. Bezençon C, Fürholz A, Raymond F, Mansourian R, Métairon S, Le Coutre J & Damak S (2008) Murine intestinal cells expressing Trpm5 are mostly brush cells and express markers of neuronal and inflammatory cells. *J. Comp. Neurol.* **509:** 514–525
27. Bhatt AS, Freeman SS, Herrera AF, Pedamallu CS, Gevers D, Duke F, Jung J, Michaud M, Walker BJ, Young S, Earl AM, Kostic AD, Ojesina AI, Hasserjian R, Ballen KK, Chen Y-B, Hobbs G, Antin JH, Soiffer RJ, Baden LR, et al (2013) Sequence-based discovery of Bradyrhizobium enterica in cord colitis syndrome. *N. Engl. J. Med.* **369:** 517–28
28. Bian ZM, Elner SG, Yoshida a, Kunkel SL, Su J & Elner VM (2001) Activation of p38, ERK1/2 and NIK pathways is required for IL-1beta and TNF-alpha-induced chemokine expression in human retinal pigment epithelial cells. *Exp. Eye Res.* **73:** 111–121
29. Bibiloni R, Fedorak RN, Tannock GW, Madsen KL, Gionchetti P, Campieri M, De Simone C & Sartor RB (2005) VSL#3 Probiotic-Mixture Induces Remission in Patients with Active Ulcerative Colitis. *Am. J. Gastroenterol.* **100:** 1539–46
30. Bjerknes M & Cheng H (2006) Neurogenin 3 and the enteroendocrine cell lineage in the adult mouse small intestinal epithelium. *Dev. Biol.***:** 722–35
31. Bjerknes M, Khandanpour C, Möröy T, Fujiyama T, Hoshino M, Klisch TJ, Ding Q, Gan L, Wang J, Martín MG & Cheng H (2012) Origin of the brush cell lineage in the mouse intestinal epithelium. *Dev. Biol.* **362:** 194–218
32. Bohórquez D V., Samsa LA, Roholt A, Medicetty S, Chandra R, Liddle RA, Bohó Rquez D V, Samsa LA, Roholt A, Medicetty S, Chandra R, Liddle RA & Klymkowsky M (2014) An Enteroendocrine Cell – Enteric Glia Connection Revealed by 3D Electron Microscopy. *PLoS One* **9:** e89881
33. Booth C, Tudor G, Tudor J, Katz BP & Macvittie T (2012) The Acute Gastrointestinal Syndrome in High-Dose Irradiated Mice. *Heal. Physiol.* **103:** 383–99

34. Boyapati R, Satsangi J & Ho G-T (2015) Pathogenesis of Crohn's disease. *F1000Prime Rep.* **7:** 44
35. Boyd-Tressler A, Penuela S, Laird DW & Dubyak GR (2014) Chemotherapeutic Drugs Induce ATP Release via Caspase-gated Pannexin-1 Channels and a Caspase/Pannexin-1-Independent Mechanism. *J. Biol. Chem.*
36. Broadhurst MJ, Leung JM, Kashyap V, McCune JM, Mahadevan U, McKerrow JH & Loke P (2010) IL-22+ CD4+ T cells are associated with therapeutic trichuris trichiura infection in an ulcerative colitis patient. *Sci. Transl. Med.* **2:** 60ra88
37. Buczacki SJA, Zecchini HI, Nicholson AM, Russell R, Vermeulen L, Kemp R & Winton DJ (2013) Intestinal label-retaining cells are secretory precursors expressing Lgr5. *Nature* **495:** 65–69
38. Burton P (2009) Genome-wide association study of 14,000 cases of seven common diseases and 3,000 shared controls. **447:** 661–678
39. Cadwell K, Liu J, Brown SL, Miyoshi H, Loh J, Lennerz J, Kishi C, Kc W, Carrero JA, Hunt S, Stone C, Brunt M, Xavier RJ, Sleckman BP, Li E, Mizushima N, Stappenbeck S & Iv HWV (2009) A unique role for autophagy and Atg16L1 in Paneth cells in murine and human intestine. *Nature* **456:** 259–263
40. Caprilli R (2008) Why does Crohn's disease usually occur in terminal ileum? *J. Crohn's Colitis* **2:** 352–356
41. Carmody RN, Gerber GK, Luevano JM, Gatti DM, Somes L, Svenson KL, Turnbaugh PJ & Turnbaugh PJ (2015) Diet dominates host genotype in shaping the murine gut microbiota. *Cell Host Microbe* **17:** 72–84
42. Chandrakesan P, May R, Qu D, Weygant N, Taylor VE, Li JD, Ali N, Sureban SM, Qante M, Wang TC, Bronze MS & Houchen CW (2015) Dclk1 + small intestinal epithelial tuft cells display the hallmarks of quiescence and self-renewal. *Oncotarget* **6:**
43. Chandrakesan P, May R, Weygant N, Qu D, Berry WL, Sureban SM, Ali N, Rao C, Huycke M, Bronze MS & Houchen CW (2016) Intestinal tuft cells regulate the ATM mediated DNA Damage response via Dclk1 dependent mechanism for crypt restitution following radiation injury. *Sci. Rep.* **6:** 37667
44. Chaudhary R & Ghosh S (2005) Infliximab in refractory coeliac disease. *Eur. J. Gastroenterol. Hepatol.* **17:** 603–604
45. Chen C, Grennan K, Badner J, Zhang D, Gershon E, Jin L & Liu C (2011) Removing batch effects in analysis of expression microarray data: an evaluation of six batch adjustment methods. *PLoS One* **6:** e17238
46. Cheng H & Leblond CP (1974a) Origin, differentiation and renewal of the four main epithelial cell types in the mouse small intestine V. Unitarian theory of the origin of the four epithelial cell types. *Am. J. Anat.* **141:** 537–561
47. Cheng H & Leblond CP (1974b) Origin, differentiation and renewal of the four main epithelial cell types in the mouse small intestine. I. Columnar cell. *Am. J. Anat.* **141:** 461–79
48. Chung H, Pamp SJ, Hill JA, Surana NK, Edelman SM, Troy EB, Reading NC, Villablanca EJ, Wang S, Mora JR, Umesaki Y, Mathis D, Benoist C, Relman DA & Kasper DL (2012) Gut immune maturation depends on colonization with a host-specific microbiota. *Cell* **149:** 1578–93
49. Clevers HC & Bevins CL (2013) Paneth cells: maestros of the small intestinal crypts. *Annu. Rev. Physiol.* **75:** 289–311
50. Cohn SM, Schloemann S, Tessner T, Seibert K & Stenson WF (1997) Crypt Stem Cell Survival in the Mouse Intestinal Epithelium Is Regulated by Prostaglandins Synthesized through Cyclooxygenase-1. *J. Clin. Invest* **99:** 1367–1379
51. Colgan SP (2016) Targeting Hypoxia in Inflammatory Disease. *J. Investig. Med.* **64:** 364–368
52. Colombel JF, Sandborn WJ, Reinisch W, Mantzaris GJ, Kornbluth A, Rachmilewitz D, Lichtiger S, D'Haens G, Diamond RH, Broussard DL, Tang KL, van der Woude CJ & Rutgeerts

P (2010) Infliximab, azathioprine, or combination therapy for Crohn's disease. *N. Engl. J. Med.* **362:** 1383–1395
53. Conn PM (2013) Animal models for the study of human disease
54. Creamer B, Shorter RG & Bamforth J (1961) The turnover and shedding of epithelial cells Part I The turnover in the gastro-intestinal tract. *Gut* **2:**
55. Crespo M, Vilar E, Tsai S-Y, Chang K, Amin S, Srinivasan T, Zhang T, Pipalia NH, Chen HJ, Witherspoon M, Gordillo M, Xiang JZ, Maxfield FR, Lipkin S, Evans T & Chen S (2017) Colonic organoids derived from human induced pluripotent stem cells for modeling colorectal cancer and drug testing. *Nat. Med.*
56. D. H & Drenckhahn D (1998) Identification of the taste cell G-protein alpha-gustducin, in brush of the rat pancreatic duct system. *Histochem. Cell Biol.* **110:** 303–9
57. Darwich AS, Aslam U, Ashcroft DM & Rostami-Hodjegan A (2014) Meta-analysis of the turnover of intestinal epithelia in preclinical animal species and humans. *Drug Metab. Dispos.* **42:** 2016–22
58. Dekaney CM, Gulati AS, Garrison AP, Helmrath MA & Henning SJ (2009) Regeneration of intestinal stem/progenitor cells following doxorubicin treatment of mice. *Am. J. Physiol. Gastrointest. Liver Physiol.* **297:** G461-70
59. Deuring JJ, Fuhler GM, Konstantinov SR, Peppelenbosch MP, Kuipers EJ, de Haar C & van der Woude CJ (2014) Genomic ATG16L1 risk allele-restricted Paneth cell ER stress in quiescent Crohn's disease. *Gut* **63:** 1081–91
60. DiMaio MF, Dische R, Gordon RE & Kattan M (1988) Alveolar brush cells in an infant with desquamative interstitial pneumonitis. *Pediatr. Pulmonol.* **4:** 185–91
61. Donaldson GP, Melanie Lee S & Mazmanian SK (2015) Gut biogeography of the bacterial microbiota.
62. Donohoe DR, Collins LB, Wali A, Bigler R, Sun W & Bultman SJ (2012) The Warburg effect dictates the mechanism of butyrate-mediated histone acetylation and cell proliferation. *Mol. Cell* **48:** 612–26
63. Drost J, van Boxtel R, Blokzijl F, Mizutani T, Sasaki N, Sasselli V, de Ligt J, Behjati S, Grolleman JE, van Wezel T, Nik-Zainal S, Kuiper RP, Cuppen E & Clevers H (2017) Use of CRISPR-modified human stem cell organoids to study the origin of mutational signatures in cancer. *Science*
64. Drost J & Clevers H (2017) Translational applications of adult stem cell-derived organoids. *Development* **144:** 968–975
65. Drost J, van Jaarsveld RH, Ponsioen B, Zimberlin C, van Boxtel R, Buijs A, Sachs N, Overmeer RM, Offerhaus GJ, Begthel H, Korving J, van de Wetering M, Schwank G, Logtenberg M, Cuppen E, Snippert HJ, Medema JP, Kops GJPL & Clevers H (2015) Sequential cancer mutations in cultured human intestinal stem cells. *Nature* **521:** 43–47
66. Durand A, Donahue B, Peignon G, Letourneur F, Cagnard N, Slomianny C, Perret C, Shroyer NF & Romagnolo B (2012) Functional intestinal stem cells after Paneth cell ablation induced by the loss of transcription factor Math1 (Atoh1). *Proc. Natl. Acad. Sci. U. S. A.* **109:** 8965–70
67. Engelstoft MS, Lund ML, Grunddal K V, Egerod KL, Osborne-Lawrence S, Poulsen SS, Zigman JM & Schwartz TW (2015) Research Resource: A Chromogranin A Reporter for Serotonin and Histamine Secreting Enteroendocrine Cells. *Mol. Endocrinol.* **29:** 1658–71
68. Erben U, Loddenkemper C, Spieckermann S, Heimesaat MM, Siegmund B & Kühl AA (2016) Histomorphology of intestinal inflammation in inflammatory bowel diseases (IBD) mouse models and its relevance for IBD in men
69. van Es JH, van Gijn ME, Riccio O, van den Born M, Vooijs M, Begthel H, Cozijnsen M, Robine S, Winton DJ, Radtke F & Clevers H (2005) Notch/gamma-secretase inhibition turns proliferative cells in intestinal crypts and adenomas into goblet cells. *Nature* **435:** 959–63
70. van Es JH, Sato T, van de Wetering M, Lyubimova A, Nee ANY, Gregorieff A, Sasaki N, Zeinstra L, van den Born M, Korving J, Martens ACM, Barker N, van Oudenaarden A &

Clevers H (2012) Dll1+ secretory progenitor cells revert to stem cells upon crypt damage. *Nat. Cell Biol.* **14:** 1099–104
71. Escobar M, Nicolas P, Sangar F, Laurent-Chabalier S, Clair P, Joubert D, Jay P & Legraverend C (2011) Intestinal epithelial stem cells do not protect their genome by asymmetric chromosome segregation. *Nat. Commun.* **2:** 258
72. Farin HF, Jordens I, Mosa MH, Basak O, Korving J, Tauriello DVF, De Punder K, Angers S, Peters PJ, Maurice MM & Clevers H (2016) Visualization of a short-range Wnt gradient in the intestinal stem-cell niche.
73. Farin HF, Karthaus WR, Kujala P, Rakhshandehroo M, Schwank G, Vries RGJ, Kalkhoven E, Nieuwenhuis EES & Clevers H (2014) Paneth cell extrusion and release of antimicrobial products is directly controlled by immune cell-derived IFN-γ. *J. Exp. Med.* **211:** 1393–405
74. Feng Y, Yao Z & Klionsky DJ (2015) How to control self-digestion: transcriptional, post-transcriptional, and post-translational regulation of autophagy. *Trends Cell Biol.* **25:** 354–363
75. Fensterheim BA, Young JD, Luan L, Kleinbard RR, Stothers CL, Patil NK, McAtee-Pereira AG, Guo Y, Trenary I, Hernandez A, Fults JB, Williams DL, Sherwood ER & Bohannon JK (2018) The TLR4 Agonist Monophosphoryl Lipid A Drives Broad Resistance to Infection via Dynamic Reprogramming of Macrophage Metabolism. *J. Immunol.* **200:** 3777–3789
76. Finck R, Simonds EF, Jager A, Krishnaswamy S, Sachs K, Fantl W, Pe'er D, Nolan GP & Bendall SC (2013) Normalization of mass cytometry data with bead standards. *Cytometry. A* **83:** 483–94
77. Finnberg NK, Gokare P, Lev A, Grivennikov SI, MacFarlane AW, Campbell KS, Winters RM, Kaputa K, Farma JM, Abbas AE-S, Grasso L, Nicolaides NC, El-Deiry WS & El-Deiry WS (2017) Application of 3D tumoroid systems to define immune and cytotoxic therapeutic responses based on tumoroid and tissue slice culture molecular signatures. *Oncotarget* **8:** 66747–66757
78. van der Flier LG & Clevers H (2009) Stem cells, self-renewal, and differentiation in the intestinal epithelium. *Annu. Rev. Physiol.* **71:** 241–60
79. van der Flier LG, van Gijn ME, Hatzis P, Kujala P, Haegebarth A, Stange DE, Begthel H, van den Born M, Guryev V, Oving I, van Es JH, Barker N, Peters PJ, van de Wetering M & Clevers H (2009) Transcription Factor Achaete Scute-Like 2 Controls Intestinal Stem Cell Fate. *Cell* **136:** 903–912
80. Foliguet B & Grignon G (1980) Type III pneumocyte: the alveolar brush-border cell in rat. *Poumon le coeur* **36:** 149–153
81. Foulke-Abel J, In J, Kovbasnjuk O, Zachos NC, Ettayebi K, Blutt SE, Hyser JM, Zeng X-L, Crawford SE, Broughman JR, Estes MK & Donowitz M (2014) Human enteroids as an ex-vivo model of host-pathogen interactions in the gastrointestinal tract. *Exp. Biol. Med. (Maywood).*
82. Fre S, Huyghe M, Mourikis P, Robine S & Louvard D (2005) Notch signals control the fate of immature progenitor cells in the intestine. *Nature* **435:**
83. Furusawa Y, Obata Y, Fukuda S, Endo TA, Nakato G, Takahashi D, Nakanishi Y, Uetake C, Kato K, Kato T, Takahashi M, Fukuda NN, Murakami S, Miyauchi E, Hino S, Atarashi K, Onawa S, Fujimura Y, Lockett T, Clarke JM, et al (2013) Commensal microbe-derived butyrate induces the differentiation of colonic regulatory T cells.
84. Garabedian EM, Roberts LJJ, McNevin MS & Gordon JI (1997) Examining the Role of Paneth Cells in the Small Intestine by Lineage Ablation in Transgenic Mice. *J. Biol. Chem.* **272:** 23729–23740
85. Gebert a, al-Samir K, Werner K, Fassbender S & Gebhard a (2000) The apical membrane of intestinal brush cells possesses a specialised, but species-specific, composition of glycoconjugates--on-section and in vivo lectin labelling in rats, guinea-pigs and mice. *Histochem. Cell Biol.* **113:** 389–399
86. Genander M, Halford MM, Xu N-J, Eriksson M, Yu Z, Qiu Z, Martling A, Greicius G, Chumley MJ, Zdunek S, Wang C, Holm T, Goff SP, Pettersson S, Pestell RG, Henkemeyer M & Frisén

J (2009) Dissociation of EphB2 signaling pathways mediating progenitor cell proliferation and tumor suppression.
87. Gerbe F, Brulin B, Makrini L, Legraverend C & Jay P (2009) DCAMKL-1 Expression Identifies Tuft Cells Rather Than Stem Cells in the Adult Mouse Intestinal Epithelium. *Gastroenterology* **137:** 2179–2180
88. Gerbe F, Van Es JH, Makrini L, Brulin B, Mellitzer G, Robine S, Romagnolo B, Shroyer NF, Bourgaux JF, Pignodel C, Clevers H & Jay P (2011) Distinct ATOH1 and Neurog3 requirements define tuft cells as a new secretory cell type in the intestinal epithelium. *J. Cell Biol.* **192:** 767–780
89. Gerbe F & Jay P (2016) Intestinal tuft cells: epithelial sentinels linking luminal cues to the immune system. *Mucosal Immunol.* **9:** 1353–9
90. Gerbe F, Legraverend C & Jay P (2012) The intestinal epithelium tuft cells: Specification and function. *Cell. Mol. Life Sci.* **69:** 2907–2917
91. Gerbe F, Sidot E, Smyth DJ, Ohmoto M, Matsumoto I, Dardalhon V, Cesses P, Garnier L, Pouzolles M, Brulin B, Bruschi M, Harcus Y, Zimmermann VS, Taylor N, Maizels RM & Jay P (2016) Intestinal epithelial tuft cells initiate type 2 mucosal immunity to helminth parasites. *Nature* **529:**
92. Gerdes MJ, Sevinsky CJ, Sood A, Adak S & Bello MO (2013) Highly multiplexed single-cell analysis of formalin-fixed , paraffin-embedded cancer tissue. **:** 2–7
93. Giecold G, Marco E, Garcia SP, Trippa L & Yuan G-C (2016) Robust lineage reconstruction from high-dimensional single-cell data. *Nucleic Acids Res.* **44:** e122
94. Giesen C, Wang H a O, Schapiro D, Zivanovic N, Jacobs A, Hattendorf B, Schüffler PJ, Grolimund D, Buhmann JM, Brandt S, Varga Z, Wild PJ, Günther D & Bodenmiller B (2014) Highly multiplexed imaging of tumor tissues with subcellular resolution by mass cytometry. *Nat. Methods* **11:** 417–22
95. Gilloteaux J, Pomerants B & Kelly TS (1989) Human Gallbladder Mucosa Ultrastructure: Evidence of Intraepithelial Nerve Strucutures. *Am. J. Anat.* **184:** 321–33
96. Glick D, Barth S & Macleod KF (2010) Autophagy : cellular and molecular mechanisms. *J. Pathol.* **221:** 3–12
97. Glover LE, Lee JS & Colgan SP (2016) Oxygen metabolism and barrier regulation in the intestinal mucosa. *J. Clin. Invest.* **126:**
98. Goodrich JK, Di Rienzi SC, Poole AC, Koren O, Walters WA, Caporaso JG, Knight R & Ley RE (2014) Conducting a microbiome study. *Cell* **158:** 250–262
99. Goulart R de A, Barbalho SM, Gasparini RG & de Carvalho A de CA (2016) Facing Terminal Ileitis: Going Beyond Crohn's Disease. *Gastroenterol. Res.* **9:** 1–9
100. Gracz A, Fordham MJ, Trotier DC, Zwarycz B, Lo Y-H, Bao K, Starmer J, Shroyer NF, Reinhardt RL & Magness ST (2017) Sox4 drives intestinal secretory differentiation toward tuft and enteroendocrine fates. *bioRxiv***:** 183400
101. Gracz AD, Samsa LA, Fordham MJ, Trotier DC, Zwarycz B, Lo Y-H, Bao K, Starmer J, Raab JR, Shroyer NF, Reinhardt RL & Magness ST (2018) Sox4 Promotes Atoh1-Independent Intestinal Secretory Differentiation Toward Tuft and Enteroendocrine Fates. *Gastroenterology* **155:** 1508–1523.e10
102. Gracz AD, Williamson IA, Roche KC, Johnston MJ, Wang F, Wang Y, Attayek PJ, Balowski J, Liu XF, Laurenza RJ, Gaynor LT, Sims CE, Galanko JA, Li L, Allbritton NL & Magness ST (2015) A high-throughput platform for stem cell niche co-cultures and downstream gene expression analysis. *Nat. Cell Biol.* **17:**
103. Grencis RK & Worthington JJ (2016) Tuft Cells: A New Flavor in Innate Epithelial Immunity. *Trends Parasitol.* **32:** 583–585
104. Grootjans J, Hodin CM, de Haan J-J, Derikx JPM, Rouschop KM a, Verheyen FK, van Dam RM, Dejong CHC, Buurman W a & Lenaerts K (2011) Level of activation of the unfolded protein response correlates with Paneth cell apoptosis in human small intestine exposed to

ischemia/reperfusion. *Gastroenterology* **140:** 529–539.e3
105. Gruber L, Kisling S, Lichti P, Martin FP, May S, Klingenspor M, Lichtenegger M, Rychlik M & Haller D (2013) High Fat Diet Accelerates Pathogenesis of Murine Crohn's Disease-Like Ileitis Independently of Obesity. *PLoS One* **8:** 1–13
106. Grun D, Lyubimova A, Kester L, Wiebrands K, Basak O, Sasaki N, Clevers H & van Oudenaarden A (2015) Single-cell messenger RNA sequencing reveals rare intestinal cell types. *Nature* **525:** 251–255
107. Guilloteau P, Martin L, Eeckhaut V, Ducatelle R, Zabielski R & Van Immerseel F (2010) From the gut to the peripheral tissues: the multiple effects of butyrate. *Nutr. Res. Rev.* **23:** 366–84
108. Gulbransen BD, Clapp TR, Finger TE & Kinnamon SC (2008) Nasal solitary chemoreceptor cell responses to bitter and trigeminal stimulants in vitro. *J. Neurophysiol.* **99:** 2929–2937
109. Gulhane M, Murray L, Lourie R, Tong H, Sheng YH, Wang R, Kang A, Schreiber V, Wong KY, Magor G, Denman S, Begun J, Florin TH, Perkins A, Cuív PÓ, Mcguckin MA & Hasnain SZ (2016) High Fat Diets Induce Colonic Epithelial Cell Stress and Inflammation that is Reversed by IL-22. *Nat. Publ. Gr.*
110. Gunawardene AR, Corfe BM & Staton C a (2011) Classification and functions of enteroendocrine cells of the lower gastrointestinal tract. *Int. J. Exp. Pathol.* **92:** 219–231
111. Haber AL, Biton M, Rogel N, Herbst RH, Shekhar K, Smillie C, Burgin G, Delorey toni M, Howitt MR, Katz Y, Tirosh I, Beyaz S, Dionne D, Zhang M, Raychowdhury R, Garrett WS, Rozenblatt-Rosen O, Shi HN, Yilmaz O, Xavier RJ, et al (2017) A single-cell survey of the small intestinal epithelium. *Nat. Publ. Gr.* **551:** 333–339
112. Habib SJ, Chen B-C, Tsai F-C, Anastassiadis K, Meyer T, Betzig E & Nusse R (2013) A localized Wnt signal orients asymmetric stem cell division in vitro. *Science* **339:** 1445–8
113. Haghverdi L, Buettner F & Theis FJ (2015) Diffusion maps for high-dimensional single-cell analysis of differentiation data. *Bioinformatics* **31:** 2989–2998
114. Halme L, Paavola-sakki P, Turunen U, Lappalainen M, Färkkilä M & Kontula K (2006) Family and twin studies in inflammatory bowel disease. *World J. Gastroenterol.* **12:** 3668–3672
115. Halpern MD, Clark J a, Saunders T a, Doelle SM, Hosseini DM, Stagner AM & Dvorak B (2006) Reduction of experimental necrotizing enterocolitis with anti-TNF-alpha. *Am. J. Physiol. Gastrointest. Liver Physiol.* **290:** G757-64
116. Hams E, Armstrong ME, Barlow JL, Saunders SP, Schwartz C, Cooke G, Fahy RJ, Crotty TB, Hirani N, Flynn RJ, Voehringer D, McKenzie ANJ, Donnelly SC & Fallon PG (2014) IL-25 and type 2 innate lymphoid cells induce pulmonary fibrosis. *Proc. Natl. Acad. Sci. U. S. A.* **111:** 367–72
117. Han M-E, Baek S-J, Kim S-Y, Kang C-D & Oh S-O (2015) ATOH1 Can Regulate the Tumorigenicity of Gastric Cancer Cells by Inducing the Differentiation of Cancer Stem Cells. *PLoS One* **10:**
118. Hansson GC (2012) Role of mucus layers in gut infection and inflammation. *Curr. Opin. Microbiol.* **15:** 57–62
119. Helmby H (2015) Human helminth therapy to treat inflammatory disorders - where do we stand? *BMC Immunol.* **16:** 12
120. Henrik P, Carstens B & Hire D (1976) Malignant fibrillocaveolated cell carcinoma of the human intestinal tract. *Hum. Pathol.* **7:** 505–17
121. Herring CA, Banerjee A, Mckinley ET, Gerdes MJ, Coffey RJ, Lau Correspondence KS, Simmons AJ, Ping J, Roland JT, Franklin JL, Liu Q, Gerdes MJ, Coffey RJ, Lau KS & Lau Correspondence KS (2018) Unsupervised Trajectory Analysis of Single-Cell RNA-Seq and Imaging Data Reveals Alternative Tuft Cell Origins in the Gut. *Cell Syst.* **6:** 37–51.e9
122. Hijiya K (1978) Electron microscope study of the alveolar brush cell. *J. electron Microsc.*

27: 223–7
123. Hijiya K, Okada Y & Tankawa H (1977) Ultrastructural study of the alveolar brush cell. *J. Electron Microsc. (Tokyo).* **26:** 321–9
124. Hildebrand F, Nguyen TLA, Brinkman B, Yunta RG, Cauwe B, Vandenabeele P, Liston A & Raes J (2013) Inflammation-associated enterotypes, host genotype, cage and inter-individual effects drive gut microbiota variation in common laboratory mice. *Genome Biol.* **14:** R4
125. Ho AWY, Wong CK & Lam CWK (2008) Tumor necrosis factor-alpha up-regulates the expression of CCL2 and adhesion molecules of human proximal tubular epithelial cells through MAPK signaling pathways. *Immunobiology* **213:** 533–544
126. Höfer D & Drenckhahn D (1992) Identification of brush cells in the alimentary and respiratory system by antibodies to villin and fimbrin. *Histochemistry* **98:** 237–42
127. Höfer D & Drenckhahn D (1996) Cytoskeletal markers allowing discrimination between brush cells and other epithelial cells of the gut including enteroendocrine cells. *Histochem. Cell Biol.* **105:** 405–12
128. Höfer D, Püschel B & Drenckhahn D (1996) Taste receptor-like cells in the rat gut identified by expression of alpha-gustducin. *Proc. Natl. Acad. Sci. U. S. A.* **93:** 6631–4
129. Hoover B, Baena V, Kaelberer MM, Getaneh F, Chinchilla S & Bohórquez D V. (2017) The intestinal tuft cell nanostructure in 3D. *Sci. Rep.* **7:** 1652
130. Howitt MR, Lavoie S, Michaud M, Blum AM, Tran S V, Weinstock J V, Gallini CA, Redding K, Margolskee RF, Osborne LC, Artis D & Garrett WS (2016) Tuft cells, taste-chemosensory cells, orchestrate parasite type 2 immunity in the gut. *Science* **351:** 1329–33
131. Igarashi M & Guarente L (2016) mTORC1 and SIRT1 Cooperate to Foster Expansion of Gut Adult Stem Cells during Calorie Restriction. *Cell* **166:** 436–450
132. Imajo M, Ebisuya M & Nishida E (2014) Dual role of YAP and TAZ in renewal of the intestinal epithelium. *Nat. Cell Biol.* **17:**
133. In JG, Foulke-Abel J, Estes MK, Zachos NC, Kovbasnjuk O & Donowitz M (2016) Human mini-guts: new insights into intestinal physiology and host-pathogen interactions. *Nat. Rev. Gastroenterol. Hepatol.* **13:** 633–642
134. Ireland H, Houghton C, Howard L & Winton DJ (2005) Cellular inheritance of a Cre-activated reporter gene to determine paneth cell longevity in the murine small intestine. *Dev. Dyn.* **233:** 1332–1336
135. Irish JM, Hovland R, Krutzik PO, Perez OD, Bruserud Ø, Gjertsen BT & Nolan GP (2004) Single cell profiling of potentiated phospho-protein networks in cancer cells. *Cell* **118:** 217–228
136. Isomaki AM (1973) A new cell type (tuft cell) in the gastrointestinal mucosa of the rat. *Acta Pathol. Microbiol. Scand.***:** 1–35
137. Isomäki AM (1973) A new cell type (tuft cell) in the gastrointestinal mucosa of the rat. A transmission and scanning electron microscopic study. *Acta Pathol. Microbiol. Scand. A.***:** Suppl 240:1-35
138. Isomaki AM & Isomäki AM (1962) Electron microscope observations on a special cell type in the gastro-intestinal epithelium of some laboratory animals. *Acta Pathol. Microbiol. Scand.* **154:** 115–8
139. Itzkovitz S, Lyubimova A, Blat IC, Maynard M, van Es J, Lees J, Jacks T, Clevers H & van Oudenaarden A (2011) Single-molecule transcript counting of stem-cell markers in the mouse intestine. *Nat. Cell Biol.* **14:** 106–14
140. Ivanov II, Frutos R de L, Manel N, Yoshinaga K, Rifkin DB, Sartor RB, Finlay BB & Littman DR (2008) Specific microbiota direct the differentiation of IL-17-producing T-helper cells in the mucosa of the small intestine. *Cell Host Microbe* **4:** 337–49
141. Jang H-J, Kokrashvili Z, Theodorakis MJ, Carlson OD, Kim B-J, Zhou J, Kim HH, Xu X, Chan SL, Juhaszova M, Bernier M, Mosinger B, Margolskee RF & Egan JM (2007) Gut-

expressed gustducin and taste receptors regulate secretion of glucagon-like peptide-1. *Proc. Natl. Acad. Sci.* **104:** 15069–15074
142. Ji Z & Ji H (2016) TSCAN: Pseudo-time reconstruction and evaluation in single-cell RNA-seq analysis. *Nucleic Acids Res.* **44:** e117
143. Jijon HB, Walker J, Hoentjen F, Diaz H, Ewaschuk J, Jobin C & Madsen KL (2005) Adenosine is a negative regulator of NF-κB and MAPK signaling in human intestinal epithelial cells. *Cell. Immunol.* **237:** 86–95
144. Johansson ME V, Ambort D, Thaher P, Schütte A, Gustafsson JK, Ermund A, Subramani DB, Holmén-Larsson JM, Thomsson KA, Bergström JH, Van Der Post S, Rodriguez-Piñeiro AM, Sjövall H, Bäckström M & Hansson GC (2011) Composition and functional role of the mucus layers in the intestine. *Cell Mol. Life Sci.* **68:** 3635–3641
145. Johnson FR & Young BA (1968) Undifferentiated cells in gastric mucosa. *J. Anat.* **102:** 541–551
146. Julia V, McSorley SS, Malherbe L, Breittmayer J-P, Girard-Pipau F, Beck A & Glaichenhaus N (2000) Priming by Microbial Antigens from the Intestinal Flora Determines the Ability of CD4+ T Cells to Rapidly Secrete IL-4 in BALB/c Mice Infected with Leishmania major. *J Immunol Ref.* **165:** 5637–5645
147. Kaiko GE, Ryu SH, Koues OI, Collins PL, Solnica-Krezel L, Pearce EJEL, Pearce EJEL, Oltz EM & Stappenbeck TS (2016) The colonic crypt protects stem cells from microbiota-derived metabolites HHS Public Access. *Cell* **165:** 1708–172005
148. Karlsson FH, Tremaroli V, Nookaew I, Bergström G, Behre CJ, Fagerberg B, Nielsen J & Bäckhed F (2013) Gut metagenome in European women with normal, impaired and diabetic glucose control. *Nature* **498:** 99–103
149. Kaser A & Blumberg RS (2011) Autophagy, microbial sensing, endoplasmic reticulum stress, and epithelial function in inflammatory bowel disease. *Gastroenterology* **140:** 1738–1747
150. Kaser A, Lee A, Franke A, Glickman JN, Tilg H, Nieuwenhuis EES, Higgins DE, Glimcher LH & Blumberg RS (2009) XBPI Links ER Stress to Intestinal Inflammation and Confers Genetic Risk for Human Inflammatory Bowel Disease. *Cell* **134:** 743–756
151. Kaske S, Krasteva G, König P, Kummer W, Hofmann T, Gudermann T, Chubanov V, K??nig P, Kummer W, Hofmann T, Gudermann T & Chubanov V (2007) TRPM5, a taste-signaling transient receptor potential ion-channel, is a ubiquitous signaling component in chemosensory cells. *BMC Neurosci.* **8:** 1–12
152. Kawamura S, Miyamoto S & Brown JH (2003) Initiation and transduction of stretch-induced RhoA and Rac1 activation through caveolae. Cytoskeletal regulation of ERK translocation. *J. Biol. Chem.* **278:** 31111–31117
153. Kayahara T, Sawada M, Takaishi S, Fukui H, Seno H, Fukuzawa H, Suzuki K, Hiai H, Kageyama R, Okano H & Chiba T (2003) Candidate markers for stem and early progenitor cells, Musashi-1 and Hes1, are expressed in crypt base columnar cells of mouse small intestine. *FEBS Lett.* **535:** 131–135
154. Kazanjian A, Noah T, Brown D, Burkart J & Shroyer NF (2010) Atonal Homolog 1 Is Required for Growth and Differentiation Effects of Notch/gamma-Secretase Inhibitors on Normal and Cancerous Intestinal Epithelial Cells. *Gastroenterology* **139:** 918–928
155. Keymeulen A Van, Rocha AS, Ousset M, Beck B, Bouvencourt G, Rock J, Sharma N, Dekoninck S & Blanpain C (2011) Distinct stem cells contribute to mammary gland development and maintenance. *Nature* **479:**
156. Kim J-A, Kim D-K, Kang O-H, Choi Y-A, Park H-J, Choi S-C, Kim T-H, Yun K-J, Nah Y-H & Lee Y-M (2005) Inhibitory effect of luteolin on TNF-alpha-induced IL-8 production in human colon epithelial cells. *Int. Immunopharmacol.* **5:** 209–217
157. Kim T-H, Escudero S & Shivdasani R a (2012) Intact function of Lgr5 receptor-expressing intestinal stem cells in the absence of Paneth cells. *Proc. Natl. Acad. Sci. U. S. A.* **109:** 3932–

7
158. Kim T-H, Li F, Ferreiro-Neira I, Ho L-L, Luyten A, Nalapareddy K, Long H, Verzi M & Shivdasani RA (2014) Broadly permissive intestinal chromatin underlies lateral inhibition and cell plasticity. *Nature* **506:** 511–5
159. Klein AM, Mazutis L, Weitz DA, Kirschner MW, Klein AM, Mazutis L, Akartuna I, Tallapragada N, Veres A, Li V & Peshkin L (2015) Droplet Barcoding for Single-Cell Transcriptomics Applied to Embryonic Stem Cells Resource Droplet Barcoding for Single-Cell Transcriptomics Applied to Embryonic Stem Cells. *Cell* **161:** 1187–1201
160. Koizumi H, Higginbotham H, Poon T, Tanaka T, Brinkman BC & Gleeson JG (2006a) Doublecortin maintains bipolar shape and nuclear translocation during migration in the adult forebrain. *Nat. Neurosci.* **9:** 779–786
161. Koizumi H, Tanaka T & Gleeson JG (2006b) doublecortin-like kinase Functions with doublecortin to Mediate Fiber Tract Decussation and Neuronal Migration. *Neuron* **49:** 55–66
162. Koloski N-A, Bret L & Radford-Smith G (2008) Hygiene hypothesis in inflammatory bowel disease: a critical review of the literature. *World J. Gastroenterol.* **14:** 165–73
163. Kontoyiannis D, Boulougouris G, Manoloukos M, Armaka M, Apostolaki M, Pizarro T, Kotlyarov A, Forster I, Flavell R, Gaestel M, Tsichlis P, Cominelli F & Kollias G (2002) Genetic dissection of the cellular pathways and signaling mechanisms in modeled tumor necrosis factor-induced Crohn's-like inflammatory bowel disease. *J. Exp. Med.* **196:** 1563–1574
164. Kontoyiannis D, Pasparakis M, Pizarro TT, Cominelli F & Kollias G (1999) Impaired On / Off Regulation of TNF Biosynthesis in Mice Lacking TNF AU-Rich Elements : Implications for Joint and Gut-Associated Immunopathologies. **10:** 387–398
165. Koo B-K & Clevers H (2014) Stem Cells Marked by the R-Spondin Receptor Lgr5. *Gastroenterology* **147:** 289–302
166. Koren O, Goodrich JK, Cullender TC, Spor A, Laitinen K, Bäckhed HK, Gonzalez A, Werner JJ, Angenent LT, Knight R, Bäckhed F, Isolauri E, Salminen S & Ley RE (2012) Host remodeling of the gut microbiome and metabolic changes during pregnancy. *Cell* **150:** 470–80
167. Kovbasnjuk O, Zachos NC, In J, Foulke-Abel J, Ettayebi K, Hyser JM, Broughman JR, Zeng X, Middendorp S, de Jonge HR, Estes MK & Donowitz M (2013) Human enteroids: preclinical models of non-inflammatory diarrhea. *Stem Cell Res. Ther.* **4 Suppl 1:** S3
168. Kozar S, Morrissey E, Nicholson A, van??der??Heijden M, Zecchini H, Kemp R, Tavar?? S, Vermeulen L & Winton D (2013) Continuous Clonal Labeling Reveals Small Numbers of Functional Stem Cells in Intestinal Crypts and Adenomas. *Cell Stem Cell***:** 626–633
169. Krutzik PO, Irish JM, Nolan GP & Perez OD (2004) Analysis of protein phosphorylation and cellular signaling events by flow cytometry: techniques and clinical applications. *Clin. Immunol.* **110:** 206–21
170. Kugler P, Höfer D, Mayer B & Drenckhahn D (1994) Nitric oxide synthase and NADP-linked glucose-6-phosphate dehydrogenase are co-localized in brush cells of rat stomach and pancreas. *J. Histochem. Cytochem.* **42:** 1317–1321
171. Kumar AA, Delgado AG, Piazuelo MB, Van Kaer L & Olivares-Villagómez D (2017) Innate CD8αα+ lymphocytes enhance anti-CD40 antibody-mediated colitis in mice. *Immunity, Inflamm. Dis.* **5:** 109–123
172. Lancaster MA & Knoblich JA (2014) Organogenesis in a dish: modeling development and disease using organoid technologies. *Science* **345:** 1247125
173. de Lange KM, Moutsianas L, Lee JC, Lamb CA, Luo Y, Kennedy NA, Jostins L, Rice DL, Gutierrez-Achury J, Ji S-G, Heap G, Nimmo ER, Edwards C, Henderson P, Mowat C, Sanderson J, Satsangi J, Simmons A, Wilson DC, Tremelling M, et al (2017) Genome-wide association study implicates immune activation of multiple integrin genes in inflammatory bowel disease. *Nat. Genet.* **49:** 256–261
174. Laplante M & Sabatini DM (2012) mTOR signaling in growth control and disease. *Cell*

149: 274–93
175. Lassen KG, Kuballa P, Conway KL, Patel KK, Becker CE, Peloquin JM, Villablanca EJ, Norman JM, Liu T-C, Heath RJ, Becker ML, Fagbami L, Horn H, Mercer J, Yilmaz OH, Jaffe JD, Shamji AF, Bhan AK, Carr S a, Daly MJ, et al (2014) Atg16L1 T300A variant decreases selective autophagy resulting in altered cytokine signaling and decreased antibacterial defense. *Proc. Natl. Acad. Sci. U. S. A.* **111:** 7741–6
176. Lau KS, Cortez-Retamozo V, Philips SR, Pittet MJ, Lauffenburger DA & Haigis KM (2012) Multi-scale in vivo systems analysis reveals the influence of immune cells on TNF-α-induced apoptosis in the intestinal epithelium. *PLoS Biol.* **10:** e1001393
177. Lau KS, Juchheim AM, Cavaliere KR, Philips SR, Lauffenburger DA & Haigis KM (2011) In vivo systems analysis identifies spatial and temporal aspects of the modulation of TNF-α-induced apoptosis and proliferation by MAPKs. *Sci. Signal.* **4:** ra16
178. Lau KS, Partridge E a., Grigorian A, Silvescu CI, Reinhold VN, Demetriou M & Dennis JW (2007) Complex N-Glycan Number and Degree of Branching Cooperate to Regulate Cell Proliferation and Differentiation. *Cell* **129:** 123–134
179. Lau KS, Schrier SB, Gierut J, Lyons J, Lauffenburger DA & Haigis KM (2013) Network analysis of differential Ras isoform mutation effects on intestinal epithelial responses to TNF-α. *Integr. Biol. (Camb).* **5:** 1355–65
180. Laukoetter MG, Nava P & Nusrat A (2008) Role of the intestinal barrier in inflammatory bowel disease. **14:** 401–407
181. Leelatian N, Doxie DB, Greenplate AR, Mobley BC, Lehman JM, Sinnaeve J, Kauffmann RM, Werkhaven JA, Mistry AM, Weaver KD, Thompson RC, Massion PP, Hooks MA, Kelley MC, Chambless LB, Ihrie RA & Irish JM (2017) Single cell analysis of human tissues and solid tumors with mass cytometry. *Cytom. B Clin. Cytom.*
182. Lei W, Ren W, Ohmoto M, Urban Jr JF, Matsumoto I, Margolskee RF, Jiang P & Lefkowitz RJ (2018) Activation of intestinal tuft cell-expressed Sucnr1 triggers type 2 immunity in the mouse small intestine. *PNAS*
183. Li F, Huang Q, Chen J, Peng Y, Roop DR, Bedford JS & Li C-Y (2010) Apoptotic cells activate the 'phoenix rising' pathway to promote wound healing and tissue regeneration. *Sci. Signal.* **3:** ra13
184. Li N, Nakauka-Ddamba A, Tobias J, Jensen ST & Lengner CJ (2016) Mouse Label-Retaining Cells Are Molecularly And Functionally Distinct From Reserve Intestinal Stem Cells. *Gastroenterology***:** 1–13
185. Li N, Yousefi M, Nakauka-Ddamba A, Jain R, Tobias J, Epstein JA, Jensen ST & Lengner CJ (2014) Single-cell analysis of proxy reporter allele-marked epithelial cells establishes intestinal stem cell hierarchy. *Stem cell reports* **3:** 876–91
186. Liu J, Banerjee A, Herring CA, Hodges E, Lau KS & Gu G (2018) Neurog3-Independent Methylation Is the Earliest Detectable Mark Distinguishing Pancreatic Progenitor Identity. *Dev. Cell* **48:** 49–63.e7
187. Liu JZ, van Sommeren S, Huang H, Ng SC, Alberts R, Takahashi A, Ripke S, Lee JC, Jostins L, Shah T, Abedian S, Cheon JH, Cho J, Dayani NE, Franke L, Fuyuno Y, Hart A, Juyal RC, Juyal G, Kim WH, et al (2015) Association analyses identify 38 susceptibility loci for inflammatory bowel disease and highlight shared genetic risk across populations. *Nat. Genet.* **47:** 979–986
188. Liu T-C & Stappenbeck TS (2016) Genetics and Pathogenesis of Inflammatory Bowel Disease. *Annu. Rev. Pathol.* **11:** 127–148
189. Lopez-Garcia C, Klein AM, Simons BD & Winton DJ (2010) Intestinal stem cell replacement follows a pattern of neutral drift. *Science* **330:** 822–5
190. Lopez J & Grinspan A (2016) Fecal Microbiota Transplantation for Inflammatory Bowel Disease. *Gastroenterol. Hepatol. (N. Y).* **12:** 374–9
191. Luciano L, Ambruckner L, Sewing KF & Reale E (1993) Isolated brush cells of the rat

stomach retain their structural polarity. *Cell Tissue Res.* **271:** 47–57
192. Luciano L, Groos S & Reale E (2003) Brush Cells of Rodent Gallbladder and Stomach Epithelia Express Neurofilaments. *J. Histochem. Cytochem.* **51:** 187–198
193. Luciano L & Reale E (1979) A new morphological aspect of the brush cells of the mouse gallbladder epithelium. *Cell Tissue Res* **201:** 37–44
194. Luciano L & Reale E (1990) Brush cells of the mouse gallbladder: a correlative light- and electron-microscopical study. *Cell Tissue Res.* **262:** 339–49
195. Luciano L & Reale E (1997) Presence of brush cells in the mouse gallbladder. *Microsc. Res. Tech.* **38:** 598–608
196. Manichanh C, Rigottier-Gois L, Bonnaud E, Gloux K, Pelletier E, Frangeul L, Nalin R, Jarrin C, Chardon P, Marteau P, Roca J & Dore J (2006) Reduced diversity of faecal microbiota in Crohn's disease revealed by a metagenomic approach. *Gut* **55:** 205–11
197. Marco E, Karp RL, Guo G, Robson P, Hart AH, Trippa L & Yuan G-C (2014) Bifurcation analysis of single-cell gene expression data reveals epigenetic landscape. *Proc. Natl. Acad. Sci. U. S. A.* **111:** E5643-50
198. Marcobal A, Kashyap PC, Nelson TA, Aronov PA, Donia MS, Spormann A, Fischbach MA & Sonnenburg JL (2013) A metabolomic view of how the human gut microbiota impacts the host metabolome using humanized and gnotobiotic mice. *ISME J.* **7:** 1933–43
199. Martin F-PJ, Wang Y, Sprenger N, Yap IKS, Rezzi S, Ramadan Z, Peré-Trepat E, Rochat F, Cherbut C, van Bladeren P, Fay LB, Kochhar S, Lindon JC, Holmes E & Nicholson JK (2008) Top-down systems biology integration of conditional prebiotic modulated transgenomic interactions in a humanized microbiome mouse model. *Mol. Syst. Biol.* **4:** 205
200. Maseda D, Banerjee A, Johnson EM, Washington MK, Kim H, Lau KS, Crofford LJ, Mauro C, Astier AL, Markiewicz MA, Crofford LJ, Maseda D, Banerjee A, Johnson EM, Washington MK, Kim H & Lau KS (2018) mPGES-1-Mediated Production of PGE2 and EP4 Receptor Sensing Regulate T Cell Colonic Inflammation. *Front. Immunol.* **9:** 2954
201. Matano M, Date S, Shimokawa M, Takano A, Fujii M, Ohta Y, Watanabe T, Kanai T & Sato T (2015) Modeling colorectal cancer using CRISPR-Cas9–mediated engineering of human intestinal organoids. *Nat. Med.* **21:** 256–62
202. Matsumoto I, Ohmoto M, Narukawa M, Yoshihara Y & Abe K (2011) Skn-1a (Pou2f3) specifies taste receptor cell lineage. *Nat. Neurosci.* **14:** 685–687
203. May R, Qu D, Weygant N, Chandrakesan P, Ali N, Lightfoot SA, Li L, Sureban SM & Houchen CW (2014) Dclk1 Deletion in Tuft Cells Results in Impaired Epithelial Repair After Radiation Injury HHS Public Access. *Stem Cells* **32:** 822–827
204. May R, Riehl TE, Hunt C, Sureban SM, Anant S & Houchen CW (2008) Identification of a Novel Putative Gastrointestinal Stem Cell and Adenoma Stem Cell Marker, Doublecortin and CaM Kinase-Like-1, Following Radiation Injury and in Adenomatous Polyposis Coli/Multiple Intestinal Neoplasia Mice. *Stem Cells* **26:** 630–637
205. May R, Sureban SM, Hoang N, Riehl TE, Lightfoot SA, Ramanujam R, Wyche JH, Anant S & Houchen CW (2009) Doublecortin and CaM kinase-like-1 and leucine-rich-repeat-containing G-protein-coupled receptor mark quiescent and cycling intestinal stem cells, respectively. *Stem Cells* **27:** 2571–9
206. McKinley ET, Sui Y, Al-Kofahi Y, Millis BA, Tyska MJ, Roland JT, Santamaria-Pang A, Ohland CL, Jobin C, Franklin JL, Lau KS, Gerdes MJ & Coffey RJ (2017a) Optimized multiplex immunofluorescence single-cell analysis reveals tuft cell heterogeneity. *JCI insight* **2:**
207. McKinley ET, Sui Y, Al-Kofahi Y, Millis BA, Tyska MJ, Roland JT, Santamaria-Pang A, Ohland CL, Jobin C, Franklin JL, Lau KS, Gerdes MJ & Coffey RJ (2017b) (SUPP INFO) Optimized multiplex immunofluorescence single-cell analysis reveals tuft cell heterogeneity. *JCI insight* **2:**
208. McNabb JD & Sandborn E (1964) Filaments in the microvillous border of intestinal cells. *Br. Notes***:** 701–704

209. Meng D, Newburg DS, Young C, Baker A, Tonkonogy SL, Sartor RB, Walker WA & Nanda Nanthakumar N (2007) Bacterial symbionts induce a FUT2-dependent fucosylated niche on colonic epithelium via ERK and JNK signaling. *Am J Physiol Gastrointest Liver Physiol* **293:** 780–787
210. Meyrick B & Reid L (1968) The alveolar brush cell in rat lung - a third pneumocyte. *J. Ultrastruct. Res.* **2900:** 71–80
211. Middelhoff M, Westphalen CB, Hayakawa Y, Yan KS, Gershon MD, Wang TC & Quante M (2017) Dclk1-expressing tuft cells: critical modulators of the intestinal niche? *Am. J. Physiol. Gastrointest. Liver Physiol.* **313:** G285–G299
212. Mills E & O'neill LAJ (2014) Succinate: a metabolic signal in inflammation. *Trends Cell Biol.* **24:** 313–320
213. Miura N, Yamamoto M, Fukutake M, Ohtake N, Iizuka S, Ishige A, Sasaki H, Fukuda K, Yamamoto T & Hayakawa S (2005) Anti-CD3 induces bi-phasic apoptosis in murine intestinal epithelial cells: possible involvement of the Fas/Fas ligand system in different T cell compartments. *Int. Immunol.* **17:** 513–522
214. Miyoshi H, Vandussen KL, Malvin NP, Ryu SH, Wang Y, Sonnek NM, Lai C-W & Stappenbeck TS (2017) Prostaglandin E2 promotes intestinal repair through an adaptive cellular response of the epithelium. *EMBO J.* **36:** 5–24
215. Molodecky N a., Soon IS, Rabi DM, Ghali W a., Ferris M, Chernoff G, Benchimol EI, Panaccione R, Ghosh S, Barkema HW & Kaplan GG (2012) Increasing incidence and prevalence of the inflammatory bowel diseases with time, based on systematic review. *Gastroenterology* **142:** 46–54.e42
216. von Moltke J, Ji M, Liang H-E & Locksley RM (2016) Tuft cell derived IL25 regulates an intestinal ILC2-epithelial response circuit. *Nature* **259:** 221–5
217. Monier B, Gettings M, Gay G, Mangeat T, Schott S, Guarner A & Suzanne M (2015) Apico-basal forces exerted by apoptotic cells drive epithelium folding. *Nature* **518:** 245–248
218. Montgomery RK, Carlone DL, Richmond CA, Farilla L, Kranendonk MEG, Henderson DE, Baffour-Awuah NY, Ambruzs DM, Fogli LK, Algra S & Breault DT (2011) Mouse telomerase reverse transcriptase (mTert) expression marks slowly cycling intestinal stem cells. *Proc. Natl. Acad. Sci. U. S. A.* **108:** 179–84
219. Mori-Akiyama Y, van den Born M, van Es JH, Hamilton SR, Adams HP, Zhang J, Clevers H & de Crombrugghe B (2007) SOX9 Is Required for the Differentiation of Paneth Cells in the Intestinal Epithelium. *Gastroenterology* **133:** 539–546
220. Morroni M, Cangiotti AM & Cinti S (2007) Brush cells in the human duodenojejunal junction: An ultrastructural study. *J. Anat.* **211:** 125–131
221. Mowat AM & Agace WW (2014) Regional specialization within the intestinal immune system. *Nat. Reivews* **14:** 667–685
222. Muñoz J, Stange DE, Schepers AG, van de Wetering M, Koo B-K, Itzkovitz S, Volckmann R, Kung KS, Koster J, Radulescu S, Myant K, Versteeg R, Sansom OJ, van Es JH, Barker N, van Oudenaarden A, Mohammed S, Heck AJR & Clevers H (2012) The Lgr5 intestinal stem cell signature: robust expression of proposed quiescent '+4' cell markers. *EMBO J.* **31:** 3079–91
223. Murthy A, Li Y, Peng I, Reichelt M, Katakam AK, Noubade R, Roose-Girma M, DeVoss J, Diehl L, Graham RR & van Lookeren Campagne M (2014) A Crohn's disease variant in Atg16l1 enhances its degradation by caspase 3. *Nature* **506:** 456–62
224. Murthy A & van Lookeren Campagne M (2014) Understanding Crohn's disease through genetics. *Cell Cycle* **13:** 2803–2804
225. Nabeyama A & Leblond CP (1974) 'Caveolated cells' characterized by deep surface invaginations and abundant filaments in mouse gastro-intestinal epithelia. *Am. J. Anat.* **140:** 147–65
226. Nadjsombati MS, McGinty JW, Lyons-Cohen MR, Jaffe JB, DiPeso L, Schneider C, Miller

CN, Pollack JL, Nagana Gowda GA, Fontana MF, Erle DJ, Anderson MS, Locksley RM, Raftery D & von Moltke J (2018) Detection of Succinate by Intestinal Tuft Cells Triggers a Type 2 Innate Immune Circuit. *Immunity* **49:** 33–41.e7

227. Nakanishi Y, Seno H, Fukuoka A, Ueo T, Yamaga Y, Maruno T, Nakanishi N, Kanda K, Komekado H, Kawada M, Isomura A, Kawada K, Sakai Y, Yanagita M, Kageyama R, Kawaguchi Y, Taketo MM, Yonehara S & Chiba T (2013) Dclk1 distinguishes between tumor and normal stem cells in the intestine. *Nat. Genet.* **45:** 98–103
228. Naser S a, Arce M, Khaja A, Fernandez M, Naser N, Elwasila S & Thanigachalam S (2012) Role of ATG16L, NOD2 and IL23R in Crohn's disease pathogenesis. *World J. Gastroenterol.* **18:** 412–24
229. Nevalainen TJ (1977) Ultrastructural characteristics of tuft cells in mouse gallbladder epithelium. *Acta Anat. (Basel).* **98:** 210–20
230. Nitzan O, Elias M, Peretz A & Saliba W (2016) Role of antibiotics for treatment of inflammatory bowel disease. *World J Gastroenterol* **22:** 1078–1087
231. Noah TK, Donahue B & Shroyer NF (2011) Intestinal development and differentiation. *Exp. Cell Res.* **317:** 2702–10
232. O'Donnell EA, Ernst DN & Hingorani R (2013) Multiparameter Flow Cytometry : Advances in High Resolution Analysis. *Immune Netw.* **13:** 43–54
233. Oike H, Wakamori M, Mori Y, Nakanishi H, Taguchi R, Misaka T, Matsumoto I & Abe K (2006) Arachidonic acid can function as a signaling modulator by activating the TRPM5 cation channel in taste receptor cells. *Biochim. Biophys. Acta - Mol. Cell Biol. Lipids* **1761:** 1078–1084
234. Okamoto K, Hanazaki K, Akimori T, Okabayashi T, Okada T, Kobayashi M & Ogata T (2008) Immunohistochemical and electron microscopic characterization of brush cells of the rat cecum. *Med. Mol. Morphol.* **41:** 145–150
235. Okayasu I, Hatakeyama S, Yamada M, Ohkusa T, Inagaki Y & Nakaya R (1990) A Novel Method in the Induction of Reliable Experimental Acute and Chronic Ulcerative Colitis in Mice
236. Palmer C, Bik EM, DiGiulio DB, Relman DA & Brown PO (2007) Development of the human infant intestinal microbiota. *PLoS Biol.* **5:** e177
237. Patel KK & Stappenbeck TS (2014) Autophagy and Intestinal Homeostasis. *Annu. Rev. Physiol.* **75:** 241–262
238. Patel VA, Massenburg D, Vujicic S, Feng L, Tang M, Litbarg N, Antoni A, Rauch J, Lieberthal W & Levine JS (2015) Apoptotic cells activate AMPK and inhibit epithelial cell growth without change in intracellular energy stores. *J. Biol. Chem.***:** jbc.M115.667345
239. Paul F, Arkin Y, Giladi A, Jaitin DA, Kenigsberg E, Keren-Shaul H, Winter D, Lara-Astiaso D, Gury M, Weiner A, David E, Cohen N, Lauridsen FKB, Haas S, Schlitzer A, Mildner A, Ginhoux F, Jung S, Trumpp A, Porse BT, et al (2015) Transcriptional Heterogeneity and Lineage Commitment in Myeloid Progenitors. *Cell* **163:** 1663–77
240. Pauli C, Hopkins BD, Prandi D, Shaw R, Fedrizzi T, Sboner A, Sailer V, Augello M, Puca L, Rosati R, McNary TJ, Churakova Y, Cheung C, Triscott J, Pisapia D, Rao R, Mosquera JM, Robinson B, Faltas BM, Emerling BE, et al (2017) Personalized In Vitro and In Vivo Cancer Models to Guide Precision Medicine. *Cancer Discov.* **7:** 462–477
241. Paulus U, Loeffler M, Zeidler J, Owen G & Potten CS (1993) The differentiation and lineage development of goblet cells in the murine small intestinal crypt: experimental and modelling studies. *J. Cell Sci.* **106 (Pt 2:** 473–483
242. Pieters T, van Roy F & van Hengel J (2012) Functions of p120ctn isoforms in cell-cell adhesion and intracellular signaling. *Front. Biosci.* **17:** 1669
243. Pizarro TT, Pastorelli L, Bamias G, Garg RR, Reuter BK, Mercado JR, Chieppa M, Arseneau KO, Ley K & Cominelli F (2011) The SAMP1/YitFc Mouse Strain: A Spontaneous Model of Crohn's Disease-Like Ileitis NIH Public Access. *Inflamm Bowel Dis* **17:** 2566–2584
244. Potten CS, Kovacs L & Hamilton E (1974) Continuous labeling studies on mouse skin and

intestine. *Cell Tissue Kinet* **7:** 271–283
245. Potten CS, Owen G & Booth D (2002) Intestinal stem cells protect their genome by selective segregation of template DNA strands. *J. Cell Sci.* **115:** 2381–8
246. Poulin EJ, Powell AE, Wang Y, Li Y, Franklin JL & Coffey RJ (2014) Using a new Lrig1 reporter mouse to assess differences between two Lrig1 antibodies in the intestine. *Stem Cell Res.* **13:** 422–430
247. Powell AE, Wang Y, Li Y, Poulin EJ, Means AL, Washington MK, Higginbotham JN, Juchheim A, Prasad N, Levy SE, Guo Y, Shyr Y, Aronow BJ, Haigis KM, Franklin JL & Coffey RJ (2012) The pan-ErbB negative regulator Lrig1 is an intestinal stem cell marker that functions as a tumor suppressor. *Cell* **149:** 146–58
248. Prater MD, Petit V, Russell IA, Giraddi RR, Shehata M, Menon S, Schulte R, Kalajzic I, Rath N, Olson MF, Metzger D, Faraldo MM, Deugnier M-A, Glukhova MA & Stingl J (2014) Mammary stem cells have myoepithelial cell properties. *Nat. Cell Biol.* **16:**
249. Pyndt Jørgensen B, Krych L, Pedersen TB, Plath N, Redrobe JP, Hansen AK, Nielsen DS, Pedersen CS, Larsen C & Sørensen DB (2015) Investigating the long-term effect of subchronic phencyclidine-treatment on novel object recognition and the association between the gut microbiota and behavior in the animal model of schizophrenia. *Physiol. Behav.* **141:** 32–39
250. Qi Z, Shen L, Zhou H, Jiang Y, Lan L, Luo L & Yin Z (2014) Phosphorylation of heat shock protein 27 antagonizes TNF-alpha induced HeLa cell apoptosis via regulating TAK1 ubiquitination and activation of p38 and ERK signaling. *Cell. Signal.* **26:** 1616–1625
251. Qiu P, Simonds EF, Bendall SC, Gibbs KD, Bruggner R V, Linderman MD, Sachs K, Nolan GP, Plevritis SK & Plevritis SK (2011) Extracting a cellular hierarchy from high-dimensional cytometry data with SPADE. *Nat. Biotechnol.* **29:** 886–91
252. Ramanan D, Bowcutt R, Lee SC, Tang MS, Kurtz ZD, Ding Y, Honda K, Gause WC, Blaser MJ, Bonneau RA, Lim YAL, Loke P & Cadwell K (2016) Helminth infection promotes colonization resistance via type 2 immunity. *Science* **352:** 608–12
253. Ritsma L, Ellenbroek SIJ, Zomer A, Snippert HJ, de Sauvage FJ, Simons BD, Clevers H & van Rheenen J (2014) Intestinal crypt homeostasis revealed at single-stem-cell level by in vivo live imaging. *Nature* **507:** 362–5
254. Rodríguez-Colman MJ, Schewe M, Meerlo M, Stigter E, Gerrits J, Pras-Raves M, Sacchetti A, Hornsveld M, Oost KC, Snippert HJ, Verhoeven-Duif N, Fodde R & Burgering BMT (2017) Interplay between metabolic identities in the intestinal crypt supports stem cell function. *Nature* **543:** 424–427
255. Rojanapo W, Lamb a J & Olson J a (1980) The prevalence, metabolism and migration of goblet cells in rat intestine following the induction of rapid, synchronous vitamin A deficiency. *J. Nutr.* **110:** 178–188
256. Rosenblatt J, Raff MC & Cramer LP (2001) An epithelial cell destined for apoptosis signals its neighbors to extrude it by an actin- and myosin-dependent mechanism. *Curr. Biol.* **11:** 1847–1857
257. Rothenberg ME, Nusse Y, Kalisky T, Lee JJ, Dalerba P, Scheeren F, Lobo N, Kulkarni S, Sim S, Qian D, Beachy PA, Pasricha PJ, Quake SR & Clarke MF (2012) Identification of a cKit(+) colonic crypt base secretory cell that supports Lgr5(+) stem cells in mice. *Gastroenterology* **142:** 1195–1205.e6
258. Roulis M, Armaka M, Manoloukos M, Apostolaki M & Kollias G (2011) Intestinal epithelial cells as producers but not targets of chronic TNF suffice to cause murine Crohn-like pathology. *Proc. Natl. Acad. Sci. U. S. A.* **108:** 5396–401
259. Roulis M, Bongers G, Armaka M, Salviano T, He Z, Singh A, Seidler U, Becker C, Demengeot J, Furtado G, Lira S, Kollias G & Kollias G (2016a) Host and microbiota interactions are critical for development of murine Crohn's-like ileitis. *Mucosal Immunol* **9:** 787–797

260. Roulis M, Bongers G, Armaka M, Salviano T, He Z, Singh A, Seidler U, Becker C, Demengeot J, Furtado GC, Lira SA & Kollias G (2016b) (SUPP INFO) Host and microbiota interactions are critical for development of murine Crohn's-like ileitis. *Mucosal Immunol.* **9:** 787–97
261. Rubin DC (2007) Intestinal morphogenesis. *Curr. Opin. Gastroenterol.* **23:** 111–4
262. Ryan DG, Murphy MP, Frezza C, Prag HA, Chouchani ET, O'Neill LA & Mills EL (2019) Coupling Krebs cycle metabolites to signalling in immunity and cancer. *Nat. Metab.* **1:** 16–33
263. Saez-Rodriguez J, Alexopoulos LG, Epperlein J, Samaga R, Lauffenburger DA, Klamt S & Sorger PK (2009) Discrete logic modelling as a means to link protein signalling networks with functional analysis of mammalian signal transduction. *Mol. Syst. Biol.* **5:** 1–19
264. Saidel-Odes L & Odes S (2014) Hygiene hypothesis in inflammatory bowel disease. *Ann. Gastroenterol.* **27:** 189–190
265. Saitoh T, Fujita N, Jang MH & Akira S (2008) Loss of the autophagy protein Atg16L1 enhances endotoxin-induced IL-1beta production. *Nature* **456:** 264–268
266. Sangiorgi E & Capecchi MR (2008) Bmi1 is expressed in vivo in intestinal stem cells. *Nat. Genet.* **40:** 915–20
267. Sartor RB & Mazmanian SK (2012) Intestinal Microbes in Inflammatory Bowel Diseases. *Am. J. Gastroenterol. Suppl.* **1:** 15–21
268. Sasaki N, Sachs N, Wiebrands K, Ellenbroek SIJ, Fumagalli A, Lyubimova A, Begthel H, van den Born M, van Es JH, Karthaus WR, Li VSW, López-Iglesias C, Peters PJ, van Rheenen J, van Oudenaarden A & Clevers H (2016) Reg4+ deep crypt secretory cells function as epithelial niche for Lgr5+ stem cells in colon. *Proc. Natl. Acad. Sci. U. S. A.* **113:** E5399-407
269. Sato A (2007) Tuft cells. *Anat. Sci. Int.* **82:** 187–199
270. Sato A, Hisanaga Y, Inoue Y, Nagato T & Toh H (2002) Three-dimensional structure of apical vesicles of tuft cells in the main excretory duct of the rat submandibular gland. *Eur. J. Morphol.* **40:** 235–239
271. Sato A & Miyoshi S (1997) Fine structure of tuft cells of the main excretory duct epithelium in the rat submandibular gland. *Anat. Rec.* **248:** 325–331
272. Sato A, Suganuma T, Ide S, Kawano J & Nagato T (2000) Tuft cells in the main excretory duct of the rat submandibular gland. *Eur. J. Morphol.* **38:** 227–231
273. Sato T & Clevers H (2013) Growing Self-Organizing Mini-Guts from a Single Intestinal Stem Cell: Mechanism and Applications. *Science (80-.).* **340:** 1190–1194
274. Sato T, Van Es JH, Snippert HJ, Stange DE, Vries RG, Van Den Born M, Barker N, Shroyer NF, Van De Wetering M & Clevers H (2011a) Paneth cells constitute the niche for Lgr5 stem cells in intestinal crypts.
275. Sato T, Stange DE, Ferrante M, Vries RGJ, Van Es JH, Van Den Brink S, Van Houdt WJ, Pronk A, Van Gorp J, Siersema PD & Clevers H (2011b) Long-term expansion of epithelial organoids from human colon, adenoma, adenocarcinoma, and Barrett's epithelium. *Gastroenterology* **141:** 1762–1772
276. Sato T, Vries RG, Snippert HJ, van de Wetering M, Barker N, Stange DE, van Es JH, Abo A, Kujala P, Peters PJ & Clevers H (2009) Single Lgr5 stem cells build crypt-villus structures in vitro without a mesenchymal niche. *Nature* **459:** 262–265
277. Sbarbati A & Osculati F (2005) The taste cell-related diffuse chemosensory system. *Prog. Neurobiol.***:** 295–307
278. Schaubeck M, Clavel T, Calasan J, Lagkouvardos I, Haange SB, Jehmlich N, Basic M, Dupont A, Hornef M, Bergen M Von, Bleich A & Haller D (2015) Dysbiotic gut microbiota causes transmissible Crohn's disease-like ileitis independent of failure in antimicrobial defence. *Gut***:** 1–13
279. Schneider C, O 'leary CE, Von Moltke J, Pellizzon M, Ma A, Locksley Correspondence RM, Liang H-E, Ang QY, Turnbaugh PJ, Radhakrishnan S & Locksley RM (2018) A Metabolite-Triggered Tuft Cell-ILC2 Circuit Drives Small Intestinal Remodeling. *Cell* **174:** 1–

14
280. Schonhoff SE, Giel-Moloney M & Leiter AB (2004) Neurogenin 3-expressing progenitor cells in the gastrointestinal tract differentiate into both endocrine and non-endocrine cell types. *Dev. Biol.* **270:** 443–54
281. Schulz MD, Atay C, Heringer J, Romrig FK, Schwitalla S, Aydin B, Ziegler PK, Varga J, Reindl W, Pommerenke C, Salinas-Riester G, Böck A, Alpert C, Blaut M, Polson SC, Brandl L, Kirchner T, Greten FR, Polson SW & Arkan MC (2014) High-fat-diet-mediated dysbiosis promotes intestinal carcinogenesis independently of obesity. *Nature* **514:** 508–12
282. Schütz B, Jurastow I, Bader S, Ringer C, von Engelhardt J, Chubanov V, Gudermann T, Diener M, Kummer W, Krasteva-Christ G & Weihe E (2015) Chemical coding and chemosensory properties of cholinergic brush cells in the mouse gastrointestinal and biliary tract. *Front. Physiol.* **6:** 87
283. Schütze S, Tchikov V & Schneider-Brachert W (2008) Regulation of TNFR1 and CD95 signalling by receptor compartmentalization. *Nat. Rev. Mol. Cell Biol.* **9:** 655–662
284. Servén D & Brummitt C (2018) pyGAM: Generalized Additive Models in Python.
285. Setty M, Tadmor MD, Reich-Zeliger S, Angel O, Salame TM, Kathail P, Choi K, Bendall S, Friedman N & Pe'er D (2016) Wishbone identifies bifurcating developmental trajectories from single-cell data. *Nat. Biotechnol.* **34:** 637–45
286. Shin J, Berg DA, Zhu Y, Shin JY, Song J, Bonaguidi MA, Enikolopov G, Nauen DW, Christian KM, Ming G & Song H (2015) Single-Cell RNA-Seq with Waterfall Reveals Molecular Cascades underlying Adult Neurogenesis. *Cell Stem Cell* **17:** 360–72
287. Shroyer NF, Helmrath MA, Wang VY– C, Antalffy B, Henning SJ & Zoghbi HY (2007) Intestine-Specific Ablation of Mouse atonal homolog 1 (Math1) Reveals a Role in Cellular Homeostasis. *Gastroenterology* **132:** 2478–2488
288. Silva DG (1966) The fine structure of multivesicular cells with large microvilli in the epithelium of the mouse colon. *J. Ultrastruct. Res.* **16:** 693–705
289. de Silva MBBS P & Korzenik J (2015) The Changing Epidemiology of Inflammatory Bowel Disease: Identifying New High-risk Populations.
290. Simmons AJ, Banerjee A, McKinley ET, Scurrah CR, Herring CA, Gewin LS, Masuzaki R, Karp SJ, Franklin JL, Gerdes MJ, Irish JM, Coffey RJ & Lau KS (2015) Cytometry-based single-cell analysis of intact epithelial signaling reveals MAPK activation divergent from TNF--induced apoptosis in vivo. *Mol. Syst. Biol.* **11:** 835–835
291. Simmons AJ, Scurrah CR, McKinley ET, Herring CA, Irish JM, Washington MK, Coffey RJ & Lau KS (2016) Impaired coordination between signaling pathways is revealed in human colorectal cancer using single-cell mass cytometry of archival tissue blocks. *Sci. Signal.* **9:** rs11
292. Van der Sluis M, De Koning BAE, De Bruijn ACJM, Velcich A, Meijerink JPP, Van Goudoever JB, Büller HA, Dekker J, Van Seuningen I, Renes IB & Einerhand AWC (2006) Muc2-Deficient Mice Spontaneously Develop Colitis, Indicating That MUC2 Is Critical for Colonic Protection. *Gastroenterology* **131:** 117–129
293. Smith PM, Howitt MR, Panikov N, Michaud M, Gallini CA, Bohlooly-Y M, Glickman JN & Garrett WS (2013) The microbial metabolites, short-chain fatty acids, regulate colonic Treg cell homeostasis. *Science* **341:** 569–73
294. Snippert HJ, van der Flier LG, Sato T, van Es JH, van den Born M, Kroon-Veenboer C, Barker N, Klein AM, van Rheenen J, Simons BD & Clevers H (2010) Intestinal crypt homeostasis results from neutral competition between symmetrically dividing Lgr5 stem cells. *Cell* **143:** 134–44
295. Song KS, Lee WJ, Chung KC, Koo JS, Yang EJ, Choi JY & Yoon JH (2003) Interleukin-1beta and tumor necrosis factor-alpha induce MUC5AC overexpression through a mechanism involving ERK/p38 mitogen-activated protein kinases-MSK1-CREB activation in human airway epithelial cells. *J. Biol. Chem.* **278:** 23243–23250

296. Spalinger MR, Rogler G & Scharl M (2014) Crohn's disease: loss of tolerance or a disorder of autophagy? *Dig. Dis.* **32:** 370–7
297. Spiga L, Winter MG, Carvalho TF de, Zhu W, Hughes ER, Gillis CC, Behrendt CL, Kim J, Chessa D, Andrews-Polymenis HL, Beiting DP, Santos RL, Hooper L V. & Winter SE (2017) An oxidative central metabolism enables Salmonella to utilize microbiota-derived succinate. *Cell Host Microbe* **22:** 291
298. Stappenbeck TS (2010) The role of autophagy in Paneth cell differentiation and secretion. *Mucosal Immunol.* **3:** 8–10
299. Stelzner M, Helmrath M, Dunn JCY, Henning SJ, Houchen CW, Kuo C, Lynch J, Li L, Magness ST, Martin MG, Wong MH, Yu J & NIH Intestinal Stem Cell Consortium (2012) A nomenclature for intestinal in vitro cultures. *Am. J. Physiol. Gastrointest. Liver Physiol.* **302:** G1359-63
300. Stuart T, Butler A, Hoffman P, Hafemeister C, Papalexi E, Mauck WM, Stoeckius M, Smibert P & Satija R (2018) Comprehensive integration of single cell data. *bioRxiv***:** 460147
301. Su J, Chen T, Ji X-Y, Liu C, Yadav PK, Wu R, Yang P & Liu Z (2013) IL-25 Downregulates Th1/Th17 Immune Response in an IL-10–Dependent Manner in Inflammatory Bowel Disease. *Inflamm. Bowel Dis.* **19:** 720–728
302. Subramanian A, Tamayo P, Mootha VK, Mukherjee S, Ebert BL, Gillette MA, Paulovich A, Pomeroy SL, Golub TR, Lander ES & Mesirov JP (2005) Gene set enrichment analysis: a knowledge-based approach for interpreting genome-wide expression profiles. *Proc. Natl. Acad. Sci. U. S. A.* **102:** 15545–50
303. Summers RW, Elliott DE, Qadir K, Urban JF, Thompson R & Weinstock J V. (2003) Trichuris suis seems to be safe and possibly effective in the treatment of inflammatory bowel disease. *Am. J. Gastroenterol.* **98:** 2034–2041
304. Summers RW, Elliott DE, Urban JF, Thompson R, Weinstock J V & Weinstock J V (2005a) Trichuris suis therapy in Crohn's disease. *Gut* **54:** 87–90
305. Summers RW, Elliott DE, Urban JF, Thompson RA & Weinstock J V. (2005b) Trichuris suis therapy for active ulcerative colitis: A randomized controlled trial. *Gastroenterology* **128:** 825–832
306. Takeda N, Jain R, LeBoeuf MR, Wang Q, Lu MM & Epstein JA (2011) Interconversion between intestinal stem cell populations in distinct niches. *Science* **334:** 1420–4
307. Tan B, Lu Z, Dong S, Zhao G & Kuo M-S (2014) Derivatization of the tricarboxylic acid intermediates with O-benzylhydroxylamine for liquid chromatography–tandem mass spectrometry detection. *Anal. Biochem.* **465:** 134–147
308. Tetteh PW, Kretzschmar K, Begthel H, van den Born M, Korving J, Morsink F, Farin H, van Es JH, Offerhaus GJA & Clevers H (2016) Generation of an inducible colon-specific Cre enzyme mouse line for colon cancer research. *Proc. Natl. Acad. Sci.***:** 201614057
309. Tian H, Biehs B, Warming S, Leong KG, Rangell L, Klein OD & de Sauvage FJ (2011) A reserve stem cell population in small intestine renders Lgr5-positive cells dispensable. *Nature* **478:** 255–9
310. Tomas J, Mulet C, Saffarian A, Cavin J-B, Ducroc R, Regnault B, Kun Tan C, Duszka K, Burcelin R, Wahli W, Sansonetti PJ, Pédron T, Bäckhed F, Hooper L V & Turnbaugh P (2016) High-fat diet modifies the PPAR-γ pathway leading to disruption of microbial and physiological ecosystem in murine small intestine. *PNAS* **113:** E5934–E5943
311. Trapnell C, Cacchiarelli D, Grimsby J, Pokharel P, Li S, Morse M, Lennon NJ, Livak KJ, Mikkelsen TS & Rinn JL (2014) The dynamics and regulators of cell fate decisions are revealed by pseudotemporal ordering of single cells. *Nat. Biotechnol.* **32:** 381–386
312. Treutlein B, Brownfield DG, Wu AR, Neff NF, Mantalas GL, Espinoza FH, Desai TJ, Krasnow M a & Quake SR (2014) Reconstructing lineage hierarchies of the distal lung epithelium using single-cell RNA-seq. *Nature* **509:** 371–5
313. Trier JS, Allan CH, Marcial MA & Madara JL (1987) Structural features of the apical and

tubulovesciular membranes of rodent small intestinal tuft cells. *Anat. Rec.* **219:** 69–77
314. Tsai Y-H, VanDussen KL, Sawey ET, Wade AW, Kasper C, Rakshit S, Bhatt RG, Stoeck A, Maillard I, Crawford HC, Samuelson LC & Dempsey PJ (2014) ADAM10 regulates Notch function in intestinal stem cells of mice. *Gastroenterology* **147:** 822–834.e13
315. Tsubouchi S & Leblond CP (1979) Migration and turnover of entero-endocrine and caveolated cells in the epithelium of the descending colon, as shown by radioautography after continuous infusion of 3H-thymidine into mice. *Am. J. Anat.* **156:** 431–51
316. Turnbaugh PJ, Ridaura VK, Faith JJ, Rey FE, Knight R & Gordon JI (2009) The effect of diet on the human gut microbiome: a metagenomic analysis in humanized gnotobiotic mice. *Sci. Transl. Med.* **1:** 6ra14
317. Turner JR (2009) Intestinal mucosal barrier function in health and disease. *Nat. Rev. Immunol.* **9:** 799–809
318. Vaishnava S, Yamamoto M, Severson KM, Ruhn K a, Yu X, Koren O, Ley R, Wakeland EK & Hooper L V (2012) The antibacterial lectin RegIIIgamma promotes the spatial segregation of microbiota and host in the intestine. **334:** 255–258
319. VanDussen KL, Carulli AJ, Keeley TM, Patel SR, Puthoff BJ, Magness ST, Tran IT, Maillard I, Siebel C, Kolterud Å, Grosse AS, Gumucio DL, Ernst SA, Tsai Y-H, Dempsey PJ & Samuelson LC (2012) Notch signaling modulates proliferation and differentiation of intestinal crypt base columnar stem cells. *Development* **139:** 488–97
320. VanDussen KL, Liu T-C, Li D, Towfic F, Modiano N, Winter R, Haritunians T, Taylor KD, Dhall D, Targan SR, Xavier RJ, McGovern DPB & Stappenbeck TS (2014) Genetic variants synthesize to produce paneth cell phenotypes that define subtypes of Crohn's disease. *Gastroenterology* **146:** 200–9
321. Vandussen KL & Samuelson LC (2010) Mouse atonal homolog 1 directs intestinal progenitors to secretory cell rather than absorptive cell fate. *Dev. Biol.* **346:** 215–223
322. Vanhoutvin SALW, Troost FJ, Hamer HM, Lindsey PJ, Koek GH, Jonkers DM a E, Kodde A, Venema K & Brummer RJM (2009) Butyrate-induced transcriptional changes in human colonic mucosa. *PLoS One* **4:** e6759
323. Verissimo CS, Molenaar JJ, Meerman J, Puigvert JC, Lamers F, Koster J, Danen EHJ, van de Water B, Versteeg R, Fitzsimons CP & Vreugdenhil E (2010) Silencing of the microtubule-associated proteins doublecortin-like and doublecortin-like kinase-long induces apoptosis in neuroblastoma cells. *Endocr. Relat. Cancer* **17:** 399–414
324. Waddington CH (1957) The strategy of the genes. A discussion of some aspects of theoretical biology. *Strateg. genes. A Discuss. some Asp. Theor. Biol. With an Append. by H. Kacser.*
325. Wehkamp J, Götz M, Herrlinger K, Steurer W & Stange EF (2016) Inflammatory Bowel Disease. *Dtsch. Arztebl. Int.* **113:** 72–82
326. Wehkamp J, Salzman NH, Porter E, Nuding S, Weichenthal M, Petras RE, Shen B, Schaeffeler E, Schwab M, Linzmeier R, Feathers RW, Chu H, Lima H, Fellermann K, Ganz T, Stange EF & Bevins CL (2005) Reduced Paneth cell alpha-defensins in ileal Crohn's disease. *Pro* **102:** 18129–18134
327. Wehkamp J, Wang G, Ku I, Nuding S, Gregorieff A, Schnabel A, Kays RJ, Fellermann K, Burk O, Schwab M, Clevers H, Bevins CL & Stange EF (2007) The Paneth Cell a-Defensin Deficiency of Ileal Crohn's Disease Is Linked to Wnt / Tcf-4 1. *J. Immunol.*
328. Welch JD, Hartemink AJ & Prins JF (2016) SLICER: inferring branched, nonlinear cellular trajectories from single cell RNA-seq data. *Genome Biol.* **17:** 106
329. Westphalen CB, Asfaha S, Hayakawa Y, Takemoto Y, Lukin DJ, Nuber AH, Brandtner A, Setlik W, Remotti H, Muley A, Chen X, May R, Houchen CW, Fox JG, Gershon MD, Quante M & Wang TC (2014) Long-lived intestinal tuft cells serve as colon cancer–initiating cells. *J. Clin. Invest.* **124:**
330. Wilen CB, Lee S, Hsieh LL, Orchard RC, Desai C, Hykes BL, McAllaster MR, Balce DR,

Feehley T, Brestoff JR, Hickey CA, Yokoyama CC, Wang Y-T, MacDuff DA, Kreamalmayer D, Howitt MR, Neil JA, Cadwell K, Allen PM, Handley SA, et al (2018) Tropism for tuft cells determines immune promotion of norovirus pathogenesis. *Science (80-.).* **360:** 204–208

331. Williams JM, Duckworth C a, Watson AJM, Frey MR, Miguel JC, Burkitt MD, Sutton R, Hughes KR, Hall LJ, Caamaño JH, Campbell BJ & Pritchard DM (2013) A mouse model of pathological small intestinal epithelial cell apoptosis and shedding induced by systemic administration of lipopolysaccharide. *Dis. Model. Mech.* **6:** 1388–99
332. Wong VWY, Stange DE, Page ME, Buczacki S, Wabik A, Itami S, van de Wetering M, Poulsom R, Wright NA, Trotter MWB, Watt FM, Winton DJ, Clevers H & Jensen KB (2012) Lrig1 controls intestinal stem-cell homeostasis by negative regulation of ErbB signalling. *Nat. Cell Biol.* **14:** 401–8
333. Wright N & Alison M (1984) The biology of epithelial cell populations
334. Wu GD, Chen J, Hoffmann C, Bittinger K, Chen Y-Y, Keilbaugh SA, Bewtra M, Knights D, Walters WA, Knight R, Sinha R, Gilroy E, Gupta K, Baldassano R, Nessel L, Li H, Bushman FD & Lewis JD (2011) Linking long-term dietary patterns with gut microbial enterotypes. *Science* **334:** 105–8
335. Wu H, Wang G, Li S, Zhang M, Li H & Wang K (2015) TNF-a- Mediated-p38-Dependent Signaling Pathway Contributes to Myocyte Apoptosis in Rats Subjected to Surgical Trauma. *Cell. Physiol. Biochem.* **150081:** 1454–1466
336. Xing Y, Su TT & Ruohola-baker H (2015) Tie-mediated signal from apoptotic cells protects stem cells in Drosophila melanogaster. *Nat. Commun.* **6:** 1–11
337. Yamashita J, Ohmoto M, Yamaguchi T, Matsumoto I & Hirota J (2017) Skn-1a/Pou2f3 functions as a master regulator to generate Trpm5-expressing chemosensory cells in mice. *PLoS One* **12:** e0189340
338. Yamashita S (2007) Heat-induced antigen retrieval: mechanisms and application to histochemistry. *Prog. Histochem. Cytochem.* **41:** 141–200
339. Yan KS, Chia LA, Li X, Ootani A, Su J, Lee JY, Su N, Luo Y, Heilshorn SC, Amieva MR, Sangiorgi E, Capecchi MR & Kuo CJ (2011) The intestinal stem cell markers Bmi1 and Lgr5 identify two functionally distinct populations. *Proc. Natl. Acad. Sci. U. S. A.* **109:** 466–71
340. Yan KS, Gevaert O, Zheng GXY, Anchang B, Probert CS, Larkin KA, Davies PS, Cheng Z, Kaddis JS, Han A, Roelf K, Calderon RI, Cynn E, Hu X, Mandleywala K, Wilhelmy J, Grimes SM, Corney DC, Boutet SC, Terry JM, et al (2017a) Intestinal Enteroendocrine Lineage Cells Possess Homeostatic and Injury-Inducible Stem Cell Activity. *Cell Stem Cell* **21:** 78–90.e6
341. Yan KS, Janda CY, Chang J, Zheng GXY, Larkin KA, Luca VC, Chia LA, Mah AT, Han A, Terry JM, Ootani A, Roelf K, Lee M, Yuan J, Li X, Bolen CR, Wilhelmy J, Davies PS, Ueno H, von Furstenberg RJ, et al (2017b) Non-equivalence of Wnt and R-spondin ligands during Lgr5(+) intestinal stem-cell self-renewal. *Nature* **545:** 238–242
342. Yano T & Kurata S (2009) An unexpected twist for autophagy in Crohn's disease. **10:** 134–136
343. Yilmaz OH, Katajisto P, Lamming DW & Sabitini DM (2012) mTORC1 in the Paneth cell niche couples ISC function to calorie intake. *Nature* **486:** 490–495
344. Yousefi M, Li L & Lengner CJ (2017) Hierarchy and Plasticity in the Intestinal Stem Cell Compartment. *Trends Cell Biol.* **xx:** 1–12
345. Yu L, Zhao Y, Xu S, Jin C, Wang M & Fu G (2014) Leptin confers protection against TNF-α-induced apoptosis in rat cardiomyocytes. *Biochem. Biophys. Res. Commun.* **455:** 126–132
346. Zachos NC, Kovbasnjuk O, Foulke-Abel J, In J, Blutt SE, De Jonge HR, Estes MK & Donowitz M (2015) Human Enteroids/Colonoids and Intestinal Organoids Functionally Recapitulate Normal Intestinal Physiology and Pathophysiology. *J. Biol. Chem.*
347. Zackular JP, Moore JL, Jordan AT, Juttukonda LJ, Noto MJ, Nicholson MR, Crews JD, Semler MW, Zhang Y, Ware LB, Washington MK, Chazin WJ, Caprioli RM & Skaar EP (2016) Dietary zinc alters the microbiota and decreases resistance to Clostridium difficile infection.

Nat. Med. **22:** 1330–1334
348. Zackular JP, Rogers MAM, Ruffin MT, Schloss PD & Schloss PD (2014) The human gut microbiome as a screening tool for colorectal cancer. *Cancer Prev. Res. (Phila).* **7:** 1112–21
349. Zheng L, Kelly CJ & Colgan SP (2015) Physiologic hypoxia and oxygen homeostasis in the healthy intestine. A Review in the Theme: Cellular Responses to Hypoxia.
350. Zhou Y, Rychahou P, Wang Q, Weiss HL & Evers BM (2015) TSC2/mTORC1 signaling controls Paneth and goblet cell differentiation in the intestinal epithelium. *Cell Death Dis.* **6:** e1631
351. Zhu J, Djukovic D, Deng L, Gu H, Himmati F, Chiorean EG & Raftery D (2014) Colorectal Cancer Detection Using Targeted Serum Metabolic Profiling. *J. Proteome Res.* **13:** 4120–4130
352. Zunder ER, Lujan E, Goltsev Y, Wernig M & Nolan GP (2015) A continuous molecular roadmap to iPSC reprogramming through progression analysis of single-cell mass cytometry. *Cell Stem Cell* **16:** 323–37